Universität Hamburg
DER FORSCHUNG | DER LEHRE | DER BILDUNG

BNITM
Bernhard Nocht Institute for Tropical Medicine

Stem cell marker analysis of glioblastoma tumor cells and infection studies using Zika virus protein E pseudotyped lentiviral particles

Dissertation

submitted to the Faculty of Mathematics, Informatics

and Natural Sciences of the University of Hamburg, Department of Chemistry,

for the acquisition of the Doctorate of Natural Sciences (Dr. rer. nat.)

submitted by

Jan Patrick Formanski

Hamburg, November 2025

First Reviewer: Prof. Dr. Andrew Torda

Second Reviewer: Dr. Michael Schreiber

Oral defense committee:

Chair: Prof. Dr. Andrew Torda

Deputy Chair: Prof. Dr. Chris Meier

Member: Prof. Dr. Zoya Ignatova

Member: Dr. Michael Schreiber

Member: Dr. Pietro Scaturro

Date of disputation:

March 27th 2026

This dissertation was performed in the period from March 2022 to November 2025. The experiments were carried out in the laboratory group of Dr. Michael Schreiber in the Department of Virology at the Bernhard Nocht Institute for Tropical Medicine in Hamburg.

I. List of publications

Pöhlking, C., Beier, S., **Formanski, J.P.**, Friese, M., Schreiber, M., & Schwalbe, B. Isolation of Cells from Glioblastoma Multiforme Grade 4 Tumors for Infection with Zika Virus prME and ME Pseudotyped HIV-1. *Int. J. Mol. Sci.* **24**, 4467 (2023).

Grunwald, V., Ngo, H. D., **Formanski, J. P.**, Jonas, J. S., Pöhling, C., Schwalbe, B. & Schreiber, M. Development of Zika Virus E Variants for Pseudotyping Retroviral Vectors Targeting Glioblastoma Cells. *Int. J. Mol. Sci.* **24**, 14487 (2023)

Ngo, H. D., **Formanski, J. P.**, Grunwald, V., Schwalbe, B. & Schreiber, M. Generation of Viral Particles with Brain Cell-Specific Tropism by Pseudotyping HIV-1 with the Zika Virus E Protein. *Methods Protoc.* **7**, 3 (2023)

Formanski, J. P., Ngo, H. D., Grunwald, V., Pöhlking, C., Jonas, J. S., Wohler, D., Schwalbe, B. & Schreiber, M. Transduction Efficiency of Zika Virus E Protein Pseudotyped HIV-1gfp and Its Oncolytic Activity Tested in Primary Glioblastoma Cell Cultures. *Cancers (Basel).* **16**, 814 (2024)

II. Table of Contents

I. List of publications I

II. Table of Contents II

III. List of Figures VII

IV. List of Tables IX

V. List of Abbreviations X

Zusammenfassung XIV

Abstract XV

1. Introduction 1

1.1. The glioblastoma brain tumor and its origin 1

1.2. Heterogeneity of glioblastoma 3

1.3. The tumor niches of glioblastoma and the role of glioblastoma stem cells 5

1.3.1. The hypoxic-necrotic niche 5

1.3.2. The perivascular niche 5

1.3.3. The invasive niche 6

1.3.4. The subventricular zone 6

1.4. Biological markers characterizing glioblastoma 8

1.4.1. Glioblastoma stem cell markers 8

1.4.1.1 SOX2 8

1.4.1.2 OCT4 9

1.4.1.3 NANOG 9

1.4.1.4 Nestin 10

1.4.1.5 CD44 11

1.4.1.6 CD133 12

1.4.1.7 ITGA6 12

1.4.1.8 GFAP 13

1.4.2. Markers associated with glioblastoma 13

1.4.2.1 EGFR 13

1.4.2.2 PD-1 14

1.4.3. Markers associated with Zika virus infection 15

1.4.3.1 AXL/Gas6 15
1.4.3.2 Integrin $\alpha_v\beta_5$ 16
1.5. Oncolytic Viruses 17
1.6. Zika virus and its tropism 18
1.7. Viral pseudotyped particles 19
1.7.1. ZIKV pseudotyped particles 19
1.8. Aim of this thesis 22
2. Material and Methods 23
2.1. Material 23
2.1.1. Devices 23
2.1.2. Consumables 24
2.1.3. Biochemicals and Kits 25
2.1.4. Antibodies and Cell Staining Reagents 27
2.1.5. Chemicals 29
2.1.6. Plasmids and primers 30
2.1.7. Cells 31
2.1.8. Software 31
2.1.9. Use of Artificial Intelligence Assisted Tools 31
2.2. Methods 33
2.2.1. Media and agar plates 33
2.2.2. Manufacturing of competent DH5α cells 33
2.2.3. Bacterial transformation with heat shock 34
2.2.4. Polymerase chain reaction 34
2.2.5. Gel electrophoresis 35
2.2.6. Gibson assembly 37
2.2.7. Mini plasmid extraction 38
2.2.8. Midi plasmid extraction 38
2.2.9. Ethanol precipitation 39

2.2.10. Measurement and adjustment of DNA concentration 39
2.2.11. Isolation and cultivation of eukaryotic tumor cells 40
2.2.12. Mammalian cell cultivation 40
2.2.13. Preparation of transfection reagent 41
2.2.14. Transfection 41
2.2.15. Infection of tumor cells 42
2.2.16. Antibody staining 43
2.2.17. Verification of integrin $\alpha_v\beta_5$ expression through antibody staining 43
3. Results 45
3.1. Diagnostic biomarkers of glioblastoma tumor samples 45
3.2. Cultivation of primary glioblastoma cell cultures 46
3.2.1. Growth characteristics of the primary glioblastoma cell culture AKH-19 47
3.2.2. Growth of AKH-17, AKH-21S, and AKH-21C 51
3.3. Identification of glioblastoma biomarkers 52
3.3.1. Characterization of primary cell culture AKH-5 53
3.3.2. Characterization of primary cell culture AKH-9 55
3.3.3. Characterization of primary cell culture AKH-10 57
3.3.4. Characterization of primary cell culture AKH-11 59
3.3.5. Characterization of primary cell culture AKH-12 61
3.3.6. Characterization of primary cell culture AKH-13 63
3.3.7. Characterization of primary cell culture AKH-14 65
3.3.8. Characterization of primary cell culture AKH-15 67
3.3.9. Characterization of primary cell culture AKH-16 69
3.3.10. Characterization of primary cell culture AKH-17 71
3.3.11. Characterization of primary cell culture AKH-18 73
3.3.12. Characterization of primary cell culture AKH-19 75
3.3.13. Characterization of primary cell culture AKH-20 77
3.3.14. Characterization of primary cell culture AKH-21S 79

3.3.15. Characterization of primary cell culture AKH-21C 81
3.3.16. Characterization of primary cell culture AKH-23 83
3.3.17. Characterization of primary cell culture AKH-24S 85
3.3.18. Characterization of primary cell culture AKH-24C 87
3.3.19. Characterization of U-87 cell culture 89
3.3.20. Summary of marker expression for all glioblastoma cell cultures 91
3.4. Cloning of E protein with a modified transmembrane region 93
3.4.1. Synthesis of expression vector pCMV-EG1 93
3.4.2. Synthesis of expression vector pMD2-EG2 96
3.5. Transfection of COS-1 cells for pseudotype generation 99
3.6. Infection of primary cell cultures with pseudotyped viral particles 102
3.6.1. Infection of AKH-13 cells 103
3.6.2. Infection of AKH-14 cells 104
3.6.3. Infection of AKH-15 cells 107
3.6.4. Infection of AKH-16 cells 107
3.6.5. Infection of AKH-17 cells 108
3.6.6. Infection of AKH-19 cells 113
3.6.7. Infection of AKH-20 cells 114
3.6.8. Infection of AKH-23 cells 115
3.6.9. Infection of AKH-24C cells 116
3.6.10. Infection of U-87 cells 117
3.7. Identification of integrin $\alpha_v\beta_5$ in primary glioblastoma cell cultures 118
4. Discussion 120
4.1. Primary glioblastoma cell culture model 120
4.2. Biomarker analysis of primary glioblastoma cell cultures 123
4.3. ZIKV E pseudotypes as therapeutics against glioblastoma 125
5. Outlook 130
6. Bibliography 131

7. Appendix 152
7.1. Appendix figures 152
7.2. List of Hazardous Substances according to GHS 159
8. Acknowledgements 161
9. Affidavit 162

III. List of Figures

Fig. 1 Glioblastoma stem cells as the main drivers of tumor recurrence. 2
Fig. 2 The subventricular zone and its associated layers in the human brain. 7
Fig. 3 Differences in virus assembly of HIV-1 and ZIKV. 21
Fig. 4 Growth characteristics of AKH-19 cells in CSF-DF. 48
Fig. 5 Growth characteristics of AKH-19 cells in CSF-DF on specific days. 49
Fig. 6 AKH-19 cell culture after 12 weeks growth in CSF-DF. 50
Fig. 7 Cell growth of AKH-17, AKH-21S, and AKH-21C. 51
Fig. 8 ZIKV receptor analysis for AKH-5. 53
Fig. 9 GSC and GBM biomarker analysis for AKH-5. 54
Fig. 10 ZIKV receptor analysis for AKH-9. 55
Fig. 11 GSC and GBM biomarker analysis for AKH-9. 56
Fig. 12 ZIKV receptor analysis for AKH-10. 57
Fig. 13 GSC and GBM biomarker analysis for AKH-10. 58
Fig. 14 ZIKV receptor analysis for AKH-11. 59
Fig. 15 GSC and GBM biomarker analysis for AKH-11. 60
Fig. 16 ZIKV receptor analysis for AKH-12. 61
Fig. 17 GSC and GBM biomarker analysis for AKH-12. 62
Fig. 18 ZIKV receptor analysis for AKH-13. 63
Fig. 19 GSC and GBM biomarker analysis for AKH-13. 64
Fig. 20 ZIKV receptor analysis for AKH-14. 65
Fig. 21 GSC and GBM biomarker analysis for AKH-14. 66
Fig. 22 ZIKV receptor analysis for AKH-15. 67
Fig. 23 GSC and GBM biomarker analysis for AKH-15. 68
Fig. 24 ZIKV receptor analysis for AKH-16. 69
Fig. 25 GSC and GBM biomarker analysis for AKH-16. 70
Fig. 26 ZIKV receptor analysis for AKH-17. 71
Fig. 27 GSC and GBM biomarker analysis for AKH-17. 72
Fig. 28 ZIKV receptor analysis for AKH-18. 73
Fig. 29 GSC and GBM biomarker analysis for AKH-18. 74
Fig. 30 ZIKV receptor analysis for AKH-19. 75
Fig. 31 GSC and GBM biomarker analysis for AKH-19. 76
Fig. 32 ZIKV receptor analysis for AKH-20. 77
Fig. 33 GSC and GBM biomarker analysis for AKH-20. 78

Fig. 34 ZIKV receptor analysis for AKH-21S. 79
Fig. 35 GSC and GBM biomarker analysis for AKH-21S. 80
Fig. 36 ZIKV receptor analysis for AKH-21C. 81
Fig. 37 GSC and GBM biomarker analysis for AKH-21C. 82
Fig. 38 ZIKV receptor analysis for AKH-23. 83
Fig. 39 GSC and GBM biomarker analysis for AKH-23. 84
Fig. 40 ZIKV receptor analysis for AKH-24S. 85
Fig. 41 GSC and GBM biomarker analysis for AKH-24S. 86
Fig. 42 ZIKV receptor analysis for AKH-24C. 87
Fig. 43 GSC and GBM biomarker analysis for AKH-24C. 88
Fig. 44 ZIKV receptor analysis for U-87. 89
Fig. 45 GSC and GBM biomarker analysis for U-87. 90
Fig. 46 Overview of the construction of pCMV-EG1. 94
Fig. 47 Codon sequence as triplets with translational amino acids of pCMV-EG1. 95
Fig. 48 Overview of the construction of pMD2-EG2. 97
Fig. 49 Codon sequence as triplets with translational amino acids of pMD2-EG2. 98
Fig. 50 Transfection of COS-1 cells. 101
Fig. 51 AKH-13 cells infected with EG1-HIV*gfp*, EG2-HIV*gfp*, and G-HIV*gfp* pseudotyped viral particles. 103
Fig. 52 AKH-14 cells infected with EG1-HIV*gfp* pseudotyped viral particles. 104
Fig. 53 AKH-14 cells infected with EG2-HIV*gfp* pseudotyped viral particles. 105
Fig. 54 AKH-14 cells infected with G-HIV*gfp* pseudotyped viral particles. 106
Fig. 55 AKH-15 cells infected with G-HIV*gfp* pseudotyped viral particles. 107
Fig. 56 AKH-16 cells infected with G-HIV*gfp* pseudotyped viral particles. 107
Fig. 57 AKH-17 cells infected with EG1-HIV*gfp* pseudotyped viral particles. 109
Fig. 58 AKH-17 cells infected with EG1-HIV*gfp* pseudotyped viral particles. 110
Fig. 59 AKH-17 cells infected with EG2-HIV*gfp* pseudotyped viral particles. 111
Fig. 60 AKH-17 cells infected with G-HIV*gfp* pseudotyped viral particles. 112
Fig. 61 AKH-19 cells infected with EG1-HIV*gfp*, EG2-HIV*gfp*, and G-HIV*gfp* pseudotyped viral particles. 113
Fig. 62 AKH-20 cells infected with EG1-HIV*gfp*, EG2-HIV*gfp*, and G-HIV*gfp* pseudotyped viral particles. 114
Fig. 63 AKH-23 cells infected with EG2-HIV*gfp* and G-HIV*gfp* pseudotyped viral particles. 115

Fig. 64 AKH-24C cells infected with ET-HIV*gfp* and G-HIV*gfp* pseudotyped viral particles. 116
Fig. 65 U87 cells infected with G-HIV*gfp* pseudotyped viral particles. 117
Fig. 66 Expression of integrin $\alpha_v\beta_5$ in different primary GBM cell cultures over time. .. 119
Fig. A1 Identification of integrin $\alpha_v\beta_5$ in AKH-5 cells. 152
Fig. A2 Identification of integrin $\alpha_v\beta_5$ in AKH-9 cells. 153
Fig. A3 Identification of integrin $\alpha_v\beta_5$ in AKH-10 cells. 154
Fig. A4 Identification of integrin $\alpha_v\beta_5$ in AKH-11 cells. 155
Fig. A5 Identification of integrin $\alpha_v\beta_5$ in AKH-12 cells. 156
Fig. A6 Identification of integrin $\alpha_v\beta_5$ in AKH-13 cells. 157
Fig. A7 Workflow for the preparation of GBM tumor tissue for cell culture. 158

IV. List of Tables

Table 1 Devices 23
Table 2 Consumables 24
Table 3 Biochemicals 25
Table 4 Biochemical Kits 26
Table 5 Primary antibodies 27
Table 6 Secondary antibodies 28
Table 7 Other immunostaining agents 28
Table 8 Chemicals 29
Table 9 Plasmids 30
Table 10 Primers 30
Table 11 Eucaryotic and procaryotic cells 31
Table 12 Used software 31
Table 13 Ingredients for the manufacturing of different growth media 33
Table 14 TFB I and TFB II buffer composition 34
Table 15 Standard PCR and approaches for synthesized plasmids 35
Table 16 PCR conditions 35
Table 17 Composition of 50x TAE buffer solution in 1 L ddH_2O 36
Table 18 5x ISO buffer 37
Table 19 Gibson assembly mix 37
Table 20 Composition for the preparation of a 1L solution of 10x PBS buffer 41

Table 21 Plasmid combinations with corresponding pseudotypes 42
Table 22 Parameters of GBM tumors used for generation of primary cell cultures 45
Table 23 Growth rates of freshly isolated tumor cells in three different media 46
Table 24 Expression patterns of markers in glioblastoma cell cultures..... 91

V. List of Abbreviations

2D	two-dimensional
3D	three-dimensional
AKH	Asklepios Clinic Nord Heidberg
APC	astrocyte-like progenitor cell
ATP	adenosine triphosphate
BSA	bovine serum albumin
CAR	chimeric antigen receptor
Cas9	CRISPR-associated protein 9
CNS	central nervous system
COS-1	CV-1 cells transformed with the SV40 large T antigen
CRISPR	Clustered Regularly Interspaced Short Palindromic Repeats
CSF	cerebrospinal fluid
CSF-DF	1:1 mixture of DMEM/10% FBS with hCSF
CY	cytoplasmic
DAPI	4′,6-diamidino-2-phenylindole
dATP	deoxyadenosine triphosphate
dCTP	deoxycytidine triphosphate
ddH_2O	double distilled water
DF	DMEM/10% FBS
dGTP	deoxyguanosine triphosphate
DMEM	Dulbecco´s Modified Eagle Medium
DNA	deoxyribonucleic acid
dNTP	deoxynucleotide triphosphate
dTTP	deoxythymidine triphosphate
DPBS	Dulbecco's Phosphate Buffered Saline
dYT	double yeast tryptone

ECM	extracellular matrix
EDTA	ethylenediaminetetraacetic acid
EGF	epidermal growth factor
EGFR	epidermal growth factor receptor
ER	endosomal reticulum
ESCRT	endosomal sorting complexes required for transport
EU	European Union
FBS	fetal bovine serum
FDA	Food and Drug Administration
FGFR1	fibroblast growth factor receptor 1
GBM	glioblastoma
GFAP	glial fibrillary acidic protein
GFP	green fluorescent protein
GPC	glial progenitor cell
GSC	glioblastoma stem cell
HA	hyaluronic acid
hCSF	human cerebrospinal fluid
HEK	human embryonic kidney
HEPES	4-(2-hydroxyethyl)-1-piperazineethanesulfonic acid
HIF	hypoxia-inducible factor
HIV-1	human immunodeficiency virus 1
HSV	herpes simplex virus
IDH-1	isocitrate dehydrogenase 1
ISO	isothermal
ITGA6	integrin α6
ITH	intratumor heterogeneity
LAV	live-attenuated virus
LB	liquid broth
LC-MS	liquid crystal mass spectrometry
LDLR	low-density lipoprotein receptor
Luc	luciferase
MGMT	O6-methylguanine-DNA-methyltransferase

MLV	murine leukemia virus
MOPS	3-(*N*-morpholino) propanesulfonic acid
MSC	mesenchymal-like cell
NAD	nicotinamide adenine dinucleotide
NPC	neural progenitor-like cell
NS	non-structural
OCT4	octamer-binding transcription factor 4
OPC	oligodendrocyte-like progenitor cell
ORF	open reading frame
OV	oncolytic virus
PBS	phosphate buffered saline
PBS-T	phosphate buffered saline with 0.05% Tween
PCR	polymerase chain reaction
PD-1	programmed cell death protein 1
PD-L1/2	programmed cell death-ligand 1/2
PDK1	3-phosphoinositide-dependent protein kinase-1
PEG	polyethylene glycol
PEI	polyethyleneimine
PTFE	polytetrafluoroethylene
PVN	perivascular niche
RNA	ribonucleic acid
rpm	rounds per minute
RT	room temperature
SARS-CoV-2	severe acute respiratory syndrome coronavirus 2
scRNA-seq	single-cell RNA sequencing
SHP-2	Src homology region 2 domain-containing phosphatase-2
siRNA	small interfering RNA
SOX2	(sex determining region Y)-box 2
SVZ	subventricular zone
TAA	tumor-associated astrocyte
TAE	TRIS acetate EDTA
TAM	tumor-associated macrophage

TERT	telomerase reverse transcriptase
TFB	transformation buffer
TIC	tumor-initiating cells
TIL	tumor-invading lymphocytes
TM	transmembrane
TRIS	tris(hydroxymethyl)aminomethane
USA	United States of America
VEGF	vascular endothelial growth factor
VSV	vesicular stomatitis virus
WHO	World Health Organization
YT	yeast tryptone
ZIKV	Zika virus

Zusammenfassung

Im Rahmen dieser Arbeit wurde ein neuartiges Zellkultursystem für Zellen des Glioblastoms (GBM) entwickelt. Dafür wurden GBM-Tumorproben verwendet, die aus Bereichen nahe der subventrikulären Zone (SVZ) entnommen wurden. Diese Bereiche enthalten eine große Anzahl GBM-Stammzellen (GSCs) und Astrozyten-ähnlicher Stammzellen. Es konnte gezeigt werden, dass die Zellkulturen mithilfe des eingesetzten CSF-DF-Mediums ihre Heterogenität über einen Zeitraum von mindestens drei Monaten beibehielten. Auf dieser Grundlage konnte ein System entwickelt werden, das eine *in vivo*-ähnliche Untersuchung von primären GBM-Tumorzellen ermöglicht. Insgesamt wurden zwölf primäre Zellkulturen etabliert (AKH-14 bis AKH-24C).

Die primären Zellkulturen wurden mittels Immunfluoreszenzfärbung auf Stammzell- und GBM-spezifische Marker sowie auf die Oberflächenproteine AXL/Gas6 und Integrin $\alpha_v\beta_5$ untersucht, die als Eintrittsrezeptoren für das Zikavirus (ZIKV) dienen. Dabei konnte die Expression der Stammzellmarker OCT4, SOX2, NANOG, Nestin, Integrin α6, CD44 und CD133 in den Zellkulturen nachgewiesen werden. Die GBM-Marker EGFR und PD-1 waren in allen primären Zellkulturen überexprimiert. Darüber hinaus konnte die Isolierung von Astrozyten-ähnlichen Stammzellen über die Expression des glialen sauren Faserproteins (GFAP) nachgewiesen werden. Die immunologische Untersuchung zeigte, dass jede Zellkultur ein einzigartiges Expressionsmuster von Biomarkern aufwies. Dies lässt auf die Existenz vieler unterschiedlicher GSC-Subpopulationen schließen. Die beiden ZIKV-Rezeptoren AXL/Gas6 und Integrin $\alpha_v\beta_5$ konnten in allen primären Zellkulturen erfolgreich nachgewiesen werden.

In dieser Arbeit wurde zusätzlich ein Pseudotyp-System entwickelt, bei dem die Transmembran- und zytoplasmatische (TMCY) Region von ZIKV gegen die TMCY-Region des Vesikulären Stomatitis Virus (VSV-G) ausgetauscht wurde. Dies repräsentiert einen alternativen Ansatz im Vergleich zu den bereits etablierten Methoden innerhalb der Arbeitsgruppe. Für diesen Ansatz wurde das ZIKV E Protein in die beiden Expressionsvektoren pCMV-VSV-G und pMD2.G kloniert. Die so hergestellten Expressionsvektoren pCMV-EG1 und pMD2-EG2 wurden in Kombination mit dem Verpackungsplasmid pNL*gfp*AM zur Herstellung der Pseudotypen EG1-HIV*gfp* und EG2-HIV*gfp* genutzt. Infektionsexperimente mit beiden Pseudotypen zeigten erfolgreiche Infektionen in den primären Zellkulturen AKH-13, AKH-14, AKH-17, AKH-19, AKH-23 und AKH-24C.

Abstract

As part of this study, a novel cell culture system for glioblastoma (GBM) cells was developed. For this purpose, GBM tumor samples from areas adjacent to the subventricular zone (SVZ) were used. These areas contain many GBM stem cells (GSCs) and astrocyte-like stem cells. It was demonstrated that the cell cultures maintained their heterogeneity for at least three months when cultured in CSF-DF medium. Based on these findings, a system was developed that enables examination of primary GBM tumor cells under conditions that closely resemble the *in vivo* environment. In total, twelve primary cell cultures were successfully established (AKH-14 to AKH-24C).

Immunological examination of the primary cell cultures revealed the presence of both stem cell- and GBM-specific markers, as well as the surface proteins AXL/Gas6 and integrin $\alpha_v\beta_5$, which act as entry receptors for the Zika virus (ZIKV). Expression of the stem cell markers OCT4, SOX2, NANOG, Nestin, integrin α6, CD44, and CD133 was detected in the cell cultures. The GBM markers EGFR and PD-1 were overexpressed in all primary cell cultures. Additionally, the isolation of astrocyte-like stem cells was demonstrated by the expression of glial fibrillary acidic protein (GFAP). Immunological analyses revealed that each cell culture exhibited a distinct biomarker expression pattern, suggesting the existence of many different GSC subpopulations. The two ZIKV receptors, AXL/Gas6 and integrin $\alpha_v\beta_5$, were successfully detected in all primary cell cultures.

This study also involved the development of a pseudotype system in which the transmembrane and cytoplasmic (TMCY) region of ZIKV was replaced with that of vesicular stomatitis virus (VSV-G). This approach differs from methods previously established within the working group. The ZIKV E protein was cloned into two expression vectors, pCMV-VSV-G and pMD2.G, to produce the expression vectors pCMV-EG1 and pMD2-EG2. These constructs were used in combination with the packaging plasmid pNL*gfp*AM to produce the pseudotypes EG1-HIVgfp and EG2-HIVgfp. Infection experiments with both pseudotypes demonstrated successful infection of the primary cell cultures AKH-13, AKH-14, AKH-17, AKH-19, AKH-23, and AKH-24C.

1. Introduction

1.1. The glioblastoma brain tumor and its origin

Brain tumors are a heterogeneous group of neoplasms, among which gliomas represent the most common type of primary central nervous system (CNS) malignancies. Gliomas are a category of brain tumors that include both low-grade tumors, such as astrocytomas and oligodendrogliomas, and high-grade malignancies. Among these, glioblastoma is known to be the most prevalent and most aggressive form of brain tumor.

Glioblastoma (GBM), formerly known as Glioblastoma multiforme grade 4, is the most common malignant primary glial brain tumor, accounting for 48.6% of all malignant tumors[1]. Today, GBM is classified as a diffuse astrocytic glioma that is isocitrate dehydrogenase 1 (IDH-1) wildtype and exhibits certain molecular features, including TERT (telomerase reverse transcriptase) promoter mutations, the simultaneous gain of chromosome 7 and loss of chromosome 10, and amplification of the EGFR (epidermal growth factor receptor) gene[2]. Other important factors for diagnosis and prognosis are the methylation status of the MGMT (O6-methylguanine-DNA-methyltransferase) gene and the Ki-67 proliferation index[3]. GBMs are primarily diagnosed in elderly people, peaking at 75-84 years, with a higher incidence in men compared to women[1]. The progression of the disease is usually rapid, with only about one in four patients surviving beyond two years after initial diagnosis. The five-year survival rate is reported to be between 5-10%, with a progression-free survival period ranging from 6.2-7.5 months and a median survival of only 14.6-16.7 months following diagnosis[4]. Standard treatment of GBM usually involves surgical resection followed by radiotherapy and chemotherapy with temozolomide[5,6]. Although there have been advances regarding GBM treatment, the current therapy protocol only prolongs the recurrence of the tumor, with no effect on the cure of the disease itself[7]. GBM recurs primarily because a small number of cancer cells survived the initial treatment. These cells can then proliferate and ultimately lead to recurrence of the tumor.

Among these cells, glioblastoma stem cells (GSCs), a subpopulation of cells within GBM, are thought to be the origin and main drivers of GBMs. These cells are self-renewing and tumorigenic, contributing to tumor initiation and progression as well as therapeutic resistance and ultimately tumor recurrence[8,9] (Fig. 1). The origin of GSCs is still controversial. However, recent studies suggest that GBM may also originate from neural stem cells (NSCs) as well as

glial precursor cells like oligodendrocyte precursor (OPCs) and astrocytic progenitor cells (APCs)[10,11].

Targeting GSCs has become increasingly important in the development of strategies to fight GBM, leading numerous scientists and medical experts to focus their efforts on these cells. One critical strategy involves the therapeutic targeting of GSC markers. Several different cell surface and intracellular proteins have been found. These can serve as markers that can possibly characterize cells as GSCs and are also linked to the promotion of tumor growth in GBM[12,13].

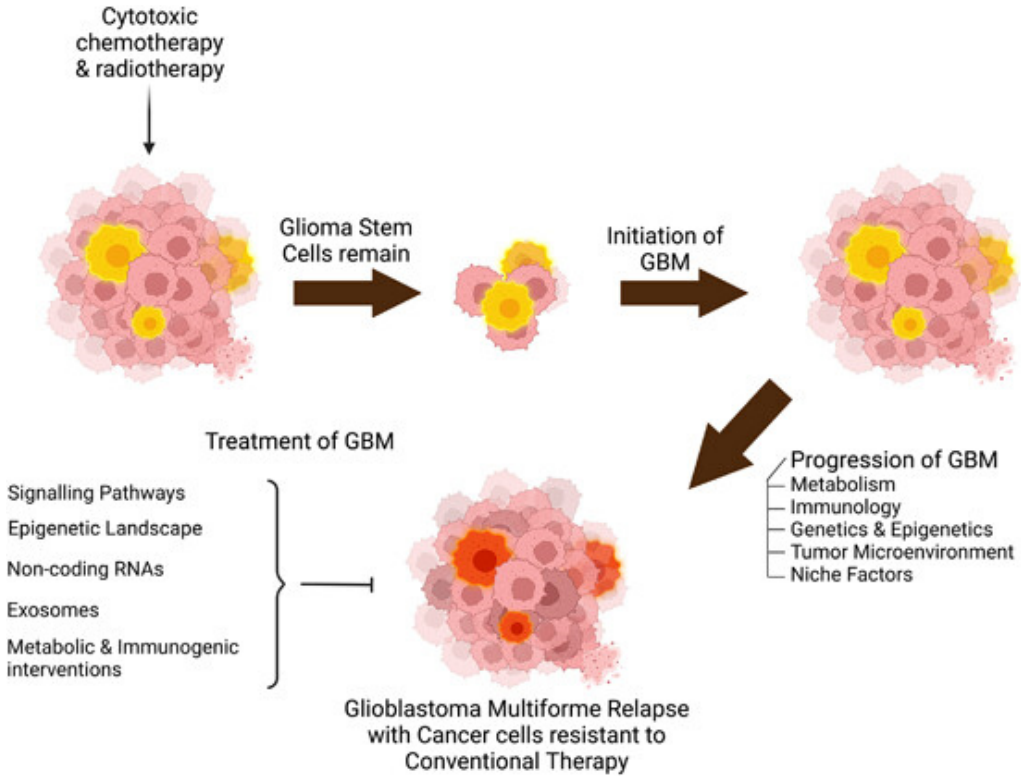

Fig. 1 Glioblastoma stem cells as the main drivers of tumor recurrence. Glioblastoma stem cells (GSCs) represent an important subpopulation within GBM. They are widely regarded as the origin and main driver of this aggressive brain tumor. These self-renewing, tumorigenic cells initiate tumor formation and significantly contribute to tumor heterogeneity through their capacity for self-renewal. As GBM progresses, GSCs infiltrate surrounding brain tissue, driving both tumor growth and resistance to standard therapies. This resistance leads to frequent tumor recurrence, underscoring the central role of GSCs in the dynamics of GBM. Given their pivotal involvement in tumor initiation, progression, and therapeutic resistance, targeting GSCs has emerged as a promising strategy to disrupt GBM progression and potentially improve clinical outcomes. Graphical abstract from Sahoo *et al*.[14]

1.2. Heterogeneity of glioblastoma

Tumor heterogeneity is a critical hallmark of cancer and is thought to significantly contribute to both tumor progression and the development of resistance to therapies[15]. The vast diversity of cell states, phenotypes, and the wide range of genetic, epigenetic, and transcriptomic features within GBM make it challenging to clearly classify tumors into subtypes and to develop targeted treatment strategies. The term inter-tumor heterogeneity describes the differences among patients with tumors having various molecular or histological features. In contrast, intra-tumor heterogeneity (ITH) describes differences within a single tumor, consisting of distinct subpopulations of cells.

GBM is characterized by a complex environment in which cancer cells attract various non-cancer cells, such as astrocytes, oligodendrocytes, microglia, macrophages, and endothelial cells, and convert them into a pro-tumor phenotype[16]. ITH adds another layer of complexity to GBM treatment due to the significant molecular differences within individual tumors[17]. The GBM tumor is composed of cancer cells that represent different subtypes, all having different genetic, transcriptomic, or epigenetic profiles[18–21]. Distinct copy number alterations in key genes like *EGFR*, *PTEN*, and *PDGFR* are inherited by these subtypes, ultimately leading to the coexistence of several cell lineages within the same tumor[22–24]. This complexity is driven by both genetic and non-genetic factors, including epigenetic modifications (such as chromatin and histone modifications and DNA methylation), transcriptional reprogramming, microenvironmental factors like hypoxia or shear stress, and the infiltration of additional immune cells, such as neutrophils or lymphocytes[21,25,26].

Transcriptional analyses of GBM tumor tissues have identified the existence of four GBM subgroups: proneural, neural, classical and mesenchymal[27]. These results were further supported by results from Herrera-Oropeza *et al*. who identified 18 specific driver genes, contributing to the significant heterogeneity of GBM at genomic and transcriptional levels[28]. They revealed distinct expression profiles of these genes that were characteristic for different molecular subtypes. For example, they found that the proneural subtype was characterized by the overexpression of the genes *MKI67* and *OLIG2*, while the classical subtype was characterized by an overexpression of *EGFR*, *NES*, *VIM*, and *TP53*. In comparison, the mesenchymal subtype showed an overexpression of *MGMT* and *VIM*. Furthermore, they found unique expression patterns in a combination of the genes *VIM*, *NES*, *EGFR*, and *OLIG2*, which are highly specific to distinct molecular subtypes. Thus, the expression patterns of these four

biomarkers are highly informative and can be used to determine the molecular subtype of a GBM tumor.

GSCs are major contributors to ITH by differentiating into diverse cellular lineages within the tumor mass[19,26,29]. Bhaduri *et al.* identified multiple GSCs subtypes within a single tumor, suggesting that the presence of different GSC subtypes may contribute to the rapid progression and invasive nature of GBM[20]. The heterogeneity of GSCs has been explored at single cell[30,31], epigenetic[32], and microenvironmental levels[33,34]. Further research revealed the presence of heterogeneous transcriptional stem cell states populating each GBM, which are divided into four different types of GSCs: neural-progenitor-like (NPCs), oligodendrocyte-progenitor-like (OPCs), astrocyte-like progenitor cells (APCs) and mesenchymal-like cells (MSCs)[26]. Furthermore, GSCs show significant plasticity which allows them to transition between these stem-like states in response to signals from the tumor microenvironment (TME).

Despite the different subtypes, the development of the tumor still seems to follow that of a normal brain. Comparing adult GBM and normal human fetal brain cells through scRNA-seq has revealed conserved neural tri-lineage hierarchy that follows a specific conserved neurodevelopmental gene program, centering around glial progenitor-like cells (GPCs)[29]. GSCs that clearly had one of the mentioned cell states could alter their identity due to their high plasticity and their surrounding TME, resulting in a variation of the frequency of states, even within the same tumor[26]. Meyer *et al.* demonstrated that clones derived from the same patient exhibited significant differences in differentiation capacity, proliferation characteristics, and responses to drug treatment, thereby highlighting the high plasticity of GBM cells[19].

The maintenance, invasion, and behavior of GSCs are heavily influenced by their microenvironment. Specific niches in the brain, including the hypoxic, perivascular, and invasive niche in GBM as well as the subventricular zone (SVZ) play critical influential roles in the regulation of GSCs and will be addressed further in the next chapter.

1.3. The tumor niches of glioblastoma and the role of glioblastoma stem cells

A single tumor can display three distinct morphologically and functionally different tumor niches, each with its own unique cellular composition. These comprise the hypoxic-necrotic niche, the perivascular niche and the invasive niche[35]. Each niche acts as a distinct attractor, triggering diverse cellular programs within GSCs, which then actively remodel the surrounding microenvironment. These interactions between GSCs and their respective niches are likely essential for sustaining the wide range of cellular states within the GSC population, thereby promoting both tumor heterogeneity and the persistent maintenance of stem-like characteristics.

1.3.1. The hypoxic-necrotic niche

The formation of the hypoxic niche in GBM can be attributed to a combination of impaired blood flow caused by regressed and abnormal vasculature, as well as the rapid proliferation that outpaces the existing blood supply. This reduced and inconsistent circulation leads to areas of low oxygen (hypoxia), often accompanied by an acidic pH. Over time, these harsh conditions result in cellular stress and ultimately cell death, giving rise to the characteristic necrotic regions found within GBMs[36,37]. Several studies have shown that hypoxia is a crucial regulator of tumor stemness, tumor cell survival, immune evasion, and resistance[38–40].

Hypoxia can influence the behavior of GSCs, supporting their maintenance, proliferation, and therapy resistance[41,42]. GSCs are found to be enriched in the hypoxic niche and in perinecrotic regions[41]. Several studies have provided evidence that hypoxia directly promotes the expansion of GSCs[42–44]. Hypoxia may also promote the differentiation of GSCs to endothelial-like cells, which leads to the formation of tumor-derived blood vessels[45,46]. Hypoxia also comes with an increase in stem cell properties and an increased expression of certain GSC markers such as CD133, SOX2, OCT4 and Nestin[41,43,47].

1.3.2. The perivascular niche

The perivascular niche (PVN) has been shown to be the primary location of GSC populations[48]. Processes occurring within the PVN create a supportive environment to maintain stemness and induce migration of GSCs through angiogenesis. Endothelial cells have been shown to selectively interact with $Nestin^+/CD133^+$ GSCs, providing factors that maintain their self-renewing and undifferentiated state[49]. Specifically, $CD133^+$ GSCs are closely related to tumor vasculature through secretion of vascular endothelial growth factor (VEGF), further promoting tumor growth[49,50]. In addition, immune cells like tumor-associated macrophages (TAMs) secrete factors that support the growth and expansion of GSCs[51].

1.3.3. The invasive niche

The invasive niche is located at the edge of the tumor and contains a variety of cells, including GSCs, endothelial cells, pericytes, activated microglia, reactive astrocytes, and neurons[52]. Compared to the PVN and hypoxic niche, the invasive tumor niche is characterized by abnormal neovascularization that allows GSCs to survive in peritumoral regions[52]. GSCs have been shown to use blood vessels to invade normal brain tissue[53].

As the tumor develops and invades the surrounding tissue, it ultimately encounters astrocytes. These are the most abundant cells in the brain and play a crucial role in regulating metabolic and fluid homeostasis, as well as controlling blood flow in the vasculature[54]. Invading tumor cells trigger astrogliosis, a process where astrocytes undergo a number of changes to form reactive astrocytes to be able to repair damage to the CNS[55]. In the context of GBM, they are further activated into tumor-associated astrocytes (TAAs)[56]. TAAs produce and secrete a variety of growth factors and cytokines that promote GBM cell proliferation, migration, survival, and invasion[57–61]. They furthermore protect GBM cells from chemotherapy by forming gap junctions, which enhance chemoresistance[62,63]. TAAs are present both in the invasive and the perivascular niches, contributing to ITH. In the PVN, these growth factors can influence blood vessel interactions and GSC maintenance, while in the invasive niche, they can facilitate tumor spread into surrounding tissues[48].

1.3.4. The subventricular zone

The SVZ is a 3-5 mm thick area on the outside wall of each lateral ventricle that harbors the largest population of NSCs in the brain[64–67]. The SVZ is organized into a series of distinct layers, each with unique cellular compositions and functional characteristics (Fig. 2). NSCs are the stem cells of the nervous system, incorporating the ability of self-renewal and to differentiate into multiple neural cell types like neurons and glial cells (e.g., astrocytes and oligodendrocytes)[68]. Studies have shown that NSCs in the SVZ carry the mutations responsible for GBM, suggesting them as a potential cell of origin[69,70].

GSCs and NSCs share many molecular and genetic characteristics, including key genes and proteins associated with stemness and self-renewal. This suggests that developmental growth patterns may be reactivated in GSCs. Recent genomic and proteomic analyses have revealed a strong connection between GBM and NSCs in the SVZ, suggesting that GBM may originate from astrocyte-like NSCs in the SVZ that acquire tumor-promoting mutations[71]. GSCs and NSCs in the SVZ have similar characteristics, including the expression of markers SOX2, Nestin, GFAP, and CD133. Both cell types possess unlimited proliferative potential, exhibit the

ability to undergo proliferation, and demonstrate high motility. Additionally, they are capable of maintaining angiogenesis, invading surrounding tissues, and communicating with other components of their respective niches[72]. Furthermore, the vasculature of the SVZ is more abundant than that of other brain regions, providing sufficient nutrients to migrating GSCs[73]. The proximity of the SVZ to the tumor sites often correlates with a more aggressive tumor phenotype and increased likelihood of relapse, since NSCs in the SVZ can leave their niche and migrate along blood vessels. GBMs that are located near the SVZ are in closer contact with cerebrospinal fluid (CSF), which may facilitate the circulation and spread of tumor cells to distant regions of the brain[74,75]. When a GBM is adjacent to or invades the SVZ, it first encounters the ependymal layer, which serves as a barrier between the ventricle and the underlying stem cell niches. As the tumor infiltrates deeper, it can disrupt the hypocellular layer and the astrocytic ribbon beneath.

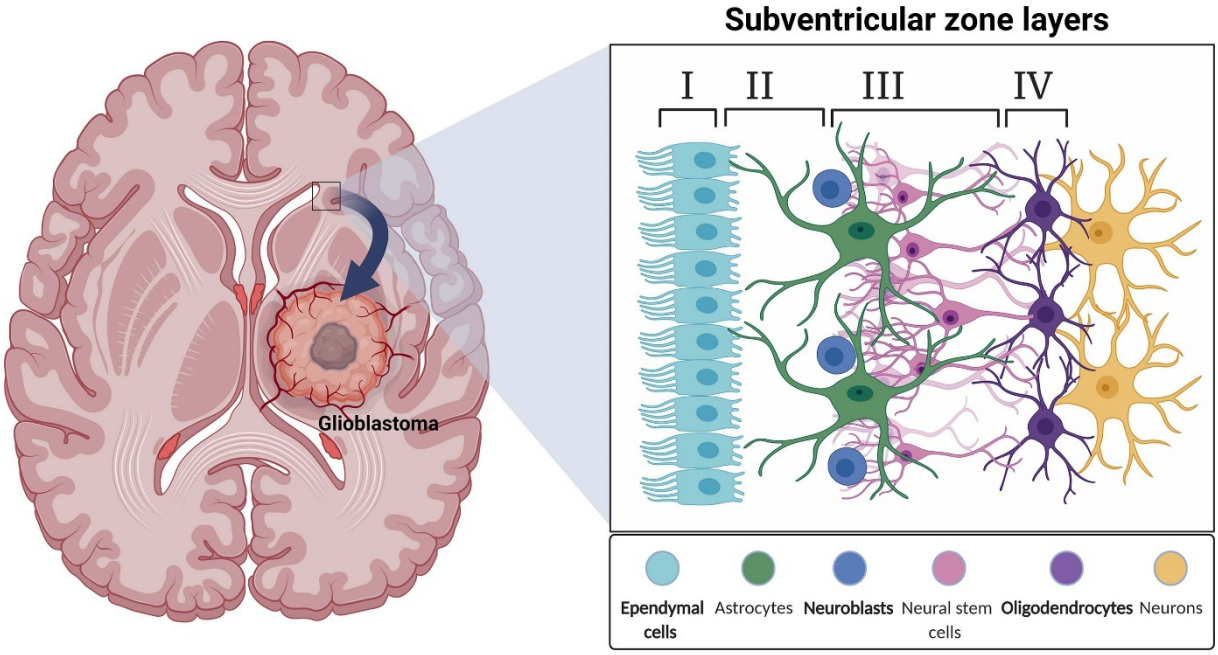

Fig. 2 The subventricular zone and its associated layers in the human brain. The subventricular zone (SVZ) is a specialized region along the walls of the lateral ventricles in the brain, recognized as one of the major sites of neurogenesis. The SVZ is organized into a series of distinct layers, each with unique cellular compositions and functional characteristics. While there are species-specific differences, the general organization, particularly observed in humans, includes four primary layers**:** The ependymal layer (Layer I) forms the cellular surface closest to the ventricular cavity and lines all SVZ regions within the brain. This layer is composed of ciliated ependymal cells that facilitate the circulation of cerebrospinal fluid (CSF) and create a barrier between the ventricle and the underlying layers of the SVZ. Layer II, known as the hypocellular layer, lies directly beneath the ependymal layer. This layer contains relatively few cells and consists mainly of the basal processes of ependymal cells as well as astrocyte processes and some diffuse astrocytic cell bodies. The hypocellular layer likely helps maintain proper separation between the ependymal lining and the more densely populated stem cell regions. Beneath the hypocellular layer is the astrocytic ribbon (Layer III), a prolific region enriched with astrocyte-like cells, many of which serve as neural stem cells (NSCs). These cells are capable of self-renewal and support ongoing neurogenesis by giving rise to transient amplifying progenitor cells and neuroblasts. The innermost layer of the SVZ is the transitional zone to the brain parenchyma (Layer IV). This region contains various neuronal and glial processes and is where neurons can be found amidst the migration of neuroblasts. It serves as a dynamic interface between the proliferative SVZ and the more differentiated cells of the brain parenchyma. Figure taken from Beiriger *et al*[76].

1.4. Biological markers characterizing glioblastoma

The characterization of tumor cells, particularly GSCs, remains a highly complex and challenging task in the field of GBM research. In this study, specific markers associated with GSCs were chosen for immunostaining to evaluate their presence in the primary GBM cell cultures. The selected markers include nuclear proteins (sex determining region Y)-box 2 (SOX2), octamer-binding transcription factor 4 (OCT4), and homeobox protein NANOG; the intermediate filament proteins neuroepithelial stem cell protein (Nestin) and glial fibrillary acidic protein (GFAP); and cell membrane proteins CD44, CD133, integrin α6 (ITGA6), programmed cell death protein 1 (PD-1), and epidermal growth factor receptor (EGFR). In addition, the two Zika virus (ZIKV) entry receptors AXL/Gas6 and integrin $\alpha_v\beta_5$ were assessed.

1.4.1. Glioblastoma stem cell markers

1.4.1.1 SOX2

The nuclear transcription factor SOX2 is highly expressed in GBM as well as a variety of other solid tumors, including prostate, breast, lung, and melanoma cancers[77]. In cancer, SOX2 plays significant roles in cell proliferation, metastasis, apoptosis, and invasiveness[78]. In GBM specifically, SOX2 is frequently upregulated and is crucial for tumor cell growth, survival, and the regulation of stem-like properties in GSCs[79]. Elevated SOX2 expression has also been linked to tumor recurrence following chemotherapy or radiotherapy[80] and is thought to be a key protein responsible for chemoresistance in GBM[79,81].

Multiple studies have demonstrated that cells with amplified or overexpressed SOX2 exhibit increased self-renewal, maintain an undifferentiated state, and possess greater invasive capacity compared to cells with reduced or absent SOX2[79,82]. *In vitro* and xenograft models (experimental setups, in which human tumor cells are transplanted into immunodeficient mice to study tumor growth and behavior) demonstrate that silencing or inhibiting SOX2 not only diminishes expression of other stem cell markers like OCT4 and Nestin, but also impairs proliferation and invasive capabilities of GSCs[79,83]. One study reported that the generation of GSCs is directly related to SOX2 expression in GBM, showing that only those cultures with SOX2 levels higher than 30% generated neurospheres[84].

Overall, these studies support that SOX2 functions as a critical regulator of stemness in GBM by sustaining self-renewal and an undifferentiated, invasive state.

1.4.1.2 OCT4

OCT4, a nuclear transcription factor, functions through multiple isoforms to enhance GSC properties, such as self-renewal and proliferation, thereby contributing to increased tumor aggressiveness[85–87]. Both the OCT4A and the cytoplasmic OCT4B-190 isoforms have been shown to promote anchorage-independent growth, a hallmark of cancer cells characterized by their ability to proliferate without attachment to a substrate. Additionally, these isoforms have been shown to promote self-renewal and proliferation in GBM cell models[86,87].

Several studies have further evaluated isoform-specific mechanisms. For instance, palmitoylation of OCT4A is required for maintaining GSC tumorigenicity, and phosphorylation of the amino acid threonine 235 [Thr235] on OCT4A enhances the proliferation of stem-like cancer cells[87,88]. Overexpression of the OCT4B-190 isoform has been correlated with anchorage-independent growth and poorer prognosis[86]. Another report showed that OCT4 expression decreases cellular sensitivity to chemotherapeutic agents by enhancing their excretion through drug efflux pumps encoded by the ATP (adenosine triphosphate) binding cassette transporter G2 gene[89].

Notably, OCT4 is strongly correlated with SOX2 under hypoxic conditions typical of the GBM TME. Bhagat *et al*. have demonstrated that hypoxia induces a (hypoxia induced factor) HIF-2α-SOX2/OCT4-Mena (INV) axis, drastically increasing the migratory potential of glioma cells[90]. In this signaling pathway, elevated HIF-2α upregulates SOX2 and OCT4, which, in turn, induce expression of the Mena (INV) isoform, a protein that promotes tumor cell invasion and metastasis[90]. Collectively, these findings suggest that OCT4 acts as a mediator of GSC tumorigenicity and aggressiveness through both isoform-specific and post-translational mechanisms.

1.4.1.3 NANOG

NANOG, a key stemness factor, plays a crucial role in GSCs by influencing self-renewal, proliferation, and therapeutic resistance. Overexpression of NANOG in GBM is associated with increased tumor growth and malignancy[91]. Being a critical marker for GSCs, NANOG influences various aspects of cancer development, including cell proliferation, self-renewal, motility, and drug resistance[92].

One recent study reported that suppression of NANOG expression in GSCs leads to increased susceptibility to temozolomide by inducing cell cycle arrest and decreasing 3-phosphoinositide-dependent protein kinase-1 (PDK1) expression. PDK1 activates the PI3K/AKT pathway, which

is known to promote cell proliferation and survival in GBM[93]. Another study found that NANOG forms an essential regulatory network with GLI1 and p53, modulating clonogenicity, $CD133^+$ stem cell behavior, and proliferation *in vivo*[94]. Furthermore, NANOG can transform p53-deficient astrocytes into GSC-like cells, thereby promoting self-renewal and tumor development[95].

Additionally, NANOG plays a critical role in regulating cell fate decisions in both embryonic and GSCs; thus, inappropriate activation of NANOG can lead to the generation of GSCs instead of normal pluripotent stem cells or differentiated somatic cells[92]. Together, these findings highlight the critical role of NANOG in GBM progression and GSC maintenance.

1.4.1.4 Nestin

Nestin, an intermediate filament protein, plays a critical role in the carcinogenesis of GBM and is widely recognized as a potential marker for GSCs[96,97]. Nestin expression is correlated with increased tumor growth, malignancy, and poor prognosis in GBM[97]. Nestin is present in both cytoplasmic and cell surface forms in GSCs[98]. Research has demonstrated that Nestin expression can be induced in cells that were originally $Nestin^-$ during tumor development, highlighting its significance in the progression of GBM[98]. Nestin is also essential in spindle assembly and cell-cycle progression in GBM cells, as its knockdown leads to cell cycle arrest and apoptosis[99].

A comparative study of various GBM markers such as NANOG and CD44 showed that, although many markers were upregulated in GBM, only high levels of Nestin and CD133 significantly correlated with patient survival. This finding highlights Nestin and CD133 as promising candidates for targeted therapies[100]. Nestin is identified as a putative marker for GSCs in various tumor types, including neurogenic, epithelial, and mesenchymal tumors[96]. Especially Nestin co-expression in the same cell with other putative markers such as CD133, OCT4, and SOX2 is considered a signature or defining feature of a GSC phenotype[96]. This co-expression provides a highly valuable tool for researchers seeking to identify and isolate GSCs from tumor samples, as it helps distinguish GSCs from other, more differentiated tumor cells or normal stem cells.

Collectively, these findings underscore the importance of Nestin as both a reliable stem cell marker and a functional regulator in GBM. Its expression, particularly in combination with other key stem cell markers, is associated with increased malignancy, invasiveness, GSC properties, and poor overall patient survival.

1.4.1.5 CD44

CD44 is a multifunctional transmembrane glycoprotein that is frequently overexpressed in GBM and plays a complex role in GSC behavior. It is predominantly expressed on the cell membrane, although it has been shown that high levels of CD44 in the cytoplasm have been associated with poor prognosis in GBM patients[101]. CD44 serves as the main receptor for hyaluronic acid (HA), the major component of the brain's extracellular matrix (ECM)[102]. Through its interaction with HA, CD44 promotes various tumor cell activities and mediates both cell-to-cell interactions and cell-to-ECM interactions. This binding activates multiple genes involved in critical cellular processes such as migration, invasion, proliferation, and tumorigenesis[102,103].

Although CD44 promotes tumor aggressiveness[104], its status as a GSC marker remains controversial. On the one hand, CD44 knockdown or low expression increases stemness traits such as sphere formation and stem cell marker expression[105]; on the other hand, it suppresses growth, induces senescence, and impairs hypoxia-related gene signatures in GBM[106]. A recent study by Nishikawa *et al.* found that the activity of CD44 is highly dependent on the tumor's hypoxic microenvironment. It was observed that severe hypoxia promotes a highly invasive phenotype in GSCs, whereas moderate hypoxia induces a less invasive, more proliferative state[107]. Moreover, GBM tumors maintain a dynamic equilibrium between $CD133^+$ and $CD44^+$ cell subpopulations, which is largely influenced by factors like hypoxia[108].

In this context, severe hypoxia activates HIF-1α and moderate hypoxia activates HIF-2α, which both differentially regulate CD44 expression and in turn lead to increased tumor invasion or proliferation, respectively. This dynamic response allows GSCs to switch between invasive and proliferative states, contributing to tumor recurrence[109,110]. Therefore, understanding the interplay between hypoxia, factors like HIFs, and CD44 is crucial for developing effective strategies against GBM recurrence.

1.4.1.6 CD133

CD133, also known as prominin-1, is a membrane-bound glycoprotein expressed on the surface of GSCs within GBM. $CD133^+$ cells are believed to drive tumor aggressiveness by promoting growth, resistance to conventional therapies, and contributing to tumor recurrence[111,112]. CD133 has been extensively studied as a prognostic biomarker and a potential therapeutic target in GBM.

Although it has been widely used as a marker for GSCs, the reliability of CD133 is still questionable. Some studies report that CD133 expression is associated with poor prognosis and decreased survival in GBM patients[113], while others have found that $CD133^-$ cells can also exhibit stem-like properties[114]. Although CD133 is widely used for the identification of GSCs, no single marker can reliably identify them across all gliomas.[115]

To improve the identification of GSCs, co-expression of CD133 with other markers has been explored. For example, the combined expression of CD133/Nestin[96,100] or CD133/CD44[108] has shown promise for defining more specific GSC subtypes. These findings support the fact that, while CD133 remains an important subject of research in GSC biology and potential therapeutic targeting, its use as a sole, reliable biomarker for GSCs remains controversial[116].

1.4.1.7 ITGA6

Integrin $\alpha 6$ has attracted considerable attention in stem cell biology due to its role as a cell surface receptor for the ECM protein laminin, facilitating cell adhesion and signaling. ITGA6 forms heterodimers with integrin $\beta 1$ and $\beta 4$, integral components of the integrin signaling pathway[117]. It is highly expressed in hematopoietic, embryonic, and neural stem cells, where it helps regulate NSC growth in the brain[118,119]. In GBM, ITGA6 is highly expressed in GSCs, regulating their self-renewal, proliferation, and tumor formation capacities[120].

ITGA6 is frequently co-expressed with conventional GSC biomarkers such as CD133 and serves both as a biomarker and a potential therapeutic target for GBM[120]. ITGA6 supports stemness in proneural GSCs, promotes radiation resistance in mesenchymal GSCs, and mediates interactions with the TME to sustain self-renewal[121,122]. Notably, ITGA6 is a conserved biomarker found in over 30 different stem cell populations, including GSCs[123].

In breast cancer models, ITGA6 is directly regulated by HIFs, enhancing both invasion and tumor-initiating cell activities[124]. High ITGA6 expression is associated with increased GSC activity, metastatic potential, and poor prognosis in breast cancer patients[124]. Moreover, recent research by Alsharany *et al.* demonstrated that ITGA6 regulates expression of fibroblast growth

factor receptor 1 (FGFR1), a key factor in GBM development and progression[125]. They also discovered a signaling pathway with a five-gene signature that was prognostic of the overall survival of GBM patients[126].

Together, these findings highlight ITGA6 as a potential therapeutic target for GBM treatment.

1.4.1.8 GFAP

GFAP is an intermediate filament protein that plays a crucial role in astrocytes, NSCs, and GSCs[127]. In GBM, GFAP contributes structurally to the formation of tunneling nanotubes between tumor cells, thereby facilitating intercellular mitochondrial transfer under stress conditions[128]. In GSCs, GFAP exhibits asymmetric distribution during mitosis, potentially influencing cell fate determination[129]. Its expression is directly regulated by the transcription factor Pax3. Pax3 overexpression promotes GFAP expression, drives differentiation, and potentially contributes to malignancy[130].

There are multiple GFAP splice variants, with GFAPα and GFAPδ being the two primary isoforms[127]. While GFAP levels do not significantly differ between GBM and normal brain tissue, the delta isoform is overexpressed in high-grade gliomas and associated with malignancy and invasiveness[100,131]. The GFAPδ/α ratio may serve as a biomarker for accessing astrocytoma malignancy and glioma classification[131]. Recent evidence suggests that $GFAP^+$ cells, such as astrocytes or radial glial cells, are more likely to be the source of GBM than classical $GFAP^-$ NSCs[132]. Moreover, multiple populations of tumor-initiating cells (TICs) may co-exist within GBM, adapting their phenotype and genotype to diverse environmental conditions[132].

Altogether, a better understanding of GFAP's role in GSCs is essential for elucidating mechanisms of tumor progression and for developing targeted therapies against diffuse gliomas.

1.4.2. Markers associated with glioblastoma

1.4.2.1 EGFR

The transmembrane receptor tyrosine kinase EGFR is the most highly enriched gene in GBM, with mutations occurring in over 50% of tumors. Notably, its mutant variant, EGFRvIII contributes to tumor growth, invasion, angiogenesis, and therapeutic resistance.[133,134]. EGFR overexpression in GBM is closely linked to GSCs and activates several molecular pathways that contribute to tumor progression[135,136]. The PI3K/AKT/mTOR and RAS/RAF/MAPK pathways are key downstream effectors of EGFR signaling in GBM[136]. Additional essential

pathways in GSCs include Notch, STAT3, Wnt/β-catenin, and HIF, all of which promote proliferation, invasion, and self-renewal while inhibiting differentiation and apoptosis[137].

The expression of EGFR allows identification of functionally distinct TIC subpopulations in GBM, with $EGFR^+$ cells displaying the most malignant phenotype[138]. EGFRvIII is frequently co-expressed with CD133, defining a GSC population with high self-renewal potential and strong tumor-initiating capability[139]. Moreover, a novel EGFR variant, EGFRx, has been shown to sustain GSC self-renewal and proliferation via STAT5 activation[140]. GSCs can also secrete autocrine factors, including EGF (epidermal growth factor), thereby supporting their self-renewal and proliferation even in the absence of external growth factors[141].

Overall, these findings highlight the complex interplay between EGFR mutations, signaling pathways, and autocrine factors in maintaining the GSC phenotype.

1.4.2.2 PD-1

PD-1 is a cell surface receptor expressed on various immune cells, particularly T cells. As an immune checkpoint receptor, PD-1 promotes self-tolerance and suppresses inflammatory T cell activity by binding to its ligands, programmed death-ligand 1 and 2 (PD-L1 and PD-L2)[142]. In GBM, PD-1 is predominantly expressed on tumor-infiltrating lymphocytes (TILs), especially T cells, leading to their functional inactivation and impaired anti-tumor responses. PD-1 expression on TILs reflects both T cells activation and exhaustion, and these cells display reduced T-cell receptor diversity compared to normal $PD\text{-}1^-$ T cells[142]. Notably, a subset of brain TICs has been reported to express PD-1, which enhances their proliferation and self-renewal via Src homology region 2 domain-containing phosphatase-2 (SHP-2)-mediated NFκB activation, independent of PD-L1 binding[143].

While PD-1 is typically not expressed in GSCs themselves, the PD-1/PD-L1 axis plays a significant role in immunosuppression within the GBM TME. This pathway supports tumor immune evasion, invasion, and growth[144]. PD-L1 is expressed in the majority of GBM samples and acts on multiple infiltrating immune cell populations in the TME, making the PD-1/PD-L1 pathway an important focus for immunotherapeutic research[145]. Neoadjuvant PD-1 blockade in recurrent GBM patients has shown promise, extending overall survival and enhancing both local and systemic antitumor responses compared to adjuvant treatment alone[146]. This strategy led to upregulation of T cell- and interferon-γ-related genes, enhanced clonal expansion of T cells, and decreased PD-1 expression on peripheral blood T cells[146].

Understanding these complex interactions is crucial for developing an effective therapy targeting the PD-1/PD-L1 pathway in GBM.

1.4.3. Markers associated with Zika virus infection

1.4.3.1 AXL/Gas6

The receptor tyrosine kinase AXL is a membrane-bound protein highly expressed in a wide range of tissues, including the lung, bladder, urinary tract, gonads, muscles, and gastrointestinal tract[147].Within the nervous system, AXL is found at high levels in various neural cell types, such as radial glial cells, astrocytes, and microglia[148]. AXL primarily functions via interaction with its ligand, growth arrest specific 6 (Gas6). Upon Gas6 binding, AXL undergoes dimerization and autophosphorylation of its intracellular domain, thereby activating its kinase function[149]. Beyond its role in cancer, AXL is involved in homeostasis, the clearance of apoptotic cells, regulation of inflammation, and vascular remodeling[150].

The name AXL derives from the Greek word *anexelekto*, meaning uncontrolled, highlighting its crucial function in cancer progression[151]. In GBM and other cancers, overexpression of AXL is strongly associated with the outcome of the disease and plays a critical role in cancer cell proliferation, migration, invasion, angiogenesis, therapeutic resistance, stemness, and poor prognosis[152–154]. Moreover, AXL has been implicated in epithelial-to-mesenchymal transition in GSCs, metastasis formation, and modulation of the TME[155]. Furthermore, AXL regulates cell signaling cascades and cellular communication between different components of the TME, including cancer cells, endothelial cells, and immune cells[156]. Activation of AXL drives tumor growth and migration, contributing to an increased risk of metastasis and reduced survival across a range of cancers, including breast[157], lung[158], ovarian[159], colon[160], prostate[161], skin[162], and GBM[163,164].

Importantly, AXL also serves as a ZIKV entry receptor for the infection of endothelial and glial cells[165–167]. Multiple studies have shown that AXL mediates ZIKV entry into glial cells. However, it has been shown that AXL inhibition or knockout significantly reduces ZIKV infection rates[165,168]. This process is dependent on Gas6, which bridges the interaction between ZIKV particles and glial cells, and is followed by clathrin-mediated endocytosis[165]. AXL/Gas6 inhibition with antibodies or by knockout protected various cell types from ZIKV infection, including endothelial cells, astrocytes, and GBM cells[168,169]. Experiments with the ZIKV strain MR-766 in human GBM cell lines have demonstrated that AXL is essential for viral entry[168]. Nevertheless, the precise mechanisms underlying this process remain unclear and require further investigation.

1.4.3.2 Integrin $\alpha_v\beta_5$

Integrin $\alpha_v\beta_5$ is a member of the integrin superfamily of cell surface receptors[170]. Integrins are heterodimeric proteins composed of alpha and beta subunits that mediate cell adhesion to the ECM and are involved in signal transduction, thereby affecting processes such as angiogenesis, migration, survival, differentiation, and proliferation[170,171]. In cancer biology, integrins play critical roles in tumor metastasis, immune evasion, metabolic reprogramming, and other cancer hallmarks[172,173]. They bind to RGD motifs (arginine-glycine-aspartic acid), which are present in common ligands and biomarkers such as fibronectin, vitronectin, osteopontin, and fibrinogen[172,174]. Research efforts have utilized RGD-containing ligands to target integrins for medical applications such as drug design, tumor imaging, immunotherapy, and biomaterial research[172,173].

In GBM, the expression levels of integrins, specifically $\alpha_v\beta_3$ and $\alpha_v\beta_5$, exhibit variations between normal and cancerous cell populations. Research has indicated that the expression of integrin $\alpha_v\beta_3$ is more prevalent than that of $\alpha_v\beta_5$, with both demonstrating increased expression compared to healthy brain tissue[174,175]. A higher level of expression has been observed in the periphery of high-grade gliomas in comparison with healthy tissue[176]. Generally, integrin expression tends to increase with tumor grade. In particular, $\alpha_v\beta_3$ expression has been shown to be an indicator of a poor prognosis GBM patients[174].

It has recently been discovered that integrin $\alpha_v\beta_5$ plays a crucial role in GBM, while also playing an important role in the ZIKV infection cycle[177]. Integrin $\alpha_v\beta_5$ is highly expressed in GSCs, where it is essential for their maintenance and function[178]. ZIKV preferentially infects and kills GSCs through a SOX2-integrin $\alpha_v\beta_5$ axis[179]. Here, integrin $\alpha_v\beta_5$ acts as an internalization factor for ZIKV, mediating virus entry into NSCs and GSCs[180]. The α_v subunit of integrin $\alpha_v\beta_5$ has been found to be upregulated in highly malignant gliomas[176]. Additionally, elevated expression of the β_5 subunit correlates with disease progression, mesenchymal subtype, and poor patient survival[181]. Integrin β_5 is also associated with immune response regulation, angiogenesis, and is required for glioma cell migration and invasion[181].

Wang *et al*. have shown that targeting integrin $\alpha_v\beta_5$ with blocking antibodies or inhibitors like SB273005 and cilengitide reduces ZIKV infection and alleviated ZIKV induced pathology, offering potential therapeutic strategies for both ZIKV and GBM[178]. Furthermore, a very recent study using ZIKV-LAV (live attenuated virus) targeting human GBM cells revealed a connection between AXL/Gas6 and integrin $\alpha_v\beta_5$ as cell surface receptors mediating ZIKV entry, highlighting their importance as targets for future research and therapy development[167].

1.5. Oncolytic Viruses

Oncolytic viruses (OVs) are naturally occurring or genetically engineered types of viruses that selectively infect and destroy cancer cells. Ideally, OVs cause minimal damage to normal tissues[182,183]. Since the infected cancer cells are destroyed by the virus, they subsequently release new infectious virus particles to facilitate the destruction of the remaining tumor. Not only can this type of viruses directly kill tumor cells but also stimulate the host immune system due to the release of new tumor antigens[183,184]. Since most mechanisms against viral infections are generally impaired in cancer cells, most viruses can replicate to a much greater extent in tumor cells than in healthy cells. A major challenge of OVs is not infecting tumor cells, but rather ensuring that the virus does not productively replicate in healthy cells[182].

Various naturally occurring OVs, including severe acute respiratory syndrome coronavirus 2 (SARS-CoV-2), herpes simplex virus 1 (HSV), vaccinia virus, adenovirus, measles virus, reovirus, ZIKV, and Newcastle disease virus have been the subject of extensive research and testing as oncolytic agents for various types of cancer[185]. Clinical trials have demonstrated the safety and feasibility of oncolytic virotherapy, with some encouraging antitumor responses observed[184,186]. The first oncolytic virus therapy, T-Vec, an oncolytic herpes virus, was approved in the United States of America (USA) and the European Union (EU) in 2015 for treatment of advanced inoperable melanoma[182].

OVs have been widely explored as therapeutic agents for GBM[187,188]. To date, more than 30 OVs have entered clinical trials for the treatment of GBM and GSCs. However, their clinical success has been limited by factors such as reduced antitumor potency, suboptimal delivery methods, and host immune responses, which resulted in only marginal improvements in overall survival and no approvals from the United States Food and Drug Administration (FDA) for GBM treatment[189,190]. Recent research focused on enhancing OV potency, understanding cellular immunity, and developing combinatorial strategies[189]. The concept of GSC plasticity challenges the assumption that eliminating GSCs is sufficient to prevent tumor recurrence, since non-GSCs may dedifferentiate into GSCs post-treatment[191]. Future directions in oncolytic virotherapy for GBM may involve preventing non-GSC to GSC dedifferentiation and optimizing OV safety and efficacy[191,192]. Researchers are exploring strategies to enhance efficacy and overcome challenges, including improving systemic delivery mechanisms and combining oncolytic virotherapy with other treatment modalities[183,186].

In contrast to all other viruses, ZIKV has demonstrated preferential infection and killing of GSCs compared to normal neural cells in preclinical models due its naturally occurring

neurotropism[177]. One approach to exploit this property of ZIKV is either in the form of an attenuated, live virus,[193] or via the incorporation of the outer envelope proteins as part of pseudotyped viral particles[194,195].

1.6. Zika virus and its tropism

ZIKV is a member of the flavivirus genus within the *Flaviviridae* family. It is primarily transmitted through bites from female mosquitoes but can also be transmitted through parenteral routes, sexual contact, or blood transfusion[196]. Members of the *Flaviviridae* family are enveloped virions, characterized by three structural membrane proteins, the capsid protein C, the precursor membrane protein prM, and the envelope protein E, with prME being relevant for viral entry[197]. The genome of ZIKV has a single open reading frame (ORF) that encodes for C, prME, and seven nonstructural proteins (NS1, NS2A, NS2B, NS3, NS4A, NS4B, and NS5) all translated into one polyprotein[198].

During the ZIKV life cycle, budding is a crucial step that enables the virus to detach from the cell and continue its infectious cycle. After viral entry, the acidic environment within the endosome induces a conformational change in the E protein, allowing it to fuse with the endosomal membrane and release its genome into the cytoplasm[199]. Once inside the cytoplasm, ZIKV begins to assemble new particles following ribonucleic acid (RNA) translation and replication[200]. After viral proteins are produced, newly assembled ZIKV particles begin to form inside the endoplasmic reticulum (ER). The process of budding is characterized by the envelopment of the viral core with a lipid bilayer acquired from the ER membrane, where the viral particles acquire their envelope and surface proteins. The transmembrane region (TM) of both prM and E plays a crucial role in the efficient assembly at the ER membrane. Especially the TM region of prM, which allows translocating the viral complex into the ER lumen[201,202]. After budding, the still immature prME virus particles are transported to the Golgi complex via the secretory pathway. Final maturation of the virions occurs at the Golgi complex and is mediated by the host furin protease, which cleaves the prM protein into the pr and M part. This leads to a conformational change from the non-infectious to an infectious state (prM to ME). Furin activation is followed by the release of matured ME containing particles[200].

Studies have shown the capacity of ZIKV to pass highly selective barriers like the blood-brain barrier (BBB) and infect cells of the CNS, including neurons, astrocytes, and both mature and immature microglia[203]. Infection can result in severe neurological outcomes such as microcephaly in newborns, characterized by an abnormally small head size and impaired brain development, and the Guillain-Barré syndrome in adults, an autoimmune disorder that causes

muscle weakness and paralysis[196,203]. This pronounced neurotropism, combined with the observed lytic effect of ZIKV on glial cells, has significantly influenced the development of novel virotherapies for gliomas, including therapies against GBM[204].

1.7. Viral pseudotyped particles

A pseudotyped virus is a virus particle that contains the core (genetic material and internal proteins) of one virus but displays the outer envelope proteins from another virus[205]. Since certain viral genes are deleted or inactivated, pseudotyped viruses cannot replicate and typically only allow for a single round of infection[205]. Viral entry is significantly influenced by their envelope proteins and their interactions with cell surface receptors[206]. By exchanging envelope proteins, pseudotyped viruses allow a controlled targeted activation of new receptors and can be designed to modify or broaden viral tropism[206].

Pseudotyped viruses are commonly based on vesicular stomatitis virus (VSV)[207] or lentiviruses like murine leukemia virus (MLV)[208] and human immunodeficiency virus 1 (HIV-1)[209]. The VSV glycoprotein (VSV-G) can bind to low-density lipoprotein receptor (LDLR) and other family members, which allows VSV to infect a broad range of cell types, making it a valuable tool for pseudotyping other viruses[210,211]. Due to their high transduction efficiency in both dividing and non-dividing cells, lentiviral vectors are often the favored packaging system for enveloped pseudotypes[212]. The production of pseudotyped particles generally involves a two-plasmid system, in which one plasmid contains the information for the envelope deleted viral core while the other plasmid encodes only the envelope protein from another virus[213]. Additionally, reporter genes such as *gfp*[214] (green fluorescent protein) or *luc*[215] (luciferase) are commonly used to visualize and quantify viral entry. A typical procedure for pseudotype production involves transfection of eukaryotic cell lines like COS-1[216] or HEK293T[217].

1.7.1. ZIKV pseudotyped particles

Due to the remarkable neurotropism of ZIKV, this virus is an excellent candidate for the design of pseudotyped viruses with enhanced selectivity for neural tumor cells. One major obstacle for the generation of ZIKV pseudotyped particles is that, like many other RNA viruses, ZIKV utilizes the ER membrane for its budding process. At this site, both viral assembly and the incorporation of envelope proteins prM and E in the viral membrane occur[200–202]. This is different to the lentiviral assembly, which takes place at the outer cell membrane (Fig. 3).

This hurdle has been overcome by exchanging the TM region of ZIKV to that of HIV-1[194,195]. HIV-1, in contrast to ZIKV, assembles at the outer cell membrane, mediated by its gp41 TM

protein[218]. Construction of pseudotyped particles involved exchanging of the TM and cytoplasmic (CY) regions of ZIKV with differently designed TM and CY regions of HIV-1 to alter the viral budding process, following the path of HIV-1 assembly. This pseudotyping effectively yielded high transduction efficient neurotropic viral particles. It has been demonstrated that ZIKV envelope proteins, prME and E, can be used to pseudotype retroviral vectors for efficient cell infections[194,195].

For the infection experiments, a cell culture system using freshly isolated GBM grade 4 tumor cells that were cultured in a mixture of human cerebrospinal fluid (hCSF) and Dulbecco's Modified Eagle Medium (DMEM) was used, enabling the study of cells under conditions that closely mimic the physiological state of the brain *in vivo*[219,220]. ZIKV pseudotyped particles have demonstrated higher transduction efficiency in GBM cells in comparison to traditional VSV-G pseudotypes. They have been observed to possess the capacity to kill infected cells after a period of seven days, whilst leaving healthy cells unharmed[220]. The specificity of ZIKV pseudotyped particles for GSCs, while leaving healthy cells unharmed, renders them promising candidates for the development of targeted therapies and OVs[194,195,219,220].

To date, only one comparable strategy has been reported, in which the TM and CY regions of ZIKV were exchanged for those of VSV-G[221]. Liu *et al.* have demonstrated that a lentiviral pseudotype that had been engineered to express ZIKV E protein and the TM/CY regions of VSV-G was capable of infecting renal cells at a rate that was 100-fold higher than that observed with a native VSV-G pseudotype[221]. Furthermore, this study demonstrated that the efficacy of pseudotype infection appeared to be pH-dependent, with the acidification of the medium proving to be an effective inhibitor of viral entry[221].

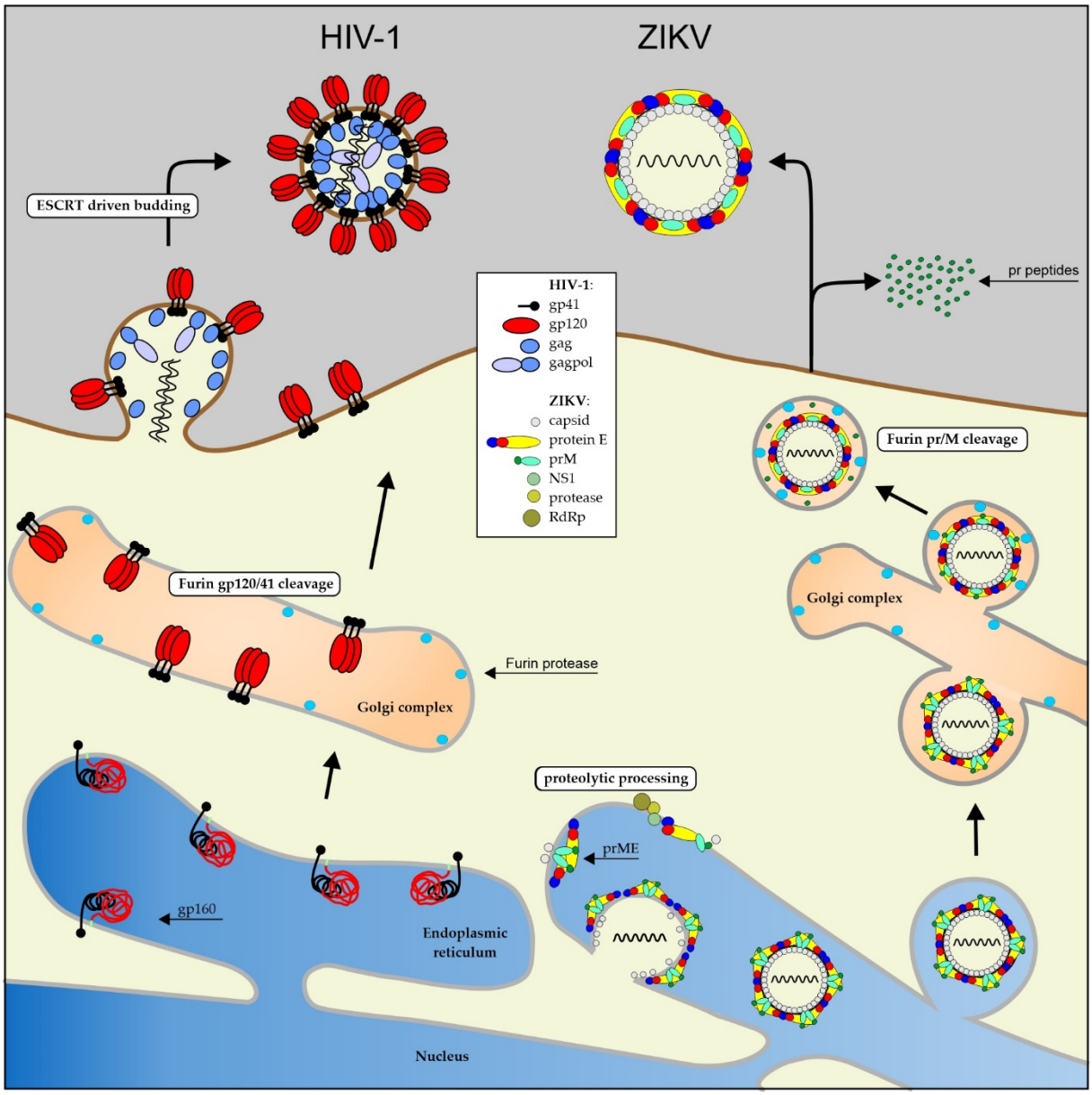

Fig. 3 Differences in virus assembly of HIV-1 and ZIKV. HIV-1: the gp160 precursor protein is inserted into the ER membrane during translation. In the Golgi complex, furin cleaves gp160 into gp41 and gp120, which then assemble into a trimeric complex. Vesicular transport then carries gp41 and gp120 to the cell membrane. There, the precursor proteins gag, gagpol and the viral genomes attach themselves. The budding process is then initiated, with the viral particle transported out by the ESCRT complex; ZIKV: the components of ZIKV are synthesized as polyprotein precursors in the ER. During budding, the immature virions accumulate in the ER lumen and are transported in individual vesicles to the Golgi apparatus. There, the prME heterodimers are restructured into E homodimers by the acidic pH of the trans-Golgi network, exposing the cleavage site of the furin protease. Furin then cleaves prM into pr and M. The neutral pH value upon leaving the cell by exocytosis releases the pr fragment. The virion is now in its mature, infectious form.

1.8. Aim of this thesis

GSCs in GBMs are difficult to eliminate due to their stem-like, drug-resistant nature and their ability to regenerate tumors. ZIKV is a promising and highly selective agent to attack and kill GSCs and is likely to play a central role in finding a cure for GBM.

This study aims to establish a cell culture system based on samples derived from GBM tumors that were near the vicinity of the SVZ. Therefore, different culturing methods had to be evaluated and compared to find the optimal conditions for maintaining stable primary GBM cell cultures. The aim is to examine primary GBM cell cultures produced from tumor samples obtained from at least ten patients.

Primary GBM cell cultures will be used to check whether they contain GSCs or stem cell-like cells. Therefore, primary GBM cell cultures will be analyzed for protein markers that are characteristic for GBM and specifically GSCs, including stem cell markers SOX2, OCT4, NANOG, Nestin, CD44, CD133, and other GBM-related biomarkers like ITGA6, PD-1, EGFR and GFAP. The cells will also be examined for the Zika virus receptors AXL/Gas6 and integrin $\alpha_v\beta_5$.

Another part of the work involves developing a lentiviral vector with a modified ZIKV E protein. To accomplish this, the TM region of the ZIKV E protein will be exchanged for the TM region of the VSV protein to ensure budding and assembly at the cellular membrane.

For pseudotype production, COS-1 cells will be transfected with two plasmids to produce ZIKV E pseudotyped lentiviral particles. The first plasmid, pNL*gfp*AM carries the lentiviral information as well as GFP as a reporter. The second plasmid carries the information for the ZIKV E protein including the VSV TM domain. The resulting ZIKV pseudotyped particles will be used to infect different primary GBM cell cultures, with infection rates compared to those achieved using VSV-G pseudotyped viral particles.

This approach will provide insight on whether GSCs can be specifically infected and inactivated by a lentiviral vector incorporating a modified ZIKV E protein.

2. Material and Methods

2.1. Material

2.1.1. Devices

Table 1 Devices

Device	Modell	Manufacturer
Analytical scale	Extend ED3202S-CW	Sartorius AG
Centrifuge	Megafuge 3.0 R	Heraeus Sepatech
	5415 C	Eppendorf AG
	5810 R	Eppendorf AG
	miniSpin	Eppendorf AG
	Biofuge Pico	Heraeus Sepatech
Dye trough with coloring insert		Glaswarenfabrik Karl Hecht GmbH & Co. KG
Electrophoresis Chamber	Horiton 58	Life Technologies GmbH
Freezer	Ultra-Low Temperature Freezer	Eppendorf AG
Fluorescence microscope	EVOS M5000 EVOS M7000	Thermo Fisher Scientific GmbH
Incubator	INE 400	Memmert GmbH
	INE 500 with rotating insert	Memmert GmbH
	CB 150	BINDER GmbH
	Shaking incubator 3031	GFL Gesellschaft für Labortechnik mbH
Light microscope	Diavert	Leica
Light source	Wild Heerbrugg	Leica
Magnetic stirrer	IKAMAG RCT	IKA-Werke GmbH & Co. KG
Micro scale	870-61	Kern & Sohn GmbH
PCR cycler	Mastercycler gradient	Eppendorf AG
	Professional Thermocycler	Biometra
pH meter	CG 840	Schott AG
Pipet controller	Accu-jet pro	Brand GmbH & Co. KG

Pipette	Multipette® plus Research® plus PIPETMAN®	Eppendorf AG Eppendorf AG Gilson Inc.
Thermomixer	Thermomixer compact Thermomixer comfort	Eppendorf AG Eppendorf AG
UV spectrometer	UV-160A	SHIMADZU
Vortexer	VF2	IKA-Werke GmbH & Co. KG
Working bench	SterilGard III Advance	The Baker Company, Inc.

2.1.2. Consumables

Table 2 Consumables

Consumable	Description	Manufacturer
Pipette tips	Biosphere Filter Tips (1250 µL, 100 to 1000 µL, 200 µL, 0.5 to 20 µL)	Sarstedt AG & Co. KG
PCR tube	0.2 mL PCR tube, Flat Cap	Starlab International GmbH
Cell culture tubes	SafeSeal tube 1.5 mL SafeSeal micro tube 2 mL	Sarstedt AG & Co. KG
Working gloves	Nitrile Gloves "L"	Labmarker
Parafilm	Parafilm	Bemis
Wipes	KIMTECH Science Precision Wipes Incidin Wipes	Kimberly-Clark Professional Ecolab
Cryo tubes	Cryo.s PP, with screw cap, sterile	Greiner Bio-One GmbH
Cell culture flasks	TC Flask T25, Cell+, Vent. Cap TC Flask T75, Stand., Vent. Cap TC Flask T75, Cell+. Vent. Cap.	Sarstedt AG & Co. KG
Cell culture plates	TC Plate 24 Well, Standard, F TC Plate 24 Well, Cell+, F TC Plate 96 Well, Standard, F TC Plate 96 Well, Cell+, F	Sarstedt AG & Co. KG
Microscope slides	Diagnostic Microscope Slides 12 Well 5 mm Numbered Nunc Lab-Tek II Chamber Slide	Thermo Scientific

Centrifuge tubes	Tube 50 mL, 114x28 mm, PP Tube 15 mL, 120x17 mm, PP	Sarstedt AG & Co. KG
Liquid blocker	Super Pap Pen Liquid Blocker	Science Services GmbH
Pipettes	Costar STRIPETTE 5 mL Serological pipette 5 mL and 10 mL	Corning, Inc. Sarstedt AG & Co. KG
Laboratory bottle	Schott® Duran laboratory bottle with blue cap + ring (1000 mL, 500 mL, 250 mL, 100 mL)	DWK Life Sciences
Cell strainer	Sterile Cell Strainer 70 µm	Fisher Scientific
Gas	CV 470 Plus	CAMPINGAZ
Dispenser tips	Combitips advanced (2.5 mL, 5 mL, 10 mL)	
Syringes	Inject Single-use syringe 20 mL	B. Braun Melsungen AG
Petri dishes	92x16mm 82.1473	Sarstedt AG & Co. KG
Sterile filter	Stericup® Quick Release, Millipore Express® PLUS 0.22 µm PES, 500 mL	Sigma Aldrich

2.1.3. Biochemicals and Kits

Table 3 Biochemicals

Name	Description	Manufacturer
Buffer	5x Phusion HF Reaction Buffer	New England Biolabs
	5x ISO buffer	Prepared in the lab
	50x TAE buffer	Prepared in the lab
	10x PBS / 10x PBS-T	Prepared in the lab
Enzymes	Taq DNA Ligase	New England Biolabs
	Taq DNA Polymerase	New England Biolabs
	Taq Phusion DNA polymerase	
	T4 Polynucleotide Kinase	New England Biolabs
	T5 exonuclease	New England Biolabs
	Q5`High-Fidelity DNA Polymerase	New England Biolabs

	Trypsin/EDTA 0.05%/0.02% in DPBS w/o: Ca, Mg	PAN Biotech
Nucleotides	dNTP Set, molecular biology grade	Carl Roth GmbH & Co. KG
DNA Ladder	O´GeneRuler 100 bp Plus DNA Ladder, ready to use	New England BioLabs
	O´GeneRuler 1 kb DNA Ladder, ready to use	New England Biolabs
Loading buffer	Loading Dye Purple 6x	New England Biolabs
Medium for cell culture	DMEM	PAN Biotech
Transfection buffer	Opti-MEM™	Gibco™
Medium additives	FBS	PAN Biotech
	hCSF*	Supplied by AKH

* Use of anonymized human cerebrospinal fluid was approved by the Ethical Commission of the Hamburg Medical Chamber under the registration number PV6041

Table 4 Biochemical Kits

Name	Manufacturer
Nucleobond® Xtra Midi	Macherey-Nagel GmbH & Co. KG
NucleoSpin® Plasmid	Macherey-Nagel GmbH & Co. KG

2.1.4. Antibodies and Cell Staining Reagents

Table 5 Primary antibodies

Name	Manufacturer	Used volume
Primary antibodies		
Mouse anti-AXL antibody [C4-A8], 2 mg/mL	Invitrogen	4 µL/mL
Mouse anti-Integrin alpha V+beta 5 antibody [P1F6], 1 mg/mL	Abcam Limited	10 µL/mL
Mouse anti-SOX2 antibody [9-9-3], 1 mg/mL	Abcam Limited	4 µL/mL
Mouse anti-OCT4 antibody [GT486], 1 mg/mL	Abcam Limited	4 µL/mL
Mouse anti-NANOG antibody [23D2-3C6], 1 mg/mL	Abcam Limited	4 µL/mL
Mouse anti-Nestin antibody [2C1.3A11], 1 mg/mL	Abcam Limited	4 µL/mL
Mouse anti-CD44 antibody [156-3C11], 0.2 mg/mL	Invitrogen	4 µL/mL
Mouse anti-Hu CD133 [TMP4]	Invitrogen	10 µL/mL
Mouse anti-ITGA6 antibody [129CT49.6.5], 0.5 mg/mL	NSJ Bioreagents	4 µL/mL
Pembrolizumab (Keytruda, anti-PD-1 antibody), 200 mg in 100 mL 0.9% NaCl solution	Merck	1 µL/mL
Mouse anti-EGFR antibody [2A2H10], 1 mg/mL	Proteintech Group, Inc.	4 µL/mL
Rabbit anti-GFAP Polyclonal Antibody	Invitrogen	4 µL/mL

Table 6 Secondary antibodies

Name	Manufacturer	Used volume
Goat Anti- Rabbit IgG (H+L) Cross-Adsorbed Secondary Antibody, Alexa Fluor 568 [2 mg/mL]	Invitrogen	2 µL/mL
Goat anti-Mouse IgG (H+L), Alexa Fluor 488 [1 mg/mL]	Invitrogen	2 µL/mL

Table 7 Other immunostaining agents

Name	Manufacturer
Alexa Fluor® Plus 647 Phalloidin	Invitrogen
ROTI®Mount FluorCare DAPI	Carl Roth GmbH & Co. KG

2.1.5. Chemicals

Table 8 Chemicals

Name	Manufacturer
Acetic acid 100%	Carl Roth GmbH & Co. KG
Acetone ≥99.5%	Carl Roth GmbH & Co. KG
Albumin Fraction V ≥98%	Carl Roth GmbH & Co. KG
Ampicillin sodium salt ≥97%	Carl Roth GmbH & Co. KG
Bacto Yeast Extract	BD
Biozym LE Agarose	Biozym Scientific GmbH
Calcium chloride anhydrous	Merck KGaA
Dimethyl sulfoxide ≥99.8%	Carl Roth GmbH & Co. KG
1,4-Dithiothreitol	Carl Roth GmbH & Co. KG
Ethidium bromide	Sigma Aldrich
Ethanol ≥99.8%	Carl Roth GmbH & Co. KG
EDTA disodium salt dihydrate	Biomol
Formaldehyde ≥37% solution	Carl Roth GmbH & Co. KG
Glycerol ≥99.5%	Carl Roth GmbH & Co. KG
Hydrochloric acid 37%	Carl Roth GmbH & Co. KG
LB Broth (Luria/Miller)	Carl Roth GmbH & Co. KG
LB agar (Luria/Miller)	Carl Roth GmbH & Co. KG
Manganese(II) chloride	Carl Roth GmbH & Co. KG
Magnesium chloride	
Na-MOPS ≥99.5%	Carl Roth GmbH & Co. KG
PEI Max® Transfection Grade (MW 40,000)	Polysciences, Inc.
PEG 6000	Merck KGaA
Propan-2-ol ≥99.5% for molecular biology	Carl Roth GmbH & Co. KG
Potassium acetate ≥99%	Carl Roth GmbH & Co. KG
Potassium chloride	Merck KGaA
Potassium dihydrogen phosphate	Merck KGaA
Rubidium chloride ≥99%	Carl Roth GmbH & Co. KG
Sodium acetate, anhydrous	Merck KGaA
Sodium chloride >99.8%	Carl Roth GmbH & Co. KG
Di-sodium hydrogen phosphate dihydrate	Merck KGaA

Sodium hydroxide, granulated	Merck KGaA
NAD^+	New England Biolabs
TRIS >99.9%	Carl Roth GmbH & Co. KG
TRIS-HCl 4x Ultrapure	GERBU Biotechnik GmbH
Triton® X-100	Merck KGaA
Tryptone/Peptone ex casein	Carl Roth GmbH & Co. KG
Tween® 20	Carl Roth GmbH & Co. KG
Yeast Extract, micro-granulated	Carl Roth GmbH & Co. KG

2.1.6. Plasmids and primers

Table 9 Plasmids

Name	Origin
pNL*gfp*AM	University of Zurich, Switzerland, Trkola laboratory; N. Friedrich
pME-Z1	BNITM, Hamburg, Schreiber laboratory; P. Kadlubowska
pCMV-VSV-G	Addgene #8454
pMD2.G	Addgene #12259
pCMV-EG1	Designed in this study
pMD2-EG2	Designed in this study

Table 10 Primers

Plasmid	#	Name	Sequence 5´- 3´	Template
pCMV-EG1	1	VSVg-ATG	CATAGTGTCAGAATTCCTGAGGG	pCMV-VSV-G
	2	VSVg TAA	TAACTCAAATCCTGCACAACAGATTC	
	3	VSVgE for Gibson	CCCTCGAGGAATTCTGACACTATGATC AGGTGCATTGGAG	pME-Z1
	4	VSVg E rev Gibson	CCAATGATTAACCCTATGATAAAGAAA AATTTGAAGGCT	
pMD2-EG2	5	ATG for VSVg	CATAGTGTCAGAATTCAGATCTCACGTGC	pMD2.G
	6	TM rev VSVg	AAAAGCTCTATTGCCTCTTTTTTCTTTATC	
	7	Gibson Z1 pMD for	GCACGTGAGATCTGAATTCTGACACTATG ATCAGGTGCATTGGAGTCAGCAATAG	pME-Z1
	8	Gibson Z1 pMD rev	GATAAAGAAAAAAGAGGCAATAGAGCTT TTGAAGGCTGCTCCAAAAATCTGGTGAATGCC	

2.1.7. Cells

Table 11 Eucaryotic and procaryotic cells

Name	Organism	Description	Origin
DH5α	*Escherichia coli*	Bacterial cells engineered to maximize transfection efficiency	BNITM
U87	*Homo sapiens*	Human Glioblastoma cell line	Cell Lines Services
COS-1	*Cercopithecus aethiops*	Immortalized fibroblast-like cell line derived from monkey tissue	American Type Culture Collection
AKH-5, -9, -10, -11, -12, -13, -14, -15, -16, -17, -18, -19, -20, -21S, -21C, -23, -24S and -24C	*Homo sapiens*	Isolated tumor cells from Glioblastoma grade 4 patients*	Patients from AKH

*Use of anonymized human tumor tissue was approved by the Ethical Commission of the Hamburg Medical Chamber under the registration number PV6041

2.1.8. Software

Table 12 Used software

Name	Distributer	Function	Version
ImageJ	Wayne Rasband	Image editing	1.54
Serial Cloner	SerialBasics	Sequence processing	2.6
SnapGene Viewer	GSL Biotech	DNA editing	7.2.1

2.1.9. Use of Artificial Intelligence Assisted Tools

All artificial intelligence assisted tools were used in accordance with the good scientific practice and no output was directly copy pasted. If suggested changes were accepted, the manuscript was corrected individually at the corresponding position.

DeepL Write was used to for language correction of individual sentences.

DeepL Translator was used to translate coherent German words or to the check whether a written sentence in English had the intended meaning by translating it into German.

UHH GPT-4.1 was used for language correction of connected sentences or paragraphs. In addition, UHHGPT was used for simple search queries, such as the explanations of error messages.

2.2. Methods

2.2.1. Media and agar plates

All substances listed in Table 13 were weighed into a 1 L Schott® bottle. After adding all substances, the bottle was filled with distilled water and then autoclaved. Prior to use, 5 mL of sterile-filtered ampicillin (60 mg/L) was added at room temperature (RT) to prevent the growth of bacteria other than those carrying a plasmid with an ampicillin resistance gene. For agar plates, the mixture had to be cooled to below 60 °C before adding the ampicillin. After adding the antibiotic, the mixture was poured into Petri dishes. Once the agar solidified, the plates were incubated overnight at 37 °C to ensure the absence of contamination and then stored upside down in a refrigerator at 7 °C until further use.

Table 13 Ingredients for the manufacturing of different growth media

	YT medium	dYT medium	YT agar plates
Agar [g]	-	-	16
Sodium chloride [g]	5	5	5
Tryptone [g]	8	16	8
Yeast extract [g]	5	10	5

2.2.2. Manufacturing of competent DH5*α* cells

To produce competent *E. coli* DH5*α*, the first step was inoculating a test tube containing 3 mL of YT medium with a single colony of *E. coli* cells. The cells were picked next to a Bunsen burner using a sterile, thin glass rod. The cultured was incubated overnight at 37 °C in a rotating incubator. The following day, 2 mL of the overnight culture was transferred into 100 mL of YT medium in a 1 L Erlenmeyer flask. The culture was then incubated in a laboratory shaker at 37 °C and 180 rpm (rounds per minute) until the optical density at 600 nm (OD_{600}) reached a value between 0.3 and 0.4. Immediately after reaching the desired OD, the cell cultured was placed on ice with gentle rotation to stop further cell growth. Once cooled down, the culture was split into two 50 mL centrifuge tubes, which were centrifuged for 15 min at 10,000 g and 4 °C. The centrifuge was pre-cooled to 4 °C to prevent reheating of the bacteria, since maintaining a cold temperature throughout the whole process is crucial. Meanwhile, 100 mL of TFB I and 5 mL of TFB II buffer (both prepared beforehand, see Table 14) were cooled to 4 °C. After centrifugation, the supernatants were discarded and the pellets were gently resuspended in 50 mL of TFB I buffer, incubated on ice for 15 min and centrifuged again at 10,000 g at 4 °C for 15 min. The supernatant was discarded, and the pellets were carefully

dissolved in 2.5 mL of TFB II buffer. The resulting competent bacteria aliquoted into PCR reaction tubes (100 µL or 50 µL each) and stored at -70 °C until needed.

Table 14 TFB I and TFB II buffer composition

TFB I – 1000 mL, pH 5.8*		TFB II – 100 mL, pH 6.8*	
Substance	*Concentration [mM]*	*Substance*	*Concentration [mM]*
Potassium acetate	30	Na-MOPS	10
Rubidium chloride	100	Rubidium chloride	10
Calcium chloride	10	Calcium chloride	75
Glycerol	15%	Glycerol	15%
Manganese chloride	50		

*Buffer solution was adjusted to needed pH using acetic acid and was sterile filtered afterwards.

2.2.3. Bacterial transformation with heat shock

For transformation, the previously manufactured competent *E. coli* DH5*α* cells were thawed on ice. Meanwhile, a YT-agar plate containing ampicillin was retrieved from the refrigerator and placed into an incubator at 37 °C. All steps were performed next to a Bunsen burner to minimize contamination. After thawing, the cells were gently mixed with deoxyribonucleic acid (DNA) and incubated on ice for 10 min. Depending on the DNA source, 1 µL was used from midi-prep DNA, 5 µL from mini-prep DNA, or the complete 20 µL from Gibson assembly. Next, the cell-DNA mixture was subjected to a heat shock at 42 °C for 3 min. Immediately after heat shock, the tube was placed back on ice and incubated for another 20 min. In the meantime, 1 mL of YT medium without ampicillin was warmed in a shaker at 37 °C using a 1.5 mL reaction tube. After 20 min recovery time, the competent cells were pipetted into the warm YT medium and incubated in a thermomixer at 37 °C and 700 rpm for 30 min. Subsequently, the agar plate was removed from the incubator, and the cell suspension was centrifuged at 8,000 g for 1 min. Up to 100 µL of the supernatant was gently discarded, and the cell pellet was resuspended in the remaining volume. The resuspended cells were then evenly spread onto the agar plate and incubated overnight at 37 °C. On the following day, the plate was examined for colonies, preferably single colonies, and afterwards stored inverted at 7 °C for up to three weeks.

2.2.4. Polymerase chain reaction

For the amplification of DNA fragments or plasmids, the polymerase chain reaction (PCR) technique was employed. All reagents were combined in a PCR tube, which was subsequently placed into a thermocycler. The PCR setups and thermocycler programs used for the plasmids synthesized during this thesis are detailed in Table 15 and Table 16, respectively. Primers were

synthesized by metabion international AG and diluted 1:10 before use to achieve a concentration of 10 pmol/µL for PCR.

Table 15 Standard PCR and approaches for synthesized plasmids

	pCMV-EG1		pMD2-EG2	
Template	pCMV-VSV-G	pME-Z1	pMD2.G	pME-Z1
ddH_2O [µL]	32.5	32.5	34.5	32.5
5x PCR buffer [µL]	10.0	10.0	10	10.0
Forward primer [µL]	2.0	2.0	1.0	2.0
Reverse primer [µL]	2.0	2.0	1.0	2.0
dNTPs [µL]	1.0	1.0	1.0	1.0
DNA [µL]	2.0[a]	2.0[a]	1.0[a]	1.0[a]
Phusion HF DNA Polymerase [µL)]	0.5	0.5	0.5	0.5

[a]plasmids were used with a dilution of 1:1000.

Table 16 PCR conditions

	Cycle	Time [min]	Temperature [°C]
Initial denaturation		2	98
Denaturation		0.75	98
Annealing	35	0.75	Primer dependent[a]
Elongation		Sequence dependent[b]	72
Final elongation		6	72

[a]pCMV-EG1: 57°C, pMD2-EG2: 55°C; pME-Z1: 52°C; [b]pCMV-EG1 and pMD2-EG2: 6 min; pME-Z1: 2 min.

2.2.5. Gel electrophoresis

For the analysis and verification of PCR reactions, agarose gel electrophoresis was employed, allowing separation of DNA fragments based on size. To prepare the gel, 0.9 g of agarose was weighed into a 200 mL laboratory flask, and 100 mL of 1x TAE buffer was added. The chemicals needed for the preparation of a 50x TAE buffer are listed in Table 17. The mixture

was microwaved until the agarose was completely dissolved. Next, approximately 25 mL of this mixture was transferred to a 50 mL tube, followed by the addition of 2 µL ethidium bromide for DNA visualization. The mixture was then poured into a gel tray with either one or two combs, each adding eight pockets to the gel, and allowed to cool and solidify. The remaining agarose mixture was stored in a 56 °C oven for up to two weeks. Once solidified, the electrophoresis chamber was filled with TAE buffer until it was just above the level of the gel. The pockets were then loaded with the DNA samples that were previously mixed with 6x purple loading dye. For amplicon size determination, a DNA ladder marker was also added to one pocket of the gel. Electrophoresis was run at 175 V for 10 minutes. The gel was afterwards visualized under UV light to analyze the DNA fragments.

Table 17 Composition of 50x TAE buffer solution in 1 L ddH_2O

Substance	Amount [g]
2 M Tris/HCl (pH 8.3)	242.3
1 M acetic acid 99%	60.05
0.1 M EDTA	41.62

2.2.6. Gibson assembly

Gibson assembly cloning was performed as described in the literature[222]. For this process, the plasmid and E fragments were previously prepared by PCR, as described in chapter 2.2.4. These fragments were mixed with 15 µL of previously prepared Gibson assembly mix to reach a final volume of 20 µL and incubated for 30-45 min at 50 °C in a PCR cycler.

Table 18 5x ISO buffer

Substance	Volume
1 M Tris-HCl, pH 7.5	500 µL
2 M $MgCl_2$	25 µL
100 mM dATP	10 µL
100 mM dCTP	10 µL
100 mM dGTP	10 µL
100 mM dTTP	10 µL
1 M DTT	50 µL
50 mM NAD^+	100 µL
PEG 6000	0.25 g
ddH_2O	≈ 285 µL
Σ	1000 µL

Aliquots of 64 µL were put into 0.5 mL reaction tubes and stored at -20 °C until use.

Table 19 Gibson assembly mix

Substance	Volume
5x ISO buffer	64 µL
T5 exonuclease	0.12 µL
Taq Phusion DNA polymerase	4 µL
Taq DNA ligase	32 µL
ddH_2O	140 µL
Σ	240 µL

Aliquots of 15 µL were put into PCR reaction tubes and stored at -20 °C until use.

2.2.7. Mini plasmid extraction

On the first day, 3 mL of dYT medium containing ampicillin was inoculated with a single cell colony picked from an agar plate stored in the freezer. The culture was then incubated overnight in a rotating incubator at 37 °C. The next day, the bacterial suspension was carefully transferred into a 1.5 mL reaction tube. Mini plasmid extraction was performed following the protocol of the manufacturer. The first step involved centrifuging the tubes at 11,000 g for 30 s to pellet the cells. The supernatant was removed, and this step was repeated with the remaining suspension. Next, the cells were resuspended in 250 µL of resuspension buffer A1. After complete resuspension of the cell pellet, 250 µL of lysis buffer A2 was added to the cells, followed by careful inversion of the tubes for a couple times. After 5 min of incubating, 300 µL of neutralization buffer A3 was added, and the tubes were inverted until the blue color of the lysis buffer disappeared, indicating a successful neutralization. The lysate was then removed by centrifugation at 11,000 g for 10 min. The supernatant was then transferred onto a NucleoSpin® column. This was repeated twice because the maximum binding volume of the column was only 700 µL per run. The flow-through was discarded and 500 µL of washing buffer AW was added to the column, followed by another centrifugation step at 11,000 g for 1 min, removing the flow-through afterwards. Next, 600 µL of wash buffer A4 was added, followed by another centrifugation, with the flow-through discarded afterwards. The penultimate step involved the removal of ethanol and drying the silica membrane of the column, which was done by centrifugation at 11,000 g for 2 min. The collection tube was then discarded and replaced by a 1.5 mL reaction tube. In the final step, 50 µL of elution buffer AE was added, incubated for 1 min at RT, and then centrifuged at 11,000 g for 1 min to elute the purified DNA. The resulting DNA was either stored at -20 °C for future use or checked via gel electrophoresis. If the gel electrophoresis confirmed successful isolation of the desired DNA fragment, the sample was prepared for sequencing, which was performed at LGC Genomics GmbH in Berlin.

2.2.8. Midi plasmid extraction

Midi plasmid extraction was performed using the NucleoBond® Xtra Midi Kit from Macherey-Nagel. First, 250 mL of dYT medium with ampicillin was transferred into a 1 L Erlenmeyer flask and inoculated with a previously transformed colony of *E. coli* DH5*α* cells containing the desired plasmid. The culture was incubated overnight at 37 °C and 180 rpm on a shaking incubator. The following day, 50 ml of the bacterial suspension was carefully transferred into a 50 mL tube and centrifuged at 10,000 g for 2 min. This step was repeated until all cells were pelleted. The cell pellet was then resuspended in 12 mL of resuspension buffer from the kit. After all cells were completely resuspended, 12 mL of lysis buffer was added, and the tube was

carefully inverted several times, followed by 5 minutes incubation. Next, 12 mL of neutralization buffer was added, and the tube was inverted until the blue color completely disappeared. The lysate was then separated by centrifugation at 10,000 g for 15 min. Meanwhile, the filter from the column was equilibrated with 15 mL of equilibration buffer. After centrifugation, the supernatant was applied to the filter, and after it flowed through, another 15 mL of equilibration buffer was added to the filter, which was then discarded. Subsequently, 25 mL of washing buffer was applied to the column, followed by elution of the DNA with 15 mL elution buffer. The DNA eluate was dripped into 12 mL of ≥99.5% pure 2-propanol to precipitate the DNA. After pelleting the DNA, a white precipitate containing salts formed at the bottom of the tube, which was resuspended with vortexing. Skipping this step could cause problems in the final dissolving of the DNA later. The DNA was then further precipitated at 15,000 g for 30 min at 4 °C. The supernatant was carefully discarded, and residual 2-propanol was removed by drying the pellet. Finally, the DNA pellet was dissolved in 500 µL of ddH_2O and transferred to a 1.5 mL reaction tube, followed by ethanol precipitation.

2.2.9. Ethanol precipitation

The DNA solution was placed on ice, and 50 µL of 3 M sodium acetate was added. Then, 1 mL of ice-cold ethanol (-20 °C, ≥99.8%) was added, and the tube inverted several times. The appearance of a slurry or cloudy precipitate indicated successful DNA precipitation. The tube was incubated on ice for an additional 15 min to ensure complete precipitation. Next, the tube was centrifuged at 11,000 g for 5 min, then immediately returned to ice to prevent overheating. This process was repeated two more times, after which the supernatant was removed. The DNA pellet was dried for 5-10 min at 72 °C, then dissolved in 200 µL of ddH_2O. The concentration of the DNA was then measured and, if necessary, adjusted accordingly.

2.2.10. Measurement and adjustment of DNA concentration

DNA concentration was measured using a UV spectrometer with 100 µL black quartz cuvettes. In this procedure, 100 µL of ddH_2O was used as the blank, while in the sample cuvette, 5 µL of DNA solution was mixed with 95 µL of ddH_2O and vigorously pipetted up and down to ensure homogeneity. The concentration was determined by measuring the optical density at 260 nm (OD_{260}). The DNA solution was then diluted with water until the OD_{260} reached a value of 1, which corresponds to a concentration of approximately 1 µg/µL. The prepared DNA was stored at -20 °C until further use.

2.2.11. Isolation and cultivation of eukaryotic tumor cells

GBM brain tumors were dissected and prepared at the Asklepios Clinic Nord Heidberg (AKH). Four tissue samples from the same tumor were, harvested near the SVZ, were placed into small tubes filled with DMEM and immediately transported to the laboratory. The tumor samples were immediately prepared and transferred into cell culture within 2-3 hours post-dissection. All cell culture steps were performed under a sterile working bench. The first step involved pressing the tissue through a 70 µm sterile cell strainer placed on a 50 mL tube, using the inner part of a 20 mL syringe. During this process, the strainer and mashed tissue were regularly washed with small amounts of DMEM, up to 20 mL. Once most of the tissue was mashed and pressed through the strainer, the remaining tissue was discarded, and the cell suspension in the tube was centrifuged for 10 min at 6,000 rpm. For a more detailed overview of the workflow, images can be found in the appendix (Fig. 73). After centrifugation, the supernatant was carefully discarded, and the pellet was washed, resuspended in approximately 20 mL of DMEM, and centrifuged again. After the second centrifugation step, the cells were resuspended in roughly 30 mL of DMEM and divided into multiple flasks (TC Flask T25/T75, Cell+, Vent. Cap). Typically, 1 mL was allocated to each T25 flask, and 2-3 mL to each T75 flask. Initially, for each tumor sample, at least three T75 and three T25 flasks with different media were prepared, one with pure human cerebrospinal fluid (hCSF), one with DMEM/hCSF/5% FBS (CSF-DF), and one with DMEM/10% FBS (DF). However, this was later changed to only use CSF-DF. Growth and cell adherence were monitored daily using a light microscope. The medium was exchanged when approximately 30% of the cells were adherent. The first passage was performed when cells reached at least 50% confluence after two weeks. Cultures with slower growth were only passaged once they achieved at least 80% confluence. Flasks that did not reach a minimum of 50% confluence after 12 weeks were discarded.

2.2.12. Mammalian cell cultivation

Cell growth was monitored via light microscopy. Cells were utilized once they reached a confluence of approximately 50-80%, ensuring an adequate cell density and cell number for subsequent experimental procedures. Excess medium and dead cells were carefully discarded into a disinfectant solution, and the flask was washed with 3-4 mL of 1x PBS buffer afterwards (Table 20Table 20 Composition for the preparation of a 1L solution of 10x PBS buffer) to ensure no residual DMEM and other non-essential components remained in the flask. To detach the cells from the flask surface, 2 mL of a Trypsin/EDTA (0.05%/0.02%) solution was added to the flask and incubated for at least 5 minutes. After that, cells were rinsed down with 8 mL DF medium and pipetted up and down to ensure an evenly distribution of all cells. From this

suspension, all further cell experiments were prepared by diluting the cells with DF (COS-1 and U-87 cells) or CSF-DF (AKH primary cell cultures). An appropriate number of cells was transferred into a new flask to ensure they could be used again within the next days. The new flask was filled up with DF for COS-1 and U-87 cells, and CSF-DF for AKH cell cultures, then placed into the incubator at 37 °C with 5% CO_2.

Table 20 Composition for the preparation of a 1L solution of 10x PBS buffer

Substance	Amount* [g]
NaCl	80
KCl	2
$Na_2HPO_4 \cdot 2\ H_2O$	17.8
KH_2PO_4	2.4

*Substances were completely dissolved in 800 mL ddH_2O, distilled water to a total volume of 1 L was added, pH adjusted to 7.4 and the mixture autoclaved

2.2.13. Preparation of transfection reagent

100 mg of PEI Max® was dissolved in 90 mL of ddH_2O over several hours, with stirring in a 250 mL bottle. After the PEI was completely dissolved, the pH was adjusted to 7 by carefully adding 1 M HCl in droplets. The mixture was sterile filtered afterwards, then prepared in aliquots of 1.5 mL and kept at -70 °C until use. After thawing, the mixture can be used for up to 4 weeks and should be stored in the fridge at 7 °C between uses.

2.2.14. Transfection

On the first day, 1 mL of COS-1 cells was transferred to a standard 24-well plate in a dilution that allowed a confluence of about 70-80% the next day. On the following day, the cells were first given 1 mL of fresh DF medium. Afterwards, PEI and DNA solutions (1 µg/µL) were prepared in separate PCR reaction tubes. In each tube, 100 µL of Opti-MEM™ was preadded, and the required amount of DNA or PEI was added afterwards. A 1:1 ratio of envelope and packaging plasmid, and a 2:3 ratio for DNA:PEI, gave the best results. Usually, 2 µg of envelope DNA and 2 µg packaging plasmid DNA were mixed with 6 µg PEI. After adding the required amount of DNA and PEI to their respective tubes, they were incubated for 5 minutes. After that, the PEI solution was carefully added to the DNA solution and gently mixed by circulating pipette tip inside the tube. The PEI/DNA mixture was incubated for 20 min at RT and then added dropwise into the respective well. The plate was carefully moved from left to right to reduce tension on the cells while mixing the solution. Cells were incubated with the transfection mix at 37 °C and 5% CO_2 for 6 hours. After 6 hours, the transfection medium was

carefully removed by tilting the plate and placing the pipette directly on the side of the well. This had to be done very carefully and slowly to avoid any detachment of the cells. Afterwards, each well was washed once with DF, and subsequently 1 mL of DF was added to each well before placing the plate back into the incubator. A slow procedure was mandatory to avoid further detachment. Since the packaging plasmid included the GFP coding sequence, transfection efficiency could be measured microscopically using a GFP filter. The transfection rate was monitored every 24 hours, and virus pseudotypes were harvested after 72 hours by collecting the supernatant from the transfection. Table 21 shows the combination of plasmids used and the names of the resulting pseudotypes for clarification.

Table 21 Plasmid combinations with corresponding pseudotypes

Envelope plasmid	Packaging plasmid	Resulting pseudotype
pCMV-EG1	pNL*gfp*AM	EG1-HIV*gfp*
pMD2-EG2	pNL*gfp*AM	EG2-HIV*gfp*
pCMV-VSV-G	pNL*gfp*AM	G-HIV*gfp*

2.2.15. Infection of tumor cells

Since all tumor cell cultures had different growth rates, each culture was prepared 1-3 days prior for infection experiments performed in a 96-well plate (Cell+, 200 µL/well) to ensure a confluence of 70-80% on the day of infection. After 72 hours, the supernatant from previously transfected cells (2.2.14) was transferred to a 1.5 mL centrifugation tube and centrifuged for 3 min at 14,000 g to ensure no transfected cells were carried over. Following centrifugation, the medium was transferred to another 1.5 mL tube and centrifuged again. Only about 950 µL was removed, leaving the cell pellet untouched to ensure that no transfected cells were transferred. After the second centrifugation, 900 µL of the supernatant were used for infection experiments. First, nearly the entire medium was removed from the cells to be infected, leaving a small amount inside each well to prevent drying out. Then, 150 µL of infection medium was added to each well, allowing infection of up to six wells simultaneously. Following infection, the cells were incubated for 72 hours at 37 °C and 5% CO_2 without medium exchange. Infected cells expressed green fluorescent protein (GFP), which was detected via fluorescence microscopy. After 72 hours, cells were examined using the GFP filter of the EVOS M5000 microscope.

2.2.16. Antibody staining

For the characterization of all tumor cell lines, immunostaining was performed using certain markers. All cell cultures were grown in 96-well plates (Cell+) at 37 °C and 5% CO_2, monitored daily until reaching an appropriate confluence that allowed for staining of both individual cells and groups of cells while maintaining characteristic morphologic features. Staining experiments were performed in quintuplets. Four wells were used for the respective antibody staining and the fifth well was used as negative control, where only the secondary antibodies were added. After removing the culture medium, each well was carefully washed with 300 µL of 1x PBS-T to remove residual culture medium and detached cells. The tumor cells were then fixed with a freshly prepared 3.7% formaldehyde solution. Specifically, 50 µL of formaldehyde solution was added to each well and incubated for 15 minutes at RT. Each well was subsequently washed three times with 200 µL of 1x PBS-T. Next, 30 µL of a 0.1% Triton® X-100 solution was added to each well and incubated for 5 minutes. After Triton® X-100 treatment, cells were again washed three times with 200 µL of 1x PBS-T. The cells were hey were blocked with 5% BSA in 1x PBS-T for 1 hour at RT. Following blocking, cells were only washed once, then treated with the primary antibody solution in 1% BSA/1x PBS-T and incubated overnight at 7 °C. Cells were co-incubated using the specific marker antibody, such as AXL, combined with a GFAP antibody to visualize astrocyte-like cells. The next day, the antibody solution was removed, and cells were washed three times with 200 µL of 1x PBS-T. Subsequently, they were co-incubated with an anti-GFAP and the respective marker secondary antibody in 1% BSA/PBS-T for 1 h in the dark at RT. After incubation, the secondary antibody solution was removed, and the wells were washed three times with 200 µL of 1x PBS-T. For phalloidin staining, a 2 µL/mL solution of Alexa Fluor® Plus 647 Phalloidin in 1% BSA/PBS-T was prepared. 30 µL of this solution was added to each well and incubated in the dark at RT for 90 min. After incubation, all wells were washed once to prevent dilution or rinsing of phalloidin. The final step involved adding one drop of ROTI®Mount FluorCare DAPI to each well, providing an antifading effect for fluorescent dyes while staining cell nuclei the same time. The plates were stored at 7 °C and could be used for up to 30 days.

2.2.17. Verification of integrin $\alpha_v\beta_5$ expression through antibody staining

The verification of integrin $\alpha_v\beta_5$ expression in GBM tumor cells was performed using 12-well glass slides. After detaching and preparing the cells as described in method 2.2.12, the remaining cells were divided between slides that had been placed into Petri dishes. The glass slides were previously prepared by immersion in different fluids, starting with warm soapy water. The excess foam was rinsed away with warm tap water, then the slides were placed into

ddH_2O, ethanol, 2-propanol, and acetone. After preparation, the slides were air-dried, placed into metal boxes, and autoclaved. For cell growth, the slides were placed into sterile Petri dishes using autoclaved tweezers. Then, 1 mL of cell suspension was placed onto the glass wells. After 5 minutes, 15 mL of CSF-DF was added, and the Petri dishes were sealed with Parafilm® and incubated at 37 °C with 5% CO_2 for up to 14 days. Once sufficient cell growth was achieved, the slides were carefully transferred into a glass container with PBS-T for 5 minutes to remove excess medium and non-adherent cells. The slides were then air-dried, and the tumor cells were fixed using 3.7% formaldehyde solution for 15 minutes at RT. The slides were washed three times with 1x PBS-T buffer solution afterwards to remove excess formaldehyde. These washing steps were repeated after each subsequent step. Cells were then treated with a 0.1% Triton® X-100 solution for 5 minutes. To prevent liquids from flowing into adjacent wells, a Super Pap Pen Liquid Block was used to encircle every well. The cells were then blocked for one hour in 5% BSA/1x PBS-T. For staining, the primary antibody against integrin $\alpha_v\beta_5$ (10 µL/mL) was diluted in 1% BSA/1x PBS-T, applying 30 µL per well. Cells were incubated at 7 °C overnight in the dark. The following day, the slides were washed three times with 1% BSA/1x PBS-T solution and then incubated with the secondary antibody (4 µL/mL, 30 µL per well, diluted in 1% BSA/1x PBS-T) for one hour at RT in the dark. Subsequently, actin was stained using Phalloidin-iFluor™ 647 conjugate in 1% BSA/1x PBS-T (2 µL/mL, 30 µL per well). Cells were incubated for 60 minutes at RT in the dark. After a final washing step, cells were ultimately treated with ROTI®Mount FluorCare DAPI, applying one drop per well. Imaging was performed using an EVOS M5000 microscope.

3. Results

3.1. Diagnostic biomarkers of glioblastoma tumor samples

Tumor samples were obtained from 16 patients and the primary GBM cell cultures were designated AKH-5 to AKH-24. As shown in Table 22, all tumors were IDH-1 wild-type (isocitrate dehydrogenase 1, wt), indicating that no IDH-1 mutations were detected, classifying all of them as World Health Organization (WHO) grade 4 glioblastomas. The tumor marker Ki-67, percentage of positive cells, was generally high (>15%) for all samples. The methylation status of the *MGMT* (O6-methylguanine-DNA-methyltransferase) gene was negative in seven tumors (AKH-5, -11, -12, -13, -14, 21, and -23), while MGMT promoter hypermethylation was detected in eight tumors (AKH-9, -10, -16, -17, -18, -19, -20, and -24). No data regarding *MGMT* methylation status were available for AKH-15.

Table 22 Parameters of GBM tumors used for the generation of primary cell cultures

AKH [#]	Ki-67 index [%]	IDH-1	MGMT methylation	OS [months]
5	30	wt	negative	n.d.
9	>40	wt	hypermethylated	7
10	>40	wt	hypermethylated	29
11	>25	wt	negative	9
12	>30	wt	negative	49
13	20	wt	negative	n.d.
14	>50	wt	negative	10
15	>40	wt	n.d.	3
16	15	wt	hypermethylated	3
17	>15	wt	hypermethylated	18
18	25	wt	hypermethylated	n.d.
19	20	wt	hypermethylated	1
20	70	wt	hypermethylated	5
21	20	wt	negative	10
23	18	wt	negative	alive*
24	20	wt	hypermethylated	alive*

wt: wild-type, OS: overall survival; n.d.: no data.; *: as of August 2025

3.2. Cultivation of primary glioblastoma cell cultures

GBM tumor samples were transferred into cell culture within three hours of resection. Due to the soft consistency of brain tissue, cell separation was performed by pressing the sample through a nylon mesh, a 70 µm sterile cell strainer. After washing the cell suspension with DMEM, tumor cells were incubated in Cell+ flasks at 37 °C and 5% CO_2. Three different media for cultivation were used, standard DF medium, pure human cerebrospinal fluid (hCSF), and CSF-DF medium. Growth was monitored daily for the appearance of adherent cells, and growth rates are presented in Table 23. The first cell passage was performed only after cultures reached at least 50% confluence and sufficient cell-cell contacts were established. Optimal cell growth was observed using CSF-DF medium. Therefore, culturing with DF and hCSF was no longer performed from AKH-18 onwards.

Table 23 Growth rates of freshly isolated tumor cells in three different media

AKH [#]	DF	hCSF	CSF-DF
5	++	+	+++
9	+++	+	+++
10	++	+	+++
11	++	-	+++
12	+++	+	+++
13	++	+	n.d.
14	++	+	+++
15	+	-	++
16	++	-	+++
17	++	-	+++
18	n.d.	n.d.	+++
19	n.d.	n.d.	+++
20	n.d.	n.d.	++
21C	n.d.	n.d.	+
21S	n.d.	n.d.	+
23	n.d.	n.d.	+++
24C	n.d.	n.d.	+++
24S	n.d.	n.d.	+++

-: cells took more than 8 weeks to reach a confluence of at least 50%, +: 4-6 weeks; ++: 2-4 weeks; +++: less than 2 weeks; n.d.: not done.

3.2.1. Growth characteristics of the primary glioblastoma cell culture AKH-19

The primary cell culture AKH-19 was monitored for 12 weeks, following initial cultivation, serving as an example of the growth behavior of primary GBM tumor cells in CSF-DF medium. Cells were observed daily during the first 14 days, and subsequently on days 21, 28, 42, and 56 (Fig. 4). Final images were taken after 12 weeks of growth and are presented in Fig. 6. Additionally, AKH-17 and AKH-21C/S cell cultures were included for comparison, imaged after seven and 14 days of culture, respectively. The initial 14 days were typically the most critical, as the cells needed to adapt to the new culture conditions.

The first adherent cells were observed after one day, exhibiting an elongated morphology and appearing as black lines under the microscope. By day two, additional adherent cells were observed. Some appeared as single, elongated cells, while others began to establish contacts with neighboring cells. In addition to adherent cells, clusters of small, round cells accumulated around them, consistently appearing brighter than the surrounding cells. On day three, both the number of adherent single cells and cell clusters increased. The small cells near the adherent cells also developed larger clusters above the adherent cells, forming a localized microenvironment. Furthermore, the adherent cells started began extending processes resembling filopodia towards neighboring cells. After five days, an increasing number of cells exhibiting filopodia were observed. On day six, these features were particularly prominent in some areas of the cell culture flasks. By day seven, small round cells were attached to nearly every adherent cell and remained visible for approximately 14 days. After that, they disappeared and were no longer detectable by day 21. From day eight onwards, some areas in the flask began to develop network-like structures. Cell growth accelerated as more cell-cell contacts were established. Between days nine and thirteen (Fig. 4), the cellular meshes extended further, connecting multiple single cells in the process. After 14 days, multiple areas packed with tight meshes of cells were observed, forming contacts via long filopodia-like features. After 21 and 28 days respectively, the cell culture exhibited a very pronounced network, showing a variety of cell morphologies like spindle-shaped, polygonal, amorphous, and large star-shaped cells (Fig. 5). After 42 days, the cells had grown to such an extent that they were overlapping one another and were establishing a greater number of cell-to-cell contacts. After eight weeks (day 56), large aggregates of adherent cells had formed, consisting of multiple cell layers, while monolayers continued to grow in other areas. These cells assembled in shapes that looked filopodia-like but consisted of many cells, rather than single cells. These structures also reached out to other bulks, further forming cell-cell contacts in large numbers (Fig. 5, day 56.).

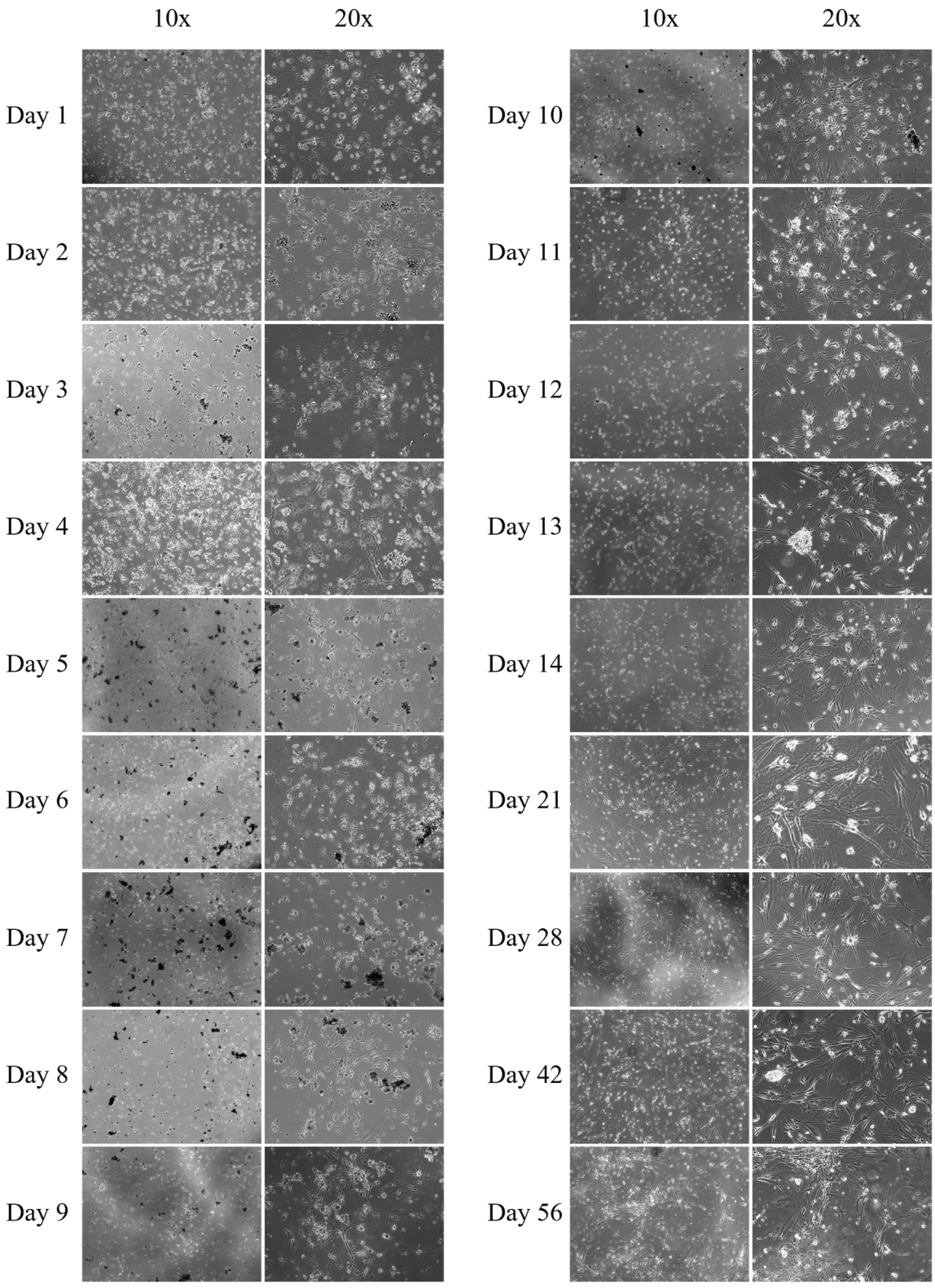

Fig. 4 Growth characteristics of AKH-19 cells in CSF-DF. Growth was observed over a course of eight weeks. Monitoring was performed daily for the first 14 days, and then on days 21, 28, 42, and 56. Images are presented at 10x and 20x magnification.

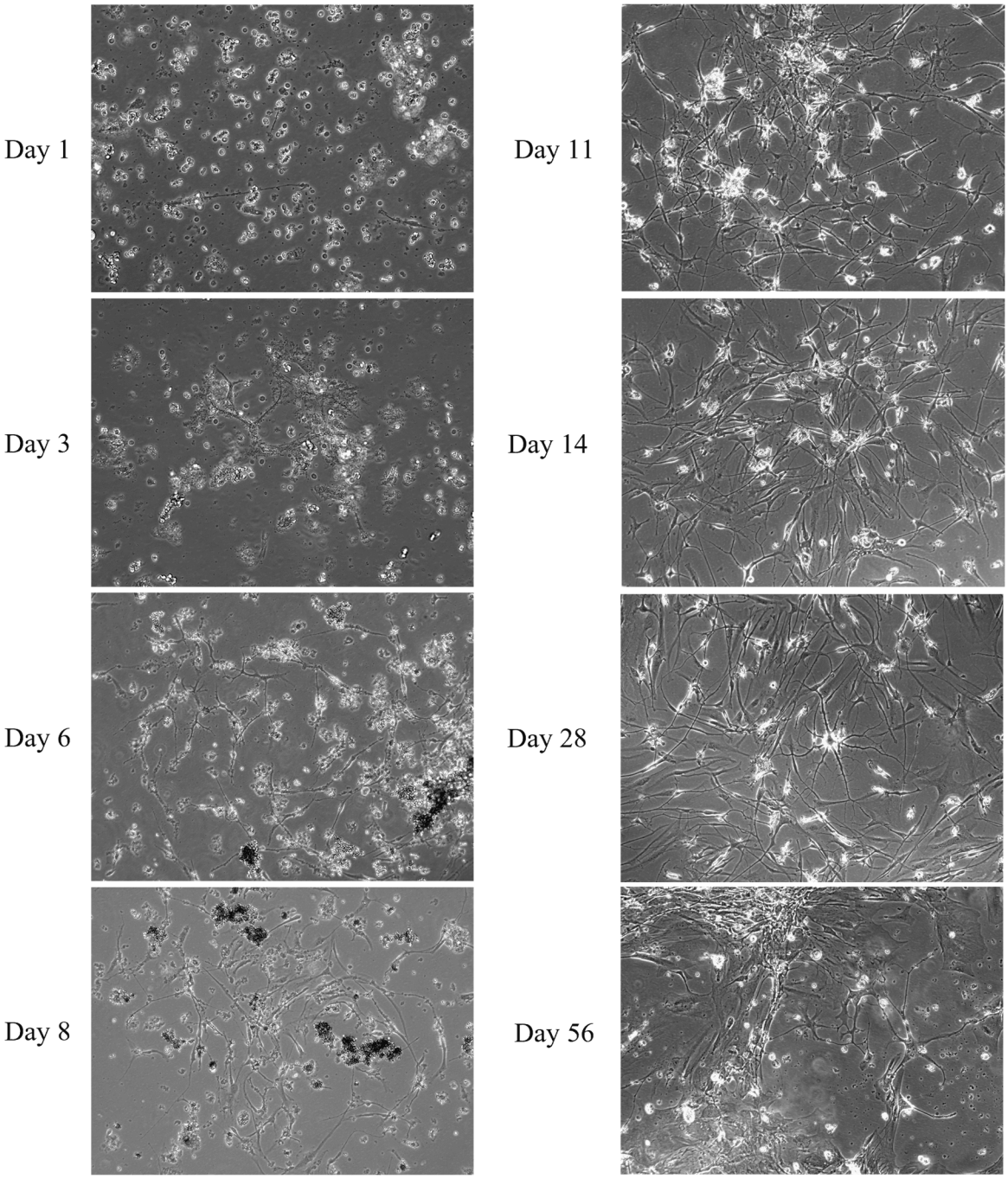

Fig. 5 Growth characteristics of AKH-19 cells in CSF-DF on specific days. Images were selected based on certain GBM features that developed over the course of eight weeks. Day 1: the first adherent cells were observed and appeared as black lines; day 3: the first cell-cell contacts were observed; day 6: cells reaching out to cells farther away by developing longer filopodia; day 8: the first structurally ordered cells were observed; day 11: a more organized network of cells in which large star-shaped cells appear, small cell bodies are featured on almost every adherent cell; day 14: an established cell network, in which only adherent cells appear, had been established; day 28: areas with large star-shaped cells were observed in the center of networks, seemingly connecting everything nearby; day 56: Structures resembling elongated single cells were observed, but instead of single cells, these contained several dozen cells. Images are presented at 20x magnification.

After twelve weeks of growth, the surface of the cell culture flask was completely covered with tumor cells (Fig. 6, A). Despite this confluence, a uniform cell culture was not established, as distinct cell types and morphologies remained evident. This suggests that AKH-19 cells retained their *in vivo* heterogeneity. At this stage, the tumor culture had developed a network in which astrocyte-like cells can be seen in central positions, developing numerous small processes to connect as many surrounding cells as possible (Fig. 6, B and C). Furthermore, huge three-dimensional cell aggregates could be observed (Fig. 6, D).

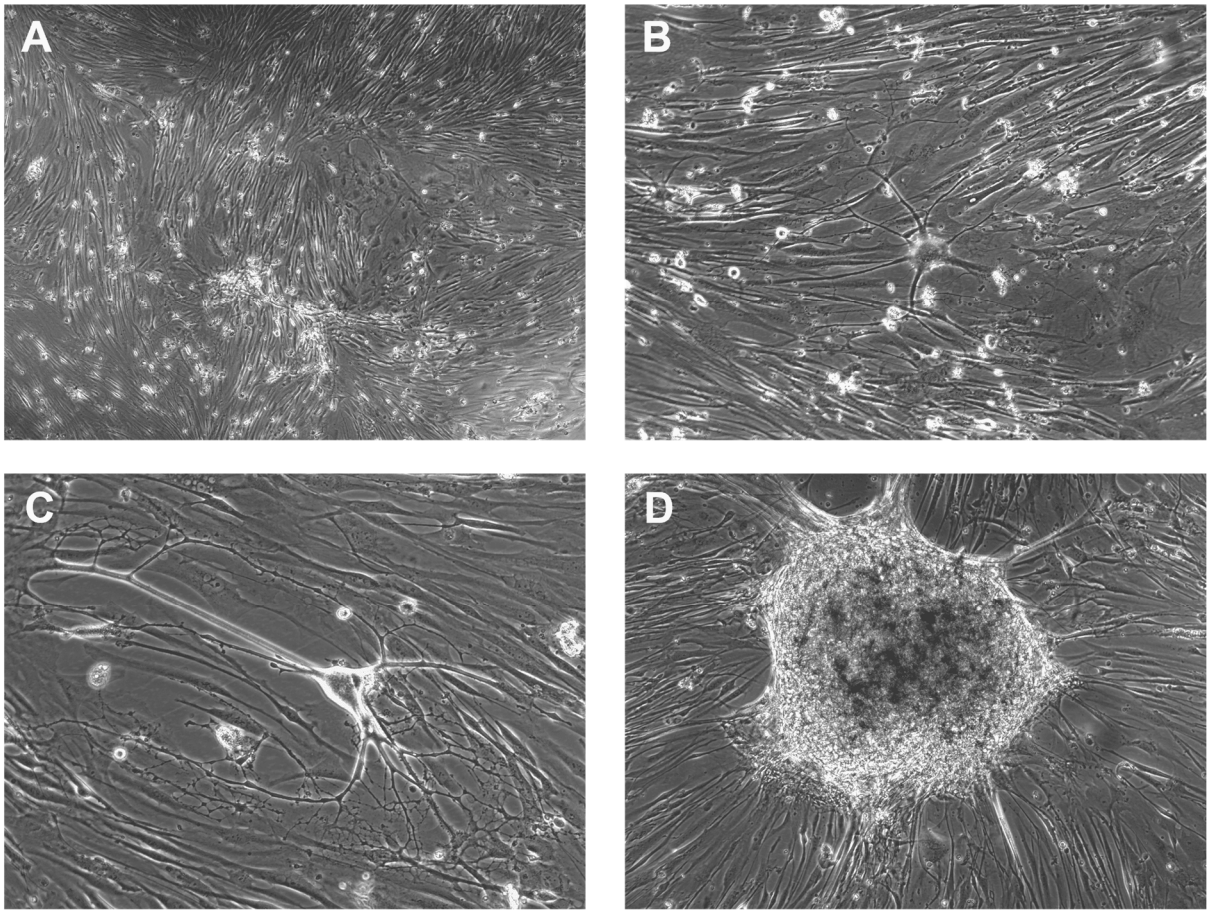

Fig. 6 AKH-19 cell culture after 12 weeks growth in CSF-DF. **A**: overview of a random area in the culture flask: cells have covered the entire surface, while still maintaining the heterogeneity of the culture; **B**: central astrocyte-like cells can be seen, connecting a large abundance of cells through their processes; **C**: astrocytes are seen as the central cell type of the cell culture, developing hundreds of small processes that branch along the whole culture; **D**: large three-dimensional cell aggregates can be observed, possibly forming because of the lack of space on the surface; image A was captured at 10x magnification, images B,C, and D at 20x magnification.

3.2.2. Growth of AKH-17, AKH-21S, and AKH-21C

For a brief overview of the heterogeneous growth behavior of every cell culture after cultivation, the growth of cell cultures AKH-17, -21S, and -21C after seven and fourteen days is shown in Fig. 7 for comparison. AKH-21S was established from tissue obtained adjacent to the SVZ, while AKH-21C originated from a sample taken near the tumor core.

AKH-17 cells had a similarly fast growth rate as AKH-19 cells. After seven days, numerous adherent cells, including small astrocyte-like cells, were observed. This number increased over the next seven days, resulting in almost complete covering of some areas in the flask, as can be seen on the left side of the image. Notably, AKH-17 cells appeared smaller than AKH-19 cells. Although derived from different tumor regions, both AKH-21S and -21C cell cultures initially showed a similar growth behavior. Compared to AKH-17 and AKH-19 cells, these cultures adapted to *in vitro* conditions more rapidly, given the number of adherent cells observed after seven days. However, after 14 days, the number of adherent cells did not increase further, with some areas showing fewer adherent cells than before. This ultimately resulted in reduced overall growth for both cultures, making them among the slowest growing cell cultures in this study.

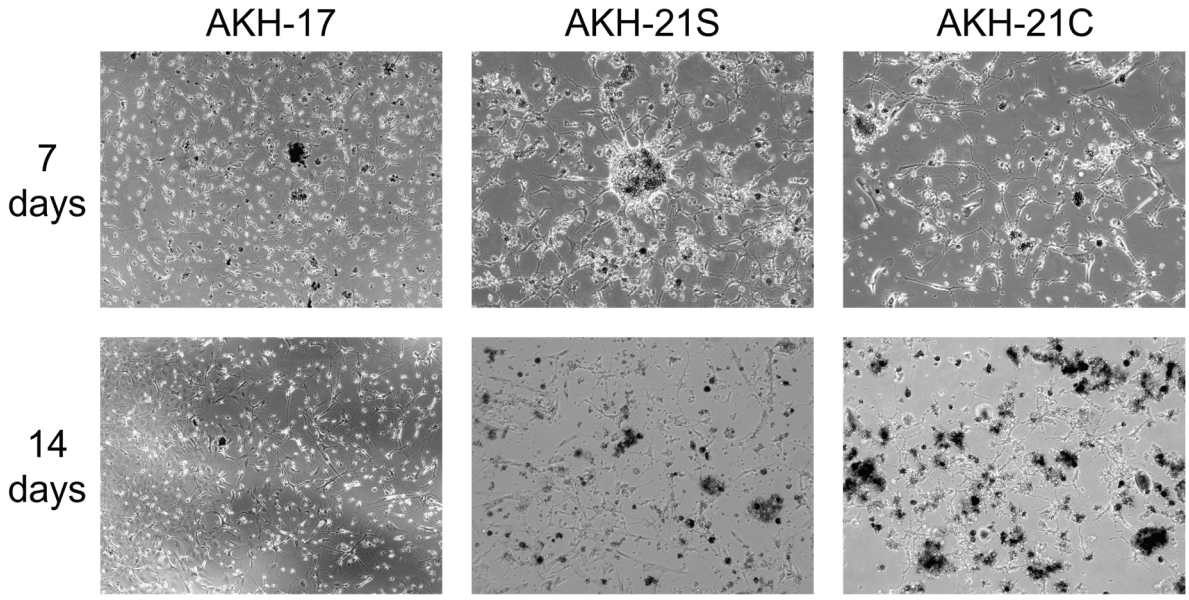

Fig. 7 Cell growth of AKH-17, AKH-21S, and AKH-21C. All cell cultures were monitored over the first 14 days, with regular imaging to document their condition. The figures provided show the cultures after seven and 14 days of growth. Overall, all cultures adapted well to the CSF-DF culturing conditions, as evidenced by the number of adherent cells. Notably, growth and adherent cell numbers from culture AKH-17 increased over time, whereas cultures AKH-21C and -21S showed no increase in growth, with a decline in the number of adherent cells observed. Images are presented at 10x magnification.

3.3. Identification of glioblastoma biomarkers

Biomarker identification was performed via immunostaining. Cells were cultured in 96-well plates until a confluence of approximately 60-80% was reached. This ensured that tumor cells developed their characteristic morphology, which might not be maintained if cell growth was too dense.

All available primary GBM cell cultures, grown in 96-well plates (Cell+), were characterized for expression of SOX2, OCT4, NANOG, Nestin, CD44, CD133, PD-1, ITGA6, and EGFR. They were also analyzed for the presence of ZIKV entry receptors AXL and integrin $\alpha_v\beta_5$. Expression of integrin $\alpha_v\beta_5$ was assessed in cells grown both on glass slides and on plastic in 96-well plates (Cell+). All markers were co-incubated with a GFAP antibody to detect GFAP-expressing cells (e.g., astrocytes, visualized by cyan fluorescence). Marker-specific primary and corresponding secondary antibodies were used for visualization (green fluorescence). Additionally, cells were stained with phalloidin to visualize the actin cytoskeleton (red fluorescence) and with DAPI to stain nuclei (blue fluorescence). The GBM ependymal cell line U-87 was used as a reference for comparison.

The tumor samples that were used to generate cultures AKH-5, -9, -10, -11, -12, and -13 were randomly selected from resected GBM tumors. Cell cultures AKH-14 to AKH-24 were established from tissue samples obtained from the outer regions of the tumor, preferably near the vicinity of the SVZ. This increases the likelihood of isolating GSCs and astrocytes, which are more frequently found in the outer regions of GBM.

Since each image represents only a section of a 96-well plate and each tumor sample exhibits different heterogeneity marker expression, representative image sections were selected show both the expression of the biomarker and $GFAP^+$ (astrocyte-like) cells. This was achieved for cultures AKH-14, -15, -17, -18, -19, -21S, -21C, -21, 24S, and -24C with GFAP-positive and negative cells in at least one of the sections. No $GFAP^+$ cells were detected in cultures AKH-5, -9, -10, -11, -12, -13, -16, -20, and U-87.

Results for all primary tumor cell cultures are presented in chapters 3.3.1 through 3.3.19 and are further summarized in Table 24, which provides an overview of the expression pattern for all markers.

3.3.1. Characterization of primary cell culture AKH-5

AXL was ubiquitously expressed on the surface and in the cytoplasm of all imaged cells, with some expression observed in the nucleus of a few cells. Integrin $\alpha_v\beta_5$ expression in 96-well plates could not be detected (Fig. 8). On glass slides however, integrin $\alpha_v\beta_5$ was detectable on being expressed on the cell surface of all tumor cells. Increased expression was observed near the nuclei of many cells.

AKH-5 cells were positive for SOX2, OCT4, Nestin, CD44, PD-1, and EGFR (Fig. 9). Conversely, GFAP, NANOG, CD133 and ITGA6 expression was absent. The number of Nestin-expressing cells was minimal.

SOX2 was predominantly localized at the nucleus and the cytoplasm (Fig. 9). OCT4 expression occurred exclusively at the nucleus. Nestin expression was located inside the cytoplasm and only expressed in two out of the 32 cells observed. CD44 and PD-1 were mostly expressed on the cell surfaces of all cells with some cells exhibiting elevated fluorescence near the nucleus. EGFR was highly expressed in clusters at the nucleus of a few cells as well as elevated in the cytoplasm and the surfaces of all cells.

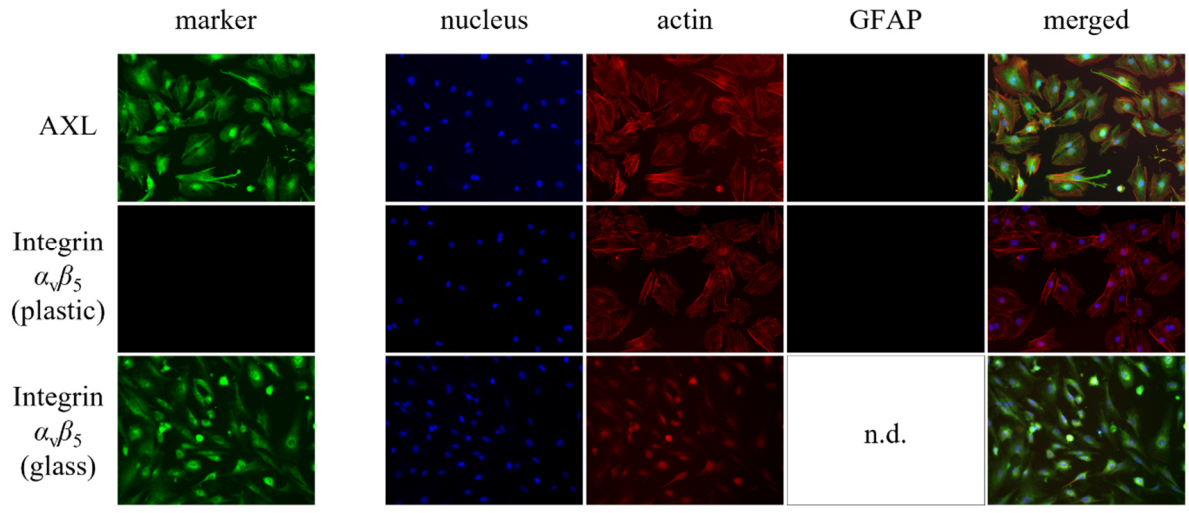

Fig. 8 ZIKV receptor analysis for AKH-5. Cells were cultured in 96-well plates (Cell+) until they reached a confluence of about 60-80%. For integrin $\alpha_v\beta_5$, cells were also cultured on glass slides for 10 days. Marker: commercial marker-specific primary antibodies were used for immunostaining and were detected by a goat anti-mouse IgG secondary antibody (Alexa Fluor ® 488, green); nucleus: nuclei were stained with DAPI (blue); actin: staining with phalloidin (Alexa Fluor® 647, red); GFAP: GFAP-specific antibody detected by a rabbit-anti mouse IgG antibody (Alexa Fluor ® 568, cyan). All images are presented at 20x magnification; n.d., not determined.

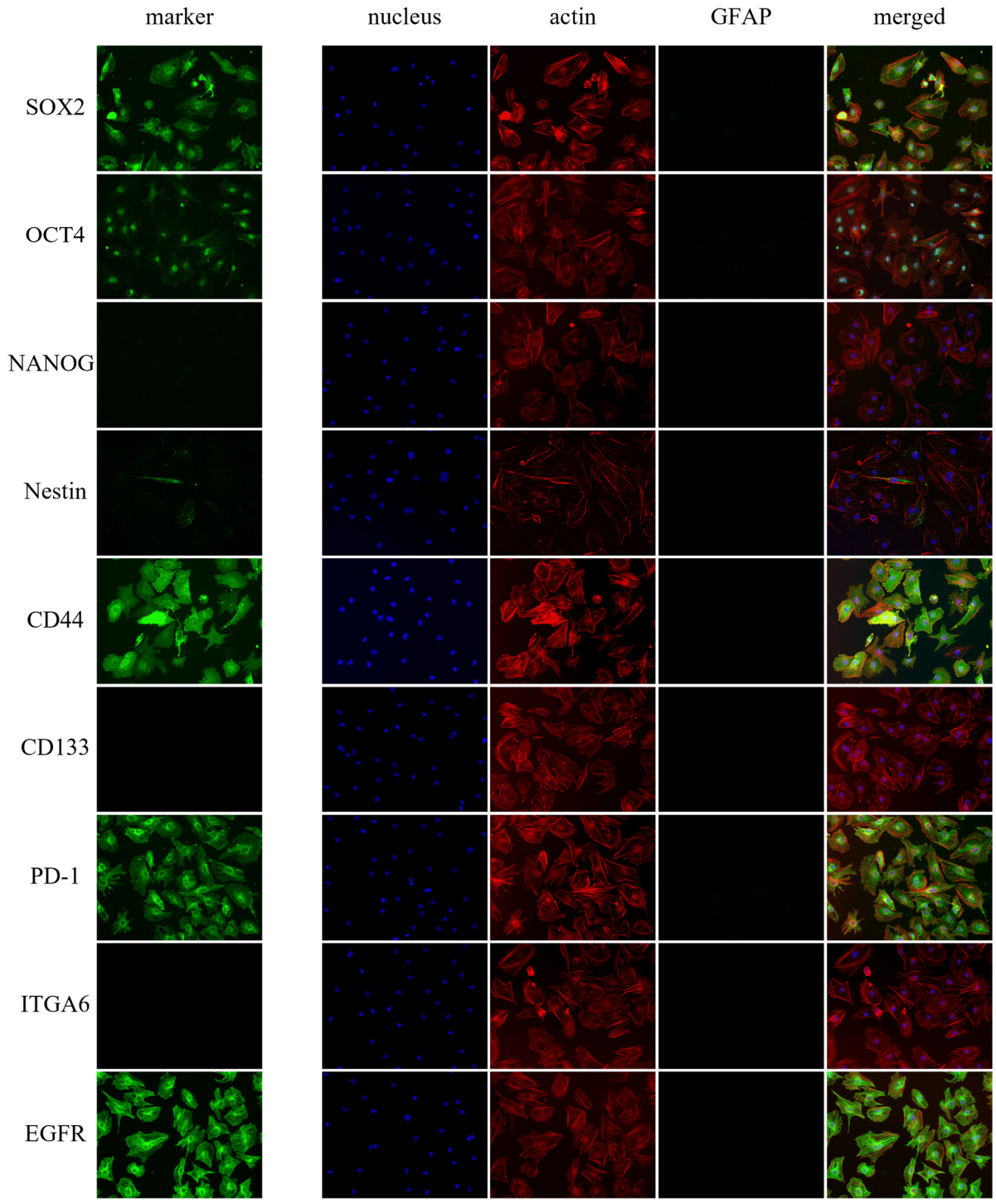

Fig. 9 GSC and GBM biomarker analysis for AKH-5. Cells were cultured in 96-well plates (Cell+) until they reached a confluence of about 60-80%. Marker: commercial marker-specific primary antibodies were used for immunostaining and were detected by a goat anti-mouse IgG secondary antibody (Alexa Fluor® 488, green); nucleus: nuclei stained with DAPI (blue); actin: actin skeleton stained with phalloidin (Alexa Fluor® 647, red); GFAP: GFAP-specific antibody detected by a rabbit-anti mouse IgG secondary antibody (Alexa Fluor ® 568, cyan). All images are presented at 20x magnification.

3.3.2. Characterization of primary cell culture AKH-9

AXL was highly expressed and was detectable at the surface and the cytoplasm of all cells (Fig. 10). Some cells exhibited increased expression around the nuclear area. No integrin $\alpha_v\beta_5$ expression was found in cells that have grown in 96-well plates. Cells that have grown on glass slides expressed large amounts of integrin $\alpha_v\beta_5$.

AKH-9 cells were tested positive for SOX2, OCT4, Nestin, CD44, PD-1, ITGA6, and EGFR (Fig. 11). The expression of Nestin and ITGA6 was very low. NANOG, CD133, and GFAP expression was negative.

SOX2 was located around the nucleus as well as the cytoplasm (Fig. 11, SOX2). Four out of ten imaged tumor cells did not express SOX2 in the nucleus. OCT4 expression was solely located at the nucleus of every cell. Nestin was expressed along the whole length of one cell, seemingly being expressed at locations where the actin skeleton was not well developed. CD44 was localized both on the surface and in the cytoplasm of every cell. One cell with five small nuclei touching each other expressed particularly large amounts of CD44 (Fig. 11). A small fraction of ITGA6 expression was found to be expressed on the surface of one cell. The expression was only located to a small part of the membrane, seemingly random. All other cells were negative for ITGA6. PD-1 was expressed in the cytoplasm and on the surface of every cell. EGFR was mostly expressed in the cytoplasm and to some extent on the cell membranes. Most cells had an increased expression around and inside the nucleus. The two cell-like structures on the bottom left expressing EGFR and actin had no nucleus (Fig. 11).

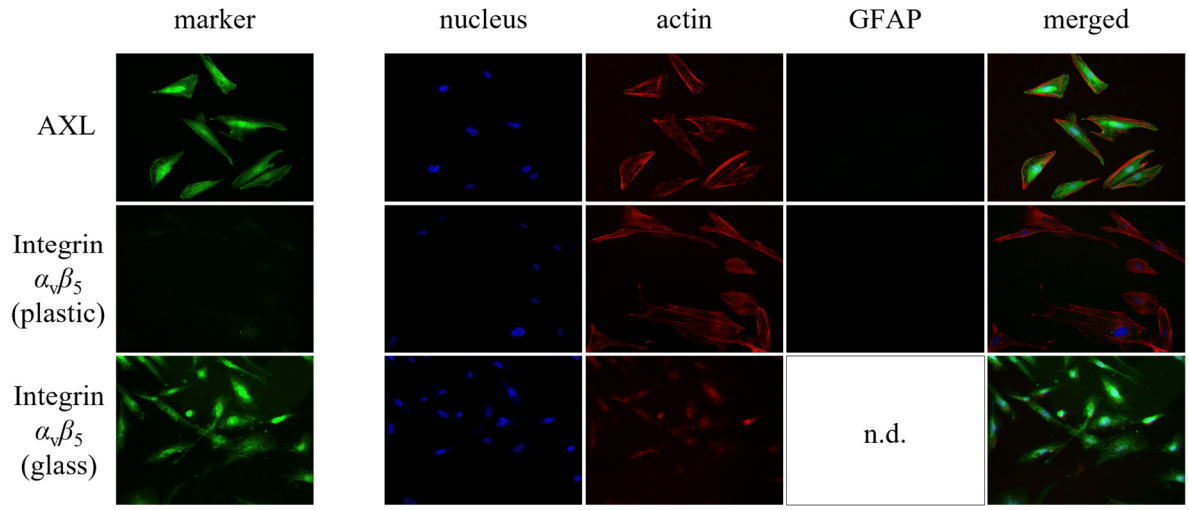

Fig. 10 ZIKV receptor analysis for AKH-9. For a detailed description, see Fig. 8.

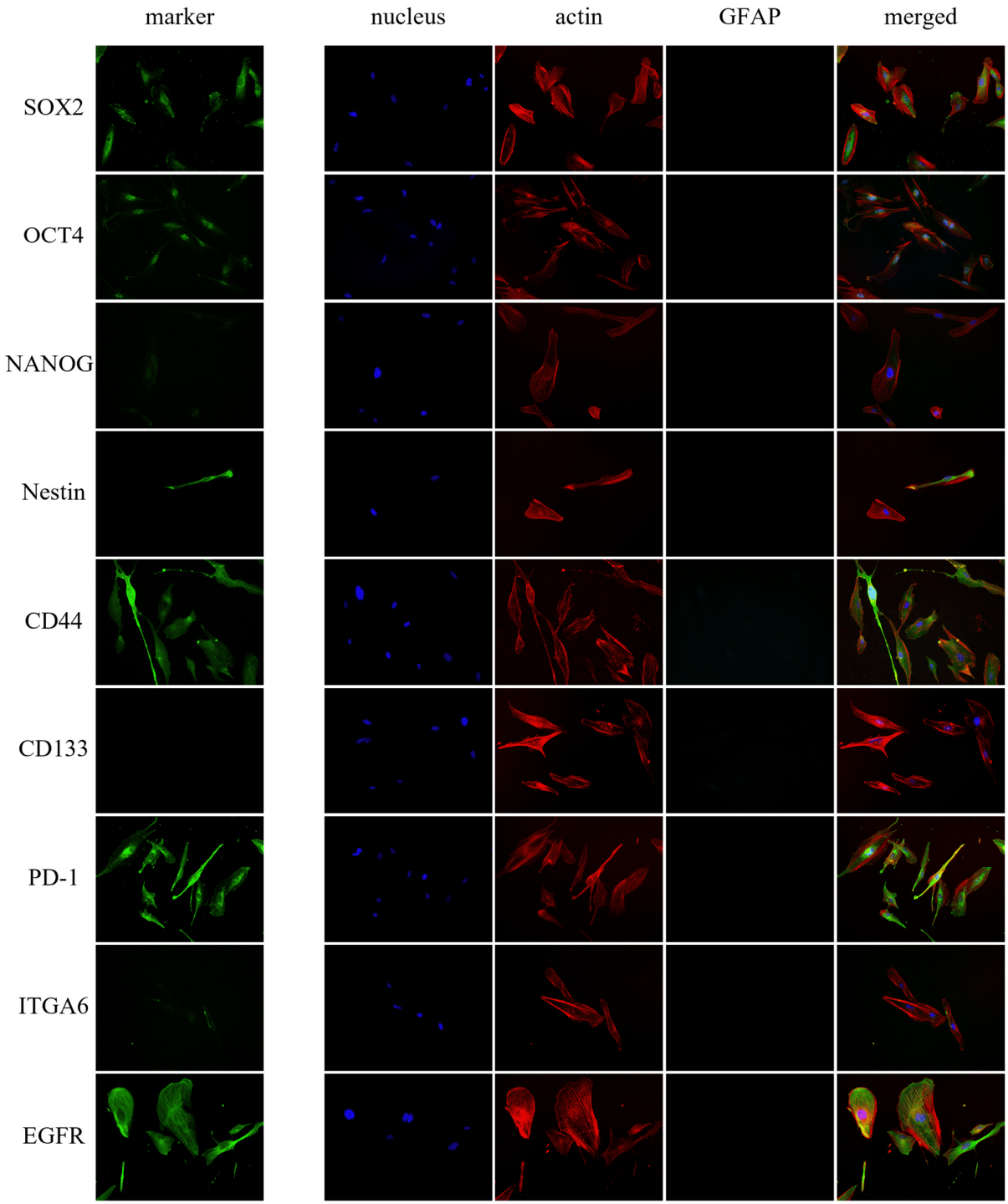

Fig. 11 GSC and GBM biomarker analysis for AKH-9. For a detailed description, see Fig. 9.

3.3.3. Characterization of primary cell culture AKH-10

Expression of AXL was found inside the cytoplasm of all cells while half of all imaged cells showed increased expression at the nucleus (Fig. 12). Integrin $\alpha_v\beta_5$ expression in cells that have grown on plastic was very low. Low amounts of integrin $\alpha_v\beta_5$ were found in nine of sixteen imaged cells that have grown on plastic (Fig. 12, $\alpha_v\beta_5$). In contrast, the expression of integrin $\alpha_v\beta_5$ was highly elevated in cells grown on glass. It was detectable in high amounts at the nucleus and inside the cytoplasm of all cells.

AKH-10 was tested positive for SOX2, OCT4, Nestin, CD44, PD, ITGA6, and EGFR. Nestin and ITGA6 expression was minimal. Expression of NANOG, CD133, and GFAP was not detected (Fig. 13).

SOX2 was found to be expressed in the nuclei and cytoplasm of all cells (Fig. 13). OCT4 expression was in the nucleus of all cells. Nestin was only found in two cells, located along their actin skeleton. The observed expression pattern suggested that the cells were connected via Nestin. CD44 was found to be at the surface of every cell. Three out of 27 imaged cells did not express CD44 (Fig. 13). PD-1 was localized to the surface and the cytoplasm of all imaged cells. EGFR expression was mostly found inside the cytoplasm while also being clustered at the nucleus. Some cells also showed increased EGFR expression inside the nucleus.

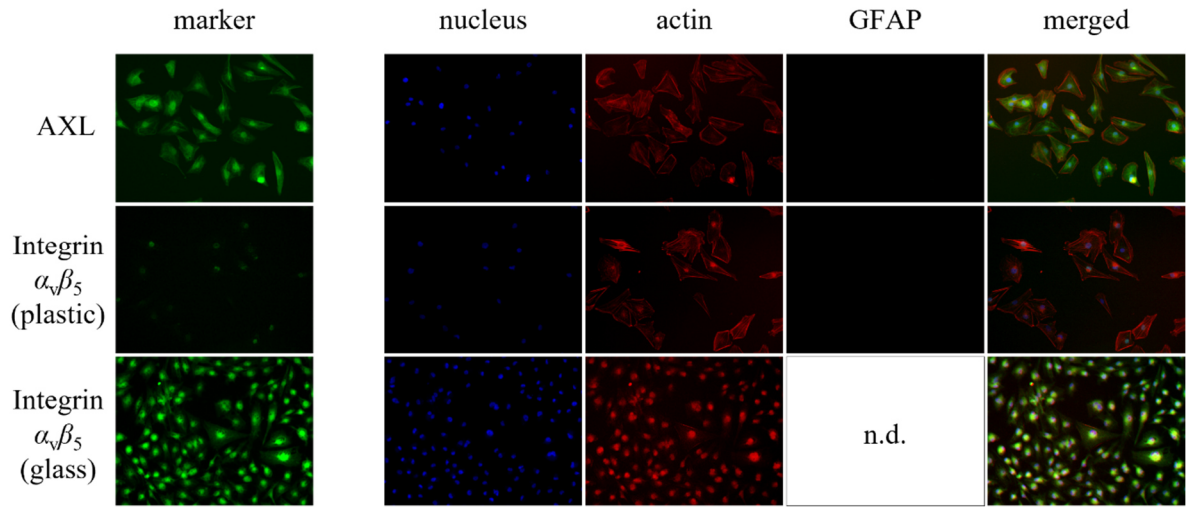

Fig. 12 ZIKV receptor analysis for AKH-10. For a detailed description, see Fig. 8.

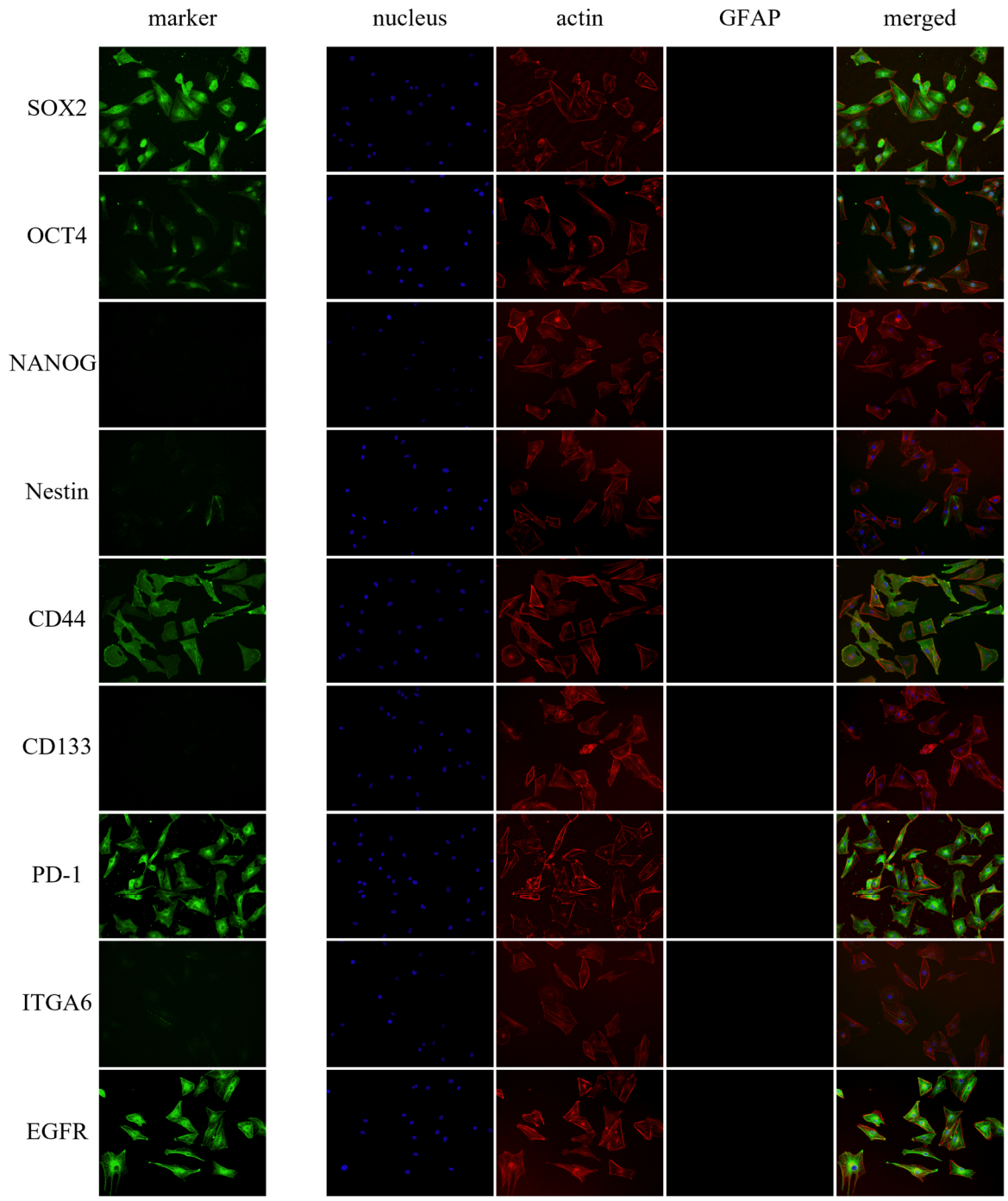

Fig. 13 GSC and GBM biomarker analysis for AKH-10. For a detailed description, see Fig. 9.

3.3.4. Characterization of primary cell culture AKH-11

AXL was ubiquitously found in all imaged tumor cells, being primarily located inside the cytoplasm and near the nucleus (Fig. 14). No integrin $\alpha_v\beta_5$ expression was detected in cells grown on plastic. In contrast, cells grown on glass exhibited high amounts of integrin $\alpha_v\beta$ on their cell surfaces. Increased expression at the nucleus was observed for dividing tumor cells (Fig. 14).

Cell culture AKH-11 was tested positive for SOX2, OCT4, CD44, PD-1, ITGA6, and EGFR (Fig. 15). No signals for NANOG, Nestin, CD133, and GFAP were found.

SOX2 was mostly localized to the cytoplasm and was elevated in the nucleus of some cells as well. OCT4 was highly expressed inside the nuclei of all imaged tumor cells. CD44 expression was found in every cell and in particularly high amounts in approximately half of all imaged cells. CD44 was localized to the cell surface, inside the cytoplasm and partly inside the nucleus. (Fig. 15). PD-1 and EGFR expression was observed inside the cytoplasm and the surface of every cell.

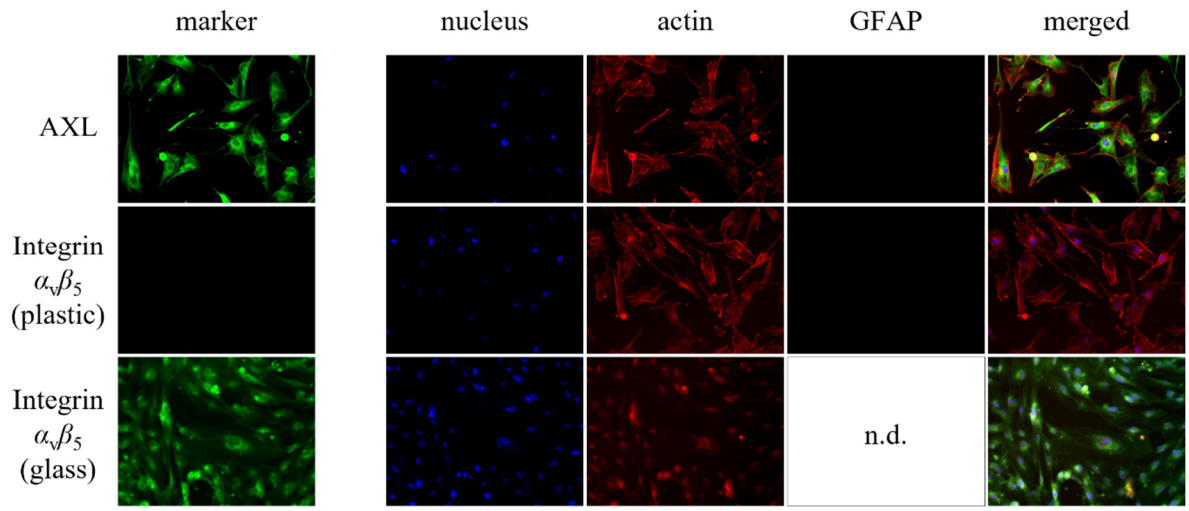

Fig. 14 ZIKV receptor analysis for AKH-11. For a detailed description, see Fig. 8.

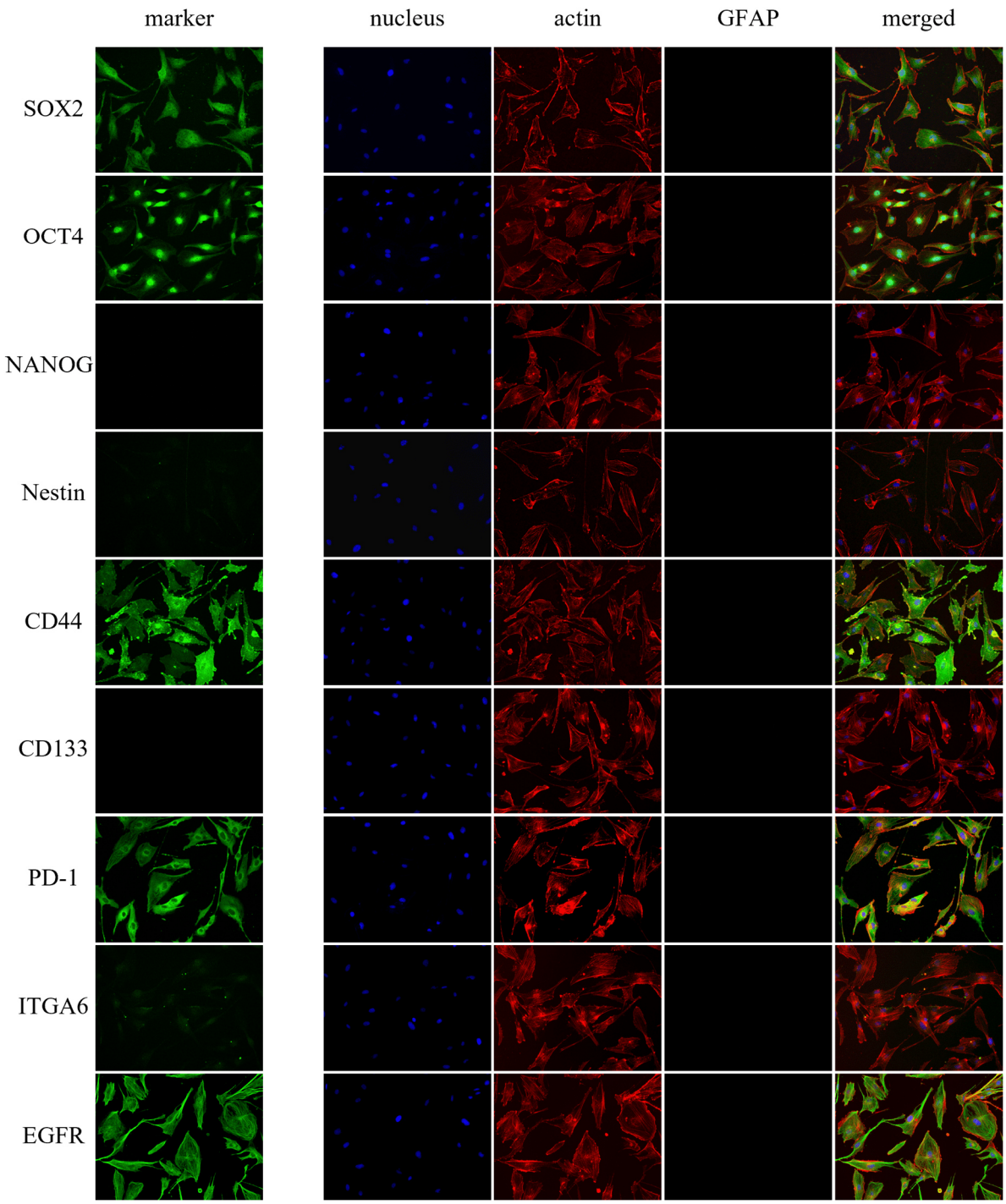

Fig. 15 GSC and GBM biomarker analysis for AKH-11. For a detailed description, see Fig. 9.

3.3.5. Characterization of primary cell culture AKH-12

Cells from cell culture AKH-12 were the first, in which the expression of integrin $\alpha_v\beta_5$ in cells grown on plastic was detectable (Fig. 16). All three imaged cells showed increased expression in the nucleus and on their surfaces. The distribution of integrin $\alpha_v\beta_5$ in cells grown on glass was more evenly distributed on the cell surfaces, with less expression observed inside the nucleus. AXL expression was observed in every imaged cell. It was mostly located in the cytoplasm and on the cell surface, though some cells showed increased expression in the nucleus. (Fig. 16).

AKH-12 cells were large compared to other cultures, partly incorporating multiple nuclei. They were tested positive for SOX2, OCT4, Nestin, CD44, PD-1, ITGA6, and EGFR (Fig. 17). NANOG, CD133, and GFAP were negative.

SOX2 expression was increased both in the nucleus and perinuclear area of all cells and was also found to be distributed over the cytoplasm. OCT4 was primarily localized to the nuclear region, with some additional signals found inside the cytoplasm. A strong fluorescent signal was observed in the cytoplasm of a large cell. Although high OCT4 expression is usually found in the nucleus, this signal was not located near any nucleus. Nestin was found in two cells, being distributed in parts of the cytoplasm (Fig. 17). Especially the huge cell in the middle, seemingly sharing three nuclei, displayed Nestin in large amounts, mostly located near the cell membrane. CD44 expression was found at the surface of all cells. PD-1 was observed in the cytoplasm and on the surface of all cells. ITGA6 expression was distributed in the cytoplasm and partly on the cell surfaces. One cell showed strong expression in the perinuclear area. EGFR was displayed at the cell nucleus, inside the cytoplasm and the cell surfaces.

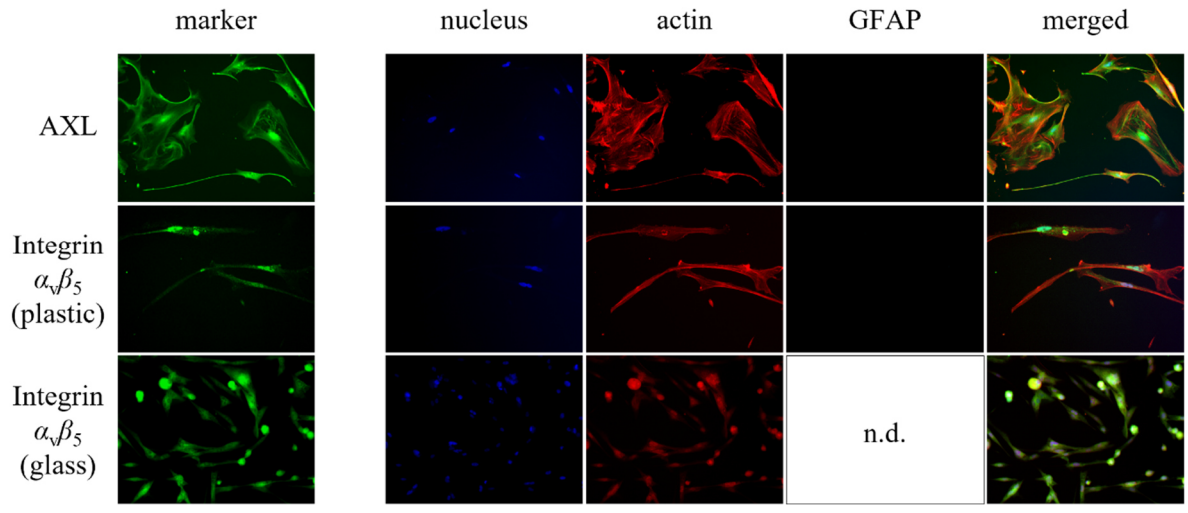

Fig. 16 ZIKV receptor analysis for AKH-12. For a detailed description, see Fig. 8.

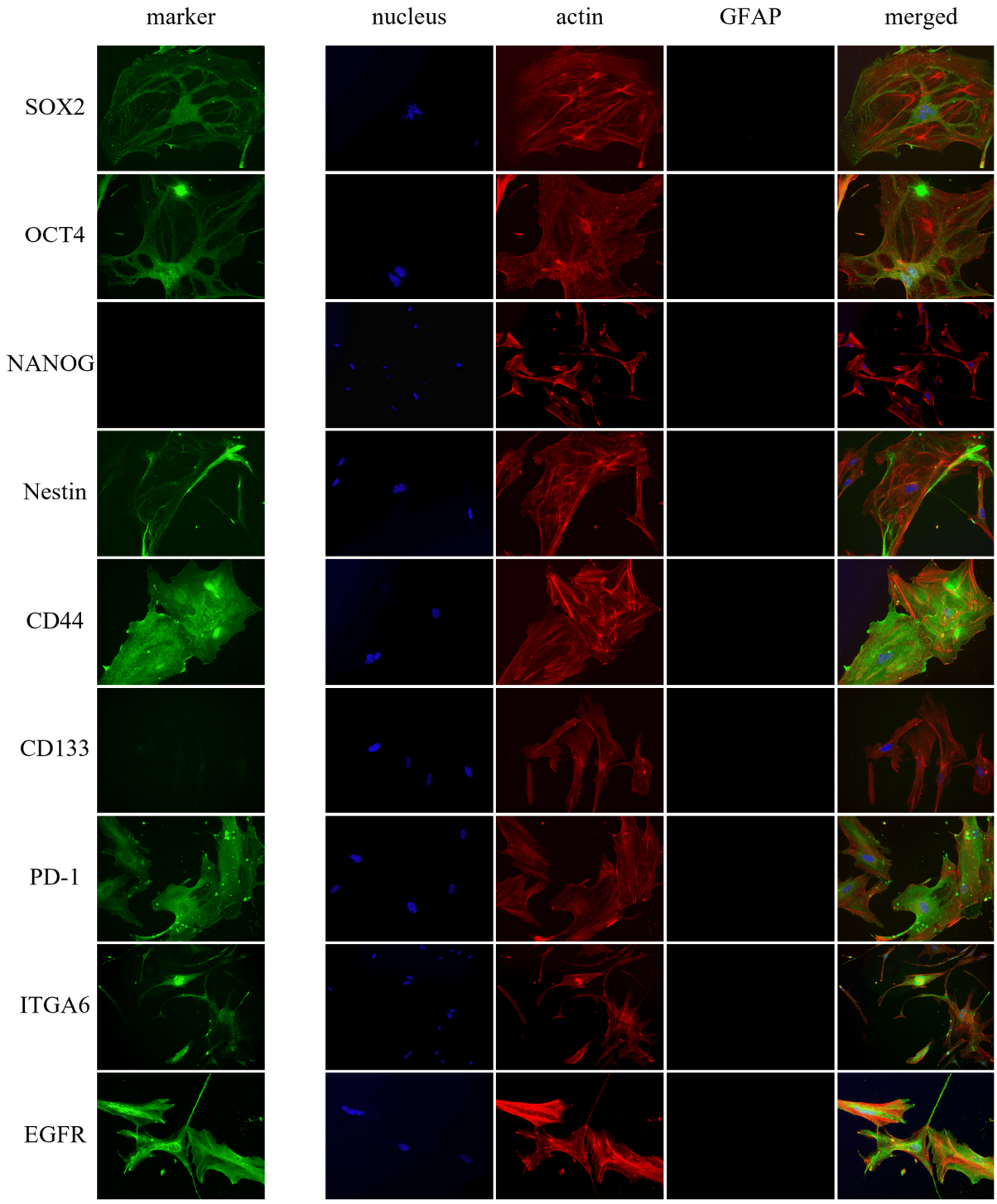

Fig. 17 GSC and GBM biomarker analysis for AKH-12. For a detailed description, see Fig. 9.

3.3.6. Characterization of primary cell culture AKH-13

AXL expression for AKH-13 cells was detected inside the cytoplasm and the surface of every cell. An increased expression in the perinuclear area was observed (Fig. 18). Integrin $\alpha_v\beta_5$ expression was observed for cells grown on glass and on plastic, mostly distributed across the cell surfaces. Furthermore, cells that had grown on glass exhibited an increased expression in the nucleus. The presence of multiple huge cells, each incorporating multiple nuclei was observed on glass.

AKH-13 cells were the first to test positive for all biomarkers except GFAP (Fig. 19), and the first cell culture in which very few $CD133^+$ cells were observed.

AKH-13 cells were smaller than those from previous cultures. A striking feature of this cell culture was the fact that some cells shed small cell bodies that also expressed high amounts of the biomarker. This effect was particularly evident for SOX2, CD44, PD-1, and EGFR.

SOX2 was mostly located inside the cytoplasm and the nucleus. OCT4 was predominantly expressed in the cytoplasm, with some cells exhibiting larger amounts inside the nucleus. NANOG expression was observed to be increased inside the nucleus, while also being distributed inside the cytoplasm of every cell. Nestin expression was increased in the cytoplasm of every imaged cell. CD44 expression was solely observed at the cell membrane of every imaged tumor cell (Fig. 19). ITGA6 was observed in the cytoplasm of all cells while EGFR was found to be localized mostly to the cytoplasm of every cell with some cells showing EGFR presence on their cell surface.

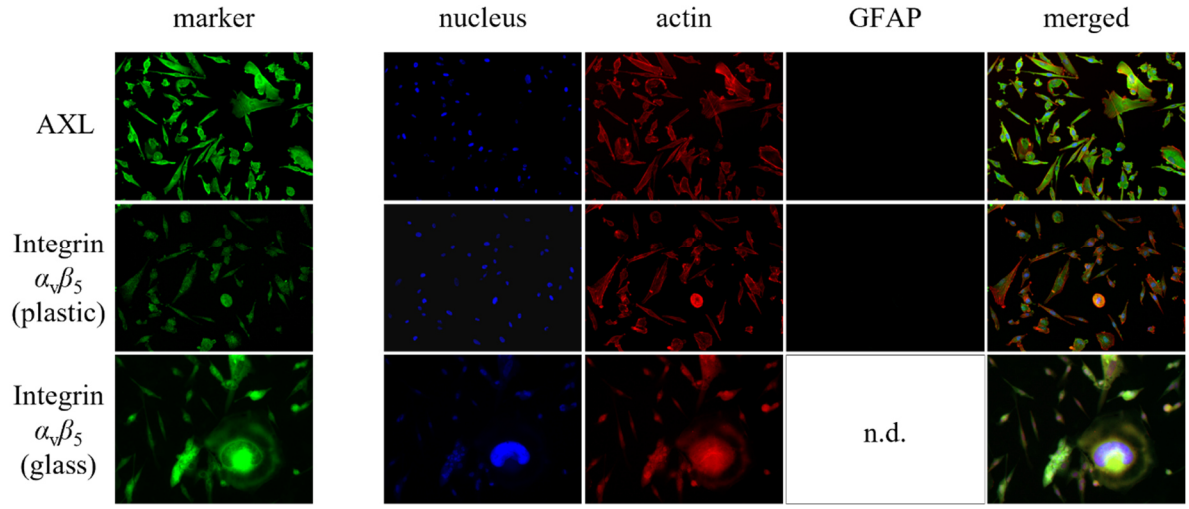

Fig. 18 ZIKV receptor analysis for AKH-13. For a detailed description, see Fig. 8.

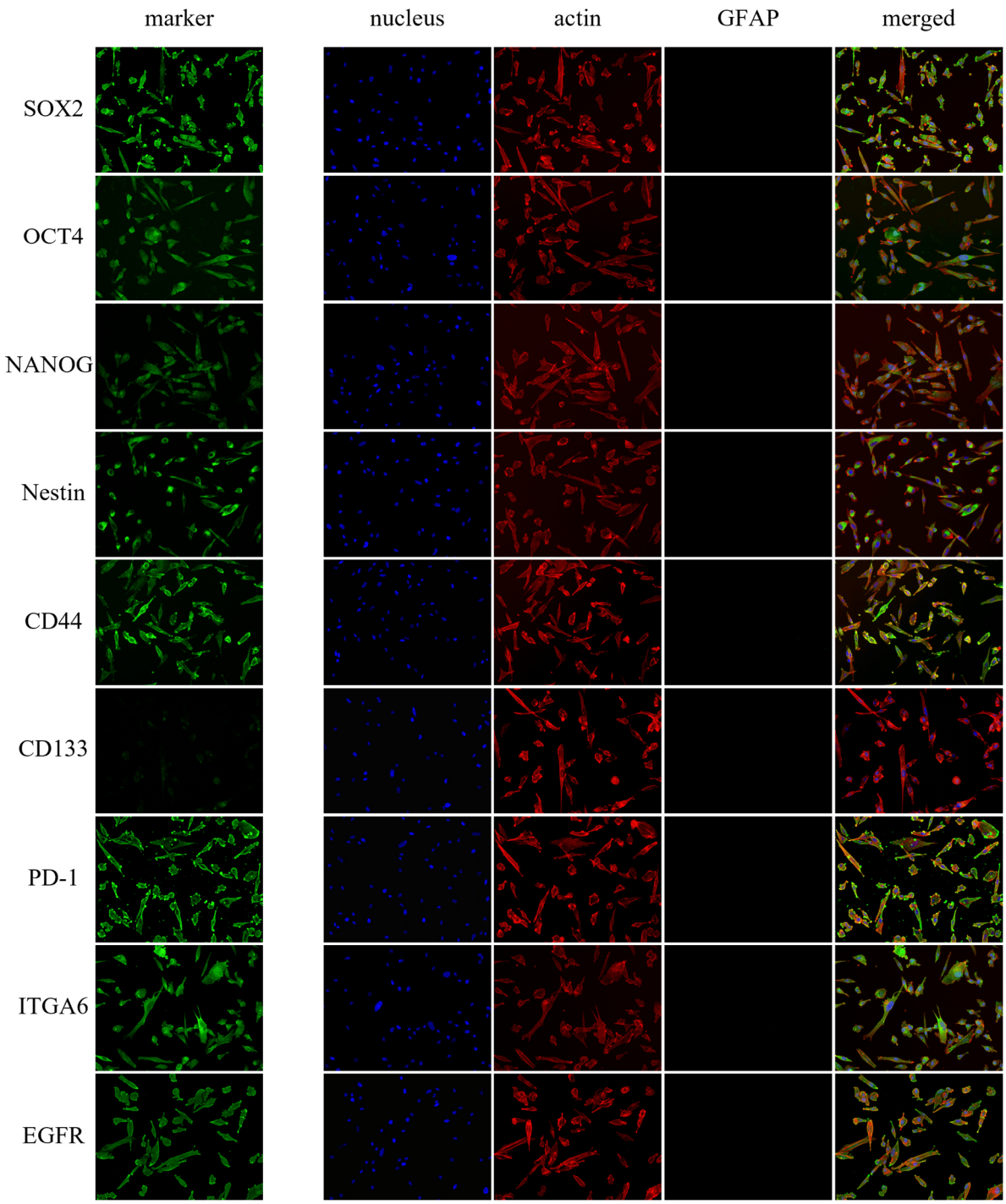

Fig. 19 GSC and GBM biomarker analysis for AKH-13. For a detailed description, see Fig. 9.

3.3.7. Characterization of primary cell culture AKH-14

No integrin $\alpha_v\beta_5^+$ cells were found in cells that have grown on plastic. Integrin $\alpha_v\beta_5$ expression was found at the cell surface in almost every imaged cell that has grown on glass (Fig. 20) After 10 days, they have developed multiple cell layers atop of each other. In the imaged section, AKH-14 cells can be seen that grew around a circular structure made of multiple cells (Fig. 20). AXL was expressed in every cell and could be found expressed in the nucleus, cytoplasm, and the cell surface. Multiple structures embodying many nuclei were observed.

AKH-14 cells were tested positive for SOX2, OCT4, CD44, PD-1, and EGFR. Expression of markers NANOG, Nestin, CD133, and ITGA6 was negative. AKH-14 had the first cells expressing GFAP with about half of all cells expressing the protein (Fig. 21).

SOX2 was predominantly localized in the cytoplasm with some cells expressing the protein in their nucleus as well. OCT4 was elevated inside the cell nucleus of every imaged cell. CD44 expression was very low. Only one cell showed high expression of CD44 on its surface. PD-1 expression found at the cell membrane of every imaged cell. EGFR was ubiquitously exhibited in every imaged cell.

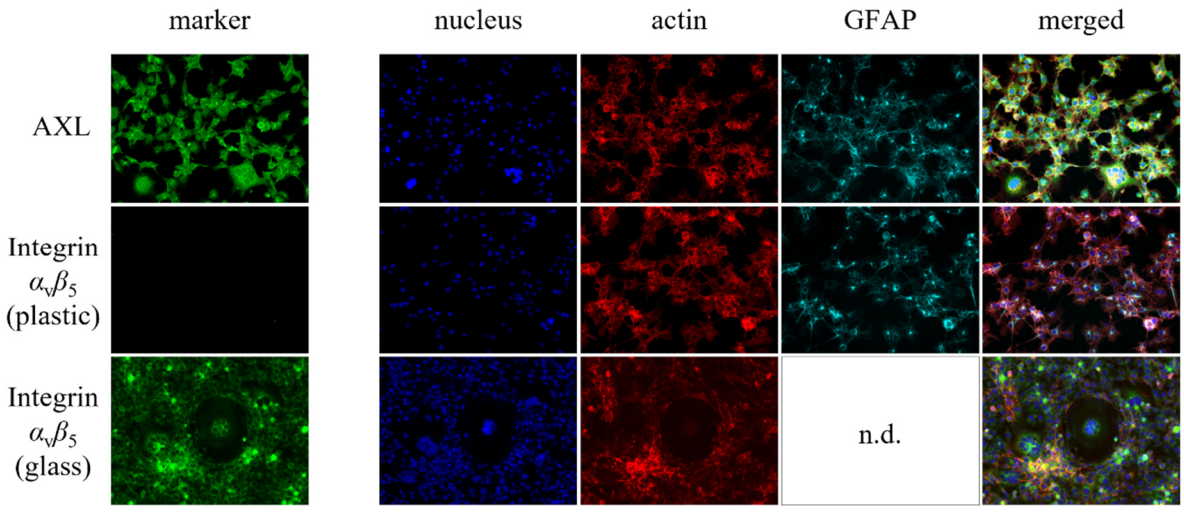

Fig. 20 ZIKV receptor analysis for AKH-14. For a detailed description, see Fig. 8.

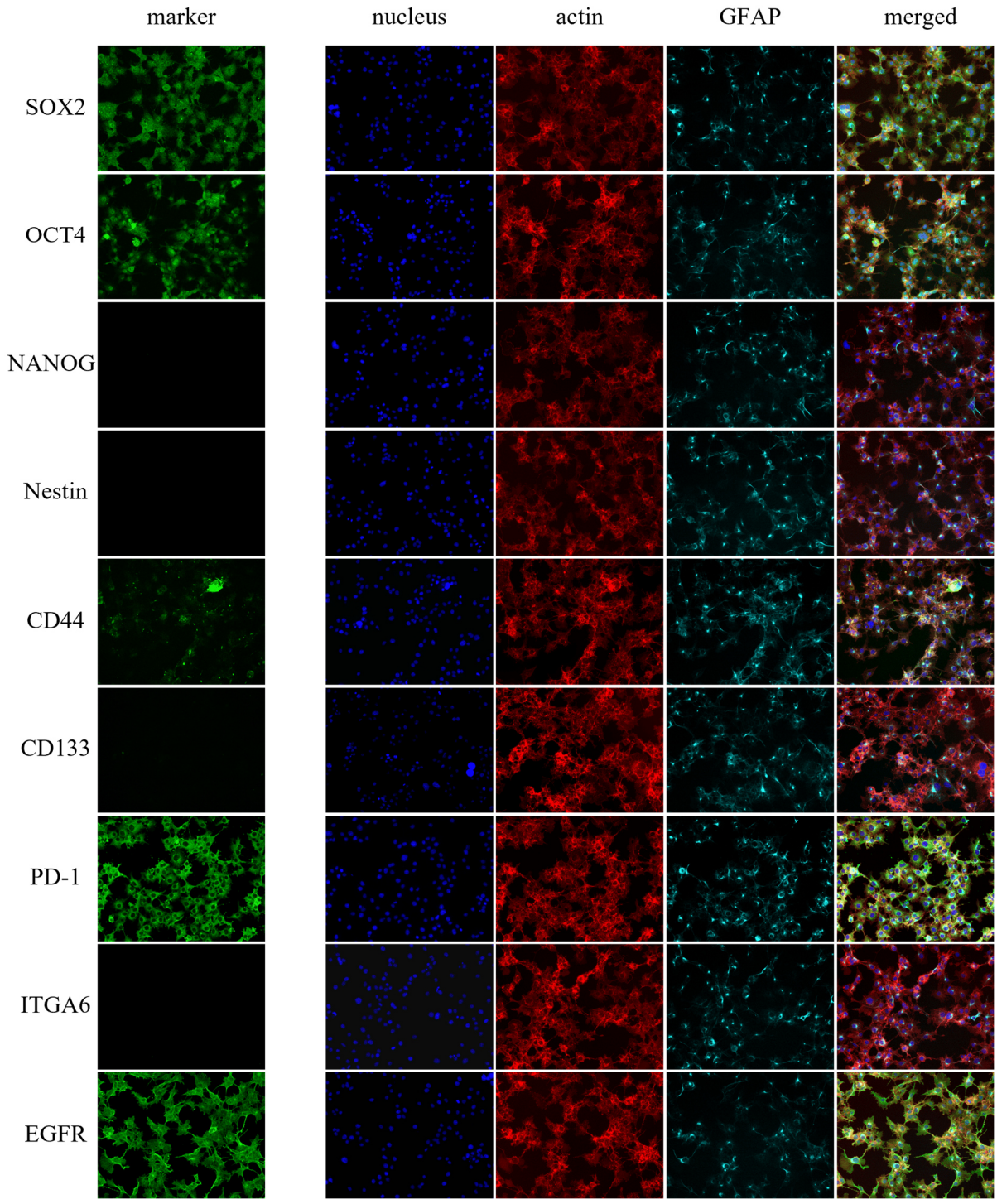

Fig. 21 GSC and GBM biomarker analysis for AKH-14. For a detailed description, see Fig. 9.

3.3.8. Characterization of primary cell culture AKH-15

AKH-15 cells were tested positive for both AXL and integrin $\alpha_v\beta_5$ (Fig. 22). Cells grown on plastic expressed a low amount of integrin $\alpha_v\beta_5$ inside the nucleus. Signals for integrin $\alpha_v\beta_5$ were increasingly found in cells grown on glass, being exhibited over their whole surface but not inside the nucleus (Fig. 22)

AKH-15 cells were tested positive for SOX2, Oc4, Nestin, CD44, PD-1, ITGA6, and EGFR (Fig. 23). PD-1 and ITGA6 signals were low. No cells expressing NANOG and CD133 were found. Multiple cells exhibiting GFAP were found, appearing in all different kinds of shapes and sizes. $GFAP^+$ cells were generally elongated, reaching out to other cells through long filopodia. $GFAP^+$ cells exhibited actin skeletons of varying degrees (Fig. 23, $GFAP^+$ cells for SOX2, OCT4, and NANOG).

Imaged cells showed greatly increased expression for SOX2 inside the nucleus. High amounts of SOX2 were also exhibited inside the cytoplasm (Fig. 23). OCT4 was predominantly found inside the cytoplasm of every cell, increased in dividing cells. Nestin was found in most cells. All imaged cells showed differently pronounced CD44 expression on the surface. Signals for PD-1 were mostly observed in low amounts around the nuclear area of some but not all imaged cells. ITGA6 was found in five out of 30 imaged cells, with no distinct location observed. EGFR signals were found in every cell, increased at the surface of some imaged cells.

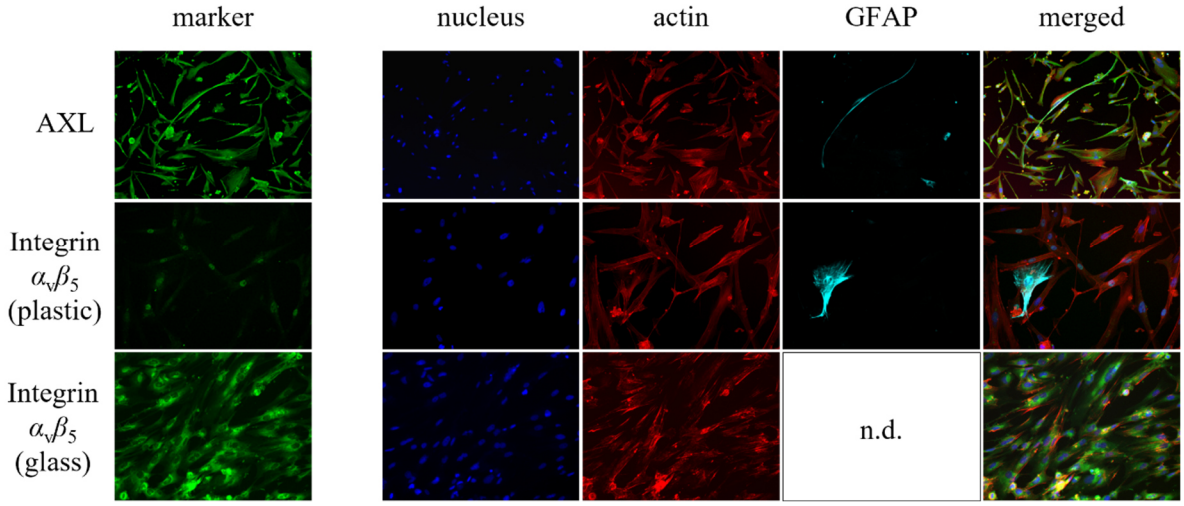

Fig. 22 ZIKV receptor analysis for AKH-15. For a detailed description, see Fig. 8.

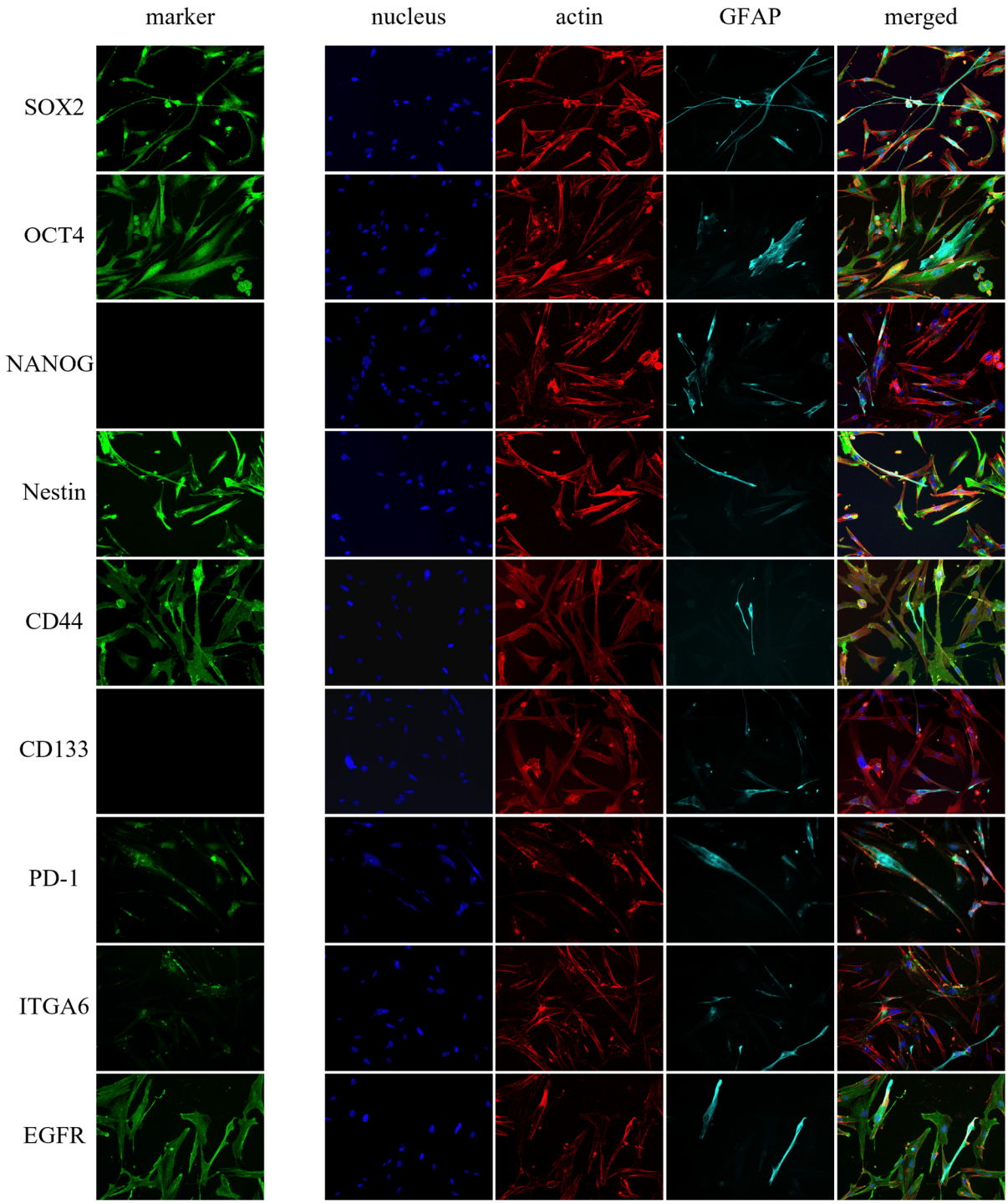

Fig. 23 GSC and GBM biomarker analysis for AKH-15. For a detailed description, see Fig. 9.

3.3.9. Characterization of primary cell culture AKH-16

Cells from AKH-16 only grew very slowly in cell culture, never reaching a sufficient confluence for imaging. This led to an overall low number of imageable cells. As for AKH-12, they were large and had cells that incorporated multiple nuclei (Fig. 25, AXL)

AXL was expressed inside the cytoplasm of the cells and highly increased around the nucleus of all imaged cells (Fig. 24). Integrin $\alpha_v\beta_5$ was observed inside the nucleus of cells that have grown on plastic. The expression was highly elevated in cells grown on glass. The imaged cells had highly increased expression inside the nucleus and their cell surface.

After AKH-13, AKH-16 was the second culture to express all biomarkers (Fig. 25). SOX2 was distributed over the cytoplasm and increasingly displayed at the nucleus. OCT4 was distributed inside the whole cells but showed no expression inside the nucleus for the imaged cells. NANOG was found in the cytoplasm of the two imaged cells. Nestin was expressed in two large cells, located to areas with seemingly low actin expression. The other two imaged cells did not express Nestin. CD44 was found on the surface of all cells. CD133 signals were predominantly found near the nucleus of the imaged cells. PD-1 expression was ubiquitously found in every imaged cell. The levels of ITGA6 were increased in the nuclear area of the imaged cells, from which it distributed over to the cytoplasm. It was also found being expressed in small surface areas and inside the nucleus. EGFR was localized inside the cytoplasm and nucleus as well as the surface of all imaged cells.

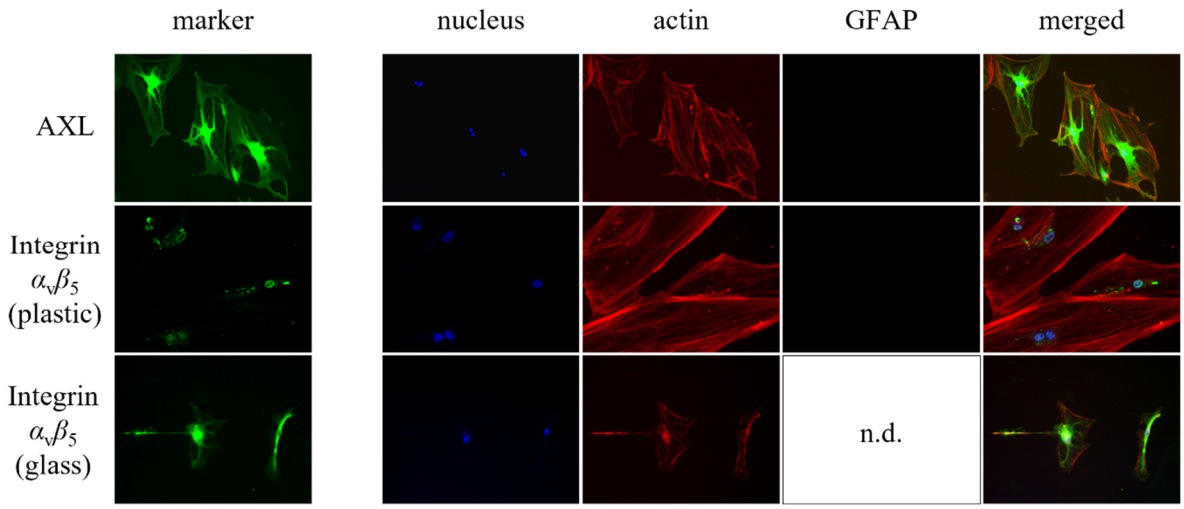

Fig. 24 ZIKV receptor analysis for AKH-16. For a detailed description, see Fig. 8.

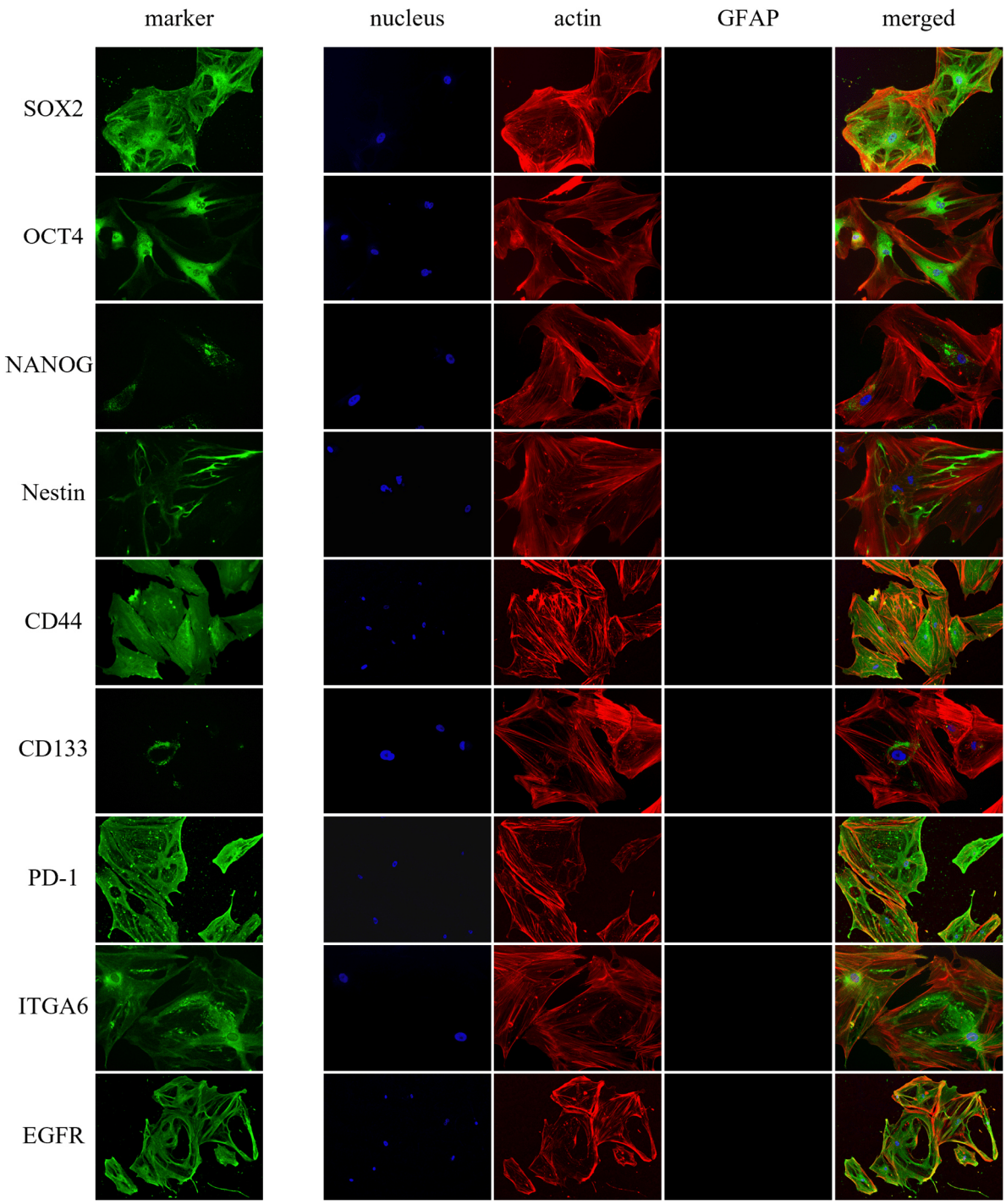

Fig. 25 GSC and GBM biomarker analysis for AKH-16. For a detailed description, see Fig. 9.

3.3.10. Characterization of primary cell culture AKH-17

AKH-17 cells did exhibit both AXL and integrin $\alpha_v\beta_5$ (Fig. 26). AXL was ubiquitously found in all cells. Integrin $\alpha_v\beta_5$ expression in cells grown on plastic was low. Only a few signals near the nucleus of a small number of cells were found. In contrast, the expression on glass was exponentially higher, being detectable in every cell, located on the cell surfaces and the cytoplasm. Most imaged cells expressed GFAP, making AKH-17 the first culture that mostly consisted of $GFAP^+$ cells (Fig. 26 and Fig. 27).

The tumor cells were tested positive for SOX2, OCT4, Nestin, CD44, PD-1, ITGA6, and EGFR (Fig. 27). No signals for NANOG and CD133 were found. ITGA6 was only found in low levels in a small number of cells.

SOX2 expression was highly elevated inside the nucleus of all cells and expressed inside the cytoplasm. OCT4 was found distributed in the cytoplasm of every imaged cell with additional expression found inside the nucleus. Nestin was highly expressed in every imaged cell, located inside their cytoplasm. CD44 was increasingly exhibited at the surface of most cells. Interestingly, the cells with less expression at the surface had increased CD44 inside the cytoplasm. PD-1 was found inside the cytoplasm of every cell. The few imaged cells that showed ITGA6 expression, had it located in small areas near the nucleus. EGFR was increasingly displayed in most tumor cells.

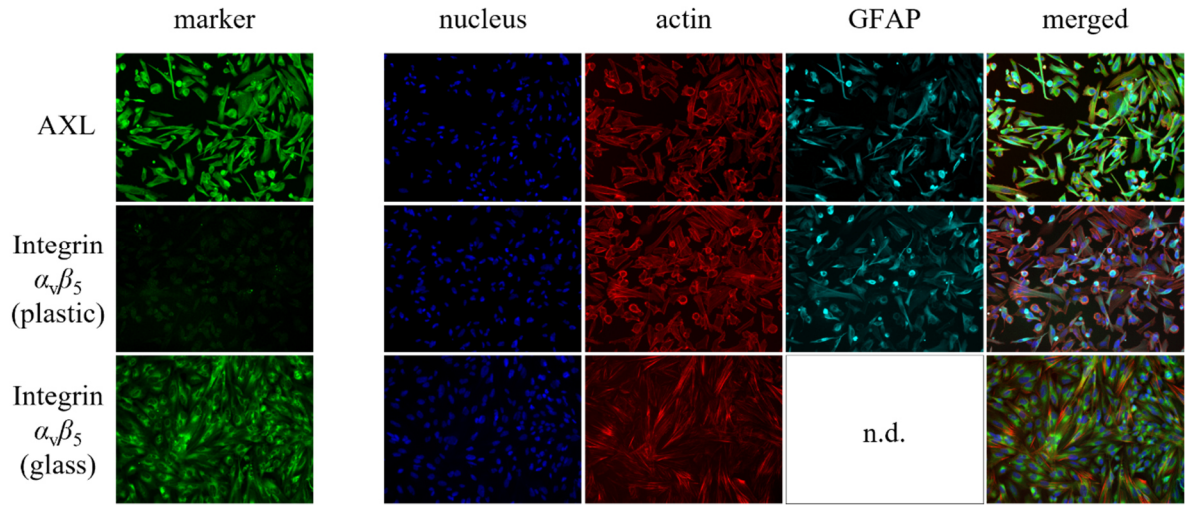

Fig. 26 ZIKV receptor analysis for AKH-17. For a detailed description, see Fig. 8.

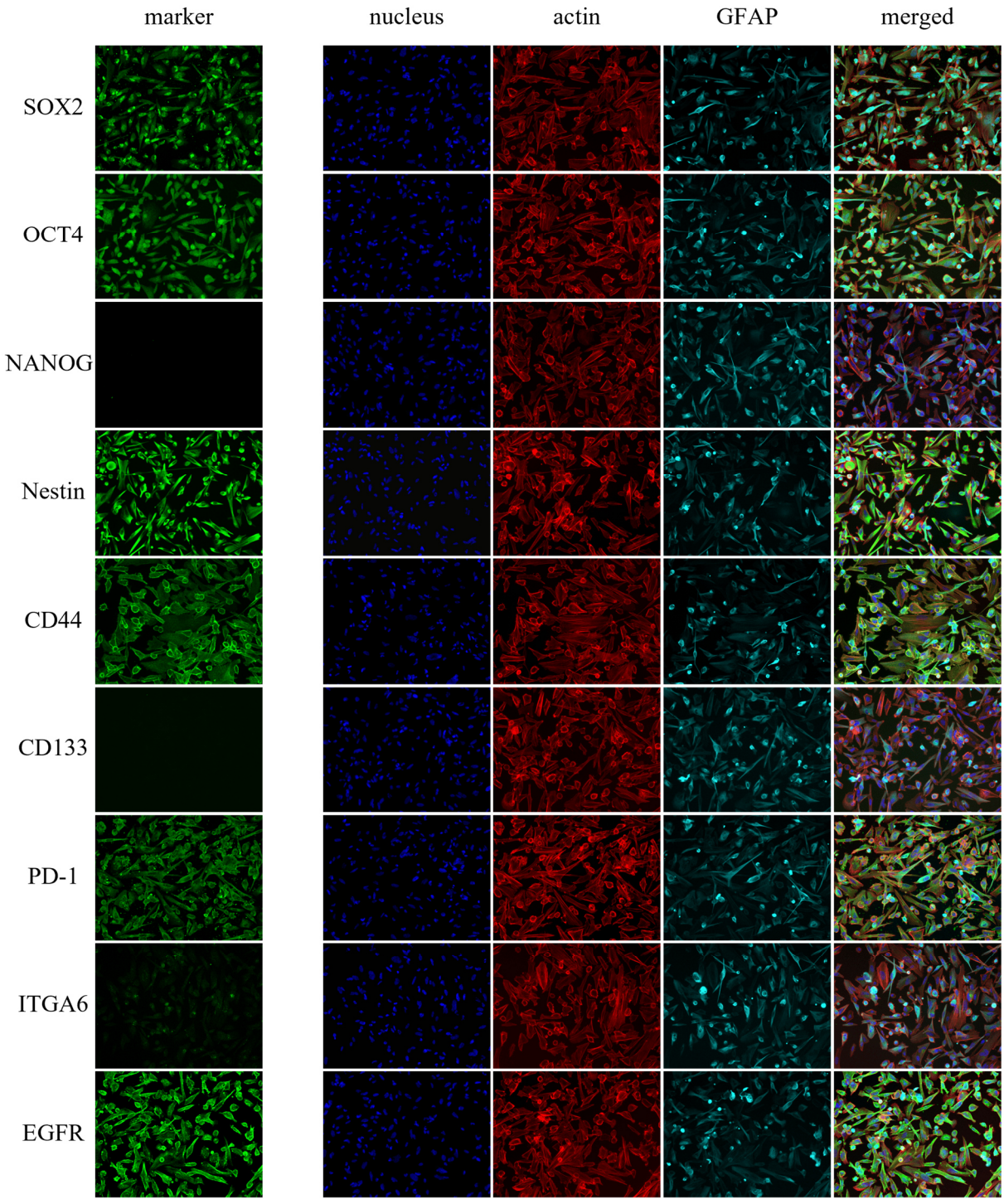

Fig. 27 GSC and GBM biomarker analysis for AKH-17. For a detailed description, see Fig. 9.

3.3.11. Characterization of primary cell culture AKH-18

AKH-18 cells had a slow growth behavior, making growing on glass impossible, so the expression of integrin $\alpha_v\beta_5$ could only be measured for cells grown on plastic. However, expression in these cells has been found to be highly increased inside the nucleus of all imaged cells (Fig. 28). AXL was found to be expressed inside the cytoplasm, nucleus, and the surface of every cell.

The cell culture was tested positive for SOX2, OCT4, NANOG, Nestin, CD44, PD-1, ITGA6, and EGFR. CD133 was negative (Fig. 29). The number of $GFAP^+$ cells was very low, only one cell was found that exhibited large amounts inside the nucleus, alongside CD44.

SOX2 was found being distributed in the cytoplasm with condensed expression at and inside the nucleus. The same was observed for OCT4. All imaged cells had high NANOG signals located inside the nucleus. Only very low amounts of Nestin were found, located in the cytoplasm and near the nucleus. PD-1 was found in high amounts on the cell surface as well as distributed inside the cytoplasm of the imaged cells. ITGA6 was highly expressed on the cell surface of a huge, imaged cell that also embodied multiple nuclei, while the other two imaged cells expressed almost no protein. EGFR was evenly exhibited inside the nucleus and the cytoplasm, along with expression on the cell surface of the imaged cell.

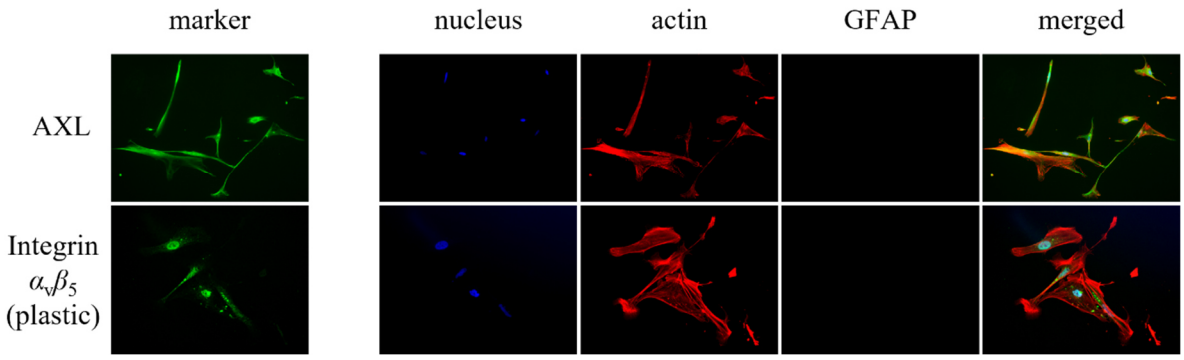

Fig. 28 ZIKV receptor analysis for AKH-18. For a detailed description, see Fig. 8.

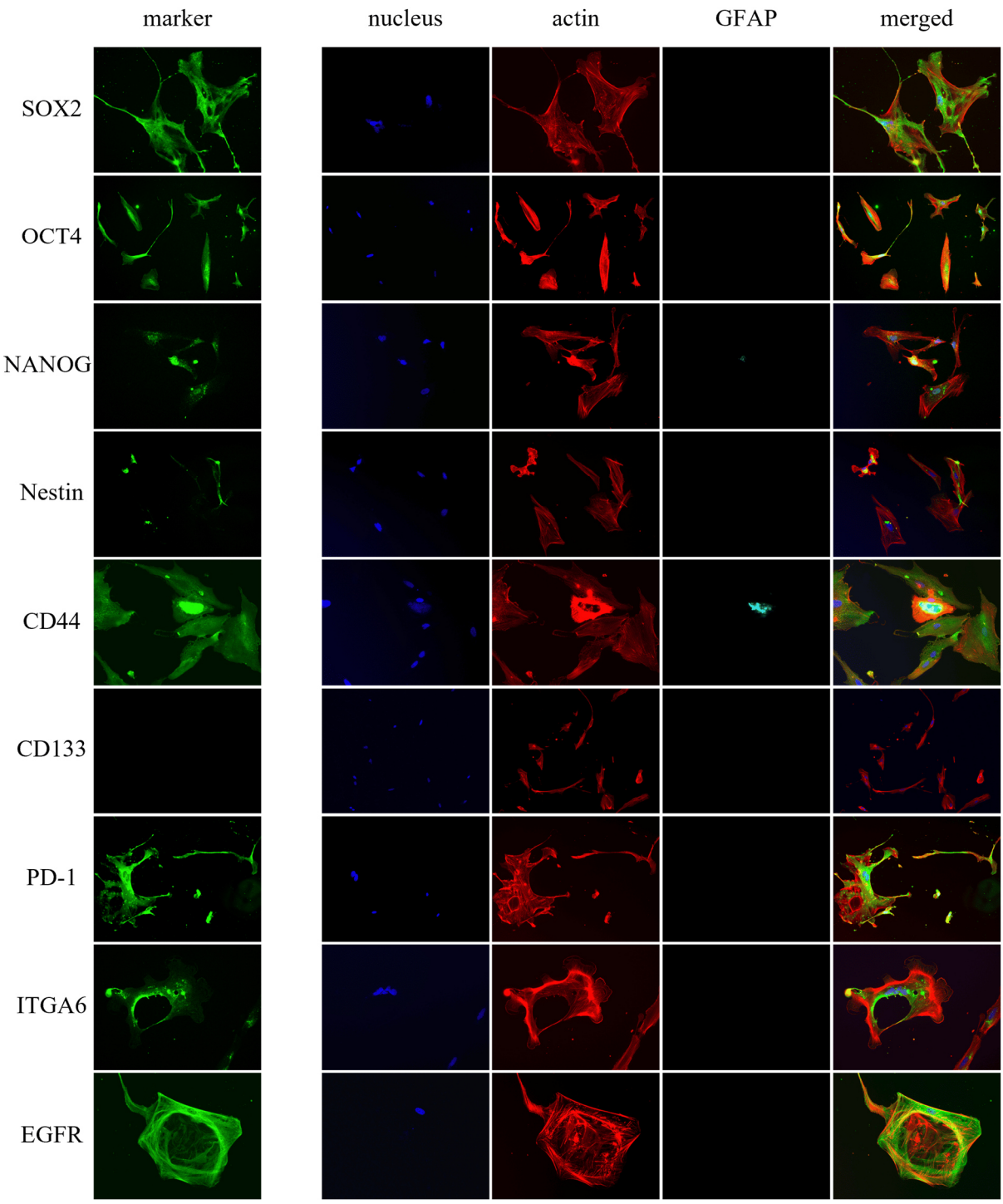

Fig. 29 GSC and GBM biomarker analysis for AKH-18. For a detailed description, see Fig. 9.

3.3.12. Characterization of primary cell culture AKH-19

AXL was highly expressed inside the cytoplasm of every imaged cell. No visible expression at the cell surface and inside the nucleus was found (Fig. 30). The expression of integrin $\alpha_v\beta_5$ was increased in cells that have grown on glass, being distributed over the whole cells. Cells grown on plastic showed decreased integrin signaling, mostly near the nuclear area.

AKH-19 cells were tested positive for SOX2, OCT4, Nestin, CD44, PD-1, ITGA6, and EGFR (Fig. 31). NANOG and CD133 were negative. SOX2 and OCT4 were found to be localized both inside the nucleus and the cytoplasm. Nestin was highly expressed in large, elongated cells while also being present in lower amounts in the cytoplasm of smaller non-elongated cells. CD44 was found on the surfaces of all imaged cells. Some $CD44^+$ cells also exhibited strong signals of the protein at their edges. PD-1 and ITGA6 signals were found in all cells. EGFR was highly elevated on the surface of all tumor cells. The number of cells expressing GFAP was very low. They were forming elongated extensions, while seemingly reaching out to other cells, trying to connect them (Fig. 31, SOX2 and NANOG).

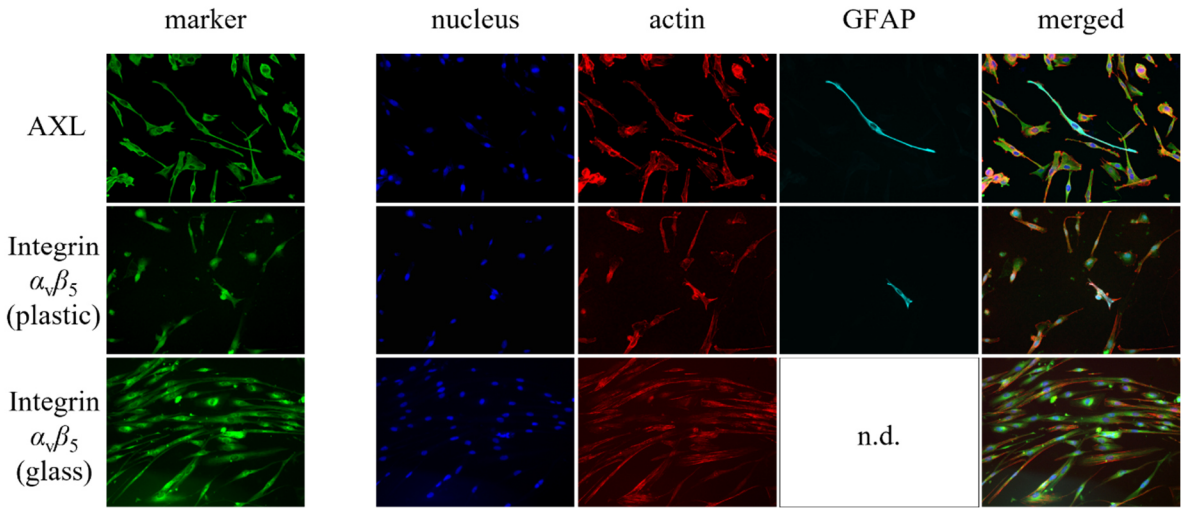

Fig. 30 ZIKV receptor analysis for AKH-19. For a detailed description, see Fig. 8.

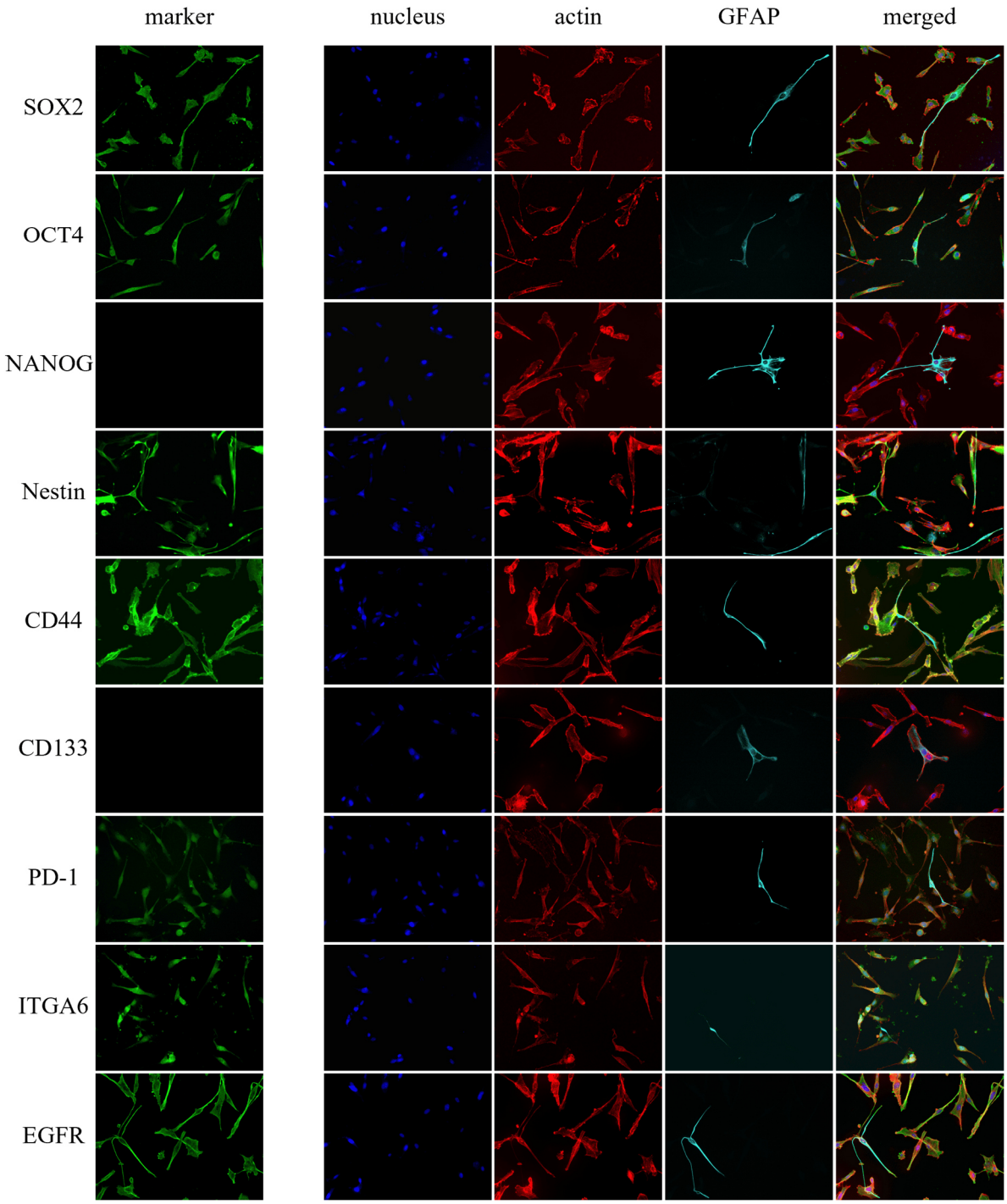

Fig. 31 GSC and GBM biomarker analysis for AKH-19. For a detailed description, see Fig. 9.

3.3.13. Characterization of primary cell culture AKH-20

AXL was located inside the cytoplasm of every imaged cell, predominantly found around the nucleus with no expression anywhere else (Fig. 32). Integrin $\alpha_v\beta_5$ in cells grown on plastic was solely located inside the nucleus of the imaged cells. Still, some cells did not express integrin $\alpha_v\beta_5$. The expression of integrin $\alpha_v\beta_5$ in cells grown on glass was detected inside the cytoplasm with little to no signals found inside the nucleus of the imaged cells. An increased expression of integrin $\alpha_v\beta_5$ around the nuclear area was observed.

AKH-20 cells were tested positive for SOX2, OCT4, NANOG, Nestin, CD44, PD-1, ITGA6, and EGFR (Fig. 33). NANOG and Nestin expression was very low; CD133 was negative. No $GFAP^+$ cells were found. SOX2 was highly expressed inside the cytoplasm of all cells with some signals found inside the nuclei. OCT4 levels were increased around and inside the nucleus of the imaged tumor cells and distributed inside the cytoplasm in half of all imaged cells. NANOG was found in two of the 14 imaged cells, being exhibited inside the nucleus of one and in the perinuclear area of the other cell. Nestin was found in one of the eight imaged cells, being increasingly expressed inside the cytoplasm. The structure of Nestin inside this cell seemed to support its cell morphology. PD-1 was highly present at the surface of every imaged cell, while also being elevated inside the cytoplasm, mostly near the cell membranes. All imaged cells exhibited low amounts of ITGA6, found near the nucleus and on the cell surface. EGFR levels were highly increased and ubiquitously found in all imaged cells.

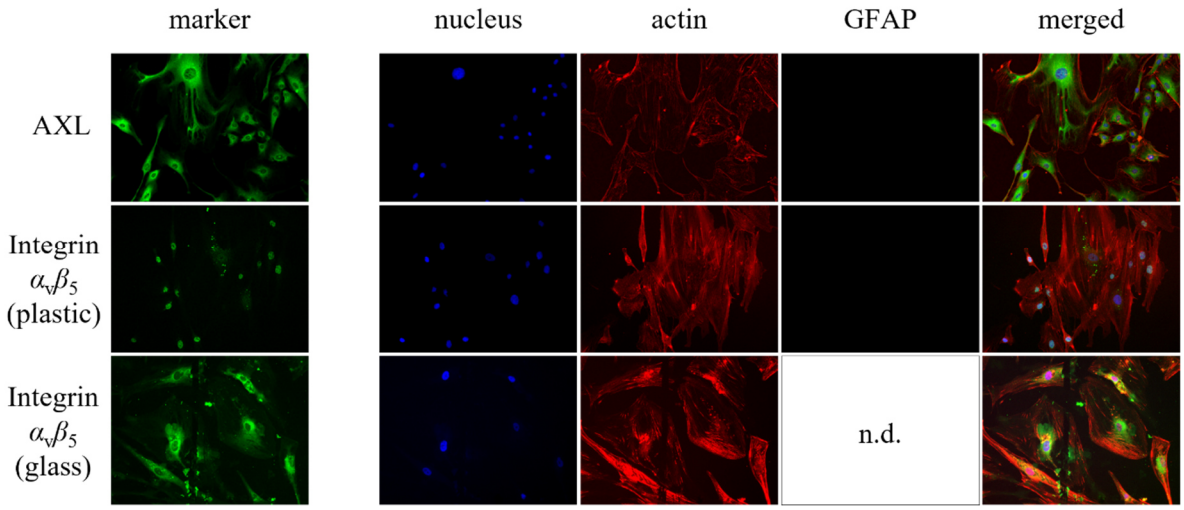

Fig. 32 ZIKV receptor analysis for AKH-20. For a detailed description, see Fig. 8.

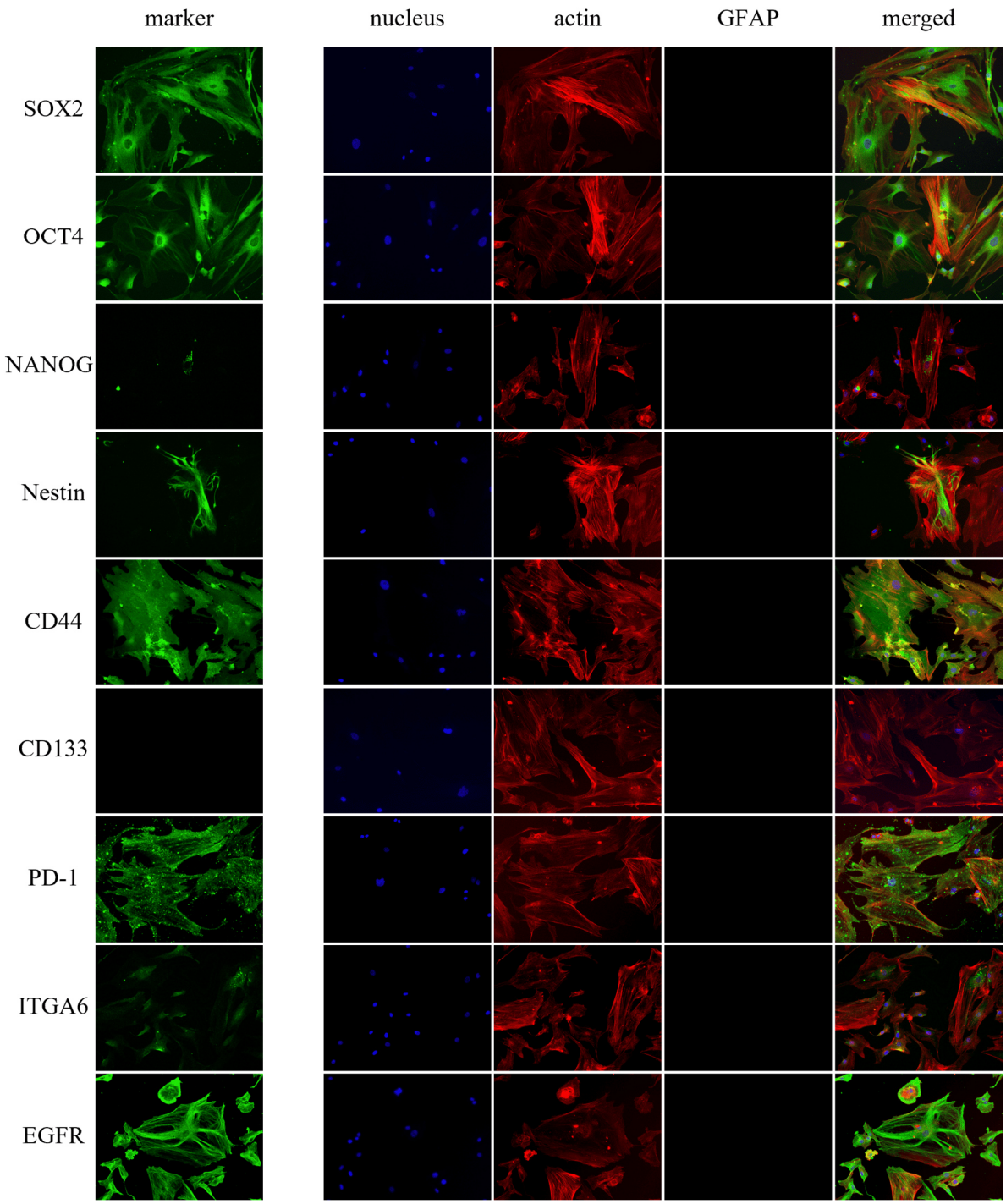

Fig. 33 GSC and GBM biomarker analysis for AKH-20. For a detailed description, see Fig. 9.

3.3.14. Characterization of primary cell culture AKH-21S

The tumor for culture AKH-21 had an increased size, which allowed to take tumor samples near the vicinity of the SVZ (AKH-21S) as well as near the tumor core (AKH-21C), resulting in two different cell cultures.

AKH-21S cells grew very poorly on plastic and on glass surfaces, comparable to AKH-12, -16, and -18 (Fig. 17, Fig. 23, and Fig. 25). They grew as slowly but the cells were much smaller.

AXL was ubiquitously found in all AKH-21S cells (Fig. 34). Two huge cells atop of each other expressed very large amounts of AXL near and inside the nuclei, mostly at the side of contact. Integrin $\alpha_v\beta_5$ was exhibited in cells grown on glass and on plastic surfaces, mostly elevated inside and near the nucleus of all imaged cells. On plastic, some cells also exhibited integrin $\alpha_v\beta_5$ inside the cytoplasm, while others did not express it at all.

AKH-21S cells were tested positive for every marker except CD133 (Fig. 35). $GFAP^+$ cells were observed, although the number was low. SOX2 was found inside the cytoplasm and the nuclei of every imaged cell. OCT4 expression was predominantly increased inside the nucleus and the cytoplasm. NANOG was solely located inside and near the nucleus of the two imaged cells. Nestin was found in all imaged cells, spread throughout the cytoplasm. CD44 was found in all imaged cells, inside the cytoplasm as well as the cell surface. PD-1 was located at the cell surface. ITGA6 was mostly found to be located near the nucleus in all imaged cells with some signals observed inside the cytoplasm and surface as well. EGFR was found to be localized to every part of each imaged cell.

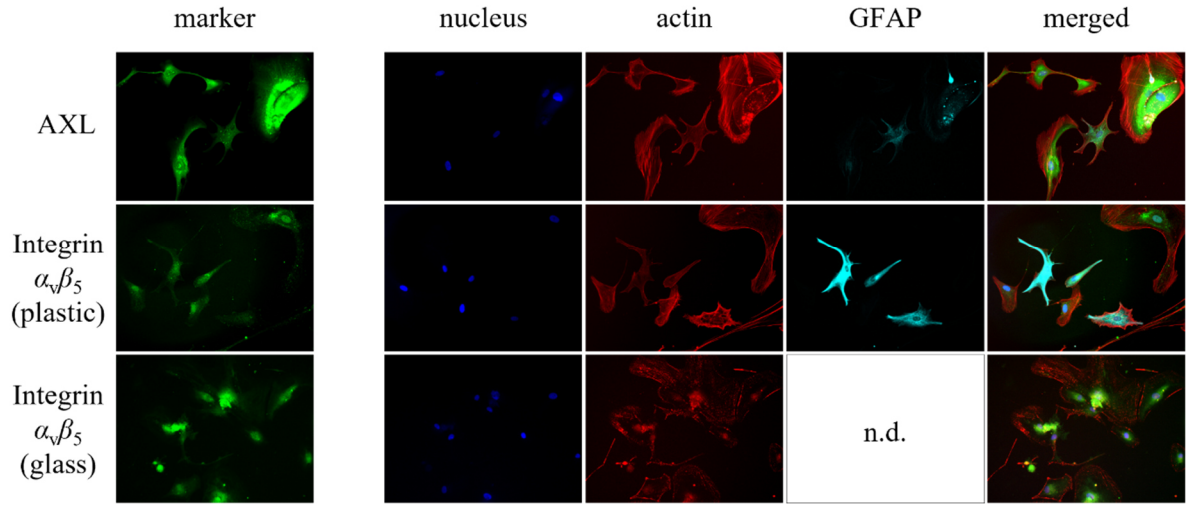

Fig. 34 ZIKV receptor analysis for AKH-21S. For a detailed description, see Fig. 8.

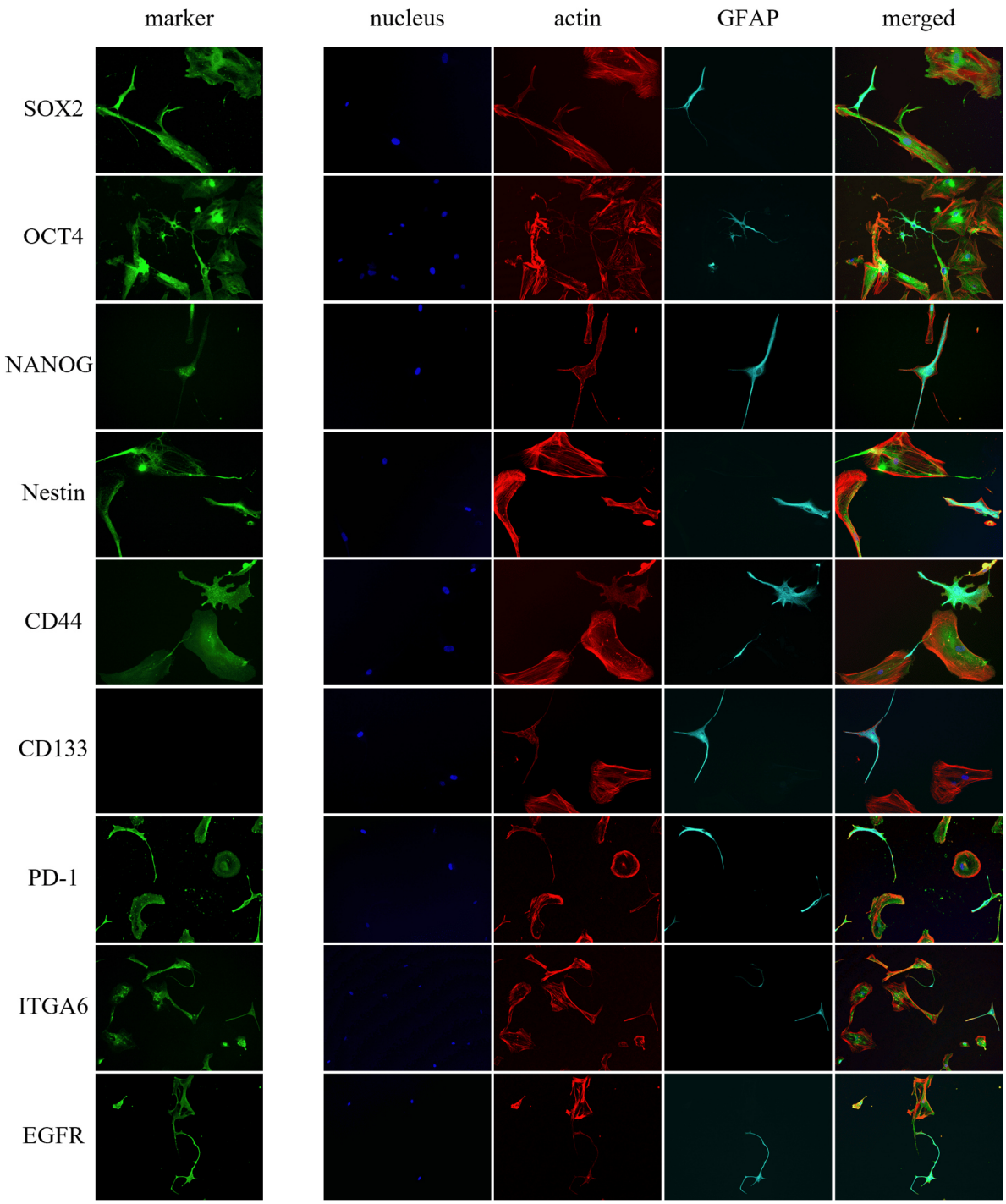

Fig. 35 GSC and GBM biomarker analysis for AKH-21S. For a detailed description, see Fig. 9.

3.3.15. Characterization of primary cell culture AKH-21C

The growth behavior from the AKH-21C tumor culture was like AKH-21S, resulting in only few cells. Few cells expressing GFAP were observed in this culture as well. The GFAP$^+$ cells were found to have an underdeveloped actin skeleton with increased expression with actin mostly found near the cell membrane.

Integrin $\alpha_v\beta_5$ expression was low in cells grown on glass, only elevated near the nucleus of the imaged cells (Fig. 36). On plastic, the strongest expression signals of integrin $\alpha_v\beta_5$ were observed near the nucleus as well as irregularly distributed inside the cells. AXL was found in high amounts inside the nucleus and increased amounts in parts of the cytoplasm. The single imaged GFAP$^+$ cell exhibited several branching filopodia and showed high levels of AXL throughout.

AKH-21C tumor cells expressed every marker except CD133. SOX2 was found in high amounts inside the cytoplasm and elevated near the nuclear area (Fig. 37). OCT4 was increased near and inside the nucleus of the imaged cells. NANOG was elevated at the nucleus of the imaged cells. Nestin$^+$ cells expressed the protein inside the whole cytoplasm, alongside GFAP in one of the imaged cells. CD44 was observed to cover the surface of the two imaged cells. PD-1 localization was observed in the cytoplasm and on the surface of the three imaged cells. ITGA6 was observed at the cell membrane and in the cytoplasm. EGFR expression was found inside the cytoplasm and on the cell membrane.

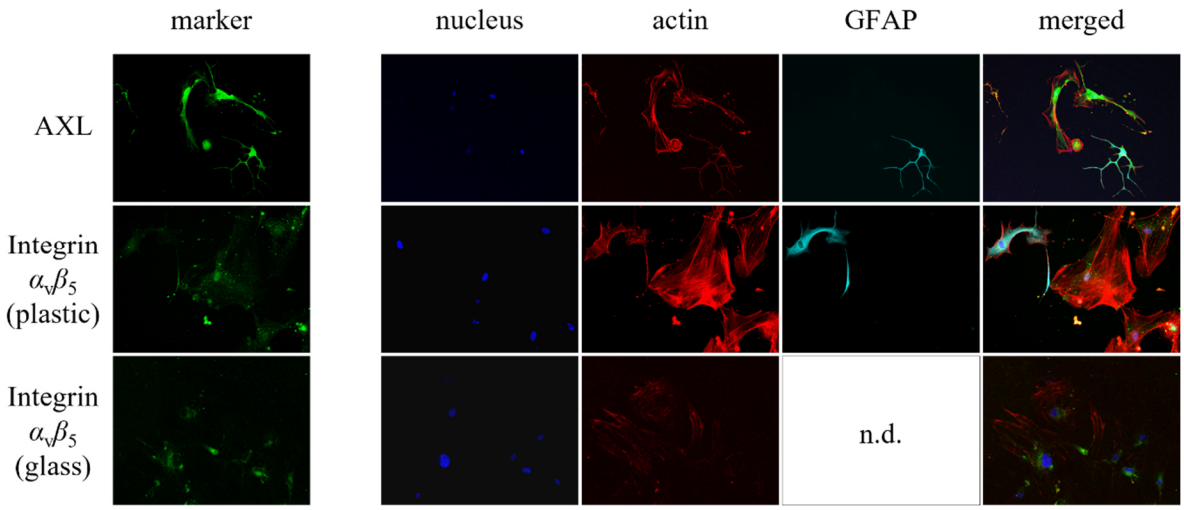

Fig. 36 ZIKV receptor analysis for AKH-21C. For a detailed description, see Fig. 8.

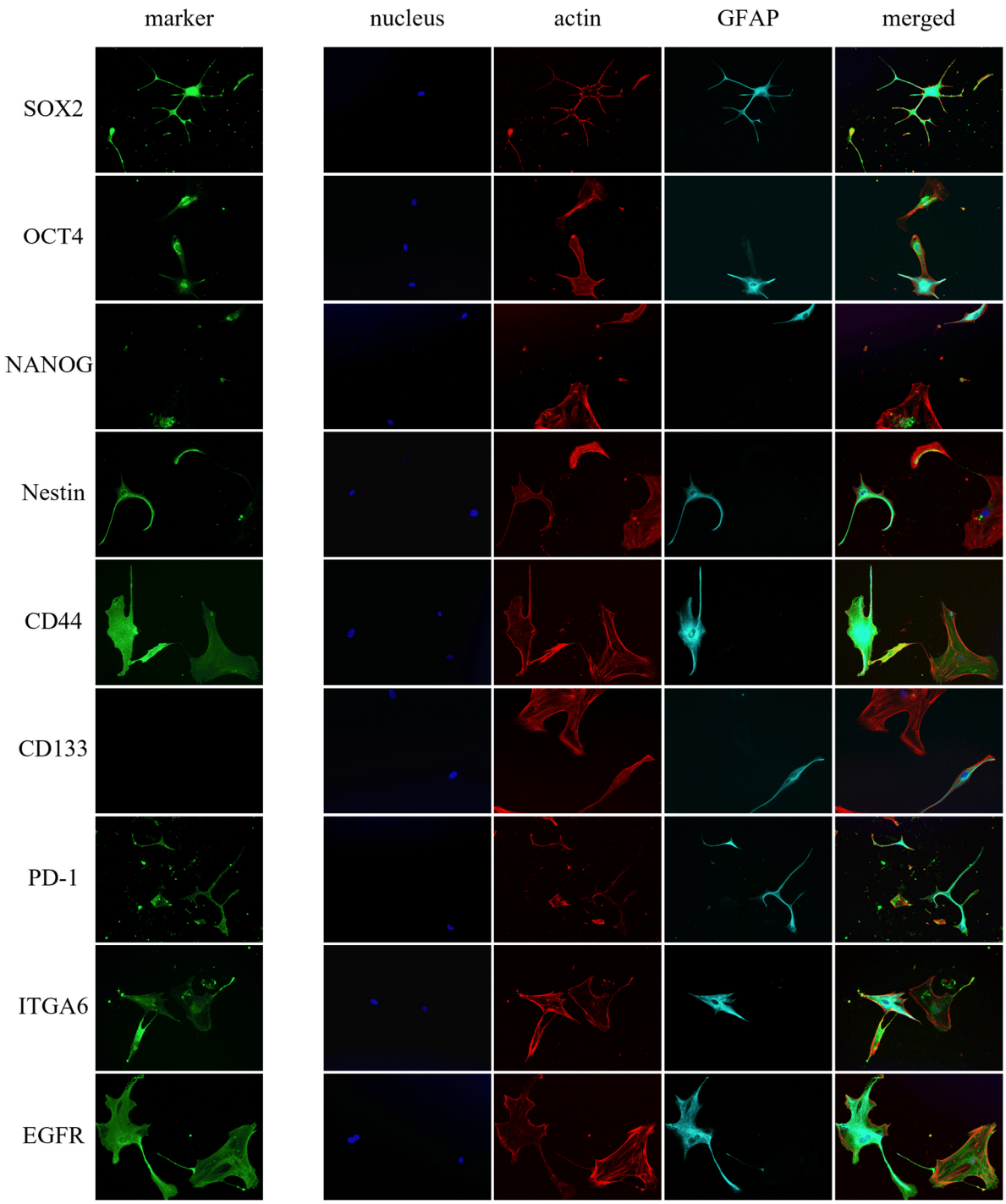

Fig. 37 GSC and GBM biomarker analysis for AKH-21C. For a detailed description, see Fig. 9.

3.3.16. Characterization of primary cell culture AKH-23

AKH-23 cells were tested positive for AXL and integrin $\alpha_v\beta_5$ (Fig. 38). No signals for integrin $\alpha_v\beta_5$ were found in cells grown on plastic. In contrast, cells grown on glass displayed large amounts of the protein.

AKH-23 cells were tested positive for SOX2, OCT4, NANOG, Nestin, CD44, PD-1, and EGFR (Fig. 39). For CD133, small fluorescence signals near the nucleus in one large cell might indicate expression. No ITGA6$^+$ cells were observed.

SOX2 was highly elevated in every cell, mostly located at and around the nucleus but also distributed throughout the cells as well. OCT4 expression was very low in the AKH-23 cell culture, mostly located in small amounts in the nucleus and found in the cytoplasm of two large cells that also expressed GFAP in high amounts (Fig. 39). GFAP$^+$ cells were rarely found in the AKH-23 culture. Nestin was found in approximately half of all imaged cells, localized to the cytoplasm, seemingly following no distinct pattern. CD44 expression was upregulated on every cell surface as well as the cytoplasm. PD-1 was observed inside the cytoplasm and on the cell surface. EGFR was highly upregulated in every imaged AKH-23 cell.

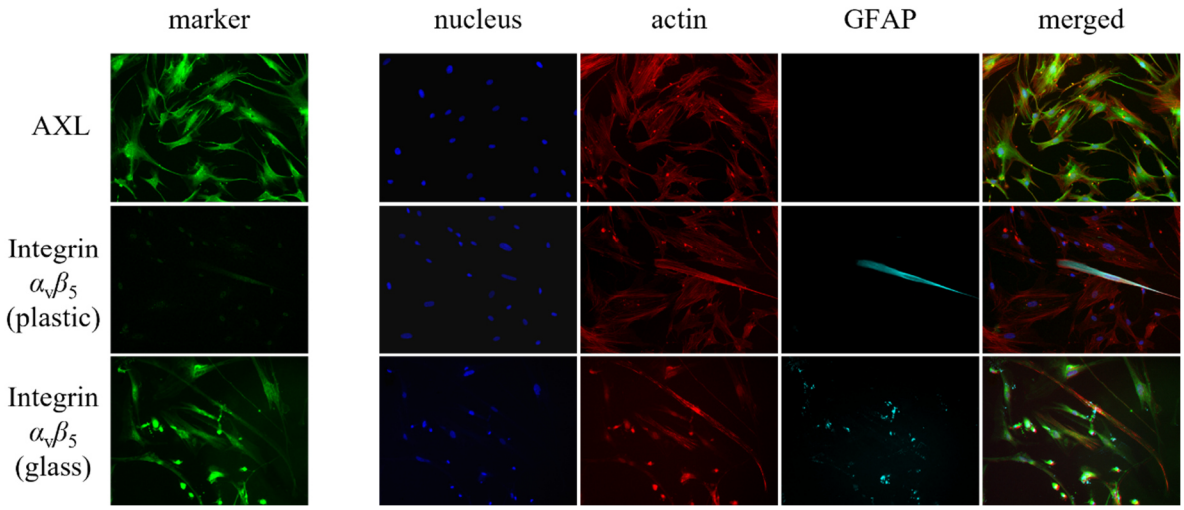

Fig. 38 ZIKV receptor analysis for AKH-23. For a detailed description, see Fig. 8.

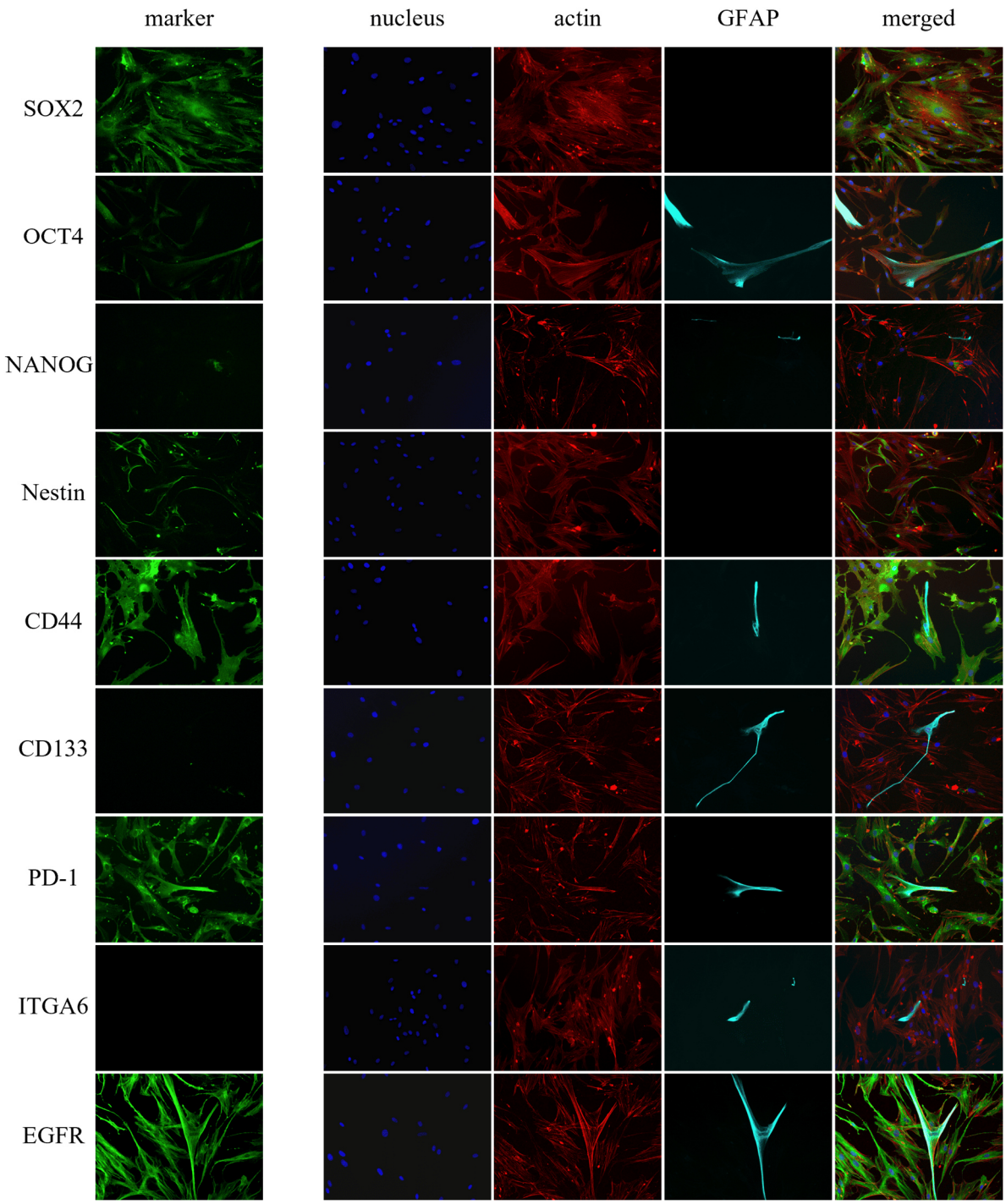

Fig. 39 GSC and GBM biomarker analysis for AKH-23. For a detailed description, see Fig. 9.

3.3.17. Characterization of primary cell culture AKH-24S

As for AKH-21, the last tumor sample allowed establishing two different cell cultures (AKH-24S and AKH-24C). Instead of establishing a stable culture prior to imaging, AKH-24 cells were immediately incubated in wells after preparation of the sample. AKH-24S cells had an unexpected intrinsic glowing inside, manifesting in small fluorescent signals. They appeared irregularly distributed in some but not all cells, which is why they were tested initially positive for all markers. Since these signals always appeared as small dots, they could be distinguished from the immunofluorescence. This glowing was also observed when cells where not treated and only placed under the microscope as well as in the negative controls.

AXL was ubiquitously found to be overexpressed in all cells. Integrin $\alpha_v\beta_5$ was negative on cells grown on plastic (only irregular dots) (Fig. 40). In contrast, integrin $\alpha_v\beta_5$ expression in cells grown on glass was highly elevated, being upregulated on the surface of the imaged cells.

AKH-24S cells were tested positive for SOX2, OCT4, Nestin, CD44, PD-1, ITGA6, and EGFR (Fig. 41). NANOG and CD133 were difficult to evaluate due to the intrinsic fluorescence. However, due to its irregular occurrence, a distinction between $NANOG^+$ and $CD133^+$ cells was possible, as their fluorescence pattern were more regular (Fig. 41). SOX2 was highly upregulated in every cell. OCT4 expression was mainly located in the cytoplasm, rarely found at the nucleus. $OCT4^-$ cells were present. Nestin was found in few small cells, surrounding a $GFAP^+$ cell that also displayed Nestin. CD44 was upregulated on the surface in half of all imaged cells. PD-1 was highly upregulated in every imaged cell, with no expression found in the nucleus. ITGA6 expression was found in a small number of cells. EGFR was detected in every imaged cell.

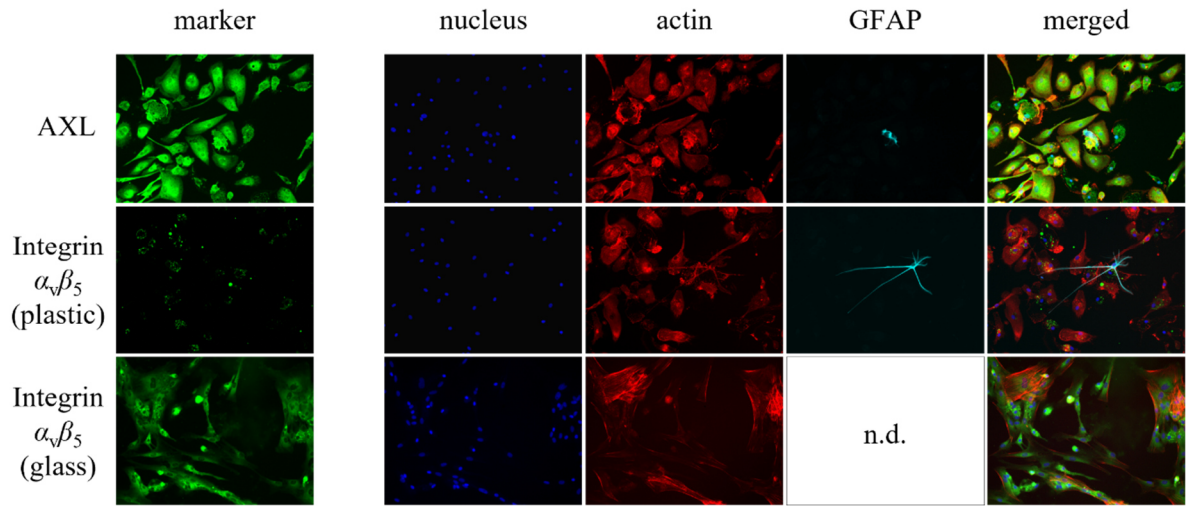

Fig. 40 ZIKV receptor analysis for AKH-24S. For a detailed description, see Fig. 8.

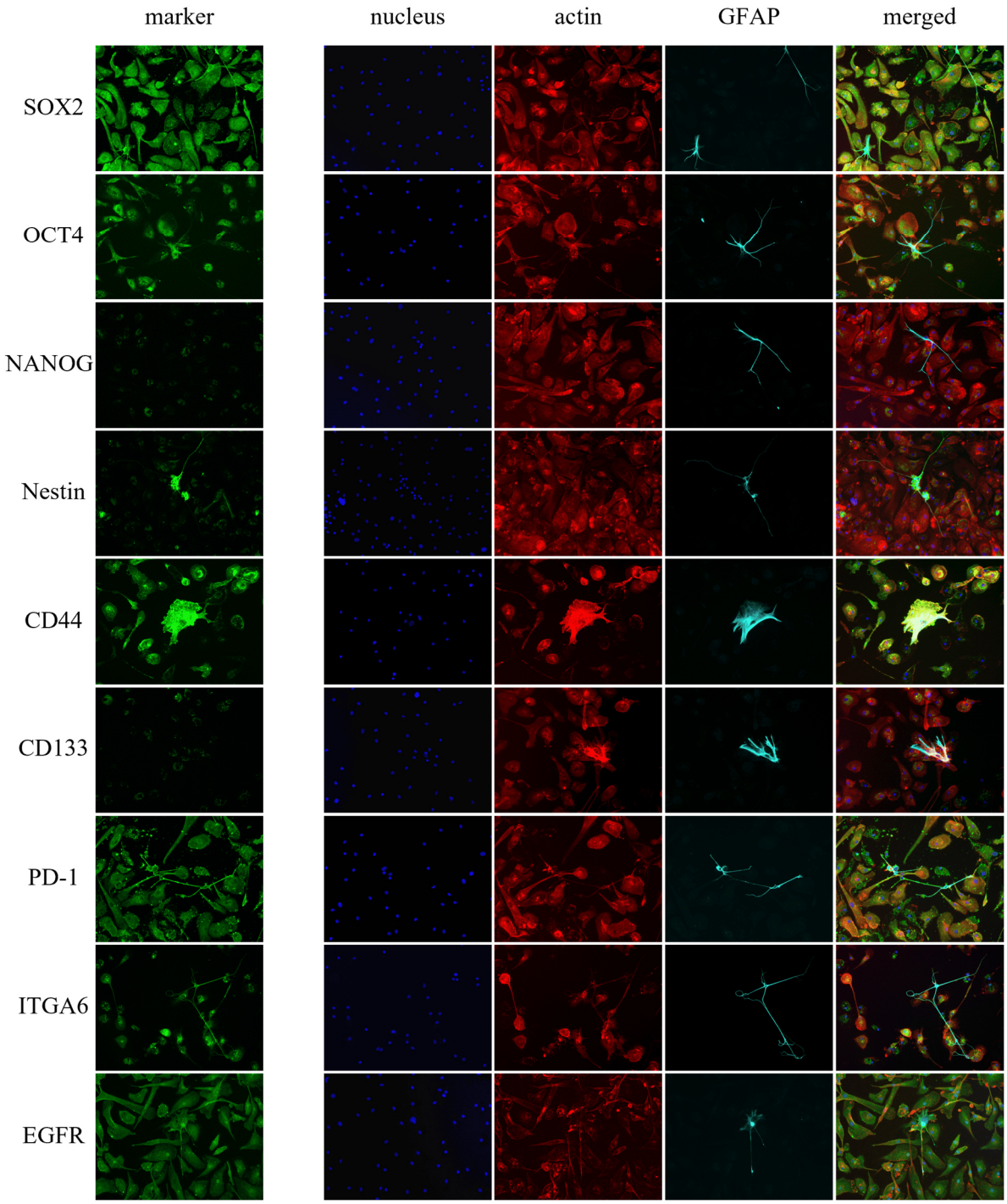

Fig. 41 GSC and GBM biomarker analysis for AKH-24S. For a detailed description, see Fig. 9.

3.3.18. Characterization of primary cell culture AKH-24C

For AKH-24C cells, the same signals as for AKH-24S cells were observed. The cells were tested positive for AXL and integrin $\alpha_v\beta_5$ (Fig. 42). Integrin $\alpha_v\beta_5$ in cells grown on plastic was upregulated in the cytoplasm in large adherent cells and highly expressed in small circular cells, mostly located near the nucleus. The high fluorescence could be attributed to the intrinsic dot-like signals present in the culture. This fluorescence was not observed in cells grown on glass slides, whereas the imaged cells showed a well-developed integrin $\alpha_v\beta_5$ expression across their surface.

The cell culture was found to be positive for SOX2, OCT4, NANOG, Nestin, CD44, PD-1, ITGA6, and EGFR (Fig. 43). CD133 was negative. NANOG appeared to be overexpressed, although the expression pattern (dot-like signals) in some cells could be due to the intrinsic fluorescence. This fluorescence is particularly visible when evaluating Nestin since this protein usually appears “stretched” (Fig. 43). The dots inside the cell culture do not belong to any Nestin expression. Nestin itself was largely displayed by cells that also exhibited GFAP. However, $GFAP^-$ cells expressing Nestin were apparent too.

CD44 was highly upregulated on the cell membrane of all imaged cells. SOX2 was mostly distributed inside the cytoplasm. OCT4 was found inside the cytoplasm and inside the nucleus. PD-1 was exhibited in nearly every cell, with no distinct localization observed. ITGA6 signals were found in half of all imaged cells, mostly at the surface and in the cytoplasm. EGFR was highly upregulated in every cell. All $GFAP^+$ cells observed were large and were found to spread across a vast number of cells. The culture also exhibited long, elongated $GFAP^+$ cells that grew long filopodia to reach out to almost every cell, effectively trying to connect them.

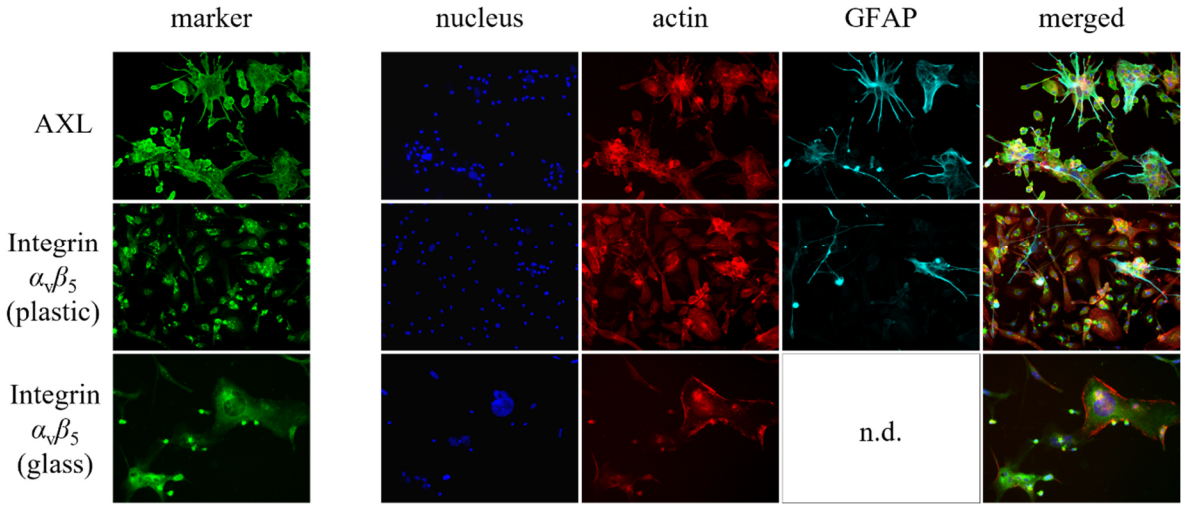

Fig. 42 ZIKV receptor analysis for AKH-24C. For a detailed description, see Fig. 8.

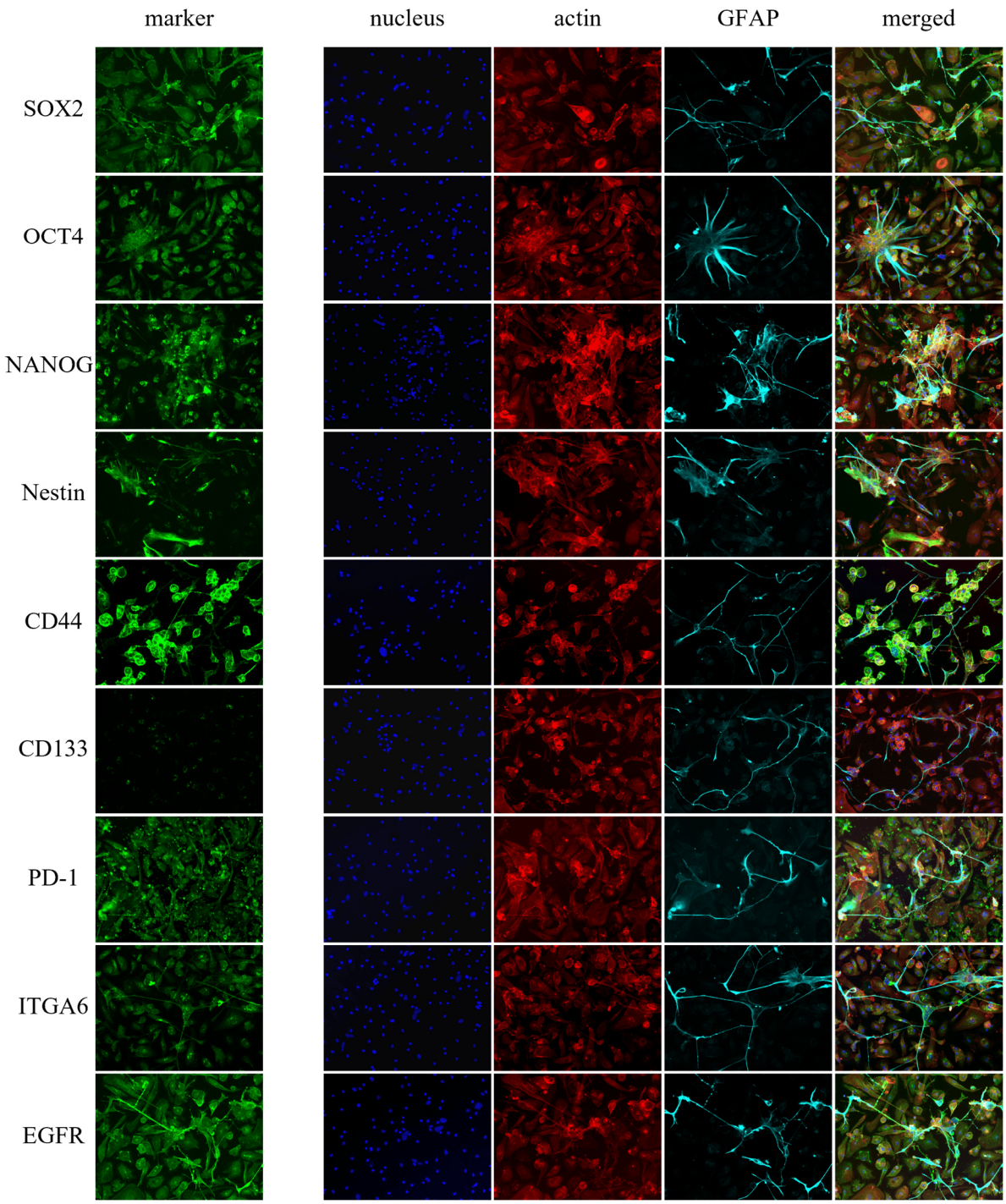

Fig. 43 GSC and GBM biomarker analysis for AKH-24C. For a detailed description, see Fig. 9.

3.3.19. Characterization of U-87 cell culture

For comparison to the primary cell cultures, the laboratory-adapted ependymal GBM cell line U-87 was examined as well.

AXL was found being upregulated on the cell membrane of all U-87 cells, with little signals found in the cytoplasm as well (Fig. 44). Integrin $\alpha_v\beta_5$ levels were low in cells grown on plastic, mostly located at the nucleus. Expression in cells grown on glass could not be examined as the cells did not survive until day 10.

U-87 cells were found to express SOX2, OCT4, NANOG, Nestin, CD44, PD-1, ITGA6, and EGFR (Fig. 45). CD133 was negative and no cells expressing GFAP were found.

SOX2 was predominantly found inside the cytoplasm of the imaged cells. OCT4 was highly upregulated inside the cytoplasm as well, with no expression observed inside the nucleus. NANOG expression was low, but apparent in all cells, mostly located in the nuclear area and the cytoplasm. Nestin was observed in almost every cell, found at various levels inside the cytoplasm. CD44 was solely localized to the cell membranes of all imaged cells. The expression of PD-1 was located mostly inside the cytoplasm and in elevated levels on the cell surface. ITGA6 was also found in every cell to some extent. Most of the imaged cells exhibited ITGA6 inside the cytoplasm and in the cell membrane, while some cells did express the protein in the nucleus. EGFR was highly upregulated on the cell surface and found in large amounts in the cytoplasm of every imaged cell.

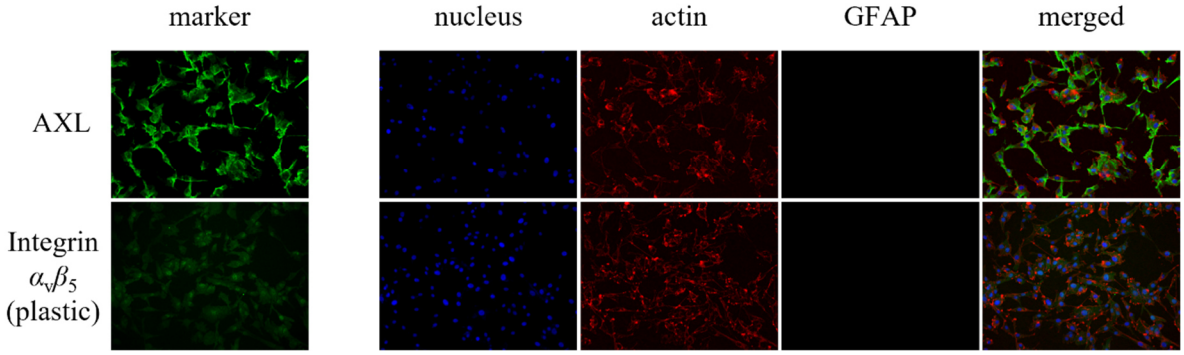

Fig. 44 ZIKV receptor analysis for U-87. For a detailed description, see Fig. 8

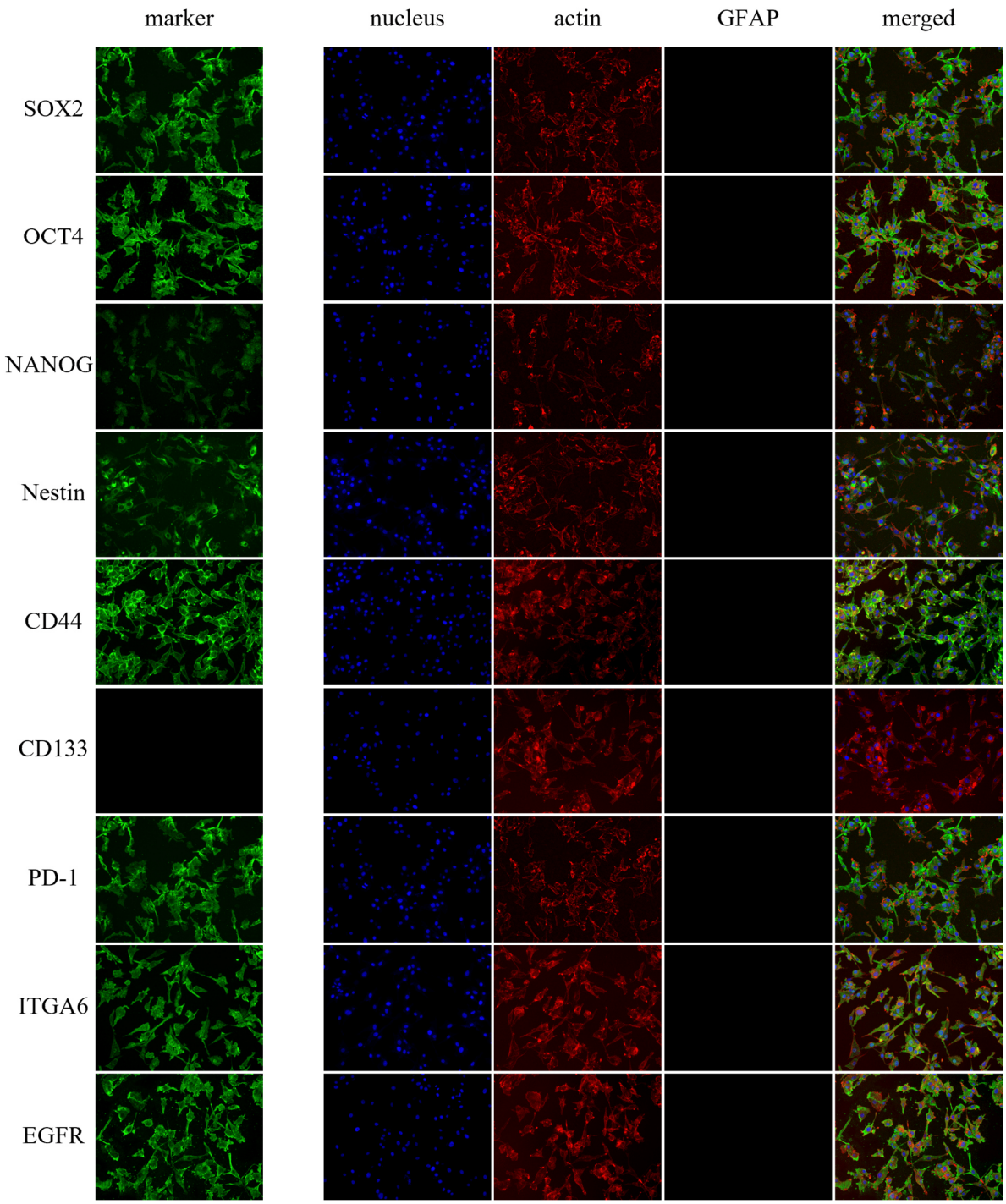

Fig. 45 GSC and GBM biomarker analysis for U-87. For a detailed description, see Fig. 9.

3.3.20. Summary of marker expression for all glioblastoma cell cultures

The results from the previous chapters are summarized in Table 24, which presents the expression patterns of all investigated stem cell markers and ZIKV entry receptors across the primary GBM cell cultures. Furthermore, it provides information on the level of marker expression, distinguishing between high and low percentages of positive cells.

Table 24 Expression patterns of markers in primary GBM cell cultures

AKH		Stem cell and GBM markers									ZIKV entry receptors		
	GFAP	SOX2	OCT4	CD44	EGFR	PD-1	Nestin	ITGA6	NANOG	CD133	AXL	$\alpha_v\beta_5$[a]	$\alpha_v\beta_5$[b]
5	-	+++	+++	+++	+++	+++	+	-	-	-	+++	-	+++
9	-	+++	+++	+++	+++	+++	++	+	-	-	+++	-	+++
10	-	+++	+++	+++	+++	+++	+	+	-	-	+++	+	+++
11	-	+++	+++	+++	+++	+++	-	++	-	-	+++	-	+++
12	-	+++	+++	+++	+++	+++	+	+++	-	-	+++	+++	+++
13	-	+++	+++	+++	+++	+++	+++	+++	+++	+	+++	+++	+++
14	+++	+++	+++	++	+++	+++	-	-	-	-	+++	-	+++
15	++	+++	+++	++	+++	++	+++	+	-	-	+++	++	+++
16	-	+++	+++	+++	+++	+++	+++	+++	+++	++	+++	+++	+++
17	+++	+++	+++	+++	+++	+++	+++	+	-	-	+++	+	+++
18	+	+++	+++	+++	+++	+++	++	++	++	-	+++	+++	n.d.
19	+	+++	+++	+++	+++	++	+++	+++	-	-	+++	+++	+++
20	-	+++	+++	+++	+++	+++	+	++	+	-	+++	+++	+++
21S	+	+++	+++	+++	+++	+++	+++	+++	+	-	+++	++	++
21C	++	+++	+++	+++	+++	+++	+	+++	++	-	+++	+	+
23	+	+++	++	+++	+++	+++	++	-	+	+	+++	-	+++
24S	+	+++	+++	++	+++	+++	+	+++	+	-	+++	+	+++
24C	+++	+++	+++	+++	+++	+++	++	++	+++	-	+++	+++	+++
U87	-	+++	+++	+++	+++	+++	+++	+++	++	-	+++	++	n.d.

Legend: +: low number of positive cells found (<20%); ++: medium percentage (20-60%); +++: high percentage (>60%; -: no positive cells found; n.d., not determined; a: cells were grown on plastic (Cell$^+$); b: cells were grown on glass for 10 days.

SOX2, OCT4, CD44, PD-1, and EGFR were highly expressed in almost every cell from all AKH cultures. Nestin and ITGA6 were also detected in most cell cultures. However, ITGA6 was absent in AKH-5, -14, and -23 and only present in low levels in AKH-9, 10, and -15. Nestin expression was not observed in AKH-11 and AKH-14 cells and was found in a low percentage of cells in cultures AKH-5, -9, -10, -20, -21C, and -24S. NANOG expression was found in a

low number of cells from AKH-16, -18, -20, -21S, and -21C, whereas its expression was found in almost every tumor cell derived from AKH-13 and AKH-24C. CD133 was the rarest marker, only found in a small fraction of cells from AKH-13, AKH-16, and AKH-23 cells. $GFAP^+$ cells were found from AKH-14 onwards, with AKH-14, -17, and -24C having the highest percentage of $GFAP^+$ cells. $GFAP^+$ cells were detected in all cell cultures following AKH-13, except in cultures AKH-16 and AKH-20.

AXL was ubiquitously expressed in every cell culture, being highly elevated in every single imaged cell. Compared to AXL, integrin $\alpha_v\beta_5$ expression was quite different in the regard that it was not well expressed when cells were grown on plastic surfaces in 96-well plates. The expression differed throughout all cell cultures. On plastic surfaces, no integrin $\alpha_v\beta_5$ signals were observed for AKH-5, -9, -11, -14, -23, and -24S cells. A low number of integrin $\alpha_v\beta_5$-expressing cells were found in AKH-10, -15, -16, and -17 cells. The highest number of integrin $\alpha_v\beta_5^+$ cells that have grown on a plastic surface were found in AKH-19 cells. In contrast, the expression of integrin $\alpha_v\beta_5$ was highly elevated in all cell cultures that have grown on a glass surface, with almost every cell expressing the protein.

3.4. Cloning of E protein with a modified transmembrane region

The aim was to modify the ZIKV E protein by exchanging its transmembrane region. As an exchange, the TM region of VSV-G was chosen. VSV-G buds at the cell membrane, in contrast to ZIKV, which buds at the ER membrane.

For the construction of the ZIKV E envelope variants, pCMV-EG1 and pMD2-EG2, the ZIKV E protein with its deleted transmembrane region ($E^{\Delta TM}$) was cloned into two different VSV-G expression vectors, pCMV-VSV-G and pMD2.G. Primers were chosen to amplify the plasmids pCMV-VSV-G and pMD2.G, including the TM region of G, but without amplifying the G protein itself. The ZIKV E protein was amplified using the pME-Z1 plasmid. The plasmids were ligated via Gibson assembly, resulting in the modified expression plasmids pCMV-EG1 and pMD2-EG2.

3.4.1. Synthesis of expression vector pCMV-EG1

For the synthesis of the expression plasmid pCMV-EG1, the plasmids pCMV-VSV-G and pME-Z1 were used. pME-Z1 incorporated the prME part of ZIKV. In a first step, the pME-Z1 plasmid was amplified with PCR, using Gibson primers 1 and 2, creating the ZIKV E ΔTMΔCY fragment. pCMV-VSV-G was amplified with PCR without the glycoprotein, using primers 3 and 4, while keeping the TM and CY domains resulting in the fragment pCMV-VSV-ΔG-$TM^{+}CY^{+}$. After successfully synthesizing both fragments via PCR, they were ligated using Gibson assembly (Fig. 46). Successful insertion of ZIKV E into the pCMV-VSV-G vector while retaining the VSV TM was confirmed via sequencing analysis (Fig. 47). Sequencing revealed the synthesis of two plasmids that each had mutations in four positions. The mutations were T15A, C1341T, G1344A, and C1359T. The resulting triplets were translated into the same amino acids; thus, they were not different from each other regarding the ZIKV E protein. For future experiments, both plasmids were considered the same and referred to as pCMV-EG1.

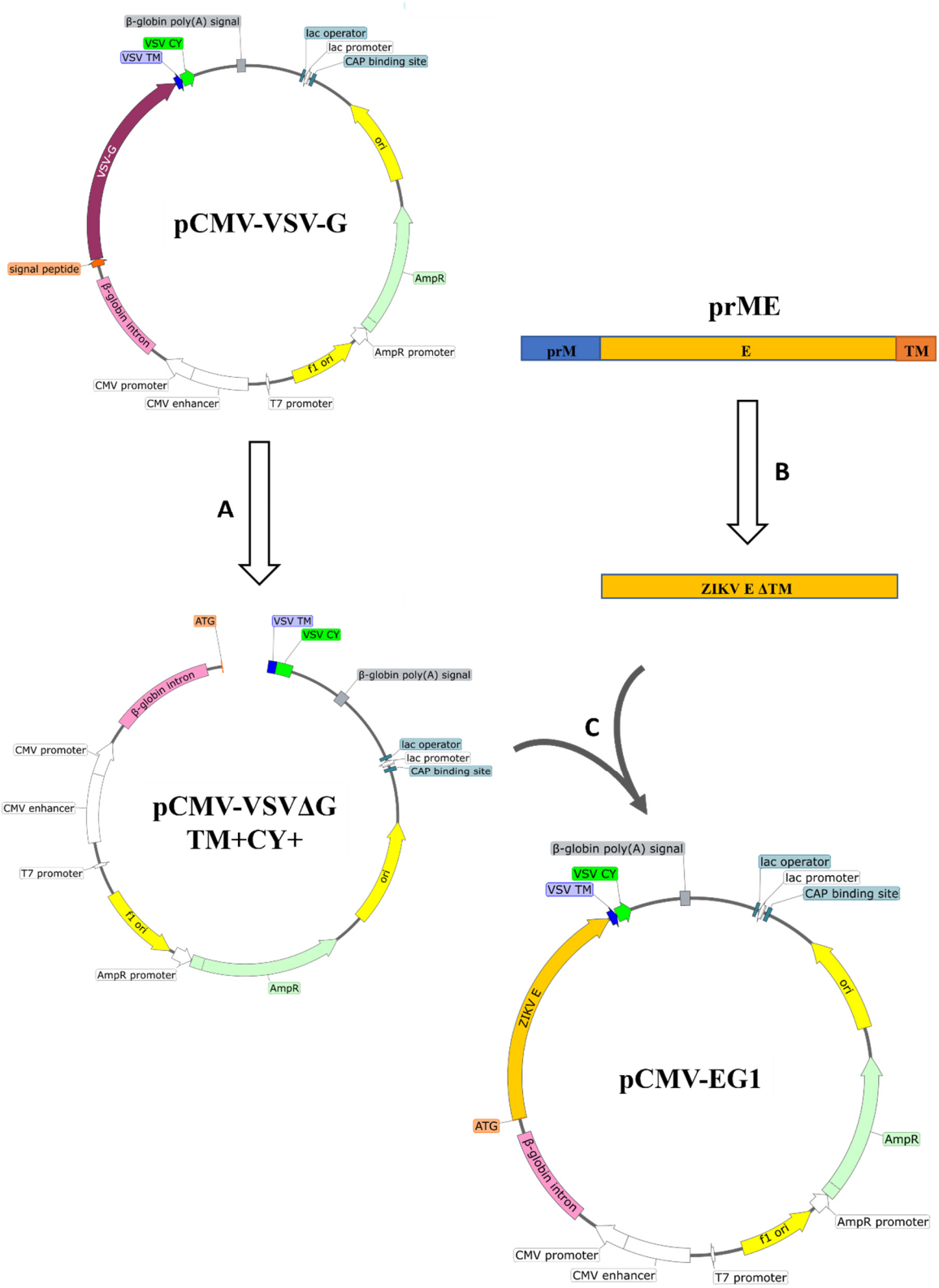

Fig. 46 Overview of the construction of pCMV-EG1. **A**: PCR using primers 1 and 2 in combination with pCMV-VSV-G to generate linear fragment pCMV-VSVΔG $TM^{+}CY^{+}$; **B**: PCR using primers 3 and 4 to isolate ZIKV E ΔTM fragment from the prME part of pME-Z1; **C**: Gibson assembly of fragments pCMV-VSVΔG $TM^{+}CY^{+}$ and ZIKV E ΔTM to generate pCMV-VSV-EG1; TM: transmembrane domain, CY: cytosolic domain; plasmid maps were created with SnapGene®.

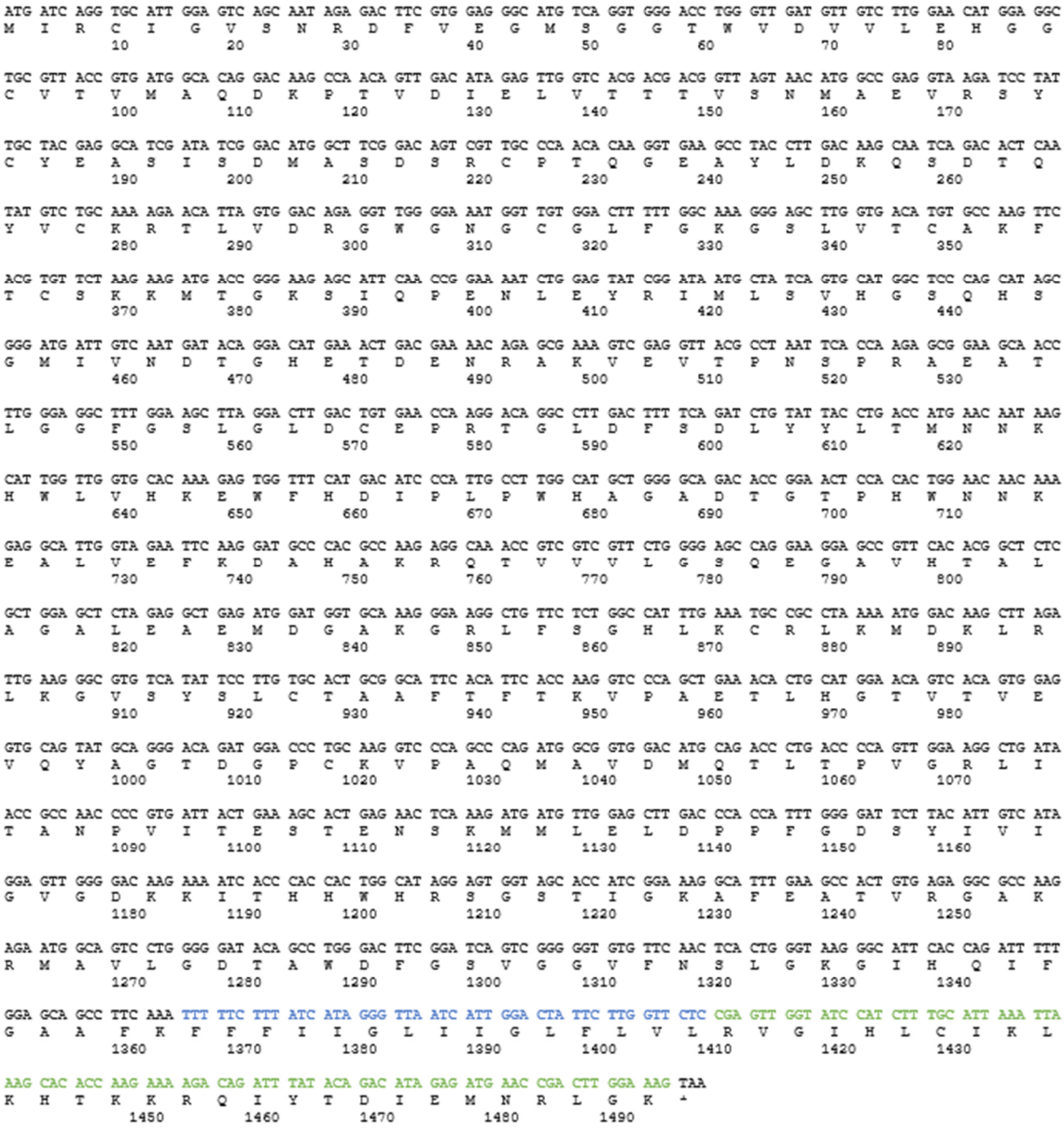

Fig. 47 Codon sequence as triplets with translational amino acids of pCMV-EG1. Black sequence: ZIKV E protein; blue sequence: TM region of VSV-G; green sequence: CY region of VSV-G; sequence was created with Serial Cloner.

3.4.2. Synthesis of expression vector pMD2-EG2

For the synthesis of pMD2-EG2, the ZIKV E protein from pME-Z1 was ligated without its TM region into the expression plasmid pMD2.G. For this, pMD2.G was amplified, using primers 7 and 8, to generate the pMD2.ΔG fragment. The ZIKV E ΔTMΔCY fragment was retrieved using Gibson primers 5 and 6. With Gibson assembly, both fragments were ligated to generate the expression vector pMD2-EG2 (Fig. 48). Successful synthesis of pMD2-EG2 was confirmed by sequencing analysis (Fig. 49).

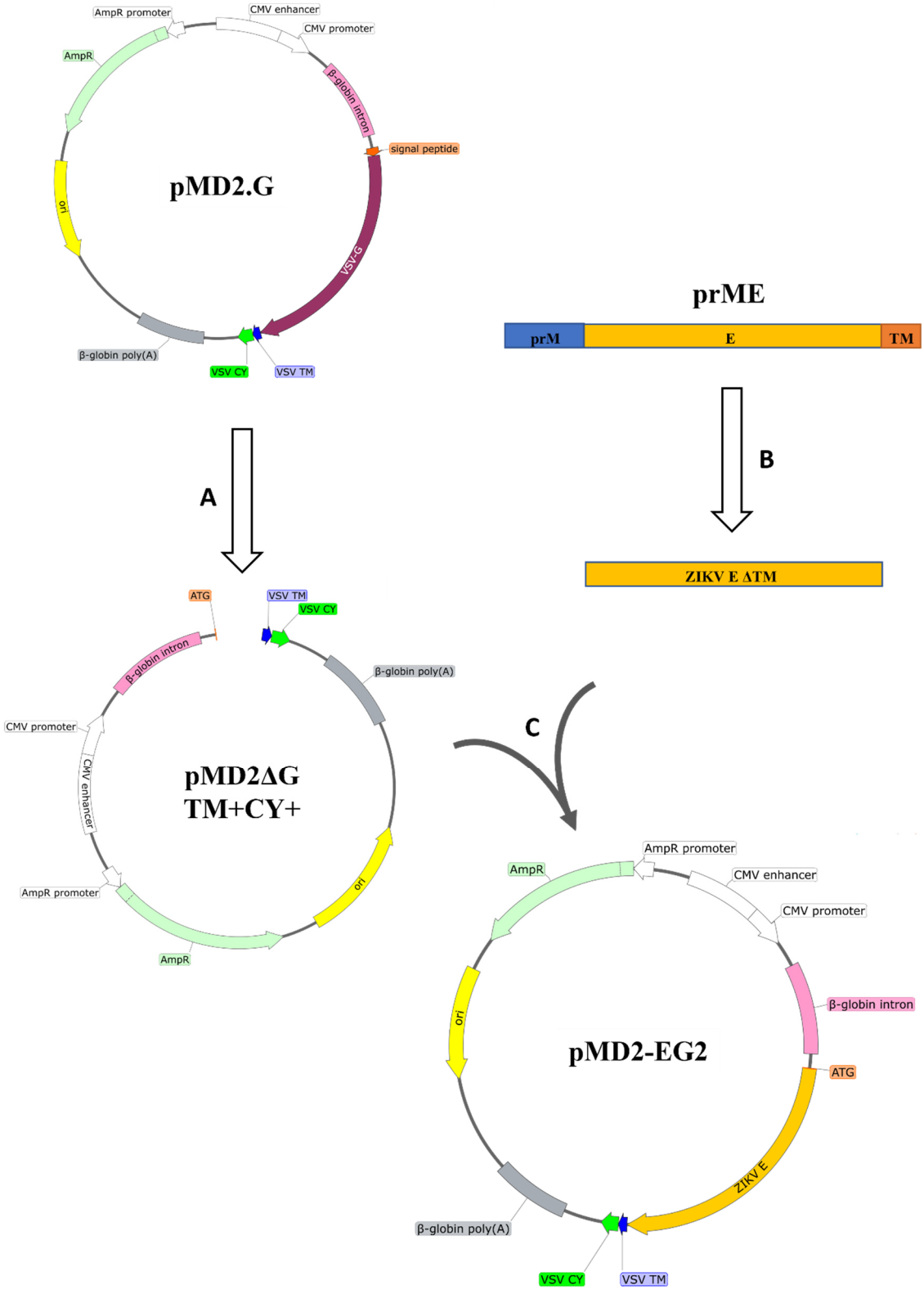

Fig. 48 Overview of the construction of pMD2-EG2. **A**: PCR using primers 1 and 2 in combination with pMD2.G to generate linear fragment pMD2ΔG TM^+CY^+; **B**: PCR using primers 3 and 4 to isolate ZIKV E ΔTM fragment from the prME part of pME-Z1; **C**: Gibson assembly of fragments pMD2ΔG TM^+CY^+ and ZIKV E ΔTM to generate pMD2-EG2; TM: transmembrane domain, CY: cytosolic domain; plasmid maps were created with SnapGene®.

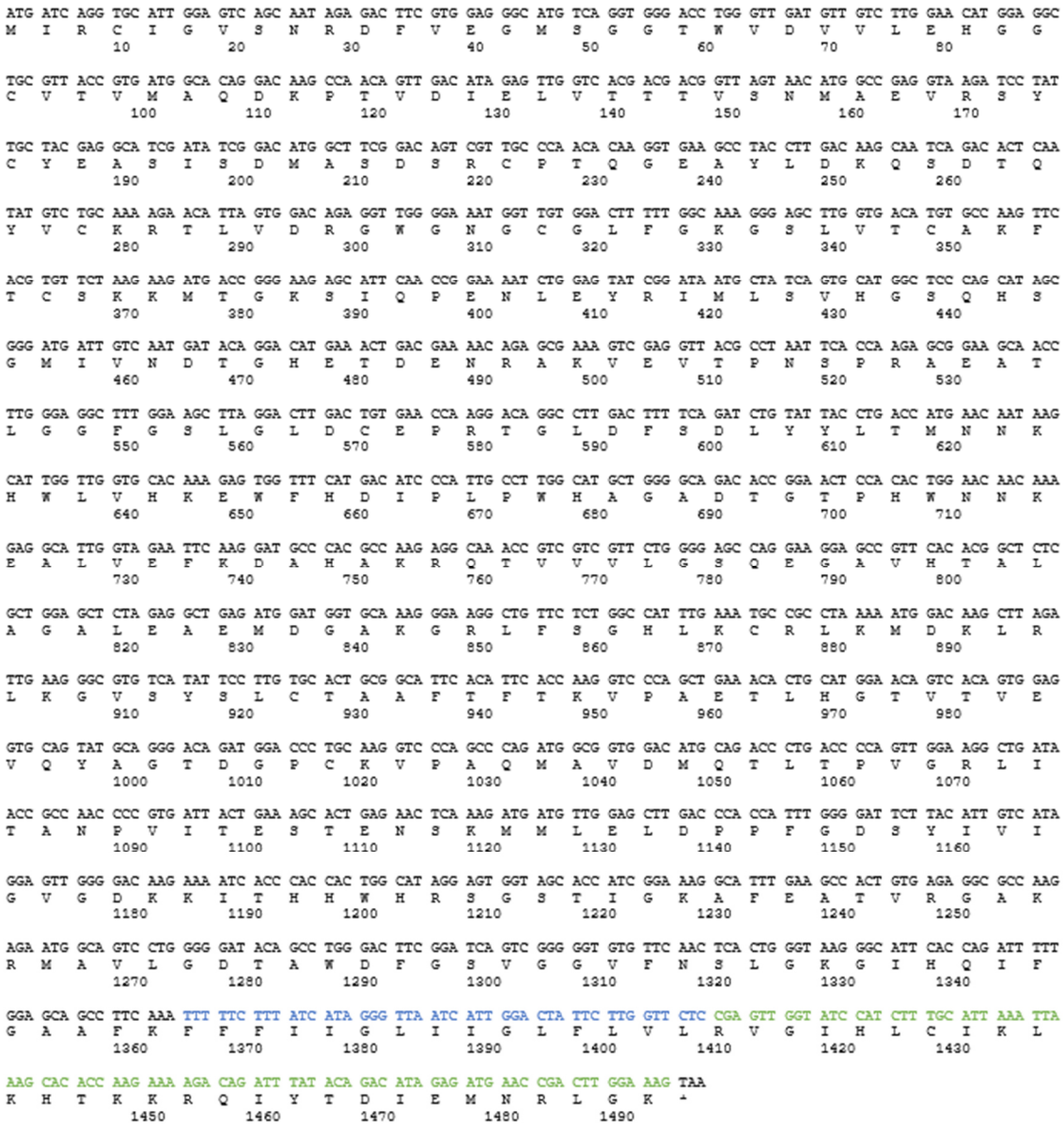

Fig. 49 Codon sequence as triplets with translational amino acids of pMD2-EG2. Black sequence: ZIKV E protein; blue sequence: TM region of VSV-G; green sequence: CY region of VSV-G; sequence was created with Serial Cloner.

3.5. Transfection of COS-1 cells for pseudotype generation

COS-1 cells were transfected using a two-plasmid system. Plasmids pCMV-EG1, pMD2-EG2, or pCMV-VSV-G, containing the envelope, were combined with the HIV-1 packaging plasmid pNL*gfp*AM. Polyethyleneimine (PEI) was used as the transfection reagent. Along with the HIV-1 proteins, pNL*gfp*AM contained the reporter gene to produce green fluorescent protein (GFP). This allowed detection of transfected cells microscopically through green fluorescence.

First, a suitable combination of plasmids and PEI was evaluated (2.2.14). The aim was to achieve the highest number of transfected cells. Transfection efficiency was checked after 72 hours, and the results can be seen in Fig. 50.

For pCMV-EG1, the highest number of transfected cells were observed for conditions C, D, E, and G. The higher the concentration of PEI, the lower the rate of transfection. Conditions A and B showed fewer transfected cells, although the concentration of PEI was low compared to others. Transfection with pMD2-EG2 was comparable to pCMV-EG1, the most transfected cells were observed for conditions C, D, and E. Both plasmids showed the highest transfection efficiency for condition D. In contrast, the highest efficiencies for pCMV-VSV-G were only observed for conditions C and D. However, using condition D led to partial detachment of cells.

In general, transfected cells were observed in all experiments, but conditions that used more than 6 µg PEI (conditions E, F, G, H, I, J) resulted in a loss of transfection efficiency as well as detachment of cells.

Overall, a DNA:PEI ratio of 2:3 gave the best results, provided the concentration of PEI was not higher than 6 µg. The best combination of vectors and PEI were those from conditions C and D (Fig. 50).

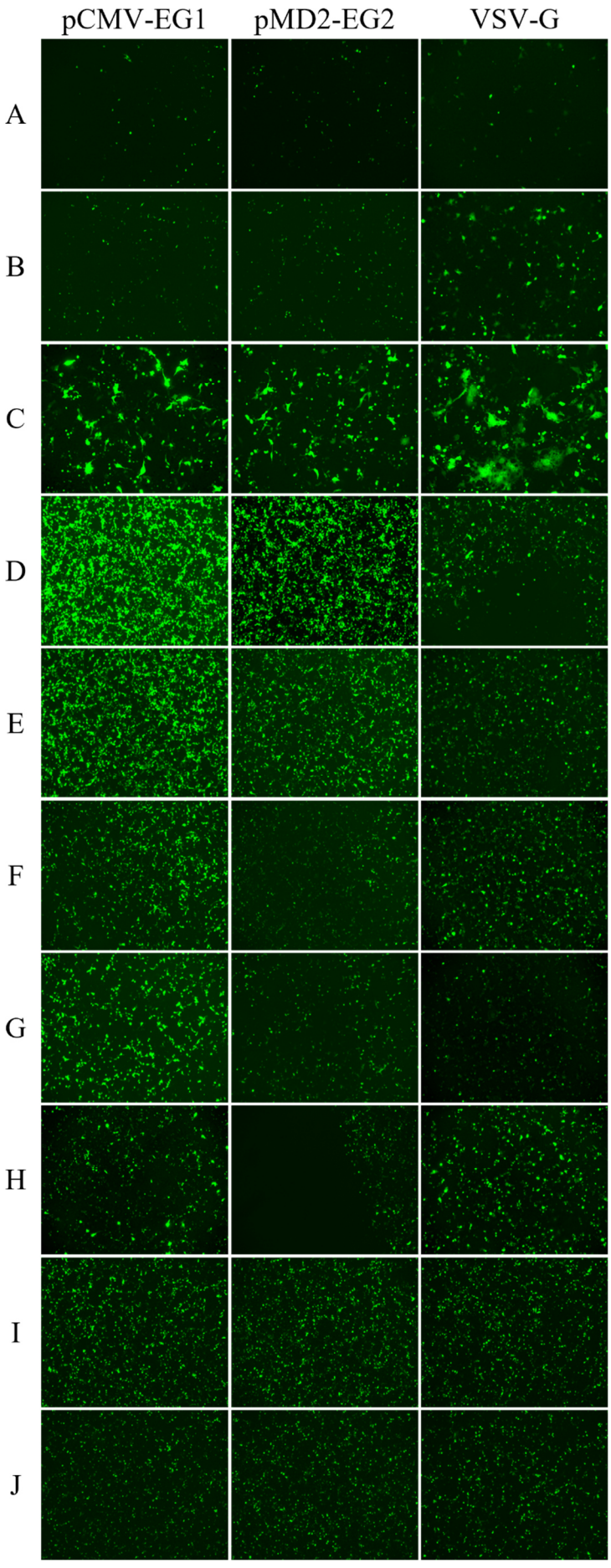
pCMV-EG1
pMD2-EG2
VSV-G
A
B
C
D
E
F
G
H
I
J

Fig. 50 Transfection of COS-1 cells. Different concentrations of pNL*gfp*AM (gfp) in combination with pCMV-EG1, pMD2-EG2, and VSV-G (env) were used. PEI was used as a transfection reagent. DNA and PEI solutions were adjusted to a concentration of 1 µg/µL prior use. **A**: 0.5 µg gfp/0.5 µg env/1.0 µg PEI; **B**: 1.0 µg gfp/1.0 µg env/2 µg PEI; **C**: 1.0 µg gfp/1.0 µg/3.0 µg PEI; **D**: 2.0 µg gfp/2.0 µg env/6.0 µg PEI; **E**: 2.0 µg gfp/4.0 µg env/9.0 µg PEI; **F**: 2.0 µg gfp/6.0 µg env/12.0 µg PEI; **G**: 2.0 µg gfp/8.0 µg env/15.0 µg PEI; **H**: 3.0 µg gfp/3.0 µg env/9.0 µg PEI; **I**: 4.0 µg gfp/4.0 µg env/12.0 µg PEI; **J**: 6.0 µg gfp/6.0 µg env/18.0 µg PEI. Successful transfection was measured after an incubation time of 72 h post transfection and shows GFP expression. Images are presented at 10x magnification.

3.6. Infection of primary cell cultures with pseudotyped viral particles

After successful transfection, generated viral particles were harvested after 72 hours (2.2.15). Infection experiments were performed on all characterized AKH cell cultures and additionally on U-87 cells. The following subchapters address those cell cultures, in which at least one infection event was observed; in some cases, this meant that only a single infected cell was detected in an entire well.

Successful infections were detected using fluorescence microscopy. In contrast to transfected cells, which produce GFP through direct transcription of the pNL*gfp*AM plasmid DNA, infected cells acquire the ability to produce GFP following a different process. Upon infection, the pseudotyped viral RNA genome is reverse transcribed into DNA, which is then integrated into the host cell genome. As a result, these cells gain the ability to express GFP from the integrated genetic material. Cells were observed after an incubation time of 72 h post-infection.

Successful infections for EG1-HIV*gfp* were observed in cultures AKH-13, -14, -17, and -19. Infections using the pseudotype EG2-HIV*gfp* were observed in cells from AKH-13, -14, -17, -19, -23, and -24C. G-HIV*gfp* pseudotypes were able to infect cells from cultures AKH-13, -14, -15, -16, -17, -19, -23, -24C, and U-87.

3.6.1. Infection of AKH-13 cells

Successful infection of AKH-13 cells was achieved with all three pseudotypes: EG1-HIV*gfp*, EG2-HIV*gfp*, and G-HIV*gfp* (Fig. 51). Infectious events using EG1-HIV*gfp* and EG2-HIV*gfp* were observed only at the higher concentrations used in previous transfections. However, only a few infections were detected. In contrast, infections using G-HIV*gfp* were more frequent.

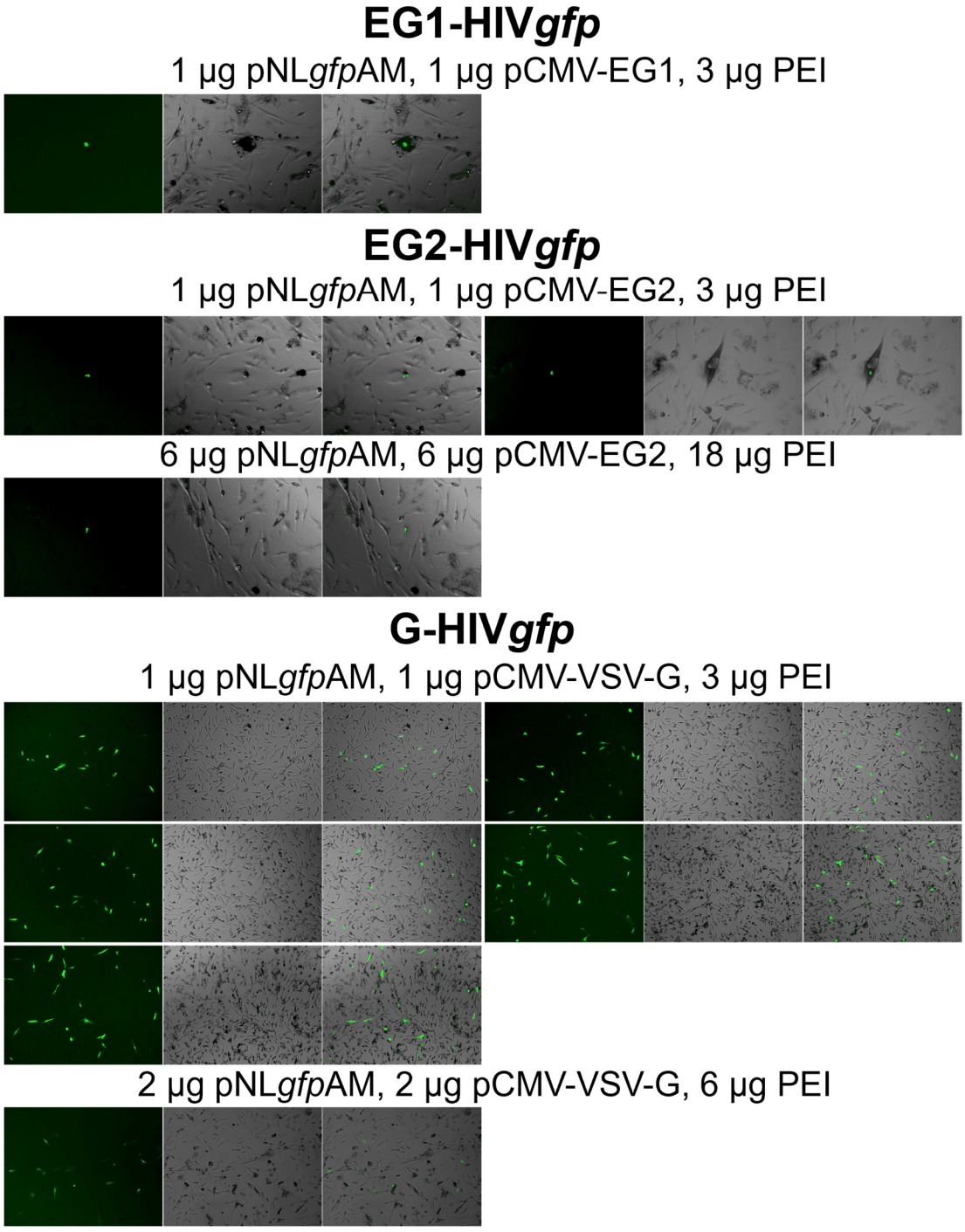

Fig. 51 AKH-13 cells infected with EG1-HIV*gfp*, EG2-HIV*gfp*, and G-HIV*gfp* pseudotyped viral particles. Infections are shown as picture triplets, left: GFP channel, middle: transmitted light, right: merged channels; cells were observed 72 h post-infection.

3.6.2. Infection of AKH-14 cells

AKH-14 cells could also be transduced with all three pseudotypes. Both EG1-HIV*gfp* and EG2-HIV*gfp* pseudotyped particles could successfully infect AKH-14 cells (Fig. 52 and Fig. 53). The number of cells infected with EG2-HIV*gfp* was higher compared to EG1-HIV*gfp* (Fig. 53). For G-HIV*gfp*, the results were comparable to those observed with EG2-HIV*gfp* (Fig. 54).

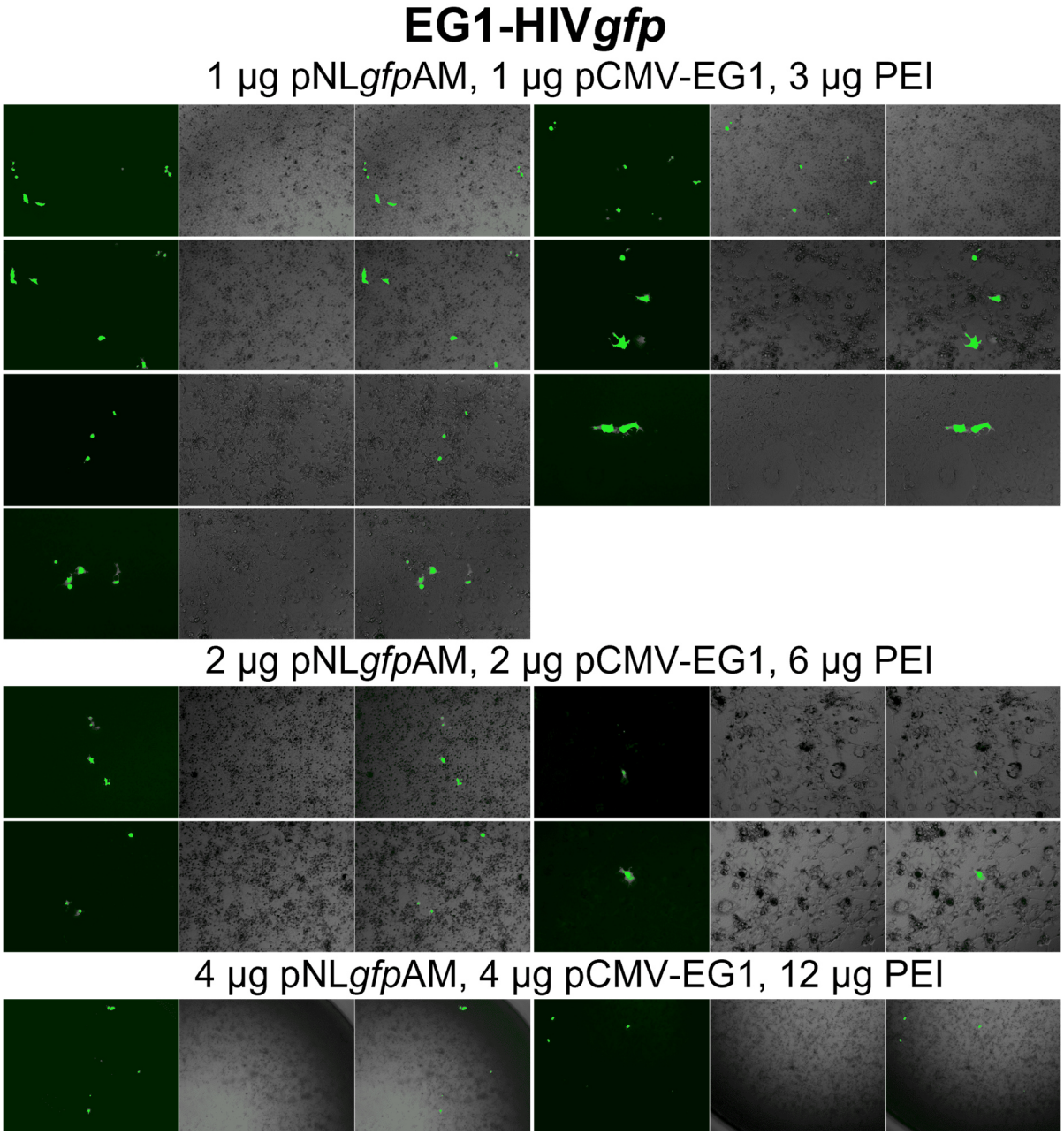

Fig. 52 AKH-14 cells infected with EG1-HIV*gfp* pseudotyped viral particles. Infections are shown as picture triplets, left: GFP channel, middle: transmitted light, right: merged channels; Cells were observed 72 h post-infection.

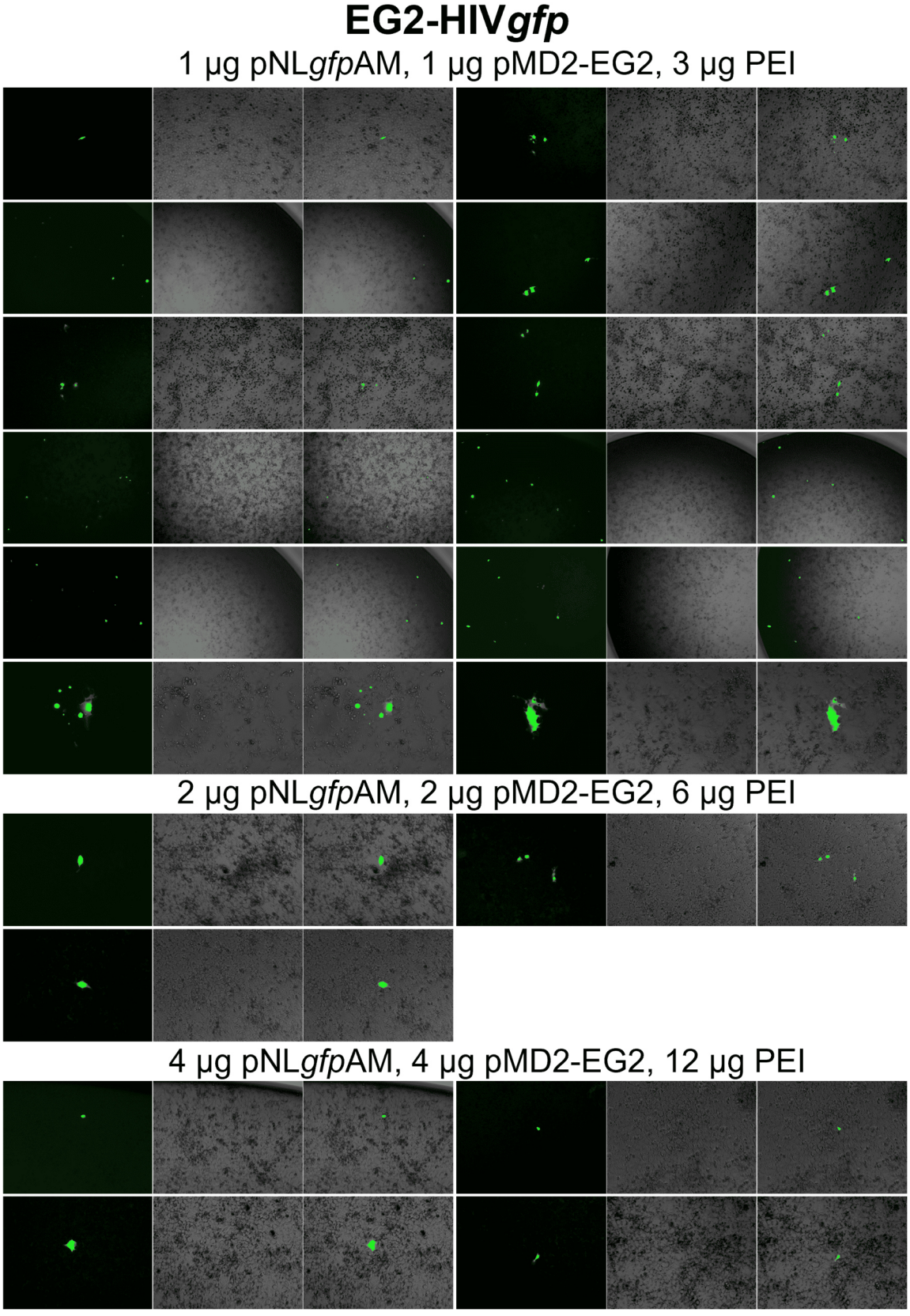

Fig. 53 AKH-14 cells infected with EG2-HIV*gfp* pseudotyped viral particles. Infections are shown as picture triplets, left: GFP channel, middle: transmitted light, right: merged channels; cells were observed 72 h post-infection.

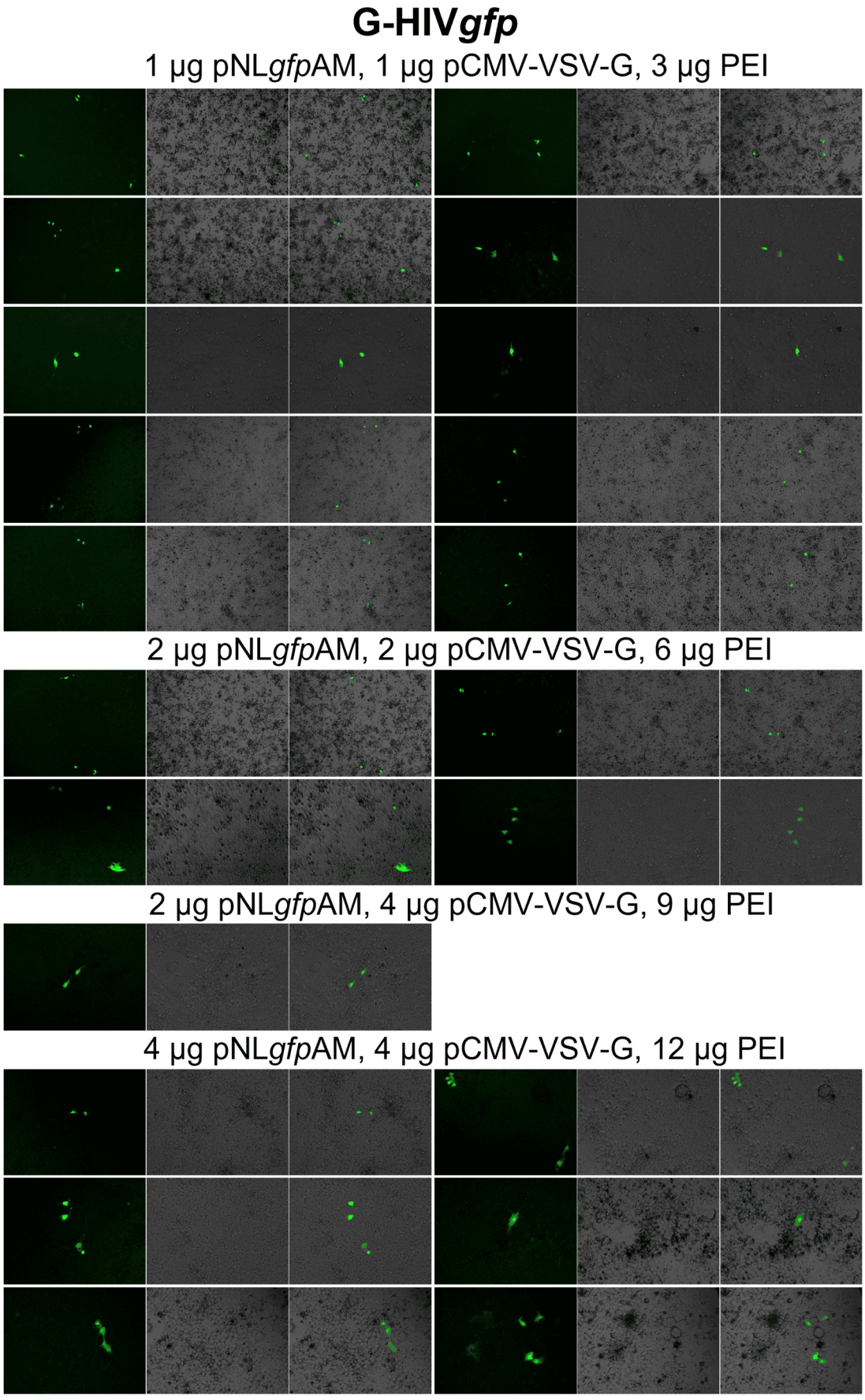

Fig. 54 AKH-14 cells infected with G-HIV*gfp* pseudotyped viral particles. Infections are shown as picture triplets, left: GFP channel, middle: transmitted light, right: merged channels; cells were observed 72 h post-infection.

3.6.3. Infection of AKH-15 cells

Infections of AKH-15 cells were only observed using G-HIV*gfp* (Fig. 55).

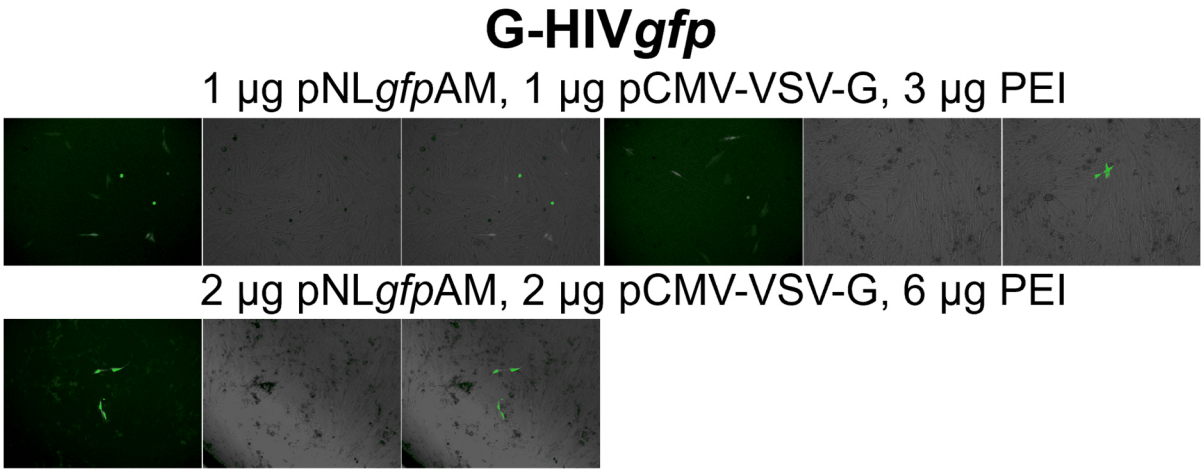

Fig. 55 AKH-15 cells infected with G-HIV*gfp* pseudotyped viral particles. Infections are shown in picture triplets, left: GFP channel, middle: transmitted light, right: merged channels; cells were observed 72 h post-infection.

3.6.4. Infection of AKH-16 cells

AKH-16 cells were successfully infected with G-HIV*gfp* (Fig. 56). No infections using EG1-HIV*gfp* or EG2-HIV*gfp* were observed.

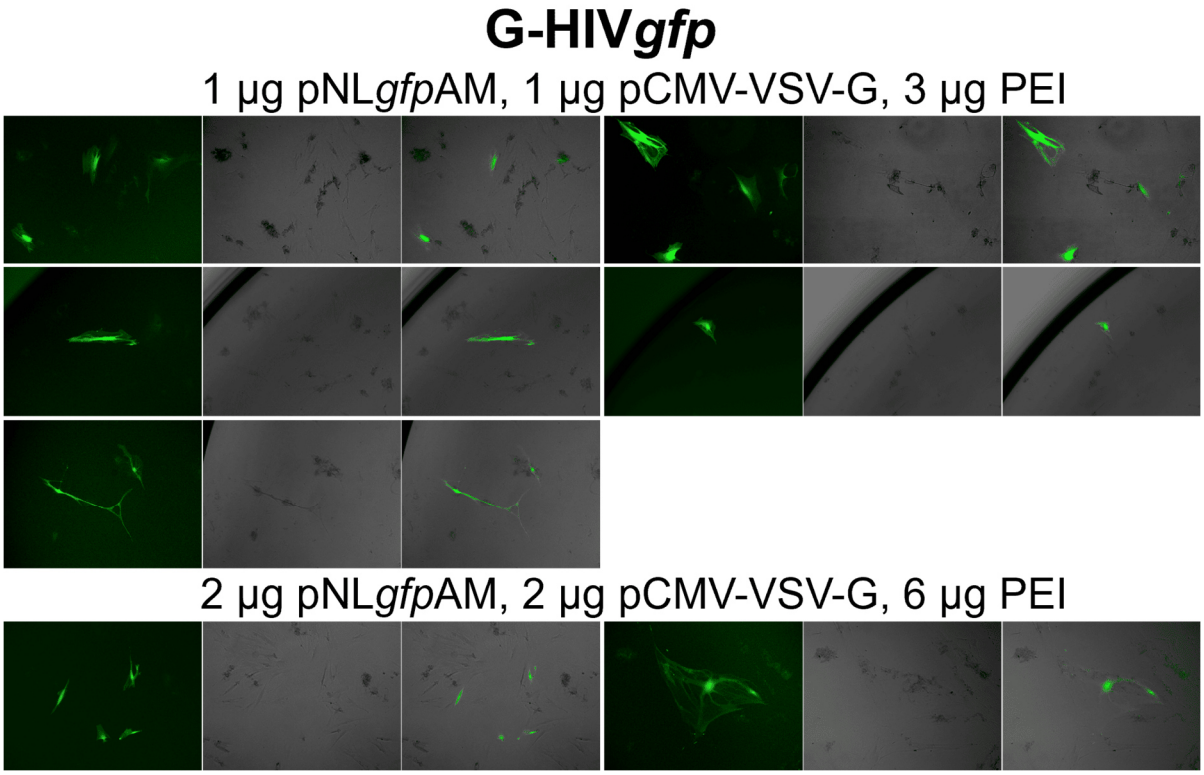

Fig. 56 AKH-16 cells infected with G-HIV*gfp* pseudotyped viral particles. Infections are shown as picture triplets, left: GFP channel, middle: transmitted light, right: merged channels; cells were observed 72 h post-infection.

3.6.5. Infection of AKH-17 cells

All three pseudotypes, EG1-HIV*gfp*, EG2-HIV*gfp*, and G-HIV*gfp*, were able to transduce cells from the AKH-17 culture. The highest number of infections was observed for G-HIV*gfp* (Fig. 60). Infections with EG1-HIV*gfp* and EG2-HIV*gfp* were only observed using transfection conditions with higher DNA and PEI concentrations. These conditions generally showed no GFP emission after three days post-transfection (Fig. 50). For G-HIV*gfp*, infections were obtained under the best conditions observed during transfections.

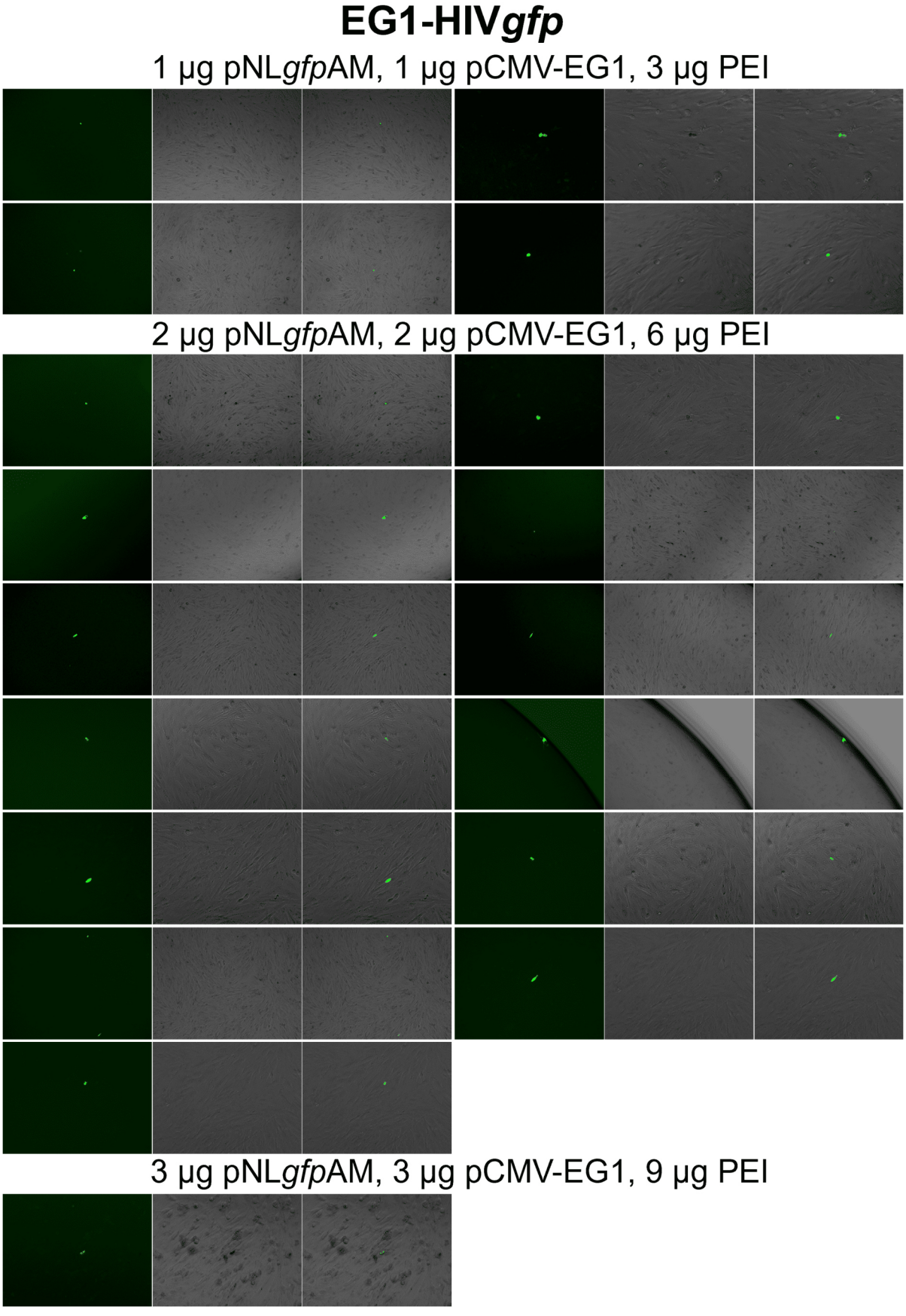

Fig. 57 AKH-17 cells infected with EG1-HIV*gfp* pseudotyped viral particles. Infections are shown as picture triplets, left: GFP channel, middle: transmitted light, right: merged channels; cells were observed 72 h post-infection.

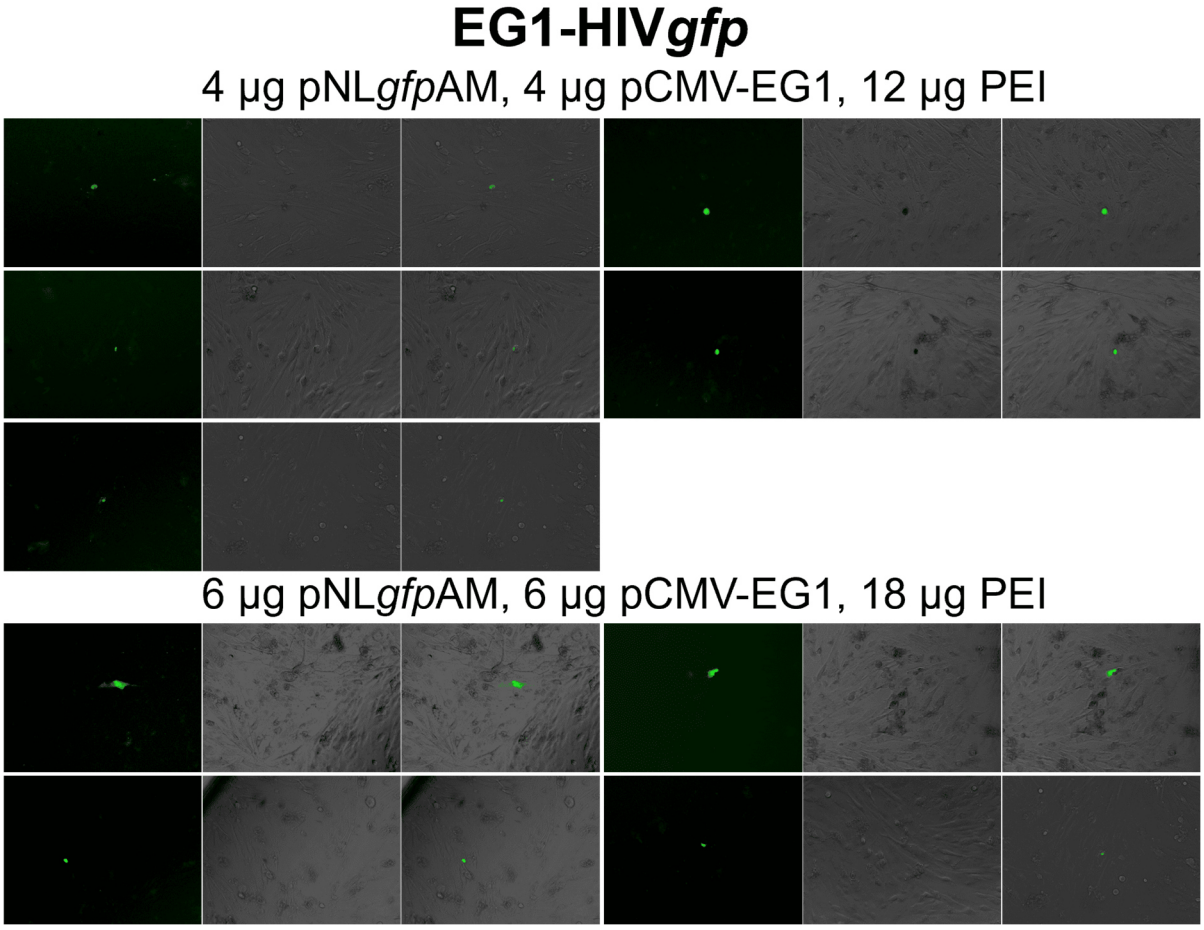

Fig. 58 AKH-17 cells infected with EG1-HIV*gfp* pseudotyped viral particles. Continued from fig. 57.

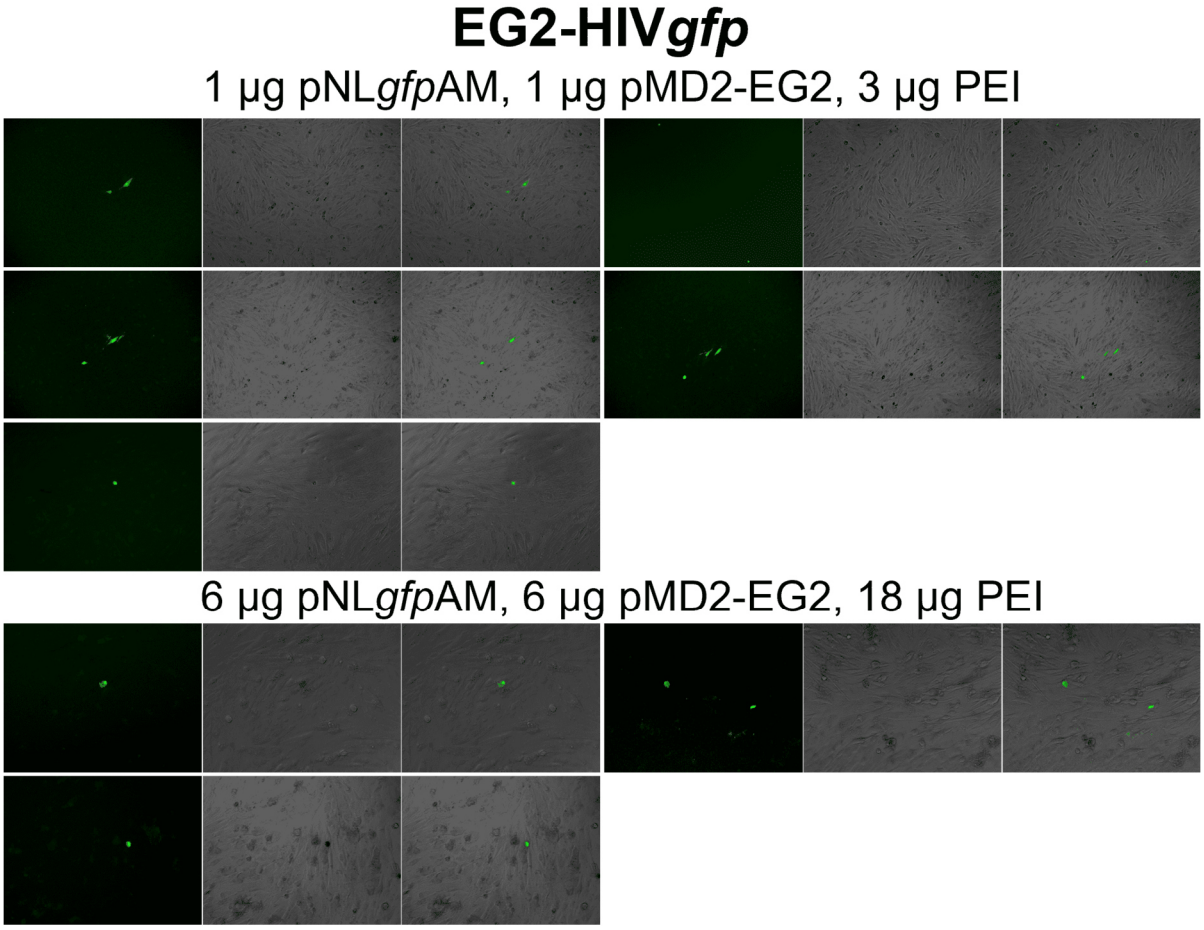

Fig. 59 AKH-17 cells infected with EG2-HIV*gfp* pseudotyped viral particles. Infections are shown as picture triplets, left: GFP channel, middle: transmitted light, right: merged channel; cells were observed 72 h post-infection.

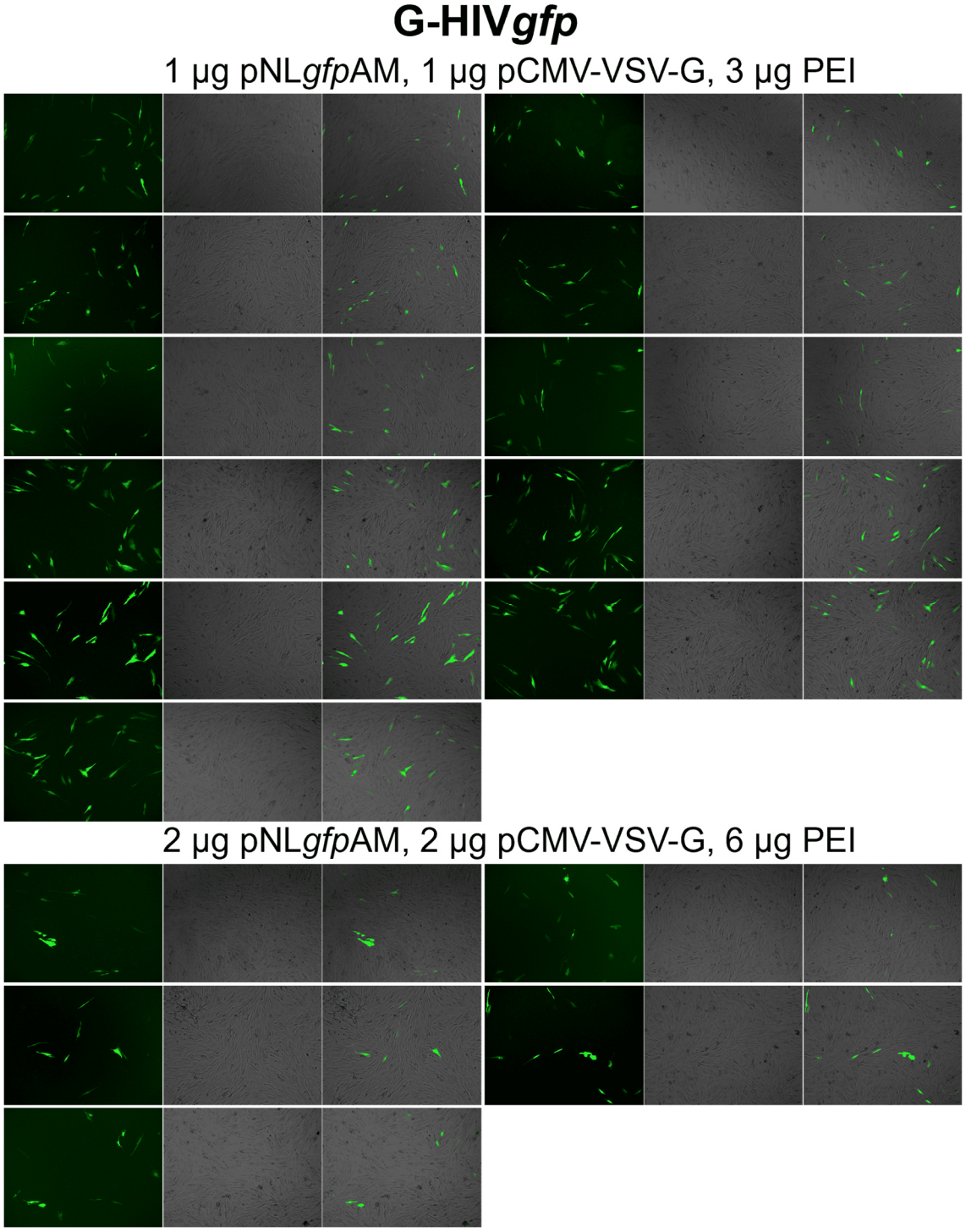

Fig. 60 AKH-17 cells infected with G-HIV*gfp* pseudotyped viral particles. Infections are shown as picture triplets, left: GFP channel, middle: transmitted light, right: merged channels; cells were observed 72 h post-infection.

3.6.6. Infection of AKH-19 cells

All three pseudotypes were able to infect AKH-19 cells (Fig. 61). For EG1- and EG2-HIV*gfp*, only a few infected cells were observed. In contrast, G-HIV*gfp* was able to infect a larger number of cells.

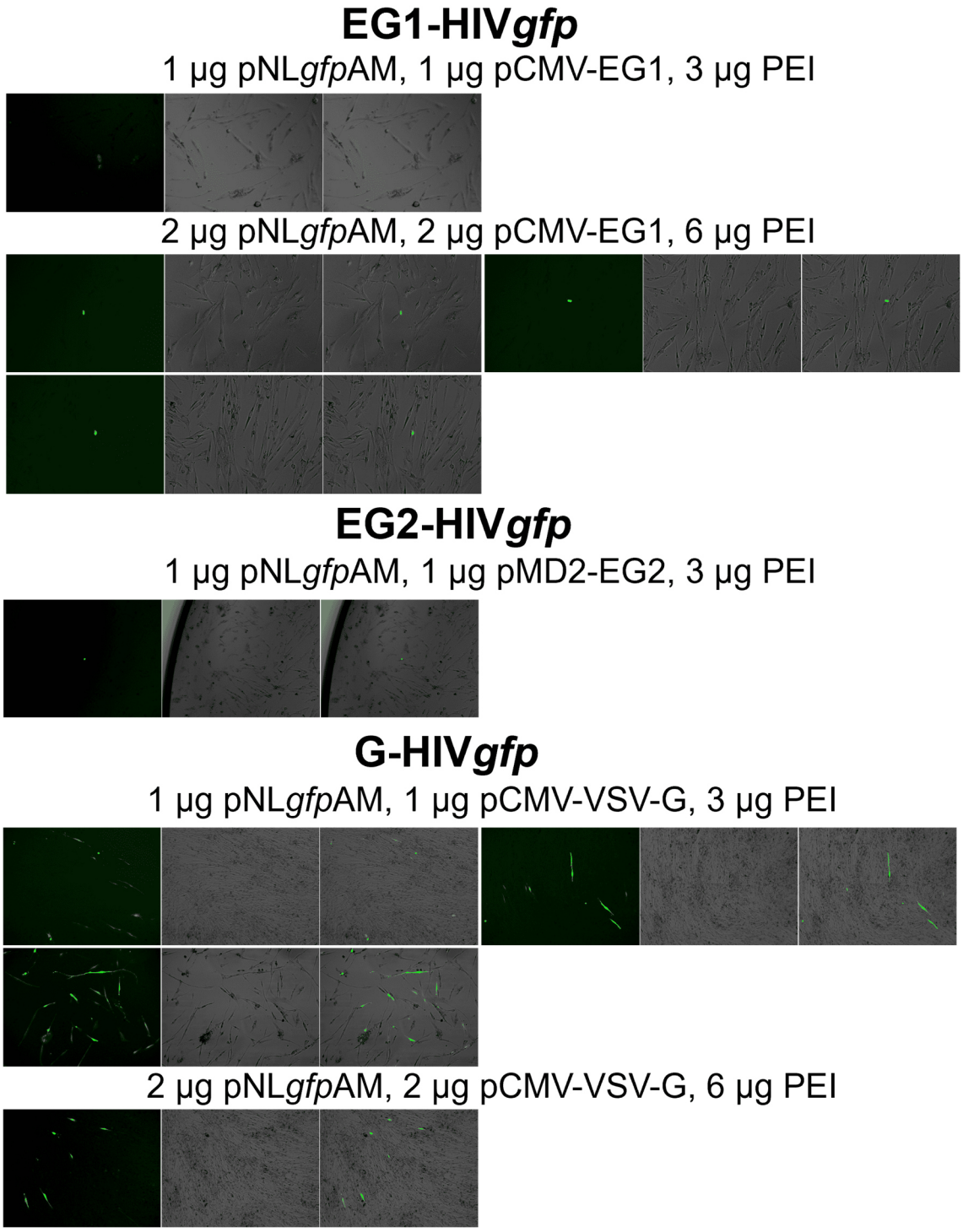

Fig. 61 AKH-19 cells infected with EG1-HIV*gfp*, EG2-HIV*gfp*, and G-HIV*gfp* pseudotyped viral particles. Infections are shown as picture triplets, left: GFP channel, middle: transmitted light, right: merged channels; cells were observed 72 h post-infection.

3.6.7. Infection of AKH-20 cells

Infections of AKH-20 cells were observed using an EVOS M7000 microscope, which allowed imaging of an entire well (Fig. 62). The best transduction results in AKH-20 cells were achieved with G-HIV*gfp*; however, infections with both EG1-HIV*gfp* and EG2-HIV*gfp* were also observed, with EG1-HIV*gfp* infecting a greater number of cells than EG2-HIV*gfp*.

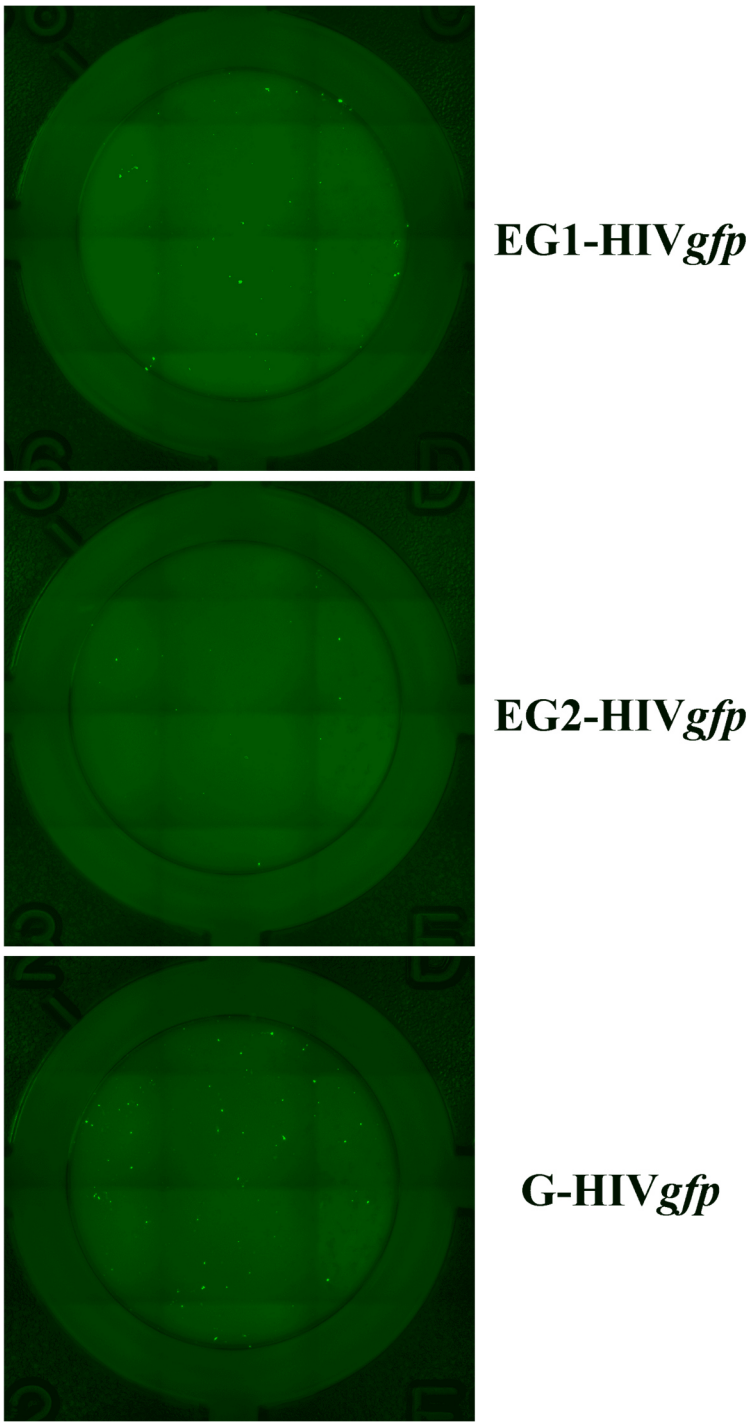

Fig. 62 AKH-20 cells infected with EG1-HIV*gfp*, EG2-HIV*gfp*, and G-HIV*gfp* pseudotyped viral particles. Shown is a complete overview of a single well from a 96-well plate at 4x magnification three days post infection. Infections were performed using 2 µg pNL*fgp*AM, 2 µg envelope plasmid, and 6 µg PEI.

3.6.8. Infection of AKH-23 cells

For AKH-23 cells, only one infection with EG2-HIV*gfp* was observed, and no infections with EG1-HIV*gfp* were found (Fig. 63). For G-HIV*gfp,* approximately 36 infected cells were detected.

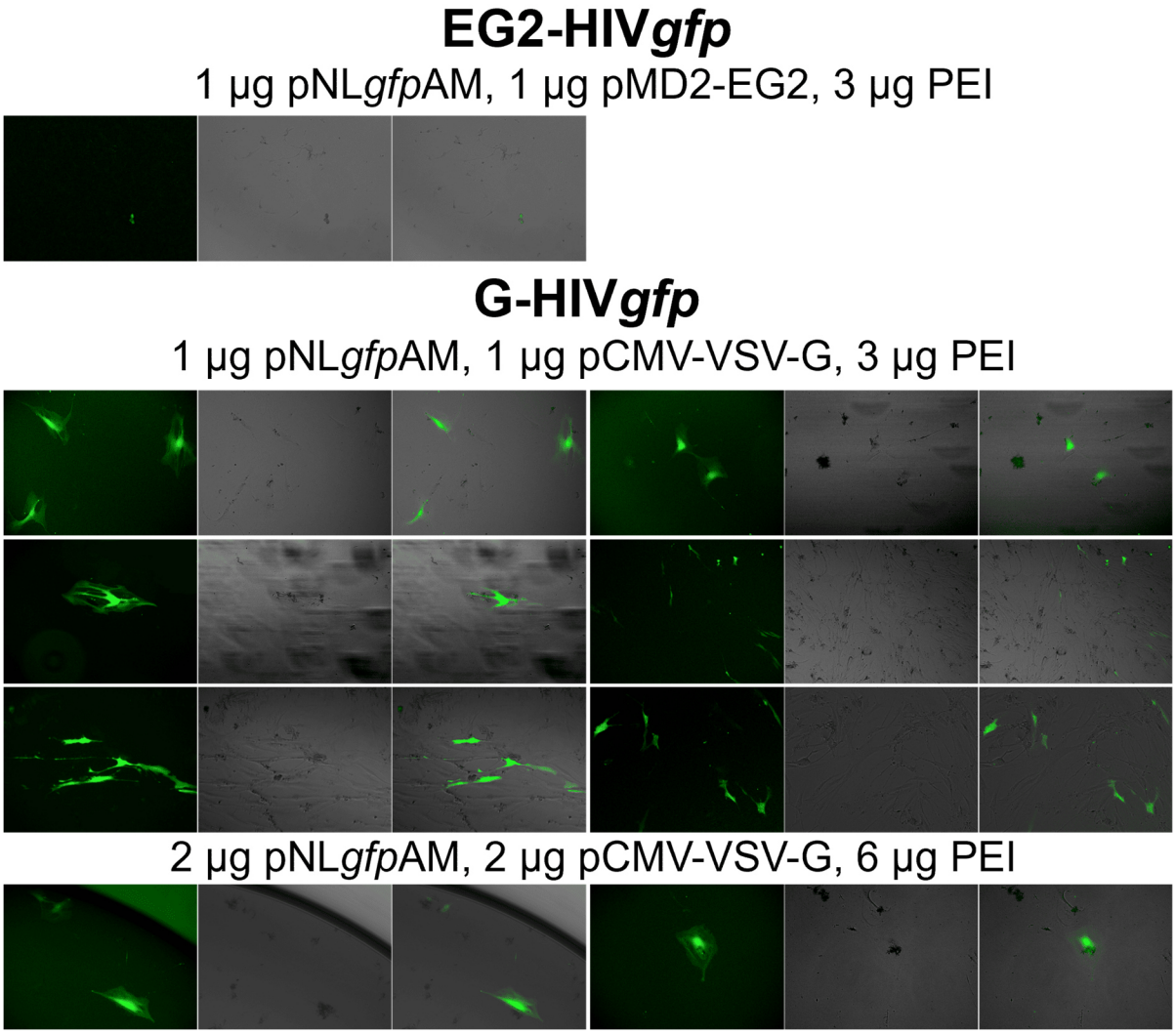

Fig. 63 AKH-23 cells infected with EG2-HIV*gfp* and G-HIV*gfp* pseudotyped viral particles. Infections are shown as picture triplets, left: GFP channel, middle: transmitted light, right: merged channels; cells were observed 72 h post-infection.

3.6.9. Infection of AKH-24C cells

AKH-24C cells were successfully infected with EG2-HIV*gfp* and G-HIV*gfp* (Fig. 64). EG2-HIV*gfp* infected two cells, while G-HIV*gfp* infected 19 cells. Since the tumor sample from AKH-24 was acquired at the end of the practical work, only a single round of infection could be performed.

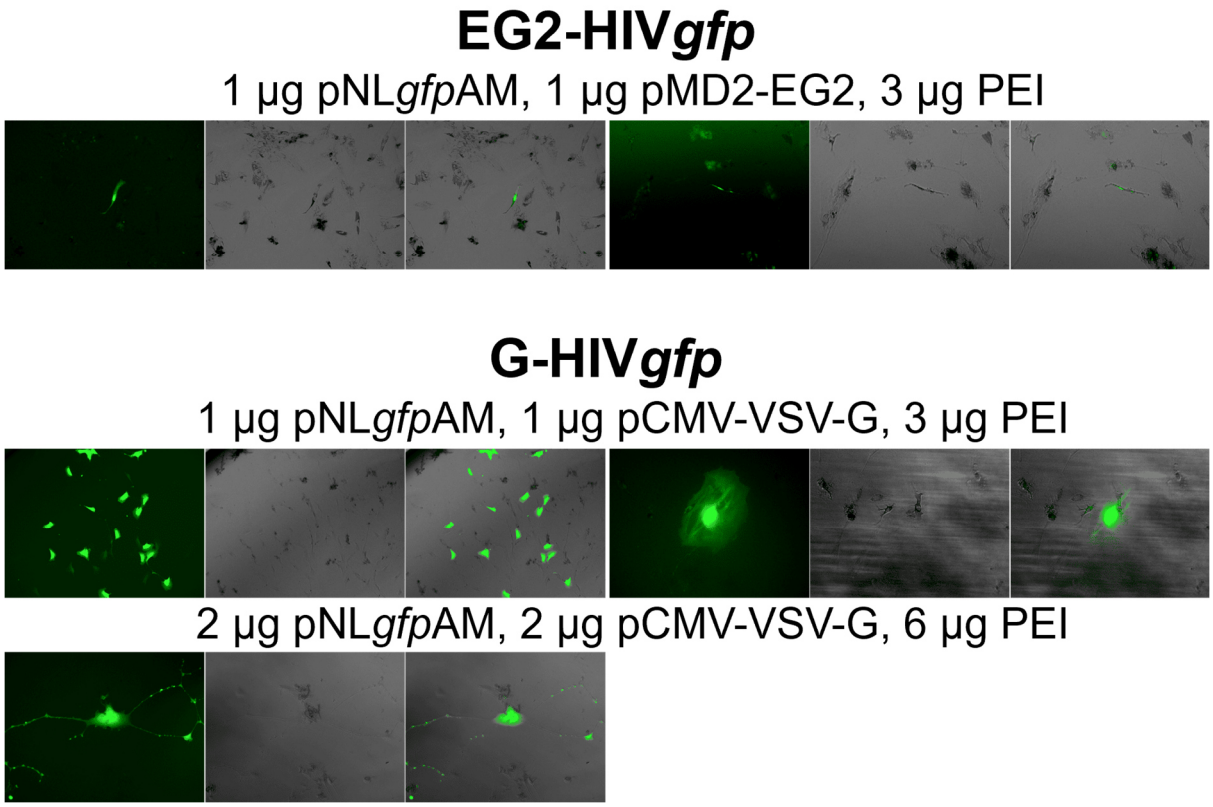

Fig. 64 AKH-24C cells infected with EG2-HIV*gfp* and G-HIV*gfp* pseudotyped viral particles. Infections are shown as picture triplets, left: GFP channel, middle: transmitted light, right: merged channels; cells were observed 72 h post-infection.

3.6.10. Infection of U-87 cells

U-87 cells could not be infected with either EG1-HIV*gfp* or EG2-HIV*gfp* but were successfully infected using G-HIV*gfp*(Fig. 65).

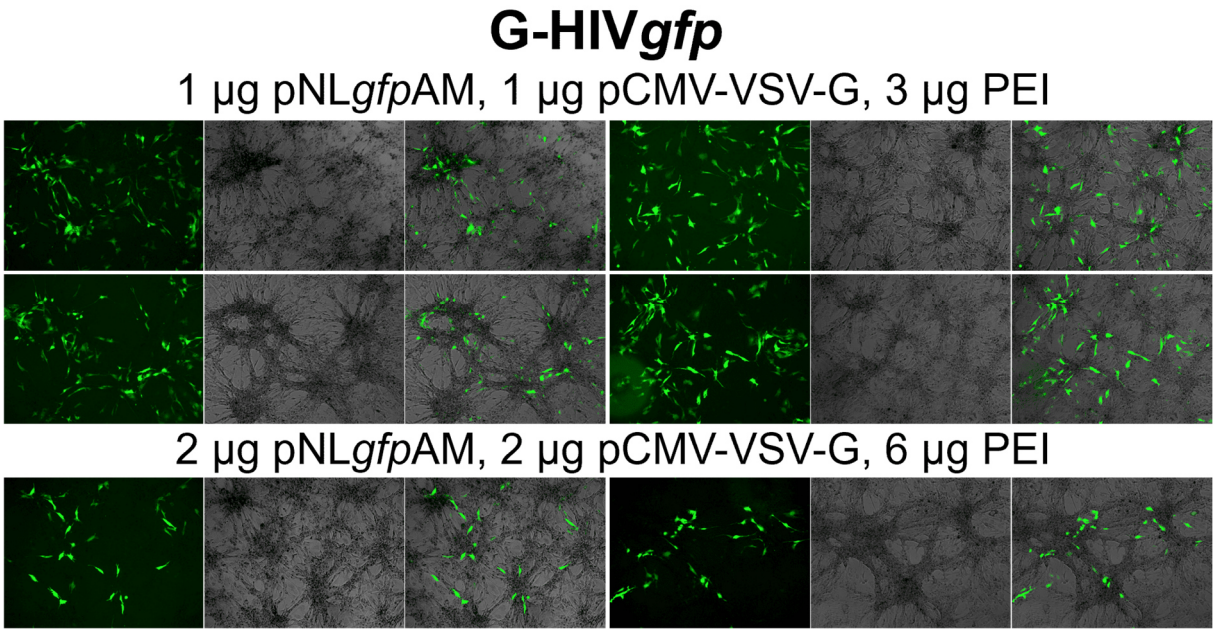

Fig. 65 U-87 cells infected with G-HIV*gfp* pseudotyped viral particles. Infections are shown as picture triplets, left: GFP channel, middle: transmitted light, right: merged channels; cells were observed 72 h post-infection.

3.7. Identification of integrin $\alpha_v\beta_5$ in primary glioblastoma cell cultures

Due to the heterogeneous expression of integrin $\alpha_v\beta_5$ observed on plastic surfaces, the detection was also performed on glass surfaces. The goal was to determine whether the expression of integrin $\alpha_v\beta_5$ is surface-dependent. For this purpose, six primary cell cultures (AKH-5, -9, -10, -11, -12, and -13) were grown on polytetrafluoroethylene (PTFE)-coated 12-well glass slides in CSF-DF medium over a period of 11 days. The glass slides were placed into Petri dishes and covered with 1 mL of a cell suspension, derived from a cell culture flask with at least 80% cell confluence (10 mL, T75, Cell+). To verify the expression of integrin $\alpha_v\beta_5$, fixed cells were first incubated with a primary integrin $\alpha_v\beta_5$-specific mouse antibody. Visualization was achieved using a secondary anti-mouse antibody conjugated with Alexa Fluor® 488 (green fluorescence). The results for cultures AKH-14 to -24 regarding integrin $\alpha_v\beta_5$ expression after 10 days of growth on glass, as well as integrin $\alpha_v\beta_5$ expression in cells grown on a plastic surface (96-well plate, Cell+), were previously presented in chapter 3.3.

As shown in Fig. 66, integrin $\alpha_v\beta_5$ was detected in all primary cell cultures, but the appearance of integrin $\alpha_v\beta_5^+$ cells varied over time. Two groups of AKH cell cultures were generally observed. The group with AKH-5, -9, and -12 exhibited delayed expression of integrin $\alpha_v\beta_5$, while in the other three cultures AKH-10, -11, and -13, integrin $\alpha_v\beta_5$ was detectable starting on day three.

For AKH-5, the first cells expressing integrin $\alpha_v\beta_5$ were found on day 9. Cells from culture AKH-9 started to express the protein on day 6, and integrin $\alpha_v\beta_5$ expression in AKH-12 cells was observed starting on day 7. In contrast, cultures AKH-10, -11, and -13 were observed to express integrin $\alpha_v\beta_5$ on the first day of observation.

The expression of $\alpha_v\beta_5$ was initially observed inside the nucleus. The longer the cells remained on glass, the more the expression was distributed along the surface of the imaged cells, accompanied by a decrease in nuclear expression. A more detailed overview of these experiments is provided in the appendix, which includes additional staining of cell nuclei and actin cytoskeletons (Fig. 67 to Fig. 72).

These results demonstrate the heterogeneity of GBM tumor cells with respect to integrin $\alpha_v\beta_5$ expression. This is particularly relevant for the infection of GSCs with ZIKV E pseudotypes since delayed expression of the ZIKV entry receptor integrin $\alpha_v\beta_5$ could hinder the successful transduction of tumor cells.

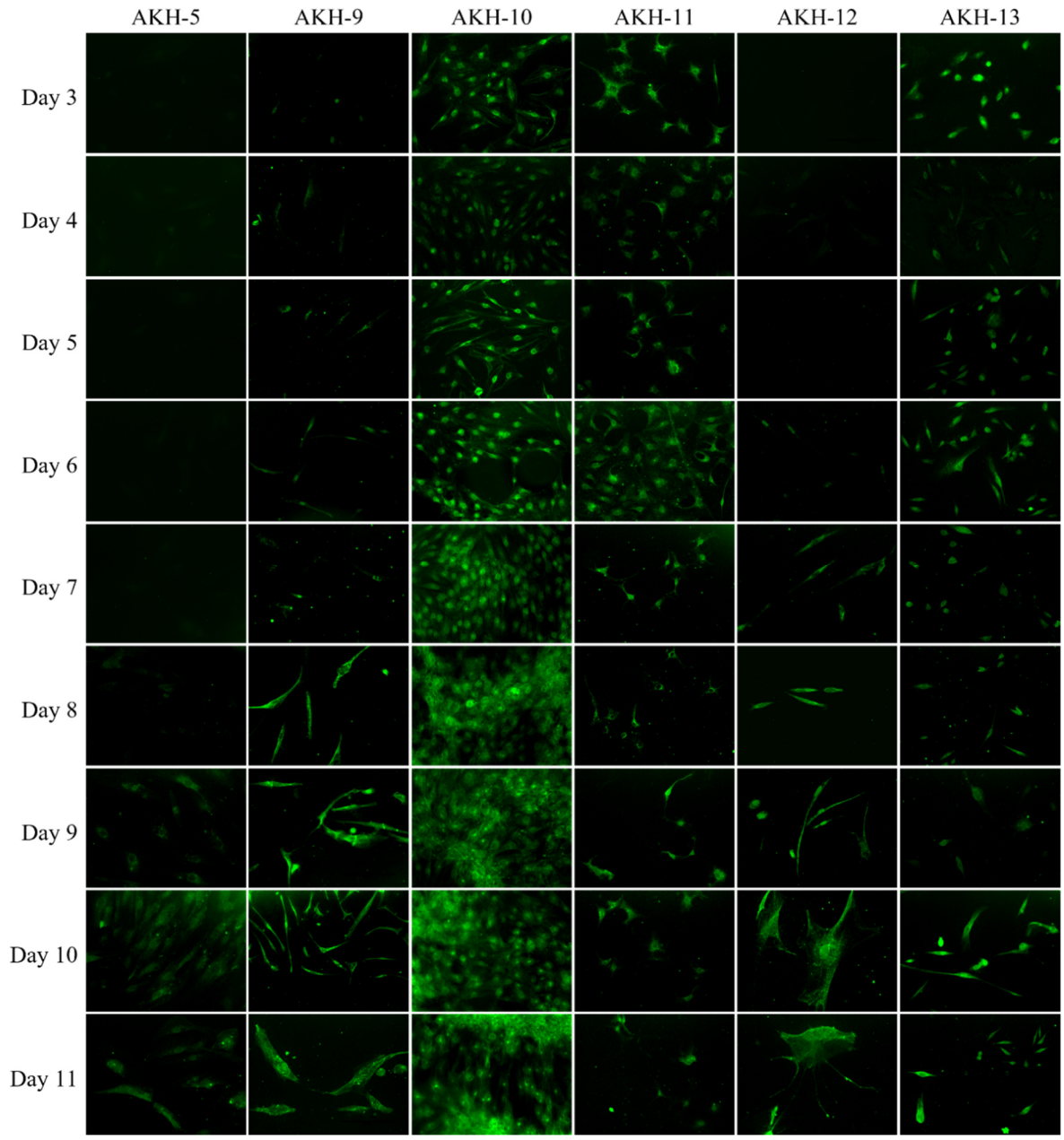

Fig. 66 Expression of integrin $\alpha_v\beta_5$ in different primary GBM cell cultures over time. Tumor cells were cultured on 12-well glass slides inside a Petri dish over a course of 11 days. 1 mL cell suspension was spread onto the glass wells and afterwards covered with culture medium CSF-DF. Integrin $\alpha_v\beta_5$ was stained using a mouse anti-integrin antibody (GFP, green) and the respective rabbit anti-mouse secondary antibody conjugated with Alexa Fluor® 488 (GFP, green). Images are presented at 20x magnification.

4. Discussion

4.1. Primary glioblastoma cell culture model

In this thesis, a cell culture model was developed to cultivate cells from tissue samples and establish primary cell cultures. Generating primary cell cultures from GBM specimens is essential for research purposes, particularly for developing lentiviral vectors (e.g., pseudotypes) to investigate disease mechanisms and explore new anti-GBM approaches. Compared to conventional laboratory-adapted GBM cell lines or GBM cells cultured over long periods, primary cultures more accurately reflect the *in vivo* situation of tumor cells. Currently, no standardized methods exist for the cultivation of GBM tumor cells[223]. The strategy in this study was based on the use of many different tumor samples, each cultured only for a limited period, to preserve the heterogeneity of the cell culture. It was particularly important to collect the tissue samples in such a way that stem cell-like cells could also be isolated, as these are thought to be the origin of GBM. Tissue samples taken near the subventricular zone (SVZ) were used for this purpose.

All primary cell cultures were established directly from patient tumor material and introduced to *in vitro* conditions within less than three hours post-surgery. This approach allows the establishment of a primary cell culture comprising both tumor and non-tumor cells from the tumor microenvironment (TME). Importantly, this facilitated the isolation of non-tumor cells, mostly immune cells, that adhere to the tumor cells and support their growth by producing growth factors. This support is only temporary, as the limited lifespan of non-tumor cells leads to their disappearance from the cultures after two to three weeks (Fig. 4 and Fig. 5).

At the start of the GBM treatment research conducted in the lab of Dr. Michael Schreiber, tissue samples were randomly collected from resected tumors[219]. In the present study, it is demonstrated that the sampling location significantly influences the establishment of a heterogeneous primary GBM cell culture. Specifically, obtaining tumor samples from areas adjacent to the SVZ, starting with AKH-14, offers the advantage of isolating a more heterogeneous population of tumor cells, including the isolation of glioblastoma stem cells (GSCs) and astrocyte-like GSCs. GSCs are thought to be the origin of GBM and therefore a prime target that has to be inactivated[70,71,76]. In primary cell cultures generated from SVZ tissue, the presence of $GFAP^+$ cells from AKH-14 onwards proves that the isolation of astrocyte-like GSCs was possible under the chosen culture conditions, while also preserving the heterogeneous composition of the cell culture. Due to the heterogeneity of GBM cells, four different tissue samples were collected from each tumor. This approach increased the likelihood

that at least one sample contained sufficient live material and no contamination. This type of sampling performed by the surgeon, combined with the sample processing in the laboratory, did not result in any contaminated cell cultures. Due to inherent differences between samples, the cultivation and cell passage conditions had to be adapted in a way that sufficient cell-cell contacts were maintained, thereby preventing extremely slow growth or loss of the culture. In total, 12 different primary cell cultures were established (AKH-14 to AKH-24C/S) using 48 different tumor samples from 10 patients.

In addition to the sampling location, the culture medium is an important factor to consider when establishing primary cell cultures. Generally, neurobasal media or DMEM are the most common choices for the *in vitro* cultivation of tumor cells[224]. Studies indicate that supplementing standard cell culture media with human cerebrospinal fluid (hCSF), or using hCSF as the sole medium, significantly enhances the proliferation and viability of GBM cells compared to conventional media such as DMEM with fetal bovine serum (FBS)[225]. The stimulating effect of hCSF is likely due to the presence of growth factors, nutrients, and signaling molecules in hCSF that are specifically adapted to the human brain[226,227]. Therefore, using hCSF ensures a physiologically more suitable environment for cultivating both tumor and non-tumor cells, making it a cell culture model that closely mimics *in vivo* conditions, particularly the *in vivo* context of GBM tumors. Moreover, hCSF-enriched media not only influence tumor cell proliferation but may also help preserve crucial cellular characteristics, such as stemness and invasive behavior, which are often lost under standard culture conditions[228]. These findings support the concept that incorporating hCSF can help maintain the clinical and biological relevance of primary GBM cultures.

Nonetheless, the use of human-derived cerebrospinal fluid (CSF) introduces variability due to donor differences and may be limited by availability and ethical considerations. Therefore, while hCSF represents a promising additive for GBM research, further studies are necessary to standardize its application and evaluate its effects on various GBM subpopulations. Within the scope of this work, the use of CSF-DF (DMEM/FBS + hCSF, 1:1) enabled the successful cultivation of all tumor samples, including the cultivation of cells with stem-like features.

It was evident that the cultivation of tumor samples from the SVZ allowed the isolation and preservation of astrocyte-like cells, resulting in more heterogeneous cell cultures. Additionally, by using CSF-DF as the culture medium, the primary cell cultures derived from SVZ samples maintained a heterogeneous composition for at least three months (Fig. 6). The preservation of heterogeneity of tumor cells was observed in every primary cell culture, potentially reflecting

the *in vivo* tumor composition. This represented an improvement over previously isolated cell cultures (AKH-1 to AKH-13), which showed no presence of $GFAP^+$ astrocytes and were largely homogeneous.[219]

The culture system also demonstrated that tumor cells developed a highly distinctive structural morphology, which is an important prerequisite for studying pseudotype infections, as tumor cell destruction can be easily monitored[220]. The primary cell cultures exhibited astrocytes and oligodendrocytes with prominent, elongated filopodia that established cell-to-cell contacts. These fine structures are disrupted by pseudotype infection, enabling clear observation of morphological changes within this 2D cell culture model[220].

This primary cell culture approach, however, relies on a consistent supply of new tumor samples, since primary cell cultures may adapt to *in vitro* culturing conditions over time and consequently lose their heterogeneity. This limitation was particularly evident in AKH-14 cells, which already exhibited more homogeneous morphologies compared to previous studies[195]. Therefore, in this study, primary cell cultures have generally not maintained for more than six months. In this context, the continuous provision of tumor samples by Dr. Dr. Birco Schwalbe, a neurosurgeon at the Asklepios Clinic Heidberg (Hamburg), was effectively coordinated. This was approved by the Ethical Commission of the Hamburg Medical Chamber under the registration number PV6041 and was of great help in conducting the research presented here.

Since GBM and its biology constitute a complex and heterogeneous system, the choice of an appropriate cell culture system should be guided by the specific scientific question. Although this system allows for the preservation of heterogeneity for up to six months, it is currently based on the presence of adherent tumor cells forming a two-dimensional (2D) network. In a 2D system, changes in the morphology of cells or the process of cell death can be more easily studied, as these changes are readily observable in individual cells. Conversely, three-dimensional (3D) approaches (e.g., neurospheres or organoids) may be better suited for the analysis of replication-competent viruses and for evaluating anti-tumor drugs in general[229–231]. However, studying pseudotype infections in a 3D system to assess if neurospheres are sensitive to lentiviral entry could be of interest, especially since the current cell culture system is restricted to the presence of adherent cells.

Considering these three aspects (tissue sampling, tumor microenvironment, and cell culture medium), it was possible to generate 2D primary cell cultures from GBM tumor samples. This enabled the observation of various kinds of cell structures and morphologies. Additionally, the

2D approach is a suitable model for studying cell destruction mediated by pseudotype lentiviruses.

4.2. Biomarker analysis of primary glioblastoma cell cultures

GBM frequently recurs near the original resection site, indicating that cells not eliminated by classical surgery are responsible for the inevitable relapse. GSCs are believed to be the origin of the GBM tumors and the main drivers of their recurrence[9]. Their resistance to conventional therapies such as radiation and chemotherapy, combined with their highly migratory and invasive nature, makes GSCs a primary target for research. However, due to the heterogeneous nature of GBM, the identification and isolation of GSCs remain challenging. In this regard, patient-derived GSC culture systems have become the preferred *in vitro* model for studying these cells, allowing molecular characterization through genotypic, transcriptomic, and epigenetic profiling[232].

The established primary cell culture system enabled the investigation of the heterogeneity of all AKH tumor cell cultures within the context of GSC and malignancy biomarkers. Following adaptation to the CSF-DF medium, all tumor cell cultures were comprehensively characterized and confirmed to express markers indicative of stemness, invasiveness, and other important GBM characteristics to varying degrees. The results demonstrate that cell cultures derived from random tissue sampling (AKH-5 to AKH-13) exhibited a more homogeneous cell composition, whereas those established from SVZ-derived samples (AKH-14 to AKH-24S/C) displayed a more heterogeneous cell population and marker expression. This was particularly evident by the presence of $GFAP^+$ astrocyte-like cells, which were found only in cultures derived from tissue samples taken adjacent to the SVZ.

GSCs are typically characterized by the expression of specific stem cell markers such as SOX2, OCT4, NANOG, and Nestin. However, no single marker can definitively identify all GSCs, and may only identify distinct cellular states rather than a single, unified subpopulation[233]. For example, among GSC surface markers, CD133 is most prominently expressed in oligodendrocyte precursor-like cells (OPCs), EGFR in astrocyte-like cells, and CD44 in mesenchymal-like cells (MSCs)[234]. These distinct GSC populations occupy different niches, highlighting the need for customized therapeutic strategies that target specific subsets within their unique microenvironments[235].

Subpopulations can be distinguished not only by specific marker expression but also by the subcellular localization of biomarkers. In this study, this observation was particularly evident

for the stem cell marker OCT4, whose localization varied across cell cultures and could be observed in both the cytoplasm and nucleus of tumor cells. In most cultures, OCT4 was expressed both inside the nucleus and the cytoplasm. However, in primary cultures AKH-5, -9, -10, and -11, OCT4 was predominantly localized to the nucleus, whereas cultures such as AKH-16 and AKH-20 showed almost no nuclear OCT4 signals. Most cell cultures exhibited OCT4 expression in both the nucleus and cytoplasm. Notably, cells from AKH-21S/C and AKH-24S/C displayed two distinct subpopulations, with OCT4 localized either exclusively to the nucleus or solely to the cytoplasm. These observations are supported by results from Lee *et al*., who demonstrated that the OCT4 isoforms OCT4A and OCT4B are localized to different cellular regions. OCT4A is found inside the nucleus, where it functions as a transcription factor, while OCT4B is mainly found in the cytoplasm[236]. This is further supported by results from Choi *et al.*, who reported that the OCT4B isoform of OCT4 is highly expressed in human GSCs and is mainly detected in the cytoplasm rather than the nucleus[237]. Collectively, these observations suggest that OCT4 localization correlates with the existence of distinct GSC subpopulations, as also demonstrated in this study.

However, the high number of potential GSC biomarkers and the existence of numerous GSC subpopulations, based on expression and localization, make a marker-specific targeting approach to combat GSCs nearly impossible. In contrast, the unique neurotropism of ZIKV enables specific targeting of all GSC subpopulations. This specificity has been shown to correlated with the expression of the stem cell marker SOX2 and integrin $\alpha_v\beta_5$[179]. Notably, SOX2 has been identified to be highly overexpressed in all primary cell cultures, indicating that all isolated tumor cells, particularly $SOX2^+$ astrocytes and oligodendrocytes, exhibit stem-like characteristics to some extent.

Based on the results shown in Table 24, each primary cell culture exhibited a distinct set of GSC subpopulations defined by the examined biomarkers. No two cultures displayed identical biomarker expression, and even if they did, the GSC subpopulations would still be different since they were derived from a different patient. Nonetheless, the stem cell markers SOX2, OCT4, and CD44 were highly upregulated in every cell culture, providing additional support that the primary cell culture system had the capability to isolate and sustain a high number of GBM tumor cells with stem-like properties. The elevated expression of stem cell markers NANOG and Nestin, along with the presence of $GFAP^+$ astrocyte-like GSCs in the cell cultures from AKH-14 onwards, further underscores these findings.

This study was limited by the number of tumor samples, which is due to the number of GBM tumors that were accessible during the cooperation with the Asklepios Clinic from 2021 to 2024. For a more definitive conclusion, a larger number of samples would need to be evaluated, which would also enhance the statistical significance of the results. It is important to note that the immunofluorescent staining performed in this study provided only qualitative information on biomarker expression.

In summary, the findings of this study indicate that GSCs, as the main drivers of tumor development, are present in the established primary cell cultures and can therefore serve as a basis for developing potential anti-tumor strategies.

4.3. ZIKV E pseudotypes as therapeutics against glioblastoma

The therapeutic genes

There are many strategies to target tumor cells. One approach involves the use of small interfering RNAs (siRNAs). siRNAs represent a recently discovered tool capable of silencing genes involved in cancer progression by inhibiting molecular pathways that promote tumor growth[238]. Most research on siRNAs in GBM therapy has focused on inhibiting pathways related to cancer cell progression and metastasis. Another powerful gene-editing technology that gaining interest for GBM treatment is the CRISPR-Cas9 system, which stands for Clustered Regularly Interspaced Short Palindromic Repeats and CRISPR-associated protein 9[239,240]. Due to its versatility, CRISPR-Cas9 is widely preferred for editing genes or genomes across various cancers, including GBM[241,242].

While both CRISPR-Cas9 and siRNAs offer high specificity and flexibility, they are limited by off-target effects, challenges in delivery efficiency, and, for siRNAs, their transient effects. Although CRISPR-Cas9 is a powerful gene-editing tool and siRNAs are effective for temporary gene silencing, both require efficient delivery into cells to function and cannot serve as gene transfer vectors themselves. Delivery methods such as functionalized nanoparticles or liposomes have been explored, but they lack cell specificity, so they do not effectively eliminate off-target effects and are mostly suitable only for *ex vivo* applications. These delivery particles also have limited cargo capacity, which is particularly important for the CRISPR-Cas9 system. To overcome these issues, artificially designed lentiviral vectors provide a versatile platform, offering sufficient space for genetic material required by both CRISPR-Cas9 and siRNA approaches, as well as enabling stable integration for long-term gene modulation.

However, practical considerations also influence vector design. Recent studies indicate that some stem cells are sensitive to the expression of fluorescent proteins like mCherry and GFP. Notably, it has been reported that mouse embryonic fibroblasts and baby hamster renal fibroblasts are highly sensitive to GFP expression, which can induce apoptosis and lead to loss of structural integrity[243]. These findings are consistent with results obtained in the Schreiber laboratory[220]. However, in the present study, no such effects were observed three days post-infection, underscoring the importance of careful vector design and controlled expression conditions for successful application in sensitive cell populations.

The gene transfer tool

Therapeutic genes must be delivered to cells via vectors. Lentiviral vectors allow an efficient transduction, since lentiviruses can transfer genetic material into both non-dividing and dividing cells, while also offering a much larger cargo capacity compared to other viral vectors[244]. This allows them to carry and transfer larger therapeutic genes. Thus, pseudotyping provides a platform to design viral transfer vectors to specifically target a certain type of cell, significantly reducing off-target effects. Pseudotyping allows the generation of viral particles, in which the original surface protein is replaced by an envelope protein from a different virus, which can either restrict or broaden the tropism of the pseudotype. The construction of pseudotypes is mainly based on lentiviruses (HIV-1), retroviruses, and rabies viruses (e.g., vesicular stomatitis virus, VSV). In this study, the tropism of pseudotyped viral particles was modified to specifically target grade 4 GBM tumor cells, preferentially GSCs[195,216,220].

The envelope protein from VSV (VSV-G) is well-suited for pseudotyping. In terms of preparation, VSV-G is stable and can withstand ultracentrifugation, achieving high viral titers, both allowing VSV-G to efficiently transduce stem cells and neurons[245,246]. However, the broad tropism of VSV-G can be undesirable for *in vivo* studies, since it can bind to and transduce many cell types before reaching the target cells, giving it the potential for off-target infectivity[247]. VSV-G enables viral entry by allowing the virus to attach to a low-density lipoprotein receptor (LDLR) or a member of the LDLR family. LDLR receptors are expressed on all human host cells[210]. The widespread expression of LDLR family members is responsible for the pantropism of VSV-G pseudotypes, which is why VSV-G-pseudotyped viral vectors are so useful for *ex vivo* gene transduction in a variety of cells. VSV-G pseudotyped lentiviral vectors have shown significant *ex vivo* use as transfer vectors in the chimeric antigen receptor (CAR) T cell therapy. CAR-T therapy is an *ex vivo* approach in which T cells are genetically engineered to produce CARs, which allow the cells to recognize and attack cancer cells more

effectively upon being returned to the patient. Although it has been approved for treating several types of cancer, CAR-T therapy still faces significant challenges in treating solid tumors[248].

The assembly problem

Efficient assembly and budding at the cell membrane are necessary for the generation of lentiviral vectors. However, since the flavivirus envelope proteins (e.g., ZIKV) assemble at the ER rather than the cell membrane, this process presents a major challenge. For efficient assembly, the E protein and the HIV-1 proteins Gag and Gag-Pol must to be localized together at the cell membrane. This is difficult because HIV-1 naturally assembles at the cell membrane, while ZIKV assembles at the ER membrane. Previous studies have addresses this issue by replacing the TM^{E} with the $TMCY^{gp41}$ region of the HIV-1 gp41 protein[195]. Furthermore, the E-ΔTM^{E}-$TMCY^{gp41}$ pseudotype yielded significantly better transduction than the VSV-G pseudotype[220].

Another approach involves exchanging TM^{E} for the transmembrane region of the VSV-G envelope protein. The pseudotypes EG1- HIV*gfp* and EG2-HIV*gfp* were generated using E-ΔTM^{E}-TM^{VSV}, designated EG1 and EG2. This strategy was based on the results of Liu *et al*., who demonstrated that exchanging TM^{E} for TM^{VSV} resulted in an E-ΔTM^{E}-TM^{VSV} pseudotype with a transduction rate 100 times higher than that of VSV-G pseudotypes in mouse kidney cells[221]. EG1- and EG2-HIV*gfp* pseudotypes generally infected cells from all primary AKH tumor cultures except AKH-15 and -16. However, G-HIV*gfp* pseudotypes infected all primary cell cultures and U-87 cells. However, none of these pseudotypes infected cell cultures AKH-18 and AKH-24C. In summary, exchanging TM^{E} for TM^{VSV} in designing EG1- and EG2-HIV*gfp* led to pseudotyped particles that could infect primary GBM tumor cells, though they did not demonstrate a significantly higher transduction rate than G-HIV*gfp*. Like HIV-1, VSV is formed at the outer cell membrane. However, compared to other designed pseudotypes such as E41.2-HIV*gfp* (with TM^{E} replaced by gp41 $TMCY^{gp41}$)[195], E-TM^{VSV} bearing pseudotypes lack the PTAP amino acid motif found in the HIV-1 p6 protein, which binds to the gp41 CY region of the HIV-1 Gag protein. The PTAP motif links the viral budding complex to the TSG101 protein, which is part of a multiprotein complex called the endosomal sorting complex required for transport (ESCRT)[249]. E41.2-HIV*gfp* showed significantly higher transduction rates than G-HIV*gfp* and could efficiently kill primary GBM tumor cells *in vitro*[195,220]. Additionally, it was shown that E41.2-HIV*gfp* did not target healthy brain cells (AKH-22)[220]. While the EG1-HIV*gfp* and EG2-HIV*gfp* pseudotypes with TM^{VSV} demonstrated potential for infecting GBM tumor cells in this study, the results suggest that the TMCY of gp41 is a more

suitable TM^E replacement[220]. These modifications resolved the assembly issue by enabling the transport of the E protein to the cell membrane. This was accomplished by constructing pseudotyped lentiviral particles that connected the ZIKV E protein connected to the gp41 TMCY region of HIV-1.

Specificity of the ZIKV E pseudotype

The ZIKV/HIV-1 chimera specifically targets GBM tumor cells, particularly GSCs, through the ZIKV E protein and its ED3 receptor-binding domain. ZIKV hijacks cells via the AXL/Gas6 and integrin $\alpha_v\beta_5$ receptor molecules, both of which were verified to be highly expressed in all primary GBM cell cultures used in this study. ZIKV exhibits differential neurotropic effects on normal neural tissue and GBM cells, preferentially infecting and killing GSCs while sparing differentiated tumor progeny and normal neuronal cells[177]. ZIKV targets neural stem cells (NSCs), neural progenitor cells (NPCs), astrocytes, and microglia, inducing apoptosis and cell cycle dysregulation[250]. Recent *in vitro* experiments using the GBM cell lines U-138 and U-251 demonstrated that ZIKV infection reduces cell viability, increases apoptosis rates, and enhances cell adhesion[251]. *In vivo* studies using mouse models showed improved survival rates when GBM cells were inoculated with a mouse-adapted ZIKV strain[177], while another study using a ZIKV live-attenuated virus (ZIKV-LAV) vaccine candidate showed efficacy in selectively killing GSCs within tumors[193]. Although ZIKV shows promise as an oncolytic agent targeting GSCs in preclinical models, more research is needed to understand its mechanisms and initiate clinical trials. For example, immune profiling revealed differences between tumor characteristics in GBM-positive mice and tumor characteristics as shown in primary patient-derived samples. This demonstrates that *in vivo* results from an animal model cannot easily be transferred to a human model[252]. To address this issue, researchers propose implementing a full clinical standard in preclinical GBM research, which could potentially improve future approaches[253].

No clear correlation was observed between the number of infected cells and the expression of ZIKV entry receptors AXL/Gas6 and integrin $\alpha_v\beta_5$. AXL has been identified as a key cell surface receptor for ZIKV entry *in vitro*. It is highly expressed in astrocytes, endothelial cells, microglia, and human radial glial cells in the developing human cortex[148,165,168]. However, recent studies have shown that AXL is not essential for ZIKV infection. Li *et al*. generated AXL-deficient mice ($AXL^{-/-}$) and infected them with ZIKV. The virus was detected in the brains of all $AXL^{-/-}$ mice. Compared to healthy mice ($AXL^{+/+}$), no difference in virus titer was observed[254]. Similar results were observed by Wang *et al.*, who demonstrated that AXL^- mice

were infected by ZIKV with no difference compared to AXL^+ mice[255]. Furthermore, genetic ablation of AXL does not protect human NPCs from ZIKV infection[256]. These results suggest that AXL might not play an essential role in ZIKV infections of the mouse brain, if any. Other receptors, such as Tyro3 and Mertk (both belonging to the same family as AXL), have also been shown not to be unnecessary for ZIKV infection of mice[257]. Additionally, since all these studies used live virus strains, their results cannot be directly translated into *in vivo* treatment, since the virus replicates within the organism, which could lead to further complications. Unlike live viruses, lentiviral pseudotypes do not replicate after infection, providing a significant advantage for safe *in vivo* application.

There are currently no clinical trials investigating the use of ZIKV as an oncolytic virus therapy. All ZIKV-related research in GBM remains at the preclinical stage. This is likely due to several important issues that still need to be addressed to ensure the safe and effective use of ZIKV. These issues include controlling the virus, determining its persistence in the body, assessing the risk of inflammation in the CNS, and developing strategies to prevent relapse. However, a phase 1 clinical trial (NCT05123222) of the first study that used a controlled human infection model for ZIKV has recently been completed[258]. This trial evaluated the effects of different doses of two ZIKV strains on clinical and virologic responses in healthy adult volunteers. Data from this trial will contribute to the development and evaluation of ZIKV vaccines in later phases of clinical trials. Notably, the results of this study will provide valuable information regarding the appropriate ZIKV doses and their potential impact on various tumor cell types.

5. Outlook

The main challenge in oncolytic virus therapy is efficiently delivering the necessary genetic material to enough target cells while minimizing transduction of non-target cells. This requires designing gene transfer vectors with optimal specificity for the intended cell type. Lentiviral vectors coated with the ZIKV envelope are particularly effective at targeting GBM cells because they exhibit a strong preference for these tumor cells.

Immunostaining of the biomarkers revealed specific GSC subpopulations in every primary cell culture. However, because this method is qualitative for each specific marker, further studies should focus on quantifying biomarker expression to strengthen the results of this thesis.

The ZIKV/VSV chimera was able to infect primary GBM tumor cells but not very efficiently. Further studies could investigate the transmembrane regions of other viruses that bud at the cell surface. Since the ZIKV/HIV-1 chimera has proven to be highly efficient in infecting stem-like cells, this approach should be explored further.

Future infection and characterization studies will require additional GBM tumor samples as well as healthy brain cells to demonstrate that the ZIKV E pseudotyped particles are harmless to healthy cells.

6. Bibliography

1. Miller, K. D. *et al.* Brain and Other Central Nervous System Tumor Statistics, 2021. *CA. Cancer J. Clin.* **71**, 381–406 (2021).

2. Louis, D. N. *et al.* The 2021 WHO Classification of Tumors of the Central Nervous System: a summary. *Neuro. Oncol.* **23**, 1231–1251 (2021).

3. Szopa, W., Burley, T. A., Kramer-Marek, G. & Kaspera, W. Diagnostic and Therapeutic Biomarkers in Glioblastoma : Current Status and Future Perspectives. *Biomed Res. Int.* **2017**, (2017).

4. Idbaih, A. *et al.* Effect of Tumor-Treating Fields Plus Maintenance Temozolomide vs Maintenance Temozolomide Alone on Survival in Patients With Glioblastoma: A Randomized Clinical Trial. *J. Am. Med. Assoc.* **318**, 2306–2316 (2017).

5. Weller, M. *et al.* EANO guidelines on the diagnosis and treatment of diffuse gliomas of adulthood. *Nat. Rev. Clin. Oncol.* **18**, 170–186 (2021).

6. Tan, A. C. *et al.* Management of Glioblastoma: State of the Art and Future Directions. *CA. Cancer J. Clin.* **70**, 299–312 (2020).

7. Lim, M., Xia, Y., Bettegowda, C. & Weller, M. Current state of immunotherapy for glioblastoma. *Nat. Rev. Clin. Oncol.* **15**, 422–442 (2018).

8. Yang, C. *et al.* Slow-Cycling Cells in Glioblastoma : A Specific Population in the Cellular Mosaic of Cancer Stem Cells. *Cancers (Basel).* **14**, 1–18 (2022).

9. Lathia, J. D., Mack, S. C., Mulkearns-Hubert, E. E., Valentim, C. L. L. & Rich, J. N. Cancer stem cells in glioblastoma. *Genes Dev.* **29**, 1203–1217 (2015).

10. Liu, C. *et al.* Mosaic Analysis with Double Markers Reveals Tumor Cell of Origin in Glioma. *Cell* **146**, 209–221 (2011).

11. Llaguno, S. A. *et al.* Article Malignant Astrocytomas Originate from Neural Stem / Progenitor Cells in a Somatic Tumor Suppressor Mouse Model. *Cancer Cell* **15**, 45–56 (2009).

12. He, J., Liu, Y. & Lubman, D. M. Targeting Glioblastoma Stem Cells : Cell Surface Markers. *Curr. Med. Chem.* **19**, 6050–6055 (2012).

13. Kalkan, R. Glioblastoma Stem Cells as a New Therapeutic Target for Glioblastoma. *Clin.*

Med. Insights **9**, 95–103 (2015).

14. Sahoo, O. S., Mitra, R. & Nagaiah, N. K. H. The hidden architects of glioblastoma multiforme: Glioma stem cells. *MedComm - Oncol.* **3**, (2024).

15. Hanahan, D. Hallmarks of Cancer : New Dimensions. *Cancer Discov.* **12**, 31–46 (2022).

16. Florian, A. I. *et al.* The Roles of miRNA in Glioblastoma Tumor Cell Communication: Diplomatic and Aggressive Negotiations. *Int. J. Mol. Sci.* **21**, 1950 (2020).

17. Qazi, M. A. *et al.* Intratumoral heterogeneity: pathways to treatment resistance and relapse in human glioblastoma. *Ann. Oncol.* **28**, 1448–1456 (2017).

18. Vendramin, R., Litchfield, K. & Swanton, C. Cancer evolution: Darwin and beyond. *EMBO J.* **40**, e108389 (2021).

19. Meyer, M. *et al.* Single cell-derived clonal analysis of human glioblastoma links functional and genomic heterogeneity. *Proc. Natl. Acad. Sci.* **112**, 851–856 (2015).

20. Segerman, A. *et al.* Clonal Variation in Drug and Radiation Response among Glioma-Initiating Cells Is Linked to Proneural-Mesenchymal Transition. *Cell Rep.* **17**, 2994–3009 (2016).

21. Patel, A. P. *et al.* Single-cell RNA-seq highlights intratumoral heterogeneity in primary glioblastoma. *Science* **344**, 1396–1401 (2014).

22. Sottoriva, A. *et al.* Intratumor heterogeneity in human glioblastoma reflects cancer evolutionary dynamics. *Proc. Natl. Acad. Sci.* **110**, 4009–14 (2013).

23. Snuderl, M. *et al.* Mosaic Amplification of Multiple Receptor Tyrosine Kinase Genes in Glioblastoma. *Cancer Cell* **20**, 810–817 (2011).

24. Szerlip, N. J. *et al.* Intratumoral heterogeneity of receptor tyrosine kinases EGFR and PDGFRA amplification in glioblastoma defines subpopulations with distinct growth factor response. *Proc. Natl. Acad. Sci.* **109**, 3041–3046 (2012).

25. Marine, J.-C., Dawson, S.-J. & Dawson, M. A. Non-genetic mechanisms of therapeutic resistance in cancer. *Nat. Rev. Cancer* **20**, 743–756 (2020).

26. Neftel, C. *et al.* An Integrative Model of Cellular States, Plasticity, and Genetics for Glioblastoma. *Cell* **178**, 835–849 (2019).

27. Wang, Q. *et al.* Tumor Evolution of Glioma-Intrinsic Gene Expression Subtypes

Associates with Immunological Changes in the Microenvironment. *Cancer Cell* **10**, 42–56 (2017).

28. Herrera-Oropeza, G. E. *et al.* Glioblastoma multiforme: a multi-omics analysis of driver genes and tumour heterogeneity. *Interface Focus* **11**, (2021).

29. Couturier, C. P. *et al.* Single-cell RNA-seq reveals that glioblastoma recapitulates a normal neurodevelopmental hierarchy. *Nat. Commun.* **11**, 4041 (2020).

30. Gulaia, V. *et al.* Single-nucleus transcriptomics of IDH1- and TP53- mutant glioma stem cells displays diversified commitment on invasive cancer progenitors. *Sci. Rep.* **12**, (2022).

31. Bhaduri, A. *et al.* Outer Radial Glia-like Cancer Stem Cells Contribute to Heterogeneity of Glioblastoma Article Outer Radial Glia-like Cancer Stem Cells Contribute to Heterogeneity of Glioblastoma. *Cell Stem Cell* **26**, 48–63 (2020).

32. Vinel, C. *et al.* Comparative epigenetic analysis of tumour initiating cells and syngeneic EPSC-derived neural stem cells in glioblastoma. *Nat. Commun.* **12**, 6130 (2021).

33. Duhamel, M. *et al.* Spatial analysis of the glioblastoma proteome reveals specific molecular signatures and markers of survival. *Nat. Commun.* **13**, (2022).

34. Dirkse, A. *et al.* Stem cell-associated heterogeneity in Glioblastoma results from intrinsic tumor plasticity shaped by the microenvironment. *Nat. Commun.* **10**, (2019).

35. Hambardzumyan, D. & Bergers, G. Glioblastoma: Defining Tumor Niches. *Trends in Cancer* **1**, 252–265 (2015).

36. Caruso, J. P. *et al.* pH, Lactate, and Hypoxia: Reciprocity in Regulating High-Affinity Monocarboxylate Transporter Expression in Glioblastoma. *Neoplasia* **19**, 121–134 (2017).

37. Rampling, R., Cruickshank, G., Lewis, A. D., Fitzsimmons, S. A. & Workman, P. Direct Measurement of pO2 Distribution and Bioreductive Enzymes in Human Malignant Brain Tumors. *Int. J. Radiat. Oncol. Biol. Phys.* **29**, 427–431 (1994).

38. Noman, M. Z. *et al.* Improving Cancer Immunotherapy by Targeting the Hypoxic Tumor Microenvironment: New Opportunities and Challenges. *Cells* **8**, 1083 (2019).

39. Chouaib, S., Noman, M., Kosmatopoulos, K. & Curran, M. Hypoxic stress: obstacles

and opportunities for innovative immunotherapy of cancer. *Oncogene* **36**, 439–445 (2018).

40. Evans, S. M. *et al.* The Relationship among Hypoxia, Proliferation, and Outcome in Patients with De Novo Glioblastoma: A Pilot Study. *Transl. Oncol.* **3**, 160–169 (2010).

41. Seidel, S. *et al.* A hypoxic niche regulates glioblastoma stem cells through hypoxia inducible factor 2*α*. *Brain* **133**, 983–995 (2010).

42. Li, Z. *et al.* Hypoxia-Inducible Factors Regulate Tumorigenic Capacity of Glioma Stem Cells. *Cancer Cell* **15**, 501–513 (2010).

43. Soeda, A. *et al.* Hypoxia promotes expansion of the CD133-positive glioma stem cells through activation of HIF-1alpha. *Oncogene* **28**, 3949–3959 (2009).

44. McCord, A. M. *et al.* Physiologic Oxygen Concentration Enhances the Stem-Like Properties of CD133 + Human Glioblastoma Cells In vitro. *Mol. Cancer Res.* **7**, 489–497 (2009).

45. Folkins, C. *et al.* Glioma Tumor Stem-Like Cells Promote Tumor Angiogenesis and Vasculogenesis via Vascular Endothelial Growth Factor and Stromal-Derived Factor 1. *Cancer Res.* **6**, 7243–7251 (2009).

46. Soda, Y. *et al.* Transdifferentiation of glioblastoma cells into vascular endothelial cells. *Proc. Natl. Acad. Sci.* **108**, 4274–4280 (2011).

47. Bar, E. E., Lin, A., Mahairaki, V., Matsui, W. & Eberhart, C. G. Hypoxia Increases the Expression of Stem-Cell Markers and Promotes Clonogenicity in Glioblastoma Neurospheres. *Am. J. Pathol.* **177**, 1491–1502 (2010).

48. Becher, O. J. *et al.* Gli activity correlates with tumor grade in platelet-derived growth factor-induced gliomas. *Cancer Res.* **68**, 2241–2249 (2008).

49. Calabrese, C. *et al.* A Perivascular Niche for Brain Tumor Stem Cells. *Cancer Cell* **11**, 69–82 (2007).

50. Bao, S. *et al.* Stem Cell–like Glioma Cells Promote Tumor Angiogenesis through Vascular Endothelial Growth Factor. *Cancer Res* **66**, 7843–7848 (2006).

51. Zhu, X. *et al.* Interaction of tumor-associated microglia / macrophages and cancer stem cells in glioma. *Life Sci.* **320**, 121558 (2023).

52. Hu, B. *et al.* Epigenetic Activation of WNT5A Drives Glioblastoma Stem Cell Differentiation and Invasive Growth. *Cell* **167**, 1281-1295.e18 (2016).

53. Westphal, M. & Lamszus, K. The neurobiology of gliomas: from cell biology to the development of therapeutic approaches. *Nat. Rev. Neurosci.* **12**, 495–508 (2011).

54. Reemst, K., Noctor, S. C., Lucassen, P. J., Hol, E. M. & Nolan, Y. The Indispensable Roles of Microglia and Astrocytes during Brain Development. **10**, 1–28 (2016).

55. Sofroniew, M. V. Astrogliosis. *Cold Spring Harb Perspect Biol* **7**, a020420 (2015).

56. Kim, J. *et al.* Tumoral RANKL activates astrocytes that promote glioma cell invasion through cytokine signaling. *Cancer Lett.* **353**, 194–200 (2014).

57. Oushy, S. *et al.* Glioblastoma multiforme-derived extracellular vesicles drive normal astrocytes towards a tumour-enhancing phenotype. *Philos Trans R Soc L. B Biol Sci.* **373**, 20160477 (2017).

58. Le, D. M. *et al.* Exploitation of Astrocytes by Glioma Cells to Facilitate Invasiveness : A Mechanism Involving Matrix Metalloproteinase-2 and the Urokinase-Type Plasminogen Activator – Plasmin Cascade. *J. Neurosci.* **23**, 4034–4043 (2003).

59. Jin, P., Shin, S., Chun, Y. & Shin, H. Astrocyte-derived CCL20 reinforces HIF-1-mediated hypoxic responses in glioblastoma by stimulating the CCR6-NF- κ B signaling pathway. *Oncogene* **37**, 3070–3087 (2018).

60. Biasoli, D. *et al.* Glioblastoma cells inhibit astrocytic p53-expression favoring cancer malignancy. *Oncogenesis* **3**, e123 (2014).

61. Oliveira, A. I. *et al.* Crosstalk between glial and glioblastoma cells triggers the "go-or-grow" phenotype of tumor cells. *Cell Commun. Signal.* **15**, 1–12 (2017).

62. Chen, W., Wang, D., Du, X., He, Y. & Chen, S. Glioma cells escaped from cytotoxicity of temozolomide and vincristine by communicating with human astrocytes. *Med Oncol.* **32**, (2015).

63. Lin, Q. *et al.* Reactive Astrocytes Protect Melanoma Cells from Chemotherapy by Sequestering Intracellular Calcium through Gap Junction Communication Channels. *Neoplasia* **12**, 748–754 (2010).

64. Castillo, M. Stem Cells, Radial Glial Cells, and a Unified Origin of Brain Tumors. *AJNR*

Am J Neuroradiol **31**, 389–390 (2010).

65. Pilkington, G. J. Cancer stem cells in the mammalian central nervous system. *Cell Prolif.* **38**, 423–433 (2005).

66. Vescovi, A. L., Galli, R. & Reynolds, B. A. Brain tumour stem cells. *Nat. Rev. Cancer* **6**, 425–436 (2006).

67. Sanai, N. *et al.* Cellular Composition and Cytoarchitecture of the Adult Human Subventricular Zone: A Niche of Neural Stem Cells. *J. Comp. Neurol.* **494**, 415–434 (2006).

68. Okano, H. & Temple, S. Cell types to order: temporal specification of CNS stem cells. *Curr. Opin. Neurobiol.* **19**, 112–119 (2009).

69. Loras, A., Gonzalez-Bonet, L. G., Gutierrez-Arroyo, J. L., Martinez-Cadenas, C. & Marques-Torrejon, M. A. Neural Stem Cells as Potential Glioblastoma Cells of Origin. *Life* **13**, 1–13 (2023).

70. Matarredona, E. R. & Pastor, A. M. Neural Stem Cells of the Subventricular Zone as the Origin of Human Glioblastoma Stem Cells. Therapeutic Implications. *Front. Oncol.* **9**, (2019).

71. Lee, J. H. *et al.* Human glioblastoma arises from subventricular zone cells with low-level driver mutations. *Nature* **560**, 243–247 (2018).

72. Bakhshinyan, D., Savage, N., Salim, S. K., Venugopal, C. & Singh, S. K. The Strange Case of Jekyll and Hyde: Parallels Between Neural Stem Cells and Glioblastoma-Initiating Cells. *Front. Oncol.* **10**, 603738 (2021).

73. Brockman, A. A., Mobley, B. C. & Ihrie, R. A. Histological Studies of the Ventricular–Subventricular Zone as Neural Stem Cell and Glioma Stem Cell Niche. *J. Histochem. Cytochem.* **69**, 819–834 (2021).

74. Jiang, H. *et al.* Classification of Progression Patterns in Glioblastoma: Analysis of Predictive Factors and Clinical Implications. *Front. Oncol.* **10**, 590648 (2020).

75. Lim, D. A. *et al.* Relationship of glioblastoma multiforme to neural stem cell regions predicts invasive and multifocal tumor phenotype. *Neuro. Oncol.* **4**, 424–429 (2007).

76. Beiriger, J. *et al.* The Subventricular Zone in Glioblastoma: Genesis, Maintenance, and

Modeling. *Front. Oncol.* **12**, 790976 (2022).

77. Gopal, K. *et al.* Oxidative stress induces the acquisition of cancer stem-like phenotype in breast cancer detectable by using a Sox2 regulatory region-2 (SRR2) reporter. *Oncotarget* **7**, 3111–3127 (2015).

78. Ren, Z.-H., Zhang, C.-P. & Ji, T. Expression of SOX2 in oral squamous cell carcinoma and the association with lymph node metastasis (Review). *Oncol. Lett.* **11**, 1973–1979 (2016).

79. Alonso, M. M. *et al.* Genetic and Epigenetic Modifications of Sox2 Contribute to the Invasive Phenotype of Malignant Gliomas. *PLoS One* **6**, e26740 (2011).

80. Vasquez, J. C. *et al.* SOX2 immunity and tissue resident memory in children and young adults with glioma. *J. Neurooncol.* **134**, 41–53 (2017).

81. Garros-Regulez, L., Aldaz, P., Arrizabalaga, O., Moncho-Amor, V. & Carrasco-Garcia, E. mTOR inhibition decreases SOX2-SOX9 mediated glioma stem cell activity and temozolomide resistance. *Expert Opin. Ther. Targets* **20**, 393–405 (2016).

82. Berezovsky, A. D. *et al.* Sox2 Promotes Malignancy in Glioblastoma by Regulating Plasticity and Astrocytic Differentiation. *Neoplasia* **16**, 193-206.e25 (2014).

83. Oppel, F. *et al.* SOX2-RNAi attenuates S-phase entry and induces RhoA-dependent switch to protease-independent amoeboid migration in human glioma cells. *Mol. Cancer* **10**, (2011).

84. Dehcordi, S. R. *et al.* Stemness Marker Detection in the Periphery of Glioblastoma and Ability of Glioblastoma to Generate Glioma Stem Cells: Clinical Correlations. *World Neurosurg.* **105**, 895–905 (2017).

85. Hattermann, K. *et al.* Stem cell markers in glioma progression and recurrence. *Int. J. Oncol.* **49**, 1899–1910 (2016).

86. Choi, S., Kim, J., Jeon, H., Eun, K. & Kim, H. Molecules and Cells OCT4B Isoform Promotes Anchorage-Independent Growth of Glioblastoma Cells. *Mol. Cells* **42**, 135–142 (2019).

87. Chen, X. *et al.* Oct4A palmitoylation modulates tumorigenicity and stemness in human glioblastoma cells. *Neuro. Oncol.* **25**, 82–96 (2023).

88. Zhao, Q.-W., Zhou, Y.-W., Li, W.-X. & Kang, B. Akt-mediated phosphorylation of Oct4 is associated with the proliferation of stem-like cancer cells. *Oncol. Rep.* **33**, 1621–1629 (2015).

89. Hosokawa, Y. *et al.* Oct-3/4 modulates the drug-resistant phenotype of glioblastoma cells through expression of ATP binding cassette transporter G2. *Biochim. Biophys. Acta* **1850**, 1197–1205 (2015).

90. Bhagat, M. *et al.* HIF-2α mediates a marked increase in migration and stemness characteristics in a subset of glioma cells under hypoxia by activating an Oct-4/Sox-2-Mena (INV) axis. *Int. J. Biochem. Cell Biol.* **74**, 60–71 (2016).

91. Runtu, F. & Hardiany, N. S. Role of NANOG in Glioma Malignancy Development and Potential as Therapeutic Target. *Biomed. Rev.* **31**, 41–47 (2020).

92. Wang, M.-L., Chiou, S.-H. & Wu, C.-W. Targeting cancer stem cells: emerging role of Nanog transcription factor. *Onco. Targets. Ther.* **6**, 1207–1220 (2013).

93. Smith, J., Field, M. & Sugaya, K. Suppression of NANOG Expression Reduces Drug Resistance of Cancer Stem Cells in Glioblastoma. *Genes (Basel).* **14**, 1276 (2023).

94. Zbinden, M., Duquet, A., Lorente-Trigos, A., Borges, I. & Ruiz, A. NANOG regulates glioma stem cells and is essential in vivo acting in a cross-functional network with GLI1 and p53. *EMBO J.* **29**, 2659–2674 (2010).

95. Moon, J.-H. *et al.* Nanog-induced dedifferentiation of p53-deficient mouse astrocytes into brain cancer stem-like cells. *Biochem. Biophys. Res. Commun.* **412**, 175–181 (2011).

96. Neradil, J. & Veselska, R. Nestin as a marker of cancer stem cells. *Cancer Sci.* **106**, 803 (2015).

97. Lu, W. J. *et al.* Inducible expression of stem cell associated intermediate filament nestin reveals an important role in glioblastoma carcinogenesis. *Int. J. Cancer* **128**, 343–51 (2011).

98. Jin, X., Jin, X., Jung, J.-E., Beck, S. & Kim, H. Cell surface Nestin is a biomarker for glioma stem cells. *Biochem. Biophys. Res. Commun.* **433**, 496–501 (2013).

99. Wang, Q. *et al.* Nestin is required for spindle assembly and cell cycle progression in glioblastoma cells. *Mol. Cancer Res.* **19**, 1651–1665 (2022).

100. Bien-Möller, S. *et al.* Association of Glioblastoma Multiforme Stem Cell Characteristics, Differentiation, and Microglia Marker Genes with Patient Survival. *Stem Cells Int.* **2018**, 9628289 (2018).

101. Si, D., Yin, F., Peng, J. & Zhang, G. High Expression of CD44 Predicts a Poor Prognosis in Glioblastomas. *Cancer Manag. Res.* 769–775 (2020).

102. Chaudhry, G.-S., Akim, A., Zafar, M. N., Safdar, N. & Sung, Y. Y. Understanding Hyaluronan Receptor (CD44) Interaction, HA-CD44 Activated Potential Targets in Cancer Therapeutics. *Adv. Pharm. Bull.* **11**, 426–438 (2021).

103. Ponta, H., Sherman, L. & Herrlich, P. A. CD44: from adhesion molecules to signalling regulators. *Nat. Rev. Mol. Cell Biol.* **4**, 33–45 (2003).

104. Mooney, K. L. *et al.* The role of CD44 in glioblastoma multiforme. *J. Clin. Neurosci.* **34**, 1–5 (2016).

105. Wang, H.-H., Liao, C.-C., Chow, N.-H., Huang, L. L.-H. & Chuang, J. Whether CD44 is an applicable marker for glioma stem cells. *Am. J. Transl. Res.* **9**, 4785–4806 (2017).

106. Kolliopoulos, C., Ali, M. M., Castillejo-Lopez, C., Heldin, C.-H. & Heldin, P. CD44 Depletion in Glioblastoma Cells Suppresses Growth and Stemness and Induces Senescence. *Cancers (Basel).* **14**, 3747 (2022).

107. Nishikawa, M., Inoue, A., Ohnishi, T., Yano, H. & Ozaki, S. Hypoxia-induced phenotypic transition from highly invasive to less invasive tumors in glioma stem-like cells: Significance of CD44 and osteopontin as therapeutic targets in glioblastoma. *Transl. Oncol.* **14**, 101137 (2021).

108. Brown, D. V *et al.* Expression of CD133 and CD44 in glioblastoma stem cells correlates with cell proliferation, phenotype stability and intra-tumor heterogeneity. *PLoS One* **12**, e0172791 (2017).

109. Heddleston, J. M., Li, Z., McLendon, R. E., Hjelmeland, A. B. & Rich, J. N. The hypoxic microenvironment maintains phenotype reprogramming towards a cancer stem cell glioblastoma stem cells and promotes. *Cell Cycle* **8**, 3274–3284 (2009).

110. Musah-Eroje, A. & Watson, S. Adaptive Changes of Glioblastoma Cells Following Exposure to Hypoxic (1% Oxygen) Tumour Microenvironment. *Int. J. Mol. Sci.* **20**, 2091 (2019).

111. Manoranjan, B. *et al.* A CD133-AKT-Wnt signaling axis drives glioblastoma brain tumor-initiating cells. *Oncogene* **39**, 1590–1599 (2020).

112. Liu, G. *et al.* Analysis of gene expression and chemoresistance of CD133+ cancer stem cells in glioblastoma. *Mol. Cancer* **5**, (2006).

113. Shabason, J. E. & Camphausen, K. Cancer stem cells as a prognostic indicator for glioblastoma multiforme. *Biomark. Med.* **4**, 127–128 (2019).

114. Brescia, P. *et al.* CD133 Is Essential for Glioblastoma Stem Cell Maintenance. *Stem Cells* **31**, 857–869 (2013).

115. Ludwig, K. & Kornblum, H. I. Molecular Markers in Glioma. *J. Neurooncol.* **134**, 505–512 (2018).

116. Joyce, T., Jagasia, S., Tasci, E., Camphausen, K. & Krauze, A. V. An Overview of CD133 as a Functional Unit of Prognosis and Treatment Resistance in Glioblastoma. *Curr. Oncol.* **30**, 8278–8293 (2023).

117. Sonnenberg, A. *et al.* Integrin alpha 6/beta 4 complex is located in hemidesmosomes, suggesting a major role in epidermal cell-basement membrane adhesion. *J. Cell Biol.* **113**, 907–917 (1991).

118. Evsikov, A. V & Solter, D. Comment on ' "Stemness": transcriptional profiling of embryonic and adult stem cells' and 'a stem cell molecular signature'. *Science (80-.).* **302**, 393 (2003).

119. Hall, P. E., Lathia, J. D., Caldwell, M. A. & Ffrench-Constant, C. Laminin enhances the growth of human neural stem cells in defined culture media. *BMC Neurosci.* **9**, (2008).

120. Lathia, J. D. *et al.* Integrin Alpha 6 Regulates Glioblastoma Stem Cells. *Cell Stem Cell* **6**, 421–432 (2010).

121. Stanzani, E. *et al.* Dual Role of Integrin Alpha-6 in Glioblastoma: Supporting Stemness in Proneural Stem-Like Cells While Inducing Radioresistance in Mesenchymal Stem-like cells. *Cancers (Basel).* **13**, 3055 (2021).

122. Bigoni-Ordóñez, G. D., Czarnowski, D., Parsons, T., Madlambayan, G. J. & Villa-Diaz, L. G. Integrin α6 (CD49f), The Microenvironment and Cancer Stem Cells. *Curr. Stem Cell Res. Ther.* **14**, 428–436 (2019).

123. Krebsbach, P. H. & Villa-Diaz, L. G. The Role of Integrin α6 (CD49f) in Stem Cells: More than a Conserved Biomarker. *Stem Cells Dev.* **26**, 1090–1099 (2017).

124. Peacock Brooks, D. L. *et al.* ITGA6 is directly regulated by hypoxia-inducible factors and enriches for cancer stem cell activity and invasion in metastatic breast cancer models. *Mol. Cancer* **15**, (2016).

125. Alshahrany, N., Begum, A., Siebzehnrubl, D., Jimenez-Pascual, A. & Siebzehnrubl, F. A. Spatial distribution and functional relevance of FGFR1 and FGFR2 expression for glioblastoma tumor invasion. *Cancer Lett.* **571**, 216349 (2023).

126. Kowalski-Chauvel, A. *et al.* Alpha6-Integrin Regulates FGFR1 Expression through the ZEB1/YAP1 Transcription Complex in Glioblastoma Stem Cells Resulting in Enhanced Proliferation and Stemness. *Cancers (Basel).* **11**, 406 (2019).

127. van Asperen, J. V, Robe, P. A. J. T. & Hol, E. M. GFAP Alternative Splicing and the Relevance for Disease - A Focus on Diffuse Gliomas. *ASN Neuro* **14**, (2022).

128. Simone, L., Capobianco, D. L., Palma, F. Di & Binda, E. GFAP serves as a structural element of tunneling nanotubes between glioblastoma cells and could play a role in the intercellular transfer of mitochondria. *Front. Cell Dev. Biol.* **11**, (2023).

129. Guichet, P.-O. *et al.* Asymmetric Distribution of GFAP in Glioma Multipotent Cells. *PLoS One* **11**, e0151274 (2016).

130. Su, X. *et al.* GFAP expression is regulated by Pax3 in brain glioma stem cells. *Oncol. Rep.* **36**, 1277–1284 (2016).

131. Radu, R., Petrescu, G. E. D., Gorgan, R. M. & Brehar, F. M. GFAPδ: A Promising Biomarker and Therapeutic Target in Glioblastoma. *Front. Oncol.* **12**, 859247 (2022).

132. Wlodarczyk, A., Grot, D., Stoczynska-Fidelus, E. & Rieske, P. Gaps and Doubts in Search to Recognize Glioblastoma Cellular Origin and Tumor Initiating Cells. *J. Oncol.* **2020**, (2020).

133. Xu, H. *et al.* Epidermal growth factor receptor in glioblastoma (Review). *Oncol. Lett.* **14**, 512–516 (2017).

134. Oprita, A. *et al.* Updated Insights on EGFR Signaling Pathways in Glioma. *Int. J. Mol. Sci.* **22**, 587 (2021).

135. Agosti, E. *et al.* Glioma Stem Cells as Promoter of Glioma Progression: A Systematic Review of Molecular Pathways and Targeted Therapies. *Int. J. Mol. Sci.* **25**, 7979 (2024).

136. Gao, Q., Lei, T. & Ye, F. Therapeutic targeting of EGFR-activated metabolic pathways in glioblastoma. *Expert Opin. Investig. Drugs* **22**, 1023–1040 (2013).

137. Hersh, A. M., Gaitsch, H., Alomari, S., Lubelski, D. & Tyler, B. M. Molecular Pathways and Genomic Landscape of Glioblastoma Stem Cells: Opportunities for Targeted Therapy. *Cancers (Basel).* **15**, 3743 (2022).

138. Mazzoleni, S. *et al.* Epidermal Growth Factor Receptor Expression Identifies Functionally and Molecularly Distinct Tumor-Initiating Cells in Human Glioblastoma Multiforme and Is Required for Gliomagenesis. *Cancer Res.* **70**, 7500–7513 (2010).

139. Emlet, D. R. *et al.* Targeting a Glioblastoma Cancer Stem-Cell Population Defined by EGF Receptor Variant III. *Cancer Res.* **74**, 1238–1249 (2014).

140. Huang, W. *et al.* A novel EGFR variant EGFRx maintains glioblastoma stem cells through STAT5. *Neuro. Oncol.* **26**, 85–99 (2024).

141. Li, G. *et al.* Autocrine factors sustain glioblastoma stem cell self-renewal. *Oncol. Rep.* **21**, 419–424 (2009).

142. Davidson, T. B. *et al.* Expression of PD-1 by T Cells in Malignant Glioma Patients Reflects Exhaustion and Activation. *Clin. Cancer Res.* **25**, 1913–1922 (2018).

143. Mirzaei, R. *et al.* PD-1 independent of PD-L1 ligation promotes glioblastoma growth through the NFκB pathway. *Sci. Adv.* **7**, eabh2148 (2021).

144. Shu, C. & Li, Q. Current advances in PD-1/PD-L1 axis-related tumour-infiltrating immune cells and therapeutic regimens in glioblastoma. *Crit. Rev. Oncol. / Hematol.* **151**, 102965 (2020).

145. Berghoff, A. S. *et al.* Programmed death ligand 1 expression and tumor-infiltrating lymphocytes in glioblastoma. *Neuro. Oncol.* **17**, 1064–1075 (2015).

146. Cloughesy, T. F. *et al.* Neoadjuvant anti-PD-1 immunotherapy promotes a survival benefit with intratumoral and systemic immune responses in recurrent glioblastoma. *Nat. Med.* **25**, 477–486 (2019).

147. Uhlén, M. *et al.* Proteomics. Tissue-based map of the human proteome. *Science* **347**,

1260419 (2015).

148. Nowakowski, T. J. *et al.* Expression Analysis Highlights AXL as a Candidate Zika Virus Entry Receptor in Neural Stem Cells. *Cell Stem Cell* **18**, 591–596 (2016).

149. Tanaka, M. & Siemann, D. W. Gas6/Axl Signaling Pathway in the Tumor Immune Microenvironment. *Cancers (Basel).* **12**, 1850 (2020).

150. Axelrod, H. & Pienta, K. J. Axl as a mediator of cellular growth and survival. *Oncotarget* **5**, 8818–8852 (2014).

151. Zhu, C., Wei, Y. & Wei, X. AXL receptor tyrosine kinase as a promising anti-cancer approach: functions, molecular mechanisms and clinical applications. *Mol. Cancer* **18**, 153 (2019).

152. Li, Y. *et al.* Axl as a potential therapeutic target in cancer: role of Axl in tumor growth, metastasis and angiogenesis. *Oncogene* **28**, 3442–3455 (2009).

153. Goyette, M.-A. & Côté, J.-F. AXL Receptor Tyrosine Kinase as a Promising Therapeutic Target Directing Multiple Aspects of Cancer Progression and Metastasis. *Cancers (Basel).* **14**, 466 (2022).

154. Tang, Y., Zang, H., Wen, Q. & Fan, S. AXL in cancer: a modulator of drug resistance and therapeutic target. *J. Exp. Clin. Cancer Res.* **42**, 148 (2023).

155. Colavito, S. A. AXL as a Target in Breast Cancer Therapy. *J. Oncol.* **2020**, 5291952 (2020).

156. Engelsen, A. S. T. *et al.* Dissecting the Role of AXL in Cancer Immune Escape and Resistance to Immune Checkpoint Inhibition. *Front. Immunol.* **13**, 869676 (2022).

157. Goyette, M., Roux, P. P. & Goyette, M. The Receptor Tyrosine Kinase AXL Is Required at Multiple Steps of the Metastatic Cascade during HER2-Positive Breast Cancer Progression. *Cell Rep.* **23**, 1476–1490 (2023).

158. Sang, Y. B. *et al.* The Development of AXL Inhibitors in Lung Cancer: Recent Progress and Challenges. *Front. Oncol.* **12**, 811247 (2022).

159. Rankin, E. B. *et al.* AXL Is an Essential Factor and Therapeutic Target for Metastatic Ovarian Cancer. *Cancer Res.* **70**, 7570–7579 (2010).

160. De Rosa, L., Di Stasi, R., Fusco, V. & D'Andrea, L. D. AXL receptor as an emerging

molecular target in colorectal cancer. *Drug Discov. Today* **29**, 104005 (2024).

161. Paccez, J. D. *et al.* The receptor tyrosine kinase Axl is an essential regulator of prostate cancer proliferation and tumor growth and represents a new therapeutic target. *Oncogene* **32**, 689–98 (2013).

162. Shao, H., Teramae, D. & Wells, A. Axl contributes to efficient migration and invasion of melanoma cells. *PLoS One* **18**, e0283749 (2023).

163. Sadahiro, H. *et al.* Activation of the Receptor Tyrosine Kinase AXL Regulates the Immune Microenvironment in Glioblastoma. *Cancer Res.* **78**, 3002–3013 (2018).

164. Scherschinski, L. *et al.* Regulation of the Receptor Tyrosine Kinase AXL in Response to Therapy and Its Role in Therapy Resistance in Glioblastoma. *Int. J. Mol. Sci.* **23**, 982 (2022).

165. Meertens, L. *et al.* Axl Mediates ZIKA Virus Entry in Human Glial Cells and Modulates Innate Immune Responses. *Cell Rep.* **18**, 324–333 (2017).

166. Richard, A. S., Shim, B.-S., Kwon, Y.-C., Zhang, R. & Otsuka, Y. AXL-dependent infection of human fetal endothelial cells distinguishes Zika virus from other pathogenic flaviviruses. *Proc. Natl. Acad. Sci.* **114**, 2024–2029 (2017).

167. Bianca, C. *et al.* Repurposing of Zika virus live-attenuated vaccine (ZIKV-LAV) strains as oncolytic viruses targeting human glioblastoma multiforme cells. *J. Transl. Med.* **22**, 126 (2024).

168. Zwernik, S. D. *et al.* AXL receptor is required for Zika virus strain MR-766 infection in human glioblastoma cell lines. *Mol. Ther. Oncolytics* **23**, 447–457 (2021).

169. Liu, S., DeLalio, L. J., Isakson, B. E. & Wang, T. T. AXL-Mediated Productive Infection of Human Endothelial Cells by Zika Virus. *Circ. Res.* **119**, 1183–1189 (2016).

170. Takada, Y., Ye, X. & Simon, S. The integrins. *Genome Biol.* **8**, (2007).

171. Eliceiri, B. P. & Cheresh, D. A. The role of alphav integrins during angiogenesis: insights into potential mechanisms of action and clinical development. *J. Clin. Invest.* **103**, 1227–1230 (1999).

172. Meyer, A., Auernheimer, J., Modlinger, A. & Kessler, H. Targeting RGD recognizing integrins: drug development, biomaterial research, tumor imaging and targeting. *Curr.*

Pharm. Des. **12**, 2723–2747 (2006).

173. Liu, F., Wu, Q., Dong, Z. & Liu, K. Integrins in cancer: Emerging mechanisms and therapeutic opportunities. *Pharmacol. Ther.* **247**, 108458 (2023).

174. Mittelbronn, M., Warth, A., Meyermann, R., Goodman, S. & Weller, M. Expression of integrins αvβ3 and αvβ5 and their ligands in primary and secondary central nervous system neoplasms. *Histol. Histopathol.* **28**, 749–758 (2013).

175. Schittenhelm, J. *et al.* Longitudinal expression analysis of αv integrins in human gliomas reveals upregulation of integrin αvβ3 as a negative prognostic factor. *J. Neurophatology Exp. Neurol.* **72**, 194–210 (2013).

176. Bello, L. *et al.* αvβ3 and αvβ5 Integrin Expression in Glioma Periphery. *Neurosurgery* **49**, 380–389 (2001).

177. Zhu, Z. *et al.* Zika virus has oncolytic activity against glioblastoma stem cells. *J. Exp. Med.* **214**, 2843–2857 (2017).

178. Wang, M., Shen, S., Hou, F. & Yan, Y. Pathophysiological roles of integrins in gliomas from the perspective of glioma stem cells. *Front. Cell Dev. Biol.* 962481 (2022). doi:10.3389/fcell.2022.962481

179. Zhu, Z. *et al.* Zika Virus Targets Glioblastoma Stem Cells through a SOX2-Integrin αvβ5 Axis. *Cell Stem Cell* **26**, 187-204.e10 (2020).

180. Tiwari, S. K. *et al.* Integrin αvβ5 Internalizes Zika Virus during Neural Stem Cells Infection and Provides a Promising Target for Antiviral Therapy. *Cell Rep.* **30**, 969–983 (2020).

181. Zhang, L. *et al.* Integrin Beta 5 Is a Prognostic Biomarker and Potential Therapeutic Target in Glioblastoma. *Front. Oncol.* **9**, 904 (2019).

182. Fukuhara, H., Ino, Y. & Todo, T. Oncolytic virus therapy: A new era of cancer treatment at dawn. *Cancer Sci.* **107**, 1373–1379 (2016).

183. Terrível, M., Gromicho, C. & Matos, A. M. Oncolytic viruses: what to expect from their use in cancer treatment. *Microbiol. Immunol.* **64**, 477–492 (2020).

184. Zeyaullah, M. *et al.* Oncolytic Viruses in the Treatment of Cancer: A Review of Current Strategies. *Pathol. Oncol. Res.* **18**, 771–781 (2012).

185. Rivera, S., Jhommara, O., Palacios, D., Sofía, Z. & Mosquera, O. Oncolytic virotherapy and tumor microenvironment modulation. *Clin. Exp. Med.* **25**, 256 (2025).

186. Eager, R. M. & Nemunaitis, J. Clinical development directions in oncolytic viral therapy. *Cancer Gene Ther.* **18**, 305–317 (2011).

187. Asija, S. *et al.* Oncolytic immunovirotherapy for high-grade gliomas: A novel and an evolving therapeutic option. *Front. Immunol.* **15**, 1118246 (2023).

188. Wollmann, G. & Ozduman, K. Oncolytic Virus Therapy for Glioblastoma Multiforme: Concepts and Candidates. *Cancer J.* **18**, 69–81 (2012).

189. Ning, J. & Wakimoto, H. Oncolytic herpes simplex virus-based strategies: toward a breakthrough in glioblastoma therapy. *Front. Microbiol.* **5**, (2014).

190. Gunasegaran, B., Ashley, C. L., Marsh-Wakefield, F., Guillemin, G. J. & Heng, B. Viruses in glioblastoma: an update on evidence and clinical trials. *BJC Reports* **2**, 33 (2024).

191. Kim, D. S. Cancer stem cell plasticity in glioblastoma multiforme: a perspective on future directions in oncolytic virotherapy. *Futur. Oncol.* **16**, 2251–2264 (2020).

192. Zhou, C., Chen, Q., Chen, Y. & Qin, C. Oncolytic Zika Virus: New Option for Glioblastoma Treatment. *DNA Cell Biol.* **42**, 267–273 (2023).

193. Chen, Q. *et al.* Treatment of Human Glioblastoma with a Live Attenuated Zika Virus Vaccine Candidate. *MBio* **9**, e01683-18 (2018).

194. Kretschmer, M. *et al.* Zikavirus prME Envelope Pseudotyped Human Immunodeficiency Virus Type-1 as a Novel Tool for Glioblastoma-Directed Virotherapy. *Cancers (Basel).* **12**, 1000 (2020).

195. Grunwald, V. *et al.* Development of Zika Virus E Variants for Pseudotyping Retroviral Vectors Targeting Glioblastoma Cells. *Int. J. Mol. Sci.* **24**, 14487 (2023).

196. Rabaan, A. A., Bazzi, A. M., Al-Ahmed, S. H., Al-Ghaith, M. H. & Al-Tawfiq, J. A. Overview of Zika infection, epidemiology, transmission and control measures. *J. Infect. Public Health* **10**, 141–149 (2017).

197. Pierson, T. C. & Diamond, M. S. Degrees of maturity: the complex structure and biology of flaviviruses. *Curr. Opin. Virol.* **2**, 168–175 (2012).

198. Hou, W. *et al.* Molecular cloning and characterization of the genes encoding the proteins of Zika virus. *Gene* **628**, 117–128 (2017).

199. Oliveira, E. R. A., de Alencastro, R. B. & Horta, B. A. C. New insights into flavivirus biology: the influence of pH over interactions between prM and E proteins. *J. Comput. Aided. Mol. Des.* **31**, 1009–1019 (2017).

200. Owczarek, K. *et al.* Zika virus: mapping and reprogramming the entry. *Commun. Signal.* **17**, 41 (2019).

201. Tréguier, Y. *et al.* The envelope protein of Zika virus interacts with apolipoprotein E early in the infectious cycle and this interaction is conserved on the secreted viral particles. *Virol. J.* **19**, 124 (2022).

202. Rana, J. *et al.* Role of Capsid Anchor in the Morphogenesis of Zika Virus. *J. Virol.* **92**, e01174 (2018).

203. Petersen, L. R., Jamieson, D. J., Powers, A. M. & Honein, M. A. Zika Virus. *N. Engl. J. Med.* **374**, 1552–1563 (2016).

204. De Noronha, L., Zanluca, C., Azevedo, M. L. V., Luz, K. G. & Nunes Duarte Dos, C. Zika virus damages the human placental barrier and presents marked fetal neurotropism. *Mem Inst Oswaldo Cruz* **111**, 287–293 (2016).

205. Li, Q., Liu, Q., Huang, W., Li, X. & Wang, Y. Current status on the development of pseudoviruses for enveloped viruses. *Rev. Med. Virol.* **28**, e1963 (2018).

206. Xiao, J. H. *et al.* Characterization of Influenza Virus Pseudotyped with Ebolavirus Glycoprotein. *J. Virol.* **92**, e00941-17 (2017).

207. Whitt, M. A. Generation of VSV pseudotypes using recombinant ΔG-VSV for studies on virus entry, identification of entry inhibitors, and immune responses to vaccines. *J. Virol. Methods* **169**, 365–374 (2010).

208. De Ravin, S. S. *et al.* Enhancers Are Major Targets for Murine Leukemia Virus Vector Integration. *J. Virol.* **88**, 4501–4513 (2014).

209. Dull, T. *et al.* A Third-Generation Lentivirus Vector with a Conditional Packaging System. *J. Virol.* **72**, 8463–8471 (1998).

210. Finkelshtein, D., Werman, A., Novick, D., Barak, S. & Rubinstein, M. LDL receptor and

its family members serve as the cellular receptors for vesicular stomatitis virus. *Proc. Natl. Acad. Sci.* **110**, 7306–7311 (2013).

211. Cronin, J., Zhang, X.-Y. & Reiser, J. Altering the Tropism of Lentiviral Vectors through Pseudotyping. *Curr. Gene Ther.* **5**, 387–398 (2005).

212. Gutierrez-Guerrero, A., Cosset, F.-L. & Verhoeyen, E. Lentiviral Vector Pseudotypes: Precious Tools to Improve Gene Modification of Hematopoietic Cells for Research and Gene Therapy. *Viruses* **12**, 1016 (2020).

213. Xu, C. *et al.* Human Immunodeficiency Viruses Pseudotyped with SARS-CoV-2 Spike Proteins Infect a Broad Spectrum of Human Cell Lines through Multiple Entry Mechanisms. *Viruses* **13**, 953 (2021).

214. Nie, J., Liu, Y., Huang, W. & Wang, Y. Development of a Triple-Color Pseudovirion-Based Assay to Detect Neutralizing Antibodies against Human Papillomavirus. *Viruses* **8**, 107 (2016).

215. Salazar-García, M. *et al.* Pseudotyped Vesicular Stomatitis Virus-Severe Acute Respiratory Syndrome-Coronavirus-2 Spike for the Study of Variants , Vaccines , and Therapeutics Against Coronavirus Disease 2019. *Front. Microbiol.* **12**, 817200 (2022).

216. Ngo, H. D., Formanski, J. P., Grunwald, V., Schwalbe, B. & Schreiber, M. Generation of Viral Particles with Brain Cell-Specific Tropism by Pseudotyping HIV-1 with the Zika Virus E Protein. *Methods Protoc.* **7**, 3 (2023).

217. Millet, J. K. *et al.* Production of Pseudotyped Particles to Study Highly Pathogenic Coronaviruses in a Biosafety Level 2 Setting. *J. Vis. Exp.* 59010 (2019).

218. Lodge, R., Gottlinger, H., Gabuzda, D., Cohen, E. A. & Lemayi, G. The Intracytoplasmic Domain of gp4l Mediates Polarized Budding of Human Immunodeficiency Virus Type 1 in MDCK Cells. *J. Virol.* **68**, 4857–4861 (1994).

219. Pöhlking, C. *et al.* Isolation of Cells from Glioblastoma Multiforme Grade 4 Tumors for Infection with Zika Virus prME and ME Pseudotyped HIV-1. *Int. J. Mol. Sci.* **24**, 4467 (2023).

220. Formanski, J. P. *et al.* Transduction Efficiency of Zika Virus E Protein Pseudotyped HIV-1gfp and Its Oncolytic Activity Tested in Primary Glioblastoma Cell Cultures. *Cancers (Basel).* **16**, 814 (2024).

221. Liu, J. *et al.* Efficient Gene Transfer to Kidney Using a Lentiviral Vector Pseudotyped with Zika Virus Envelope Glycoprotein. *Hum. Gene Ther.* **33**, 1269–1278 (2022).

222. Gibson, D. G. *et al.* Enzymatic assembly of DNA molecules up to several hundred kilobases. *Nat. Methods* **6**, 343–345 (2009).

223. Ledur, P. F., Onzi, G. R., Zong, H. & Lenz, G. Culture conditions defining glioblastoma cells behavior: what is the impact for novel discoveries? *Oncotarget* **8**, 69185–69197 (2017).

224. Zhang, L. *et al.* The necessity for standardization of glioma stem cell culture: a systematic review. *Stem Cell Res. Ther.* **11**, 1–7 (2020).

225. Izsak, J., Seth, H., Theiss, S., Hanse, E. & Illes, S. Human Cerebrospinal Fluid Promotes Neuronal Circuit Maturation of Human Induced Pluripotent Stem Cell-Derived 3D Neural Aggregates. *Stem Cell Reports* **14**, 1044–1059 (2020).

226. Reiber, H. Dynamics of brain-derived proteins in cerebrospinal fluid. *Clin. Chim. Acta* **310**, 173–186 (2001).

227. Spector, R., Snodgrass, S. R. & Johanson, C. E. A balanced view of the cerebrospinal fluid composition and functions: Focus on adult humans. *Exp. Neurol.* **273**, 57–68 (2015).

228. Albini, A. *et al.* Cancer stem cells and the tumor microenvironment: interplay in tumor heterogeneity. *Connect. Tissue Res.* **56**, 414–425 (2015).

229. Soares, C. P. *et al.* 2D and 3D-Organized Cardiac Cells Shows Differences in Cellular Morphology, Adhesion Junctions, Presence of Myofibrils and Protein Expression. *PLoS One* **7**, (2012).

230. Rashidi, R., Hadjighassem, M. & Negahdari, B. Unraveling the complexity of glioblastoma microenvironment: A comparative study of 3D and 2D cultures in response to combination drug therapy. *Brain Res.* **1864**, (2025).

231. Su, X. *et al.* Human Brain Organoids as an In Vitro Model System of Viral Infectious Diseases. *Front. Immunol.* **12**, 1–10 (2022).

232. Balvers, R. K., Dirven, C. M. F., Leenstra, S. & Lamfers, M. L. M. Malignant Glioma In Vitro Models: On the Utilization of Stem-like Cells. *Curr. Cancer Drug Targets* **17**, 255–266 (2017).

233. Lu, C. *et al.* Combined targeting of glioblastoma stem cells of different cellular states disrupts malignant progression. *Nat. Commun.* **16**, (2025).

234. Suvà, M. L. & Tirosh, I. The Glioma Stem Cell Model in the Era of Single-Cell Genomics. *Cancer Cell* **37**, 630–636 (2020).

235. Jin, X. *et al.* Targeting glioma stem cells through combined BMI1 and EZH2 inhibition. *Nat. Med.* **23**, 1352–1361 (2017).

236. Lee, J., Kim, H. K., Rho, J., Han, Y.-M. & Kim, J. The Human OCT-4 Isoforms Differ in Their Ability to Confer Self-renewal. *J. Biol. Chem.* **281**, 33554–33565 (2006).

237. Choi, S.-H., Kim, J.-K., Jeon, H.-Y., Eun, K. & Kim, H. Molecules and Cells OCT4B Isoform Promotes Anchorage-Independent Growth of Glioblastoma Cells. *Mol. Cells* **42**, 135–142 (2019).

238. Ashrafizadeh, M. *et al.* Biomedical application of chitosan-based nanoscale delivery systems: Potential usefulness in siRNA delivery for cancer therapy. *Carbohydr. Polym.* **260**, (2021).

239. Khlidj, Y. What did CRISPR-Cas9 accomplish in its first 10 years? *Biochem Med* **33**, 1–12 (2023).

240. Peixoto, J. *et al.* Using a Dual CRISPR/Cas9 Approach to Gain Insight into the Role of LRP1B in Glioblastoma. *Int. J. Mol. Sci.* **24**, 1–24 (2023).

241. Ding, S., Liu, J., Han, X. & Tang, M. CRISPR/Cas9-Mediated Genome Editing in Cancer Therapy. *Int. J. Mol. Sci.* **24**, (2023).

242. Gallo, K. *et al.* Inducible Knockout of 14-3-3β Attenuates Proliferation and Spheroid Formation in a Human Glioblastoma Cell Line U87MG. *Brain Sci.* **13**, (2023).

243. Liu, H.-S., Jan, M.-S., Chou, C.-K., Chen, P.-H. & Ke, N.-J. Is Green Fluorescent Protein Toxic to the Living Cells? *Biochem. Biophys. Res. Commun.* **717**, 712–717 (1999).

244. Deng, L., Liang, P. & Cui, H. ScienceDirect Pseudotyped lentiviral vectors: Ready for translation into targeted cancer gene therapy? *Genes Dis.* **10**, 1937–1955 (2023).

245. Joglekar, A. V & Sandoval, S. Pseudotyped Lentiviral Vectors: One Vector, Many Guises. *Hum. Gene Ther. Methods* **28**, 291–301 (2017).

246. Hioki, H. *et al.* Efficient gene transduction of neurons by lentivirus with enhanced

neuron-specific promoters. *Gene Ther.* **14**, 872–882 (2007).

247. Sakuma, T., Barry, M. A. & Ikeda, Y. Lentiviral vectors: basic to translational. *Biochem. J.* **443**, 603–618 (2012).

248. Zugasti, I. *et al.* CAR-T cell therapy for cancer: current challenges and future directions. *Signal Transduct. Target. Ther.* **10**, (2025).

249. Votteler, J. & Sundquist, W. I. Virus Budding and the ESCRT Pathway. *Cell Host Microbe* **14**, 232–241 (2013).

250. Komarasamy, T. V., Amelia, N., Adnan, A., James, W. & Balasubramaniam, V. R. M. T. Zika Virus Neuropathogenesis: The Different Brain Cells, Host Factors and Mechanisms Involved. *Front. Immunol.* **13**, 773191 (2022).

251. Marinowic, D. R. *et al.* Influence of Zika virus on the cytotoxicity, cell adhesion, apoptosis and inflammatory markers of glioblastoma cells. *Oncol. Lett.* **27**, 176 (2024).

252. Francipane, M. G. *et al.* Zika Virus: A New Therapeutic Candidate for Glioblastoma Treatment. *Int. J. Mol. Sci.* **22**, 10996 (2021).

253. Ziani-Zeryouh, A. *et al.* Toward more accurate preclinical glioblastoma modeling: Reverse translation of clinical standard of care in a glioblastoma mouse model. *Methods Cell Biol.* **183**, 381–397 (2024).

254. Li, F. *et al.* AXL is not essential for Zika virus infection in the mouse brain. *Emerg. Microbes Infect.* **6**, 5–7 (2017).

255. Wang, Z.-Y. *et al.* Axl is not an indispensable factor for Zika virus infection in mice. *J. Gen. Virol.* **98**, 2061–2068 (2017).

256. Wells, M. F. *et al.* Genetic Ablation of AXL Does Not Protect Human Neural Progenitor Cells and Cerebral Organoids from Zika Virus Infection. *Cell Stem Cell* **19**, 703–708 (2016).

257. Hastings, A. K. *et al.* TAM Receptors Are Not Required for Zika Virus Infection in Mice. *Cell Rep.* **19**, 558–568 (2017).

258. Evaluation of Two Zika Viruses for Use in Controlled Human Infection Models (CHIM). Available at: https://clinicaltrials.gov/study/NCT05123222.

7. Appendix

7.1. Appendix figures

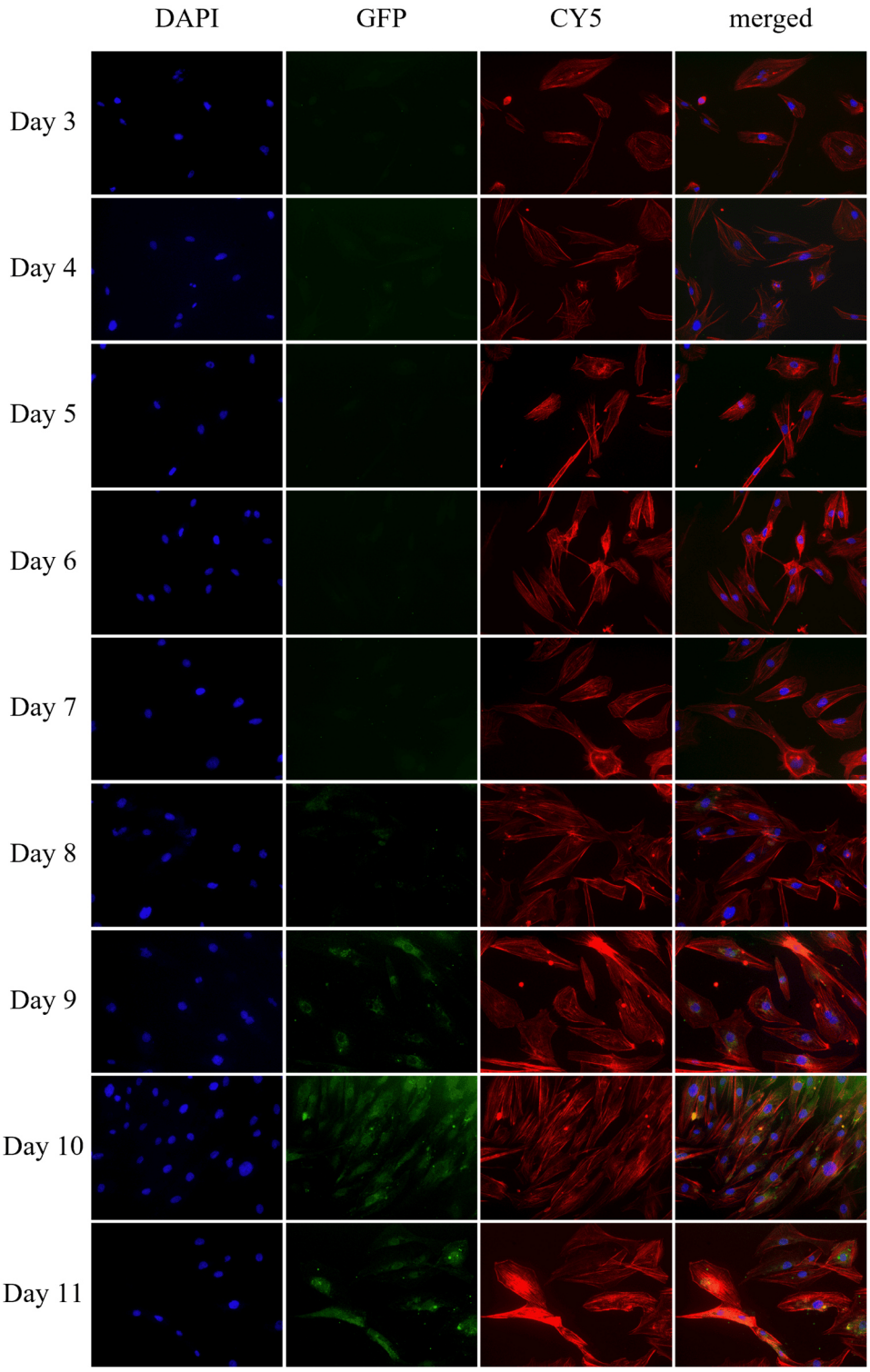

Fig. 67 Identification of integrin $\alpha_v\beta_5$ in AKH-5 cells. Tumor cells were cultured on 12-well glass slides placed inside a Petri dish over a course of 11 days. 1 mL cell suspension was spread onto the glass wells and afterwards covered with culture medium CSF-DF. DAPI: nuclei were stained with DAPI (blue); GFP: commercial integrin $\alpha_v\beta_5$-specific antibody detected by a goat anti-mouse IgG antibody conjugated with Alexa Fluor® 488 (green); Cy5: actin skeleton was stained with a phalloidin Alexa Fluor® 647 conjugate (red); all images are presented at 20x magnification.

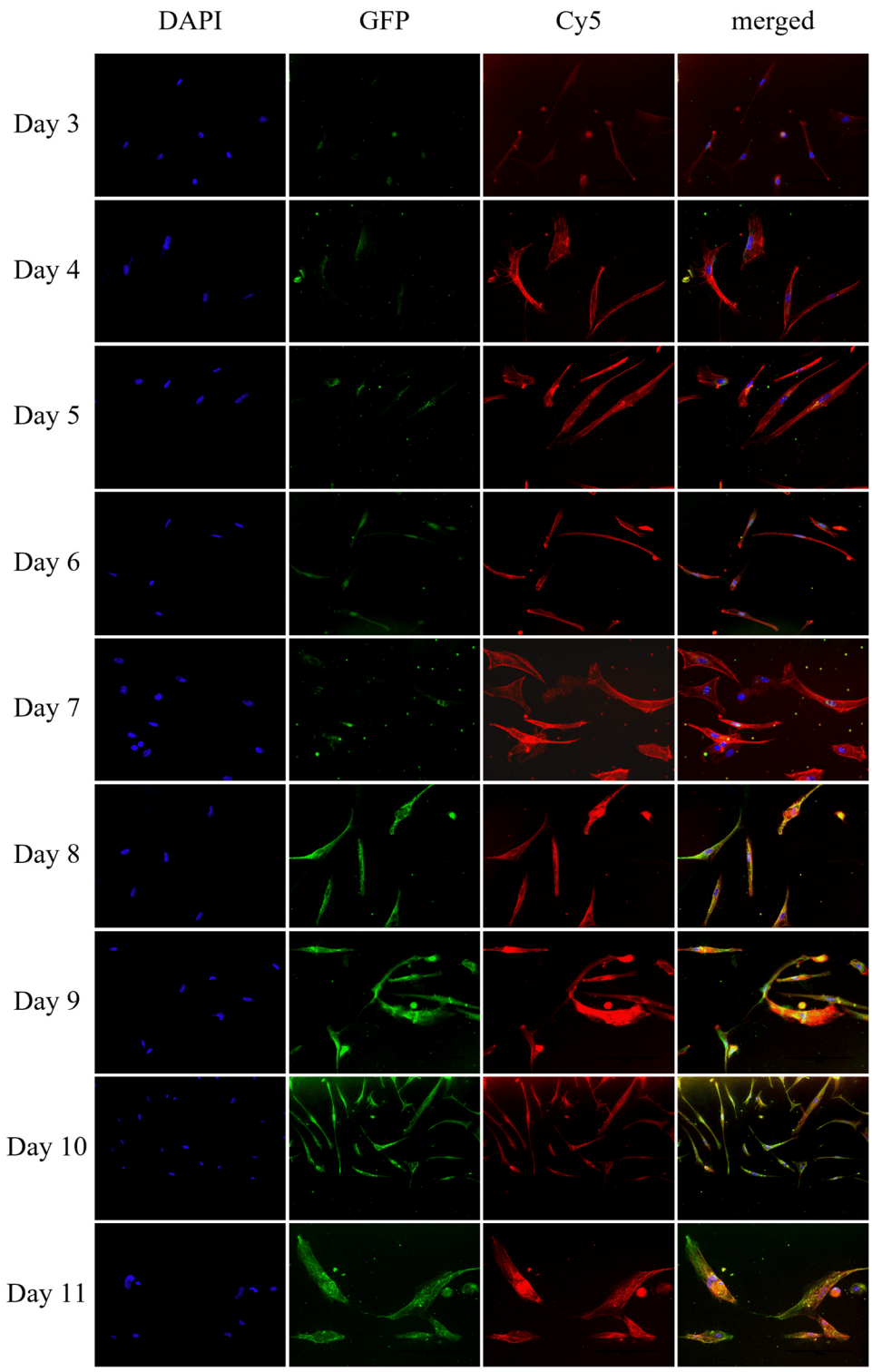

Fig. 68 Identification of integrin $\alpha_v\beta_5$ in AKH-9 cells. Tumor cells were cultured on 12-well glass slides placed inside a Petri dish over a course of 11 days. 1 mL cell suspension was spread onto the glass wells and afterwards covered with culture medium CSF-DF. DAPI: nuclei were stained with DAPI (blue); GFP: commercial integrin $\alpha_v\beta_5$-specific antibody detected by a goat anti-mouse IgG antibody conjugated with Alexa Fluor® 488 (green); Cy5: actin skeleton was stained with a phalloidin Alexa Fluor® 647 conjugate (red); all images are presented at 20x magnification.

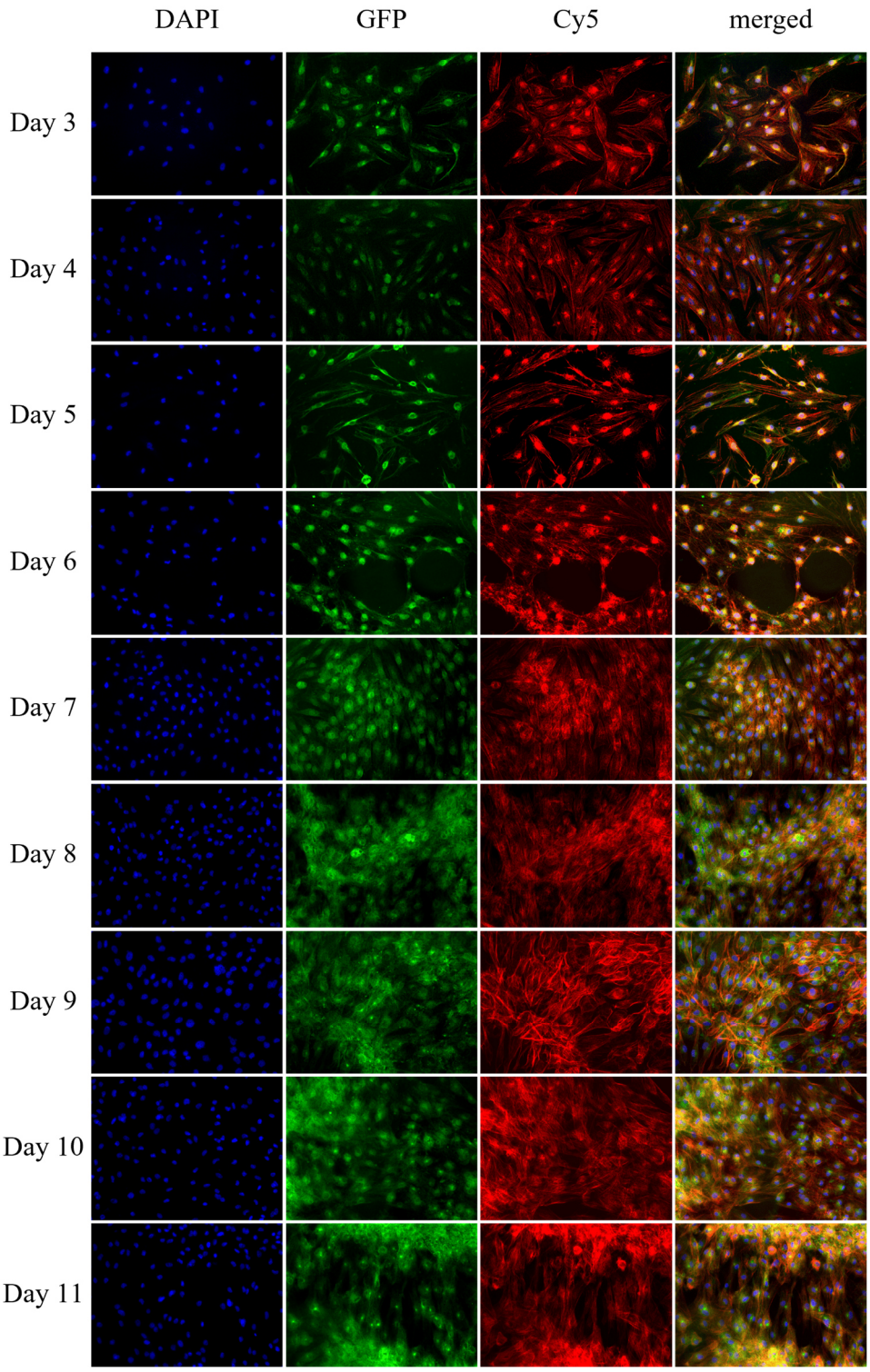

Fig. 69 Identification of integrin $\alpha_v\beta_5$ in AKH-10 cells. Tumor cells were cultured on 12-well glass slides placed inside a Petri dish over a course of 11 days. 1 mL cell suspension was spread onto the glass wells and afterwards covered with culture medium CSF-DF. DAPI: nuclei were stained with DAPI (blue); GFP: commercial integrin $\alpha_v\beta_5$-specific antibody detected by a goat anti-mouse IgG antibody conjugated with Alexa Fluor® 488 (green); Cy5 actin skeleton was stained with a phalloidin Alexa Fluor® 647 conjugate (red); all images are presented at 20x magnification

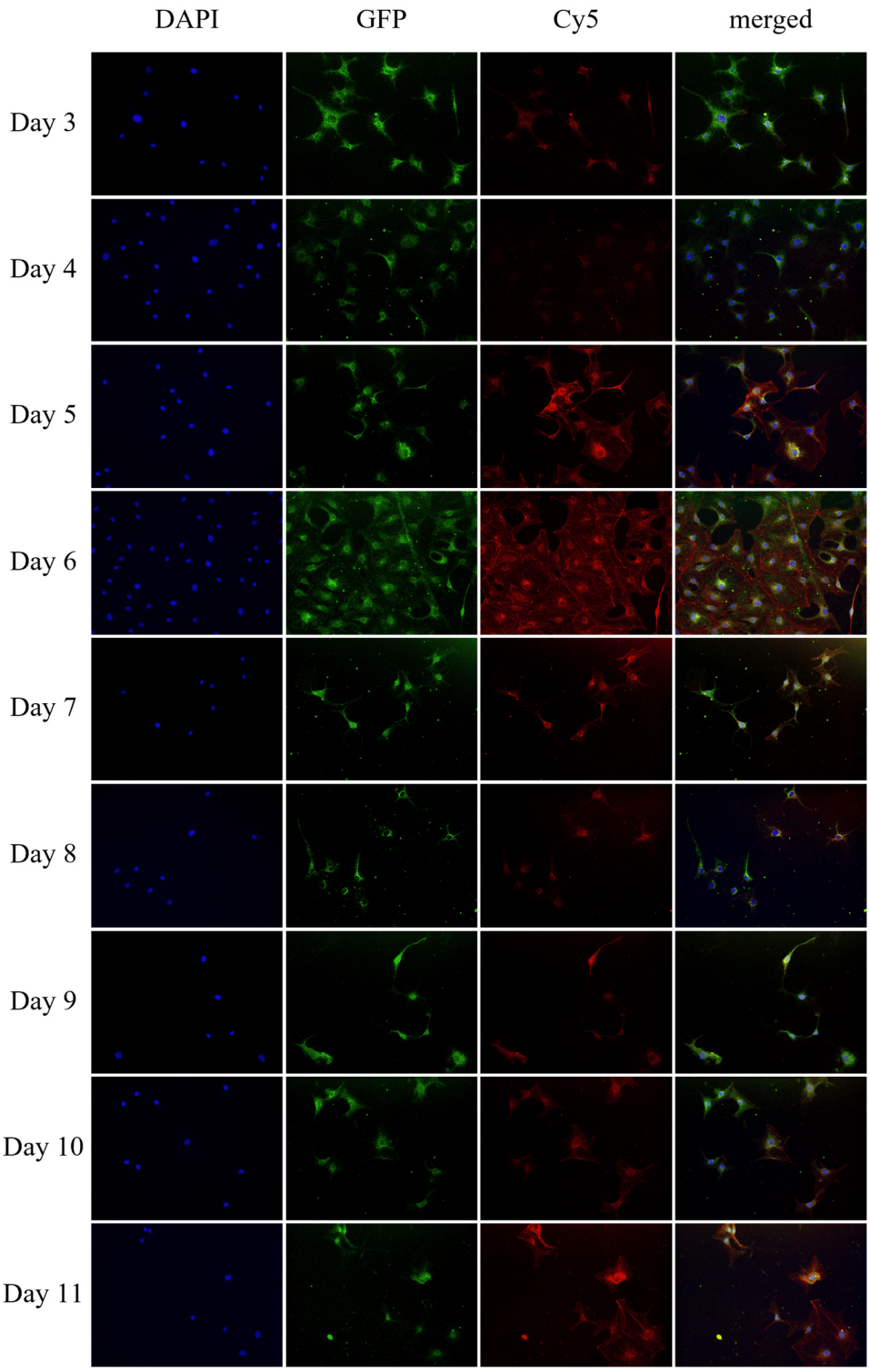

Fig. 70 Identification of integrin $\alpha_v\beta_5$ in AKH-11 cells. Tumor cells were cultured on 12-well glass slides placed inside a Petri dish over a course of 11 days. 1 mL cell suspension was spread onto the glass wells and afterwards covered with culture medium CSF-DF. DAPI: nuclei were stained with DAPI (blue); GFP: commercial integrin $\alpha_v\beta_5$-specific antibody detected by a goat anti-mouse IgG antibody conjugated with Alexa Fluor® 488 (green); Cy5: actin skeleton was stained with a phalloidin Alexa Fluor® 647 conjugate (red); all images are presented at 20x magnification.

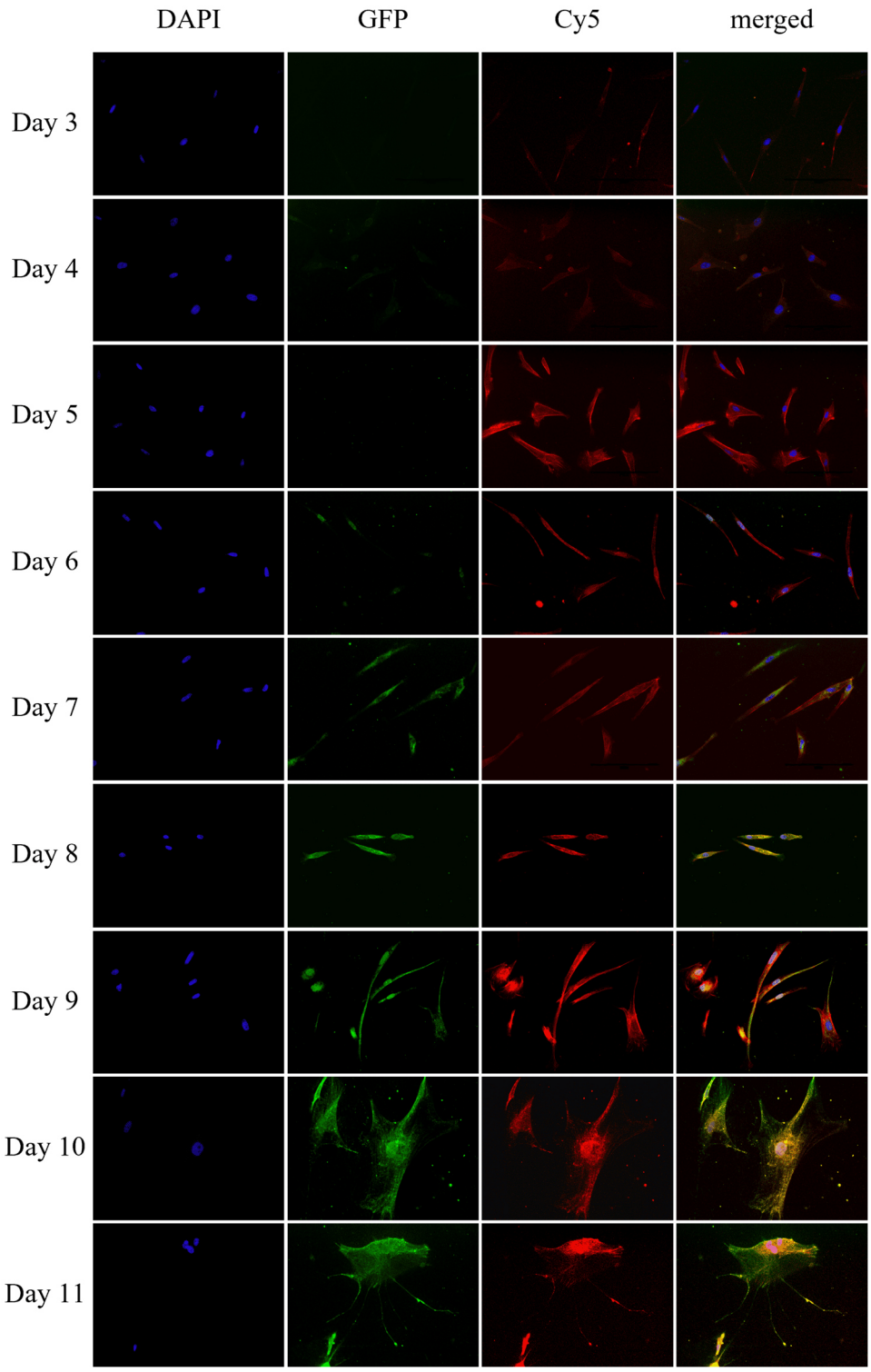

Fig. 71 Identification of integrin $\alpha_v\beta_5$ in AKH-12 cells. Tumor cells were cultured on 12-well glass slides placed inside a Petri dish over a course of 11 days. 1 mL cell suspension was spread onto the glass wells and afterwards covered with culture medium CSF-DF. DAPI: nuclei were stained with DAPI (blue); GFP: commercial integrin $\alpha_v\beta_5$-specific antibody detected by a goat anti-mouse IgG antibody conjugated with Alexa Fluor® 488 (green); Cy5: actin skeleton was stained with a phalloidin Alexa Fluor® 647 conjugate (red); all images are presented at 20x magnification.

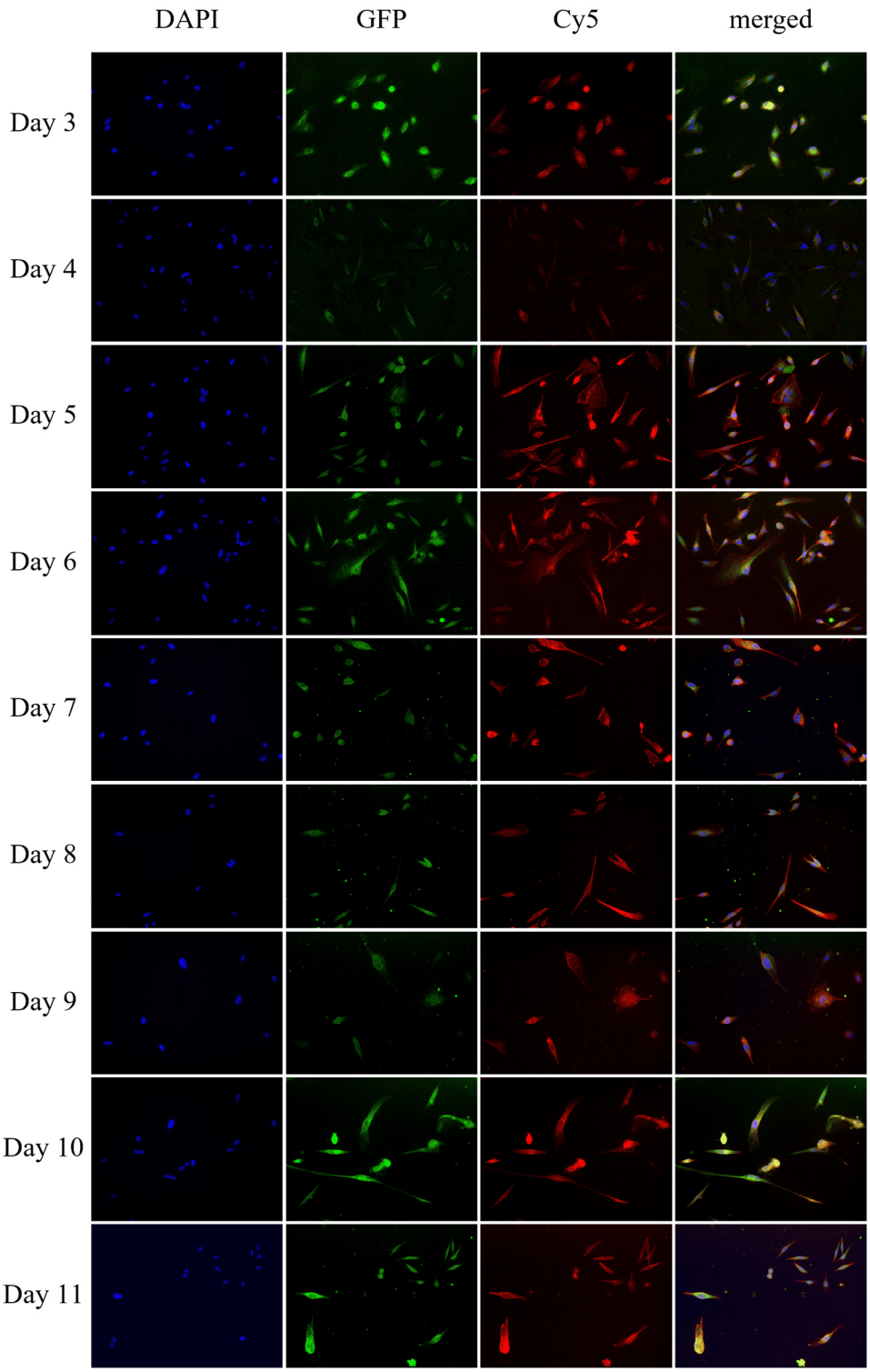

Fig. 72 Identification of integrin $\alpha_v\beta_5$ in AKH-13 cells. Tumor cells were grown on 12-well glass slides placed inside a Petri dish over a course of 11 days. 1 mL cell suspension was spread onto the glass wells and afterwards covered with culture medium CSF-DF. DAPI: nuclei were stained with DAPI (blue); GFP: commercial integrin $\alpha_v\beta_5$-specific antibody detected by a goat anti-mouse IgG antibody conjugated with Alexa Fluor® 488 (green); Cy5: actin skeleton was stained with a phalloidin Alexa Fluor® 647 conjugate (red); all images are presented at 20x magnification

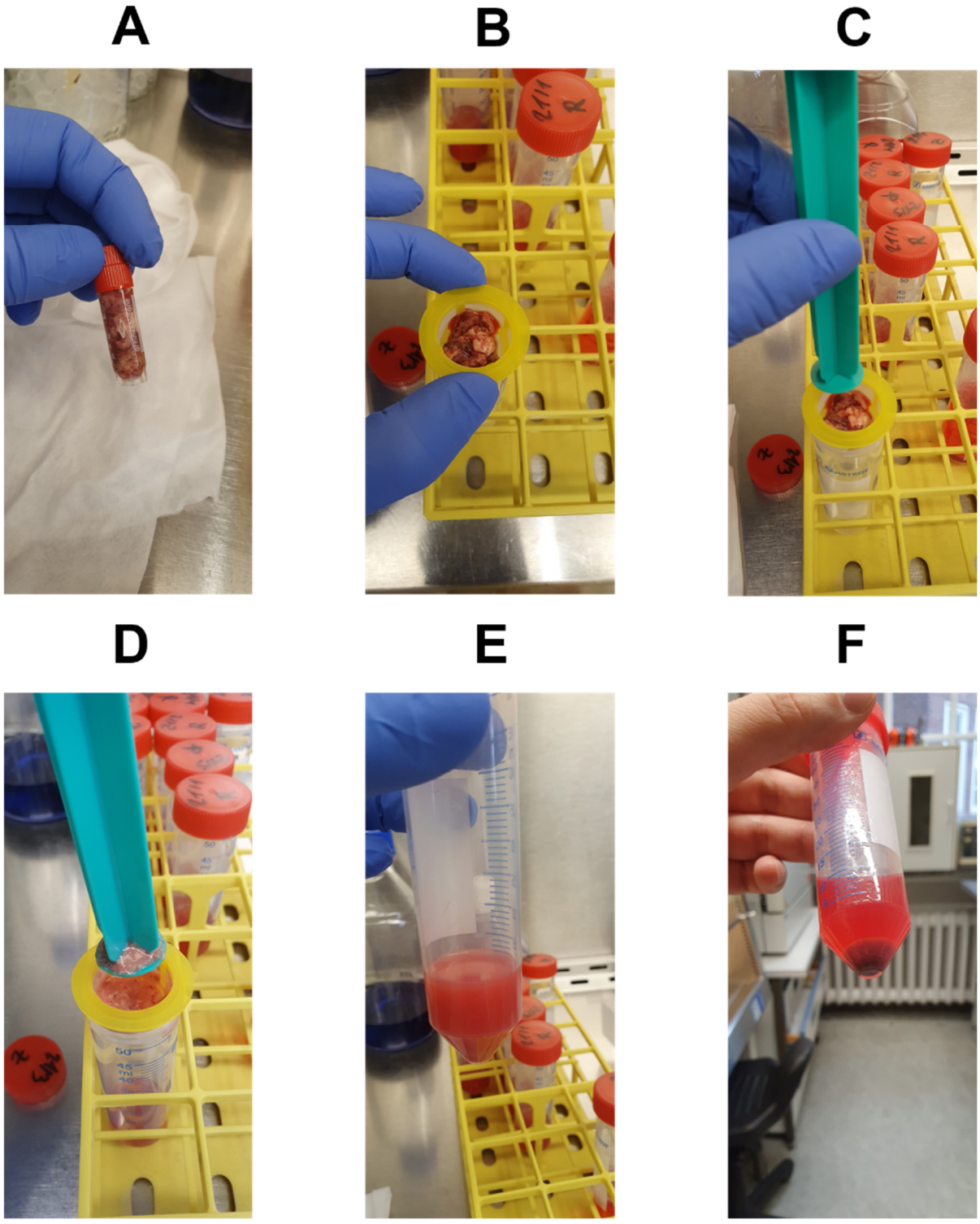

Fig. 73 Workflow for the preparation of GBM tumor tissue for cell culture. **A**: fresh tumor tissue 2-3 hours after dissection; **B**: tumor tissue was placed in a sterile molecular sieve which was placed above a 50 mL tube; **C**: tumor tissue before mashing it through a molecular sieve with a sterile stamp from a syringe; **D**: tumor tissue after mashing it through the molecular sieve; **E**: cell suspension in DMEM before centrifugation; **F**: cell suspension after centrifugation.

7.2. List of Hazardous Substances according to GHS

Chemical compound	GHS symbol	Hazard Statements	Precautionary Statements
Acetic acid	 Danger	H226, H314	P210, P280 P301+P330+P331 P303+P361+P353 P310
Acetone	 Danger	H225, H319, H336	P210 P305+P351+P338 P403+P233
Ampicillin sodium salt	 Danger	H317, H334	P261, P280 P302+P352 P342+P311
Calcium chloride, anhydrous	 Warning	H319	P280 P305+P351+P338 P337+P313
1,4,-dithiothreitol	 Warning	H302, H315, H319, H335, H412	P260, P280 P305+P351+P338 P337+P313
Ethidium bromide	 Danger	H302, H330, H341	P264, P280 P301+P330+P331 P304+P340 P310
Ethanol	 Danger	H225, H319	P210, P233 P305+P351+P338
EDTA	 Warning	H319, H332, H373	P280, P312 P304+P340 P305+P351+P338 P337+P313
Formaldehyde	 Danger	H301, H330, H311, H314, H318, H317, H341, H350, H370, H335	P202, P261, P280 P303+P361+P353 P304+P340+P310 P350+P351+P338 P308+P310
Hydrochloric acid	 Danger	H290, H314, H335	P234, P261, P271, P280 P303+P361+P353 P305+P351+P338
Manganese(II) chloride	 Danger	H301, H318, H373, H411	P273, P280 P301+P310+P330 P305+P351+P338+P310 P314
2-Propanol	 Danger	H225, H319, H336	P210, P233, P240, P241, P242 P305+P351+P338

Sodium hydroxide	 Danger	H290, H314	P234, P260, P280 P303+P361+P353 P304+P340+P310 P305+P351+P338
Triton® X-100	 Danger	H302, H318, H411	P270, P273, P280 P305+P351+P338 P310

8. Acknowledgements

Completing this doctoral thesis was a difficult but extremely rewarding journey, which would I not have been able to complete without the support, guidance, and encouragement of so many people. I want to say a heartfelt thank you to everyone who contributed to this work in so many different ways.

I am very grateful to my supervisor and mentor, Dr. Michael Schreiber. He gave me expert guidance and constant support, while giving me the freedom to conduct my research with a high degree of independence.

I would like to thank Prof. Dr. Andrew Torda for agreeing to be my supervisor and always being there for me.

My sincere thanks go to Dr. Dr. Birco Schwalbe for providing me with a constant supply of tumor samples, which made this project possible in the first place.

I am very thankful to all my colleagues in the Schreiber group at the Bernhard Nocht Institute for their collegial support, interesting conversations, and for creating such a positive and productive atmosphere.

Thank you to everyone who took the time to proofread my dissertation.

I would like to say a big thank you to my family, especially my mother, stepfather, and sister. They have supported me from the very beginning and always believed in my success.

Finally, my deepest gratitude goes to my girlfriend Soraya, whose constant motivation and unwavering support have encouraged me to be the best I can be. Without you, none of this would have been possible.

Thank you everyone for being a part of this journey.

9. Affidavit

Hiermit versichere ich an Eides statt, die vorliegende Dissertationsschrift selbst verfasst und keine anderen als die angegebenen Hilfsmittel und Quellen benutzt zu haben. Sofern im Zuge der Erstellung der vorliegenden Dissertationsschrift generative Künstliche Intelligenz (gKI) basierte elektronische Hilfsmittel verwendet wurden, versichere ich, dass meine eigene Leistung im Vordergrund stand und dass eine vollständige Dokumentation aller verwendeten Hilfsmittel gemäß der Guten wissenschaftlichen Praxis vorliegt. Ich trage die Verantwortung für eventuell durch die gKI generierte fehlerhafte oder verzerrte Inhalte, fehlerhafte Referenzen, Verstöße gegen das Datenschutz- und Urheberrecht oder Plagiate.

I hereby declare under oath that I have written this dissertation myself and have used no sources or aids other than those indicated. If, while writing this dissertation, I have used electronic aids based on generative artificial intelligence (gAI). If generative artificial intelligence (gAI)-based electronic aids were used while writing this dissertation, I affirm that my own work was paramount, and that complete documentation of all aids used is available in accordance with good scientific practice. I bear responsibility for any incorrect or distorted content generated by the gAI, incorrect references, violations of data protection and copyright laws, or plagiarism.

Halstenbek, 15th of November 2025

……..

Jan Patrick Formanski